Exciton Dynamics in π-Conjugated Polymers



Isabel Gonzálvez Pérez

Brasenose College

University of Oxford

A thesis submitted for the degree of

Doctor of Philosophy

Hilary 2025

Abstract

Conjugated polymers have generated a significant amount of interest due to their unique combination of semiconducting properties with the mechanical flexibility and chemical tunability of plastics. As a result, the use of these materials has steadily increased over the past fifty years, with applications in optoelectronic devices such as organic photovoltaics (OPVs), light-emitting diodes (OLEDs), and field-effect transistors (OFETs).

From a theoretical perspective, however, the study of their properties continues to present significant challenges. These materials are composed of long polymer chains containing hundreds to thousands of monomers, resulting in systems with tens of thousands of electrons. Furthermore, their optical and transport properties are equally controlled by electronic correlations and the strong coupling to nuclear degrees of freedom. As a result, the intermediate regime in which they belong lies beyond the reach of traditional quantum chemistry, usually limited to small molecules, while simultaneously requiring a more detailed many-body treatment than that provided by standard solid-state approaches, which typically describe crystalline semiconductors in terms of delocalised band-like states. To address these challenges, multiple theoretical approaches have been proposed, each targeting a specific area of exciton behaviour in conjugated polymers.

In this thesis, a unified multiscale framework is developed to follow the complete lifecycle of the exciton and the dynamical processes after photoexcitation, including ultrafast intrachain relaxation and long-range interchain migration. This approach is based on large-scale simulations designed to further the current understanding of exciton dynamics across multiple spatial and temporal scales. The intrachain dynamics following photoexcitation are modelled using the Frenkel–Holstein Hamiltonian, which explicitly includes coupling between localised electronic excitons and both high-frequency vibrational and low-frequency torsional phonons. The exciton–phonon coupling is identified as the primary mechanism responsible for the ultrafast decoherence and localisation of the exciton, and its subsequent relaxation into lower-energy states. The Frenkel-Holstein Hamiltonian is approached through Density Matrix Renormalisation Group (DMRG) methods which achieve an efficient

truncation of the Hilbert space by retaining only the components with the largest value in the spectrum of the reduced density matrix, thereby preserving the entanglement structure essential to the exciton–phonon dynamics. In particular, the dynamics are computed using the Time-Evolving Block Decimation (TEBD) algorithm, which allows for the study of the time evolution of large quantum systems within this framework.

Subsequent exciton dynamics on longer timescales, involving interchain transfer, are modelled using a Förster-type rate theory adapted to disordered polymer films. Within this framework, the effects of energetic disorder and macromolecular structural variations on exciton migration efficiency across coexisting disordered and ordered domains are examined.

To connect the theoretical framework with experimental observables, time-resolved fluorescence anisotropy is introduced as a viable probe for examining the processes of exciton relaxation in these materials. On the ultrafast timescale, a multi-exponential decay in the fluorescence anisotropy is observed, indicating a complex exciton localisation process. The analysis of the fluorescence anisotropy spectra reveals three distinct phases: exciton decoherence caused by the coupling to high-frequency C–C stretches within 4 fs, followed by relaxation from a high-energy delocalised state to a lower-energy localised exciton state, and further localisation driven by coupling to torsional phonons. Finally, fluorescence anisotropy is also used to survey the impact of film morphology; by resolving anisotropy as a function of time, information can be extracted about local order within the polymer film.

Acknowledgements

It's surprisingly difficult to find the right words to write this section. This journey has taken me along a considerably different and longer path from what I could have expected when I first embarked on it. Along the way, I have been fortunate to receive more patience and support than I could ever truly account for, and while I can't thank everyone as fully as they deserve, what follows is a sincere attempt.

Firstly, I would like to thank my supervisor, Professor William Barford. I am fully aware that I have not always been the easiest student to guide, and I am incredibly grateful for the patience, understanding, and grace he has shown me. I am also deeply thankful for the time and effort he has dedicated to discussing my work, and not least for carefully reading and commenting on this project. I would like to thank everyone I have encountered in the Barford Group over the years, in particular László and Darren for the many conversations and much-needed encouragement, especially whenever technology decided to work against me.

Many things have changed since I first set out on this path, and I am grateful beyond words to those who have stood by me along the way. Nobody figures everything out or holds everything together alone, sometimes it truly does take a community. I would like to thank my family and friends: Jaime and Ángeles, for weathering many storms alongside me, Tom, for always being ready with a coffee and a more balanced perspective when it was most needed, and Giuliano, for filling the gaps left by frustration and setbacks with good food and laughter. Special thanks are also due to Vicky, whose strength, unwavering support, and, maybe a few beers, have kept me standing through difficult times; we both know that I would not be here without her kindness and encouragement.

Finally, I would like to take a moment to appreciate those who are no longer here, those I lost along the way. I am grateful for their support in this journey. I still think of them, and I will always carry them with me wherever I go. I am especially grateful to Isabel, thank you for the whimsy, and for teaching me everything that is truly worth knowing. I think I am finally ready to do the things you hoped I could reach, I am sorry it took me a while to get here.

Contents

List of Figures **viii**

List of Abbreviations **x**

1 Introduction **1**

1.1 Conjugated polymers and their applications 2

1.1.1 The structure of conjugated polymers 2

1.1.2 Applications of π-conjugated polymers 7

1.1.3 Challenges and advances in applications 10

1.2 Properties of π-conjugated polymers 12

1.2.1 MEH-PPV 14

1.2.2 Thermal influence on morphological transitions 16

1.2.3 Solvent effects on the structure 18

1.2.4 Spectroscopic probes for the study of exciton dynamics in conjugated polymers 22

1.3 Thesis structure 25

2 Theoretical background **27**

2.1 Excitons in π-conjugated polymers 28

2.1.1 Wannier-Mott excitons 28

2.1.2 Frenkel excitons 29

2.2 Exciton dynamics 31

2.2.1 The Frenkel Hamiltonian 31

2.2.2 The role of disorder 33

2.2.3 Exciton-phonon interactions 37

2.2.4 Exciton-polarons 43

2.2.5 Coupling of the exciton to torsional degrees of freedom . . . 47

2.3 Intermolecular dynamics: FRET 53

2.3.1 Efficiency of FRET 58

2.4 Spectroscopical methods as a probe of conformational order in conjugated polymers 59

2.4.1 Vibronic structure 59
2.4.2 Polar fluorescence anisotropy 65
2.4.3 Time-resolved polar fluorescence anisotropy 69

3 Computational methods 71
3.1 From conventional methods to TEBD: addressing computational limitations 72
3.1.1 Density Matrix Renormalisation Group 74
3.1.2 The Matrix Product State formalism 75
3.1.3 Time evolution: the TEBD algorithm 79
3.2 Open quantum systems 83
3.2.1 The quantum jump trajectories method 84

4 Intramolecular dynamics 88
4.1 Experimental observations and contextualisation 90
4.2 Modelling intrachain exciton dynamics in conjugated polymers . . . 92
4.2.1 Truncation errors arising from the TEBD algorithm 96
4.3 Exciton decoherence 97
4.4 Energy dissipation and further localisation 99
4.5 Ultrafast fluorescence depolarisation 106
4.6 Discussion and concluding remarks on ultrafast exciton dynamics . 109

5 Intermolecular dynamics 112
5.1 Exciton evolution through intermolecular interactions 113
5.1.1 FRET transfer rate calculations: vibronic transitions 117
5.1.2 Effects of disorder in FRET 120
5.2 Fluorescence anisotropy as a probe of intermolecular dynamics . . . 127
5.3 Exciton migration in films 133
5.3.1 Structural observations through fluorescence anisotropy . . . 136
5.4 Discussion 141

6 Conclusions and further work 144

Appendices

A Simulation parameters 149
A.1 Physical parameters for the simulations 149
A.2 Computational details: intramolecular simulations 150
A.3 Computational details: intermolecular simulations 150

B Technical details of the simulations **152**
B.1 Simulation box: initial configurations 152
B.2 Nematic order parameter calculations 154

C The effective Hamiltonian **157**
C.1 Derivation of the effective Hamiltonian 157

D Extraction of transport coefficients from kinetic data **160**
D.1 Dwell time and distance per hop 160
D.2 Evolution in time of the mean squared displacement 162

References **166**

List of Figures

1.1 Formation of the π and π^* molecular orbitals and band structure. . 3
1.2 Energy band structure of PPV. 6
1.3 The wide range of applications of π-conjugated polymers. 7
1.4 Comparative of conversion efficiency in photovoltaic cells by material. 8
1.5 Jablonski diagram. 12
1.6 Absorption spectra of MEH-PPV. 15
1.7 The blue and the red phase of MEH-PPV, absorption and emission spectra. 18
1.8 Atomic force microscopy images of P3HT films. 21

2.1 Disorder induced changes in the exciton density. 34
2.2 LEGS of π-conjugated polymers. 35
2.3 Exciton density for LEGS and QEES. 36
2.4 Vibrational and torsional phonon modes in PPV derivatives. 38
2.5 The vibrational modes within PPV derivatives. 39
2.6 Representation of the Franck-Condon principle and the nuclear displacement 41
2.7 Exciton-phonon correlation function 45
2.8 Exciton localisation via exciton-roton coupling. 49
2.9 FRET and Dexter energy transfer processes. 54
2.10 The angle between the absorption and emission dipoles in TRFA. . 67

3.1 DMRG: the finite and the infinite algorithms. 75
3.2 The TEBD algorithm, a graphical representation. 82
3.3 Two quantum jump trajectories from equal initial states. 87

4.1 Coherence length as a function of time in PPV chains. 98
4.2 Exciton density evolution with a single jump. 100
4.3 Exciton density evolution for the relaxation from QEES to LEGS showcasing multiple jumps. 101

4.4 Exciton density localisation driven by coupling to torsional phonon modes. 103
4.5 Localisation length in time for a simulation of PPV. 105
4.6 Fluorescence anisotropy decay from an initial QEES state. 108

5.1 Schematic representation of interchain and intrachain angle nomenclature. 116
5.2 Schematic representation for the 4 lowest vibronic transitions. . . . 118
5.3 Effects of torsional disorder in the exciton lifetime. 121
5.4 Effects of torsional disorder in the exciton diffusion length. 123
5.5 Exciton diffusion length increase with nematic order. 126
5.6 Nematic order vs polar fluorescence anisotropy. 130
5.7 Non-linear relationship between the nematic order and the fluorescence anisotropy. 130
5.8 Heterogeneity within π-conjugated polymer films. 131
5.9 Average distance per hop, comparison of samples with different structural order. 132
5.10 Average dwell time per hop, comparison of samples with different structural order 133
5.11 Predicted MSD as a function of time. 134
5.12 Log–log plot of the MSD as a function of accumulated time. 135
5.13 Exciton energy over time. 136
5.14 Experimental pump-probe anisotropy decays for MEH-PPV films. . 137
5.15 Nematic order profile across distances for MEH-PPV films. 138
5.16 Fluorescence anisotropy decay for P3HT films. 139
5.17 Nematic order profile for P3HT/MEHPPV. 140

B.1 Configuration of the simulation box 155
B.2 Schematic representation of the initial configuration for the simulation box 156
B.3 Initial configuration, $S \simeq 0.5$ 156
B.4 Initial configuration, quasi-parallel chains 156

D.1 Linear fitting for the average dwell time taken per hop. 161
D.2 Distance per hop, fitting for a sub-linear evolution. 162
D.3 Linear fitting for the MSD vs time. 163

List of Abbreviations

CC . . . . . Coupled Cluster

CI . . . . . Configuration Interaction

DADA . . . . . Donor-Acceptor (copolymers)

DFT . . . . . Density Functional Theory

DMRG . . . . Density Matrix Renormalisation Group

F8 . . . . . 9,9-Dioctylfluorene

F8BT . . . . . Poly(9,9-Dioctylfluorene-alt-benzothiadiazole)

FRET . . . . . Förster Resonance Energy Transfer

HOMO . . . . Highest Occupied Molecular Orbital

LEGS . . . . . Local Exciton Ground States

LUMO . . . . Lowest Unoccupied Molecular Orbital

MEH-PPV . . Poly(2-methoxy-5-(2'-ethylhexyloxy)-*p*-phenylene vinylene)

MeLPPP . . . Methyl-Substituted Ladder-Type Poly(para-phenylene)

m-LPPP . . . Methoxy-Substituted Ladder-Type Poly(para-phenylene)

MPS . . . . . Matrix Product State

OLED . . . . . Organic Light-Emitting Diode

OFET . . . . . Organic Field-Effect Transistor

OPV . . . . . Organic Photovoltaic (cell)

P3AT . . . . . Poly(3-Alkyl Thiophenes)

P3HT . . . . . Poly(3-Hexylthiophene)

PA . . . . . Polyacetylene

PDA . . . . . Polydiacetylene

PL . . . . . Photoluminescence

PPP . . . . . Polyphenylene

PPV . . . . . Poly(*p*-Phenylene-Vinylene)

QEES . . . . . Quasi-Extended Exciton States

SMS . . . . . Single Molecule Spectroscopy

SSH . . . . . Su-Schrieffer-Heeger

TDSE . . . . . Time-Dependent Schrödinger Equation

TEBD . . . . . Time-Evolving Block Decimation

THF . . . . . Tetrahydrofuran

TNT . . . . . Tensor Network Theory

TRFA . . . . . Time-Resolved Fluorescence Anisotropy

2C3PEPS . . . Two-Colour Three-Pulse Photon Echo Spectroscopy

3PEPS . . . . Three-Pulse Photon Echo Spectroscopy

1 Introduction

The past three decades have witnessed a remarkable expansion in the research of π-conjugated polymers towards commercial applications. This growth has been directed, at least in part, by the pursuit of efficient, renewable energy sources, for which synthetic semiconducting materials present a less expensive alternative to the widely used naturally occurring materials such as silicon [1].

The first instance of conducting polymers was reported by Shirakawa, MacDiarmid and Heeger in 1977 [2, 3], a discovery for which they received the Nobel Prize in Chemistry in 2000 [4–6]. Just ten years later, in 1987, doped π-conjugated polymers were being synthesised with significantly high electrical conductivity, reaching levels as high as $20,000\ Scm^{-1}$ [7]. Furthermore, as research on doped conjugated π-polymers advanced some characteristics traditionally associated with metals only were observed, including an increase in conductivity at lower temperatures, and the ability to reflect electromagnetic waves [8].

Since their discovery, substantial advancements have been made towards understanding the relationship between the structure and the physical properties of these materials. This has been accompanied by the fast development of new synthetic

routes for their production, thus improving the accessibility and widespread adoption of organic semiconductors. As a result, conducting polymers have surpassed the initial expectations for their performance, even exceeding some of the capabilities of conventional inorganic semiconductors.

1.1 Conjugated polymers and their applications

1.1.1 The structure of conjugated polymers

The defining characteristic of conjugated polymers is the delocalisation of the electrons along the polymer backbone, which is a direct result of the alternating single and double bonds within the chain and confers conjugated polymers their unique properties. These carbons, with sp^2 hybridisations, form a planar configuration that enables the effective overlap of the p-orbitals; corresponding to the π bonding and π^* antibonding molecular orbitals, this is represented in Figure 1.1. This π-electron system is responsible for the notable optical and electronic properties observed in conjugated polymers.

Brief overview of the theoretical models for π-systems

In order to describe the electrons within these π-conjugated systems, the simplest method is the Hückel model [9], which considers uniquely the π-electron interactions, neglecting any contribution from the σ-bond. This model provides a foundational qualitative understanding of π-molecular orbitals, as schematically represented in Figure 1.1 (b). As the system size increases, the difference between the energy of these states diminishes, which eventually results in the formation of the π-π^* bands. Without any additional interactions in the Hückel system, these bands would form a continuous spectrum, however, when the electron-lattice coupling is included through the Peierls formalism, these bands are separated by an energy gap E_g (as

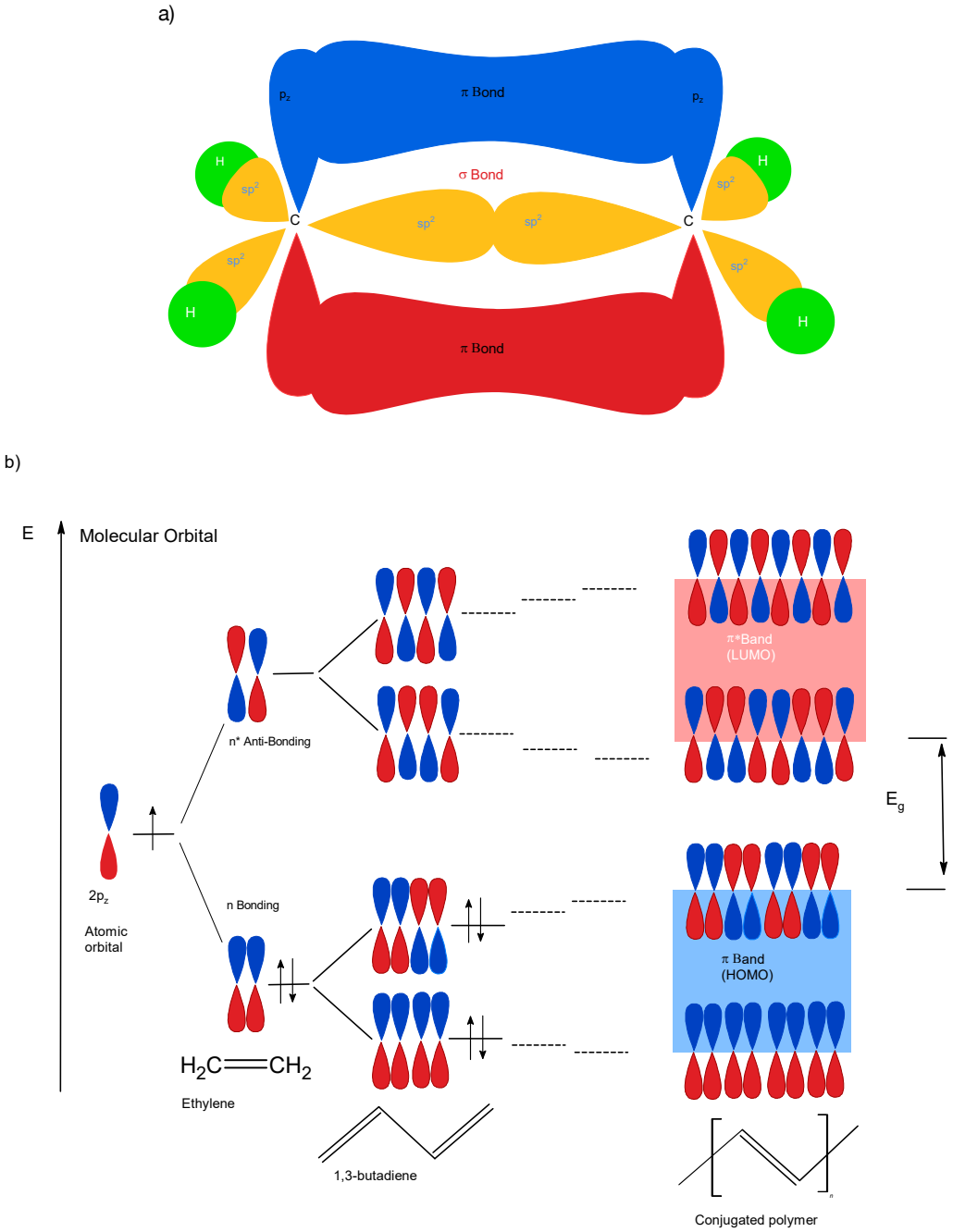


Figure 1.1: Formation of the π and π^* molecular orbitals and band structure in π-conjugated systems. (a) Representation of a double bond and the structure of sp^2 hybridisation. (b) Schematic representation of the progression from discrete energy levels of the π and π^* molecular orbitals to the formation of continuous bands, the π-band (HOMO) and π^*-band (LUMO).

shown in Figure 1.1), known as the band gap. The electronic Hamiltonian for the Hückel model, which describes a non-interacting electron model, is given by:

$$\hat{H}_{\mathrm{HMO}} = \sum_{i} E_i \hat{n}_i - \sum_{i,\sigma} t_i \left(\hat{c}^{\dagger}_{i+1\sigma} \hat{c}_{i\sigma} + \hat{c}^{\dagger}_{i\sigma} \hat{c}_{i+1\sigma} \right) \tag{1.1.1}$$

where E_i is the energy of the electron at site i, t_i is the transfer (hopping) integral, which represents the electronic coupling between adjacent sites and quantifies the probability of electron transfer between neighbouring orbitals. The operators $\hat{c}^{\dagger}_i$ and $\hat{c}_i$ are the creation and annihilation operators for an electron at site i, with spin σ, and, $\hat{n}_i$ is the number operator given by $\hat{c}^{\dagger}_i \hat{c}_i$ which measures the occupancy of an electron at site i. The transfer integral t_i, determines the degree of electronic delocalisation along the conjugated backbone. Larger values of t_i correspond to a stronger coupling between neighbouring sites, promoting in turn delocalisation which results in lower energy excitations, while smaller values lead to localisation of the electronic wavefunction and higher energy states.

This model can be expanded by including the coupling between the electrons and lattice displacements, as in the Peierls and Su-Schrieffer-Heeger (SSH) model [10], or by incorporating electron-electron interactions, as in the Pariser-Parr-Pople (PPP) model [11–13]. The considerations included in the Peierls model are central for understanding the dimerisation of one-dimensional systems [14, 15]. The spontaneous rearrangement of the lattice into alternating short and long bonds, known as the Peierls distortion, lowers the system's total energy by opening a gap at the Fermi level, transforming it from a conducting to a semiconducting state [16], which is shown in Figure 1.2. The Peierls gap between the valence band and the conduction bands impacts the electronic and optical properties of π-conjugated polymers. The SSH model extends this framework by implementing a dynamic treatment of the electron-phonon interactions. These significantly affect

the electronic structure and enable the analysis of solitons. Thus, this model is particularly useful in analysing the electronic properties of π-conjugated polymers and is widely used to understand the properties of polyacetylene, where these non-linear excitations play an important role [17]. The Hamiltonian corresponding to the SSH model is as follows [16]:

$$\begin{aligned}\hat{H}_{\mathrm{SSH}} = &\sum_i E_i \hat{n}_i - \sum_{i,\sigma} \left[(t_0 - \alpha_i (u_{i+1} - u_i)) \left(\hat{c}^\dagger_{i\sigma} \hat{c}_{i+1\sigma} + \hat{c}^\dagger_{i+1\sigma} \hat{c}_{i\sigma} \right) \right] \\ &+ \sum_i \left(\frac{P_i^2}{2M} + \frac{K}{2} (u_{i+1} - u_i)^2 + K\delta r (u_{i+1} - u_i) \right) \end{aligned} \tag{1.1.2}$$

where α_i represents the electron-phonon coupling constant and u_i represents the displacement of the i-th site from its equilibrium position. K is the elastic constant associated with the lattice vibration. The last term $K\delta r(u_{i+1} - u_i)$ corresponds to a linear potential that arises in non-uniform conditions, accounting for deviations from the equilibrium bond length determined by the σ-electrons.

The PPP model, which is semi-empirical in nature, introduces electron-electron interactions into the system; this model provides high accuracy predictions in systems where electron correlation plays a significant role. However, the model requires experimental data for some of the parametrisation, which impacts the transferability of the conclusions obtained between systems [19]. The PPP model for a linear conjugated polymer system is given by [16]:

$$\hat{H}_{\mathrm{PPP}} = \hat{H}_{\mathrm{HMO}} + \sum_i U_i \hat{n}_{i\uparrow} \hat{n}_{i\downarrow} + \sum_{i<j} V_{ij} (\hat{n}_i - z_i)(\hat{n}_j - z_j) \tag{1.1.3}$$

where U_i describes the on-site Coulomb repulsion, while V_{ij} represents the long-range Coulomb interaction between electrons at different sites i and j.

When both electron-electron and electron-lattice interactions are significant, as is often the case in conjugated polymers the method can be modified to include the

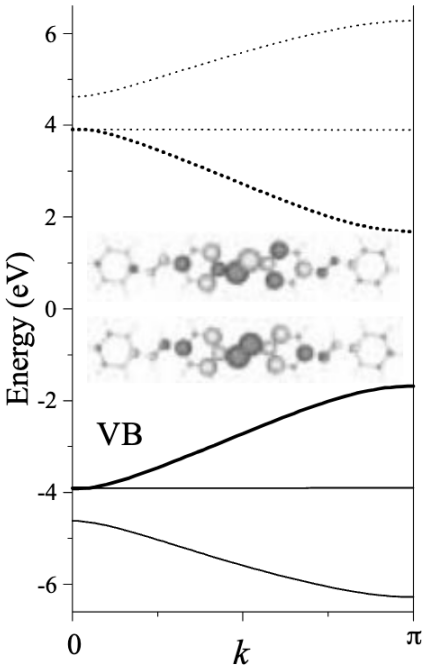


Figure 1.2: Energy band structure of poly(*p*-phenylene-vinylene) calculated using Hartree-Fock with the PPP model. The figure shows the highest valence and lowest conduction bands. Figure reproduced from [18].

electron-phonon coupling terms from the Peierls model into the PPP model, leading to the Pariser-Parr-Pople-Peierls (PPPP) formalism [19, 20]. This approach accounts for static lattice distortions while still capturing the electron-electron interactions.

Some of these π-conjugated systems have also been studied with advanced computational methods such as Density Functional Theory (DFT), Coupled Cluster (CC) theory and Configuration Interaction (CI) [18, 19, 21]. Although these approaches provide accurate results, the computational costs increase significantly as the system size grows, and the accuracy diminishes as a result of error accumulation. In summary, these approaches are effective for characterising moderately sized systems and are often used in conjunction with theoretical models, such as PPPP, but encounter difficulties with larger systems, especially when considering intermolecular interactions required in practical applications [22].

1.1.2 Applications of π-conjugated polymers

The distinctive optoelectronic characteristics, stemming from the delocalised π-electron system, underpin the diverse range of applications for conjugated polymer materials. This section provides an overview of several of these applications, some of which can be found in Figure 1.3.

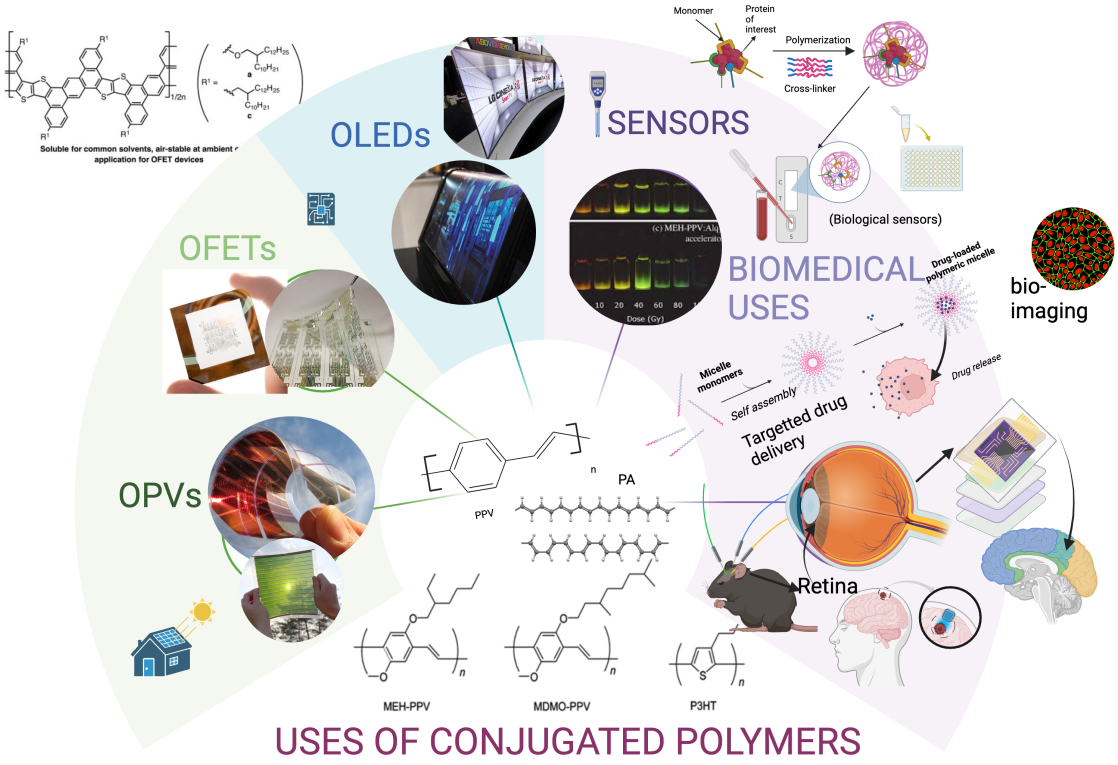


Figure 1.3: The wide range of applications of π-conjugated polymers. Contains parts adapted from figures found in [23–30].

Photovoltaic cells

Photovoltaic technology has become one of the most successful applications of π-conjugated polymers as a result of the broad absorption spectrum observed in these materials [31]. Historically, their use was limited due to the lower efficiencies achieved by organic photovoltaic cells, hovering around 9%, compared to the consistently

higher efficiencies of traditional inorganic photovoltaic cells. For instance, inorganic cells based on mono-crystalline silicon achieved efficiencies of 24.7%, and multi-junction cells have surpassed 30% [32]. However, recent advances in material design

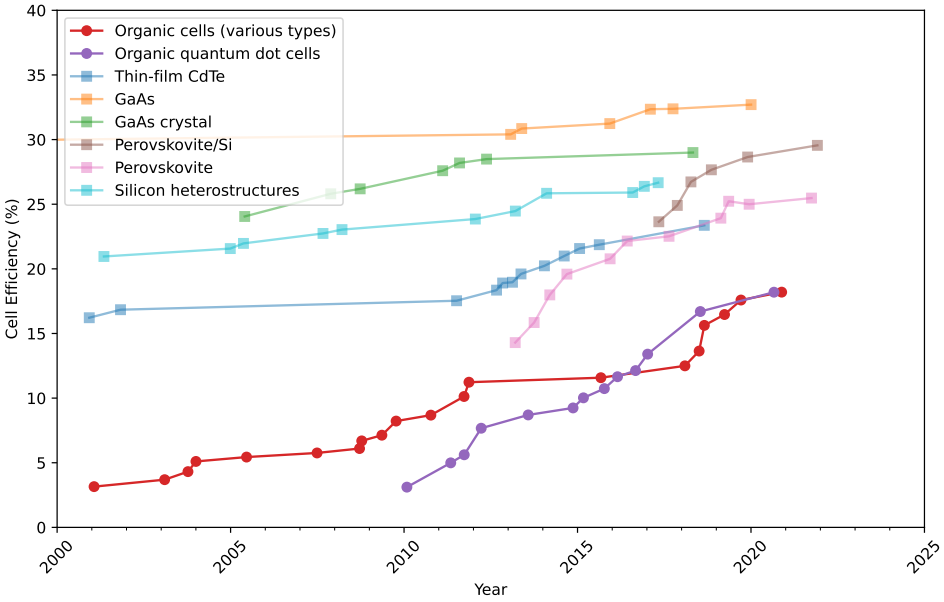


Figure 1.4: Highest confirmed conversion efficiency for research cells across a range of photovoltaic technologies. Coloured according to material and structure characterisation. The data represented as points show solar cells made with a significant contribution of organic semiconductors of different structures. Figure created from publicly reported data documented in [33].

have allowed for a significant increase in their market competitiveness. To this end, Figure 1.4 illustrates the upward trajectory in the maximum reported for the efficiencies of various solar cell types, categorised by material composition. In red and purple, the considerable improvement in the efficiency of OPVs can be observed [33]. This figure includes the highest recorded efficiency for organic cells which reached 19.3% in 2022 for single-junction organic solar cells [34] and 18.1% through the use of quantum dot technologies in combination with perovskite and organic semiconductors in 2024 [35]. These improvements, along with the flexible and lightweight nature of this type of photovoltaic cells which are used for

diverse applications (e.g., vehicles, building materials), underscore OPVs potential to transform energy generation.

Light-emitting and electronic applications: OLED and OFET

The potential for light-emitting and conductive applications of π-conjugated polymers was rapidly recognised from their very early days [36, 37]. At present, organic light-emitting diodes (OLEDs) have revolutionised display technology, despite the greater durability and efficiency of traditional LEDs, owing to their ability to enable the fabrication of ultra-thin, flexible screens, which are now commonly used in consumer electronics such as smartphones and TVs [38].

Similarly, organic field-effect transistors (OFETs) constitute a promising alternative to conventional silicon-based transistors that offer advantages through lower production costs and an increased flexibility of the final devices [31, 39, 40].

Sensors

Due to the tunability of their molecular architecture, it is possible to engineer polymers with specific pendant or side chains with reactive groups that react to specific environmental stimuli. These reactions sufficiently alter their molecular structure, resulting in changes to their optoelectronic properties, which are harnessed for applications in chemical sensing. As a result, research focused on amplifying these changes has led to the development of highly selective sensors capable of detecting ions, gases, and other analytes [41, 42].

One important advantage offered by conjugated polymers towards their use as sensors is the reversibility of their reactions with target molecules which enables them to be reused after appropriate treatment [43]. This feature reduces the waste associated with disposable sensors, making conjugated polymers a viable environmentally sustainable choice. Furthermore, the unique physical characteristics

of π-conjugated polymers materials enable their processing into films and arrays, thus, simplifying their integration into different sensor platforms. This versatility has extended their use to safety applications, such as detecting explosives [44], and medicine, where they are used for detecting DNA, specific proteins and viruses [45].

Biomedical applications

Alongside the previously discussed better-known applications, the use of conjugated polymers has contributed to essential progress in the biomedical sciences in the last decade. Within this field, they are employed in drug delivery systems, bio-imaging applications, neuronal activation and retinal implants, as well as in photodynamic therapy for combating antibiotic resistance [38, 46–52].

However, despite their current success in this field, at first, the application of conjugated polymers in biomedical fields presented considerable challenges due to their inherently hydrophobic and low-polarity nature. To overcome these limitations, surface modifications, such as conjugation with hydrophilic biomolecules or polyethylene glycol, have been developed [53–58]. On the other hand, despite the initial concern, the characteristic hydrophobicity of these polymers is advantageous for applications requiring interactions with biological membranes. This hydrophobicity can be harnessed to control cellular processes for the use of conjugated polymers for drug delivery systems, antimicrobial coatings, gene delivery and tissue engineering [59–62].

1.1.3 Challenges and advances in applications

Conjugated polymers have attracted considerable attention in different fields of technology including; advanced electronic devices (as discussed above), energy storage systems and functional coatings [63–66]. Despite nearly five decades of progress, the

field of conjugated polymers continues to face significant challenges towards their practical application, including lower efficiencies, reduced device lifetimes and the requirement for significantly more demanding synthesis and purification processes in comparison to those required by inorganic semiconductors [67].

Nevertheless, recent advances in understanding the fundamental physics of these materials have led to targeted polymer design strategies aimed at overcoming some of these limitations. For instance, the design of ladder-type polymers containing a significantly lower proportion of structural defects has streamlined the purification processes [68, 69]. In a similar context, the creation of donor-acceptor copolymers, which alternate between electron-rich and electron-deficient monomers, has enabled the control of the band-gap in these materials and the fine-tuning of their electronic properties [70–73].

In parallel, research efforts in OFETs have focused on enhancing both charge carrier mobility and stability, which heavily depend on developing methods for the control of the structural properties of these materials. These morphological features can be varied through the control of chain conformations at the molecular level and the control of crystallinity on a larger scale [74, 75]. Moreover, the optimisation of film morphologies also has a positive impact on the efficiency of OLEDs by reducing the quenching effects caused by aggregation [76–78].

On the other hand, biomedical applications present some unique challenges, such as the need for high selectivity for specific reactions and environments, and a requirement for high stability, which can be improved through enhancing the homogeneity of the material to avoid degradation *in vivo* conditions [52, 56, 57, 79–82].

Additionally, scaling the production of conjugated polymers from the laboratory to large-scale deployment in the medical field presents a unique set of difficulties.

Among these, the issue of reproducibility in medical devices, which is hindered by structural disorder in conjugated polymers, stands out as especially significant [83].

Despite these challenges, the broad range of applications for conjugated polymers, coupled with the rapid advancement in their targeted design, highlights the strong future potential for this field. A deeper understanding of their underlying structure could be pivotal in overcoming existing obstacles and expanding their use across diverse industries.

1.2 Properties of π-conjugated polymers

Following the detailed examination of the various applications of conjugated polymers, this section will shift focus towards the primary objective of this work: to deepen the understanding of the fundamental mechanisms that underline the distinctive properties of π-conjugated polymers.

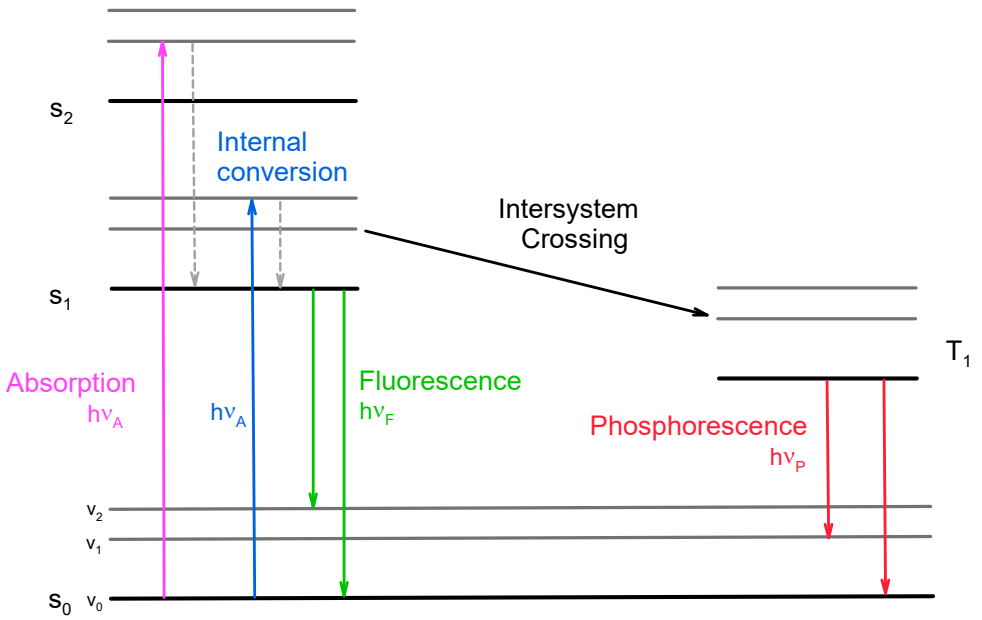


Figure 1.5: Jablonski diagram illustrating the key photophysical processes in π-conjugated polymers: photon absorption, non-radiative internal conversion, fluorescence, and phosphorescence.

A critical aspect of the utility of these materials lies in their interaction with light, encompassing a series of photophysical processes that are summarised in the Jablonski diagram depicted in Figure 1.5. In π-conjugated polymers, the absorption of photons results in the excitation of electrons from the ground state S_0 to an excited electronic state, typically a singlet state such as S_1 or S_2. This excitation occurs through a vertical transition, as described by the Franck-Condon principle. In this approximation, the electronic transitions are considered significantly faster than nuclear motion, allowing any changes to the nuclear structure to be neglected during these nearly instantaneous excitations without a substantial loss in accuracy [84, 85]. If the molecule is initially excited to a higher vibrational level, the excess vibrational energy is dissipated through a non-radiative relaxation process, which results in the population of the lowest vibrational level of the excited state. In accordance with Kasha's rule, radiative decay occurs then predominantly from this lowest vibrational level of S_1 to S_0, a process known as fluorescence [86]. The resulting emitted photon exhibits a Stokes shift as a result of the energy loss caused by the vibrational relaxation prior to emission. In π-conjugated polymers, fluorescence generally occurs on the nanosecond timescale and is highly dependent on the molecular structure of the polymer [87].

Alternatively, the initial excited state may undergo intersystem crossing to a triplet state T_1 aided by spin-orbit coupling. The subsequent radiative decay from this triplet state back to the ground state is known as phosphorescence. This process is characterised by longer decay times, typically ranging from tens to hundreds of milliseconds [88].

The classification of π-conjugated polymers includes a broad range of molecules with variations in both their structure and their characteristic properties. Traditionally, they are categorised into four subgroups based on their structural

backbone: polyacetylenes (PA), polydiacetylenes (PDA), polyphenylenes (PPP), and poly(phenylene vinylene)s (PPV). PAs, which were the first to be synthesised, are notable for their high electrical conductivity capabilities, but, their practical applications are severely restricted due to their instability in air. In contrast, PDAs exhibit a greater resistance to degradation, resulting from their tendency to form highly ordered crystal structures [89]. PPPs, defined by a backbone composed entirely of aromatic carbons, exhibit increased rigidity and thermal stability. Within this class, para-linked polyphenylenes demonstrate enhanced electronic conjugation, making them suitable for high-performance electronic devices, while ortho-linked and meta-linked polyphenylenes are more commonly used in applications requiring superior mechanical stability [90]. Finally, PPVs, which have an alternating aromatic and olefinic backbone, are distinguished by their smaller energy band gap and tunable optical properties, these polymers are the primary focus of this work. In addition, there are conjugated polymers that incorporate non-carbon atoms, such as sulfur, nitrogen, or oxygen, within their backbone. The inclusion of these atoms can modify their optoelectronic properties, making them highly versatile for a wide range of applications [91].

1.2.1 MEH-PPV

This thesis studies the underlying mechanisms of exciton dynamics, with a primary focus on PPV-based conjugated polymers. Most of the simulations are performed on poly(2-methoxy-5-(2'-ethylhexyloxy)-1,4-phenylenevinylene) (MEH-PPV), a soluble derivative of PPV widely studied for its optical and electronic properties. Nevertheless, this work aims to extend the conclusions drawn from the obtained results to similar polymers.

MEH-PPV exhibits significantly higher solubility in organic solvents compared to the base polymer, PPV, which is attributed to the methoxy ($-OCH_3$) and ethyl-hexyloxy ($-OCH_2CH(C_2H_5)(CH_2)_3CH_3$) side chains [92]. The main differences between the spectra of MEH-PPV and PPV have been attributed to the relative greater torsional flexibility of the phenyl rings in PPV in comparison to MEH-PPV. The reasoning for this is found in the limitations imposed by the steric hindrance of the bulkier side groups present in MEH-PPV, which constrain any torsional motion and lead to a more planar backbone structure [18, 93–95].

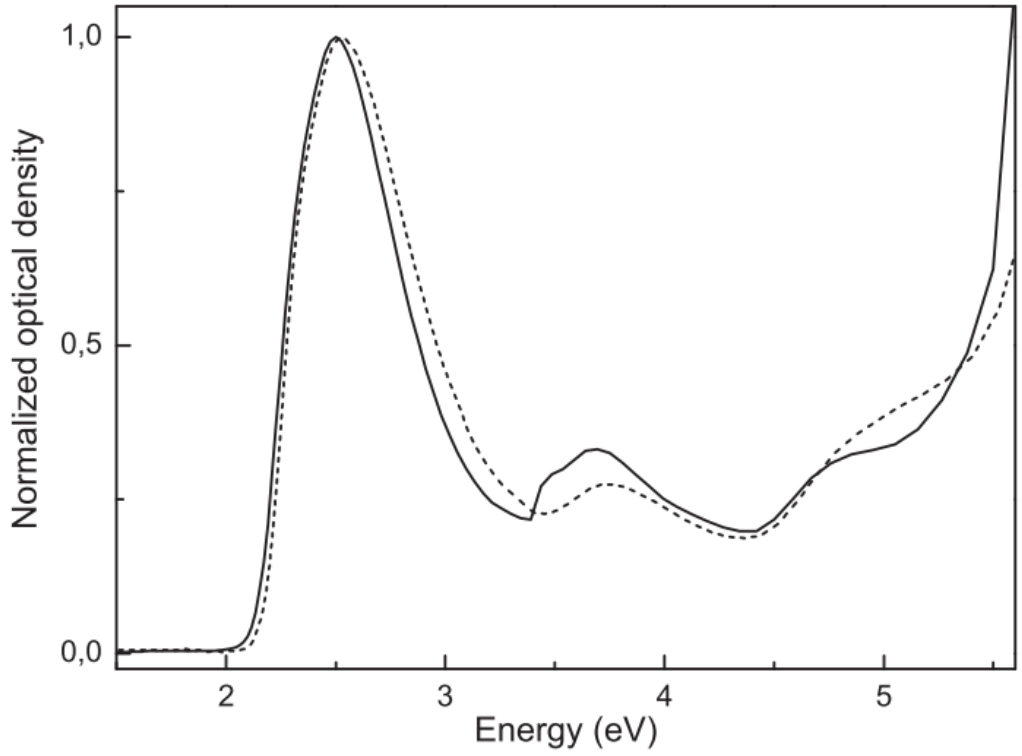


Figure 1.6: Absorption spectra of MEH-PPV in film (solid line) and chloroform solution (dashed line). Figure reproduced from [96].

MEH-PPV exhibits absorption across the UV and visible spectrum, with emission limited to visible light, even under intense UV excitation [96]. This property makes MEH-PPV highly suitable for optoelectronic technologies, as evidenced by its early use in the development of OLEDs [40, 97, 98], white-light organic LEDs [99], and

organic lasers [100, 101] while also being a common material in early stages of photovoltaic devices [102–104]. Furthermore, MEH-PPV is commonly used for research purposes as its high solubility enables single-molecule spectroscopy studies, facilitating clearer observations into the effects of chain conformation [99, 105].

As shown in Figure 1.6, the absorption spectrum of MEH-PPV presents four distinct absorption bands, with a maximum at 2.5 eV attributed to the main HOMO-LUMO transition. Two additional absorption bands are identified at higher energies around 3.6 eV involving both delocalised and localised electronic states. The final band, with a peak close to 6 eV is assigned to an electron-hole interaction localised on the phenyl ring of the MEH-PPV backbone [96, 106].

1.2.2 Thermal influence on morphological transitions

External environmental factors strongly affect the molecular conformations of conjugated polymers, thereby influencing their electronic properties. As temperature increases, polymers undergo a significant structural transformation, from the more planar conformations favoured at lower temperatures to more coiled chains. This results in an observable blue shift in the emission spectra [107, 108].

MEH-PPV exemplifies this behaviour by adopting a planar conformation that enhances electronic conjugation and a red-shift in the emission spectra at lower temperatures [109]. These conformational changes occur through a second-order phase transition at approximately $180 - 204$ K [110, 111]. This critical transition is cooperative, driven by a balancing between the electronic stabilisation arising from longer conjugation lengths due to increased planarisation and the entropic cost associated with this ordering.

Figure 1.7 illustrates the marked differences in the absorption and emission spectra resulting from temperature-induced structural variations in the polymer. At

higher temperatures, shown in Figure 1.7(a), both the absorption spectrum, which extends from 2.2 eV to 3.4 eV, and the photoluminescence (PL) spectrum, from 1.6 eV to 2.4 eV, exhibit a pronounced blue shift. At lower temperatures, as shown in Figure 1.7 (b), both the absorption and photoluminescence spectra undergo a red-shift and separate into distinct, narrower bands, providing evidence of reduced homogeneous disorder. Figure 1.6 also demonstrates an increase in the ratio of the $0-0$ to $0-1$ intensity peaks in the PL spectrum of MEH-PPV for the red phase in comparison to the disordered blue-phase. These spectral features suggest an increase in the overal structure within different chains and are evidence of intramolecular interactions characteristic of J-aggregation within the red-phase material [112].

As with other conjugated polymers, aggregation in MEH-PPV films modulates their optical and electronic properties [113, 114]. The red phase is characterised by increased planarisation within individual polymer chains, which facilitates close molecular packing and promotes the formation of ordered aggregates [110]. The aggregation in MEH-PPV has been shown to present characteristics of both H-aggregates and J-aggregates, involving delocalisation along the polymer chain as well as coupling between adjacent chains. These features can enhance charge transport and exciton diffusion, which makes the red phase particularly suitable for applications requiring high charge mobility, such as field-effect transistors [112]. Conversely, at room temperature, MEH-PPV primarily exists in the disordered blue phase which is more well-suited for light-emitting applications.

As discussed in this section, controlling the degree of aggregation in MEH-PPV and other π-conjugated polymers influences their performance in optoelectronic devices, and enables for the control of the colour of the light emitted which can be exploited in OLEDs [115, 116]. Additionally, the degree of aggregation can impact the quantum efficiency and operational stability of these devices. Likewise, for

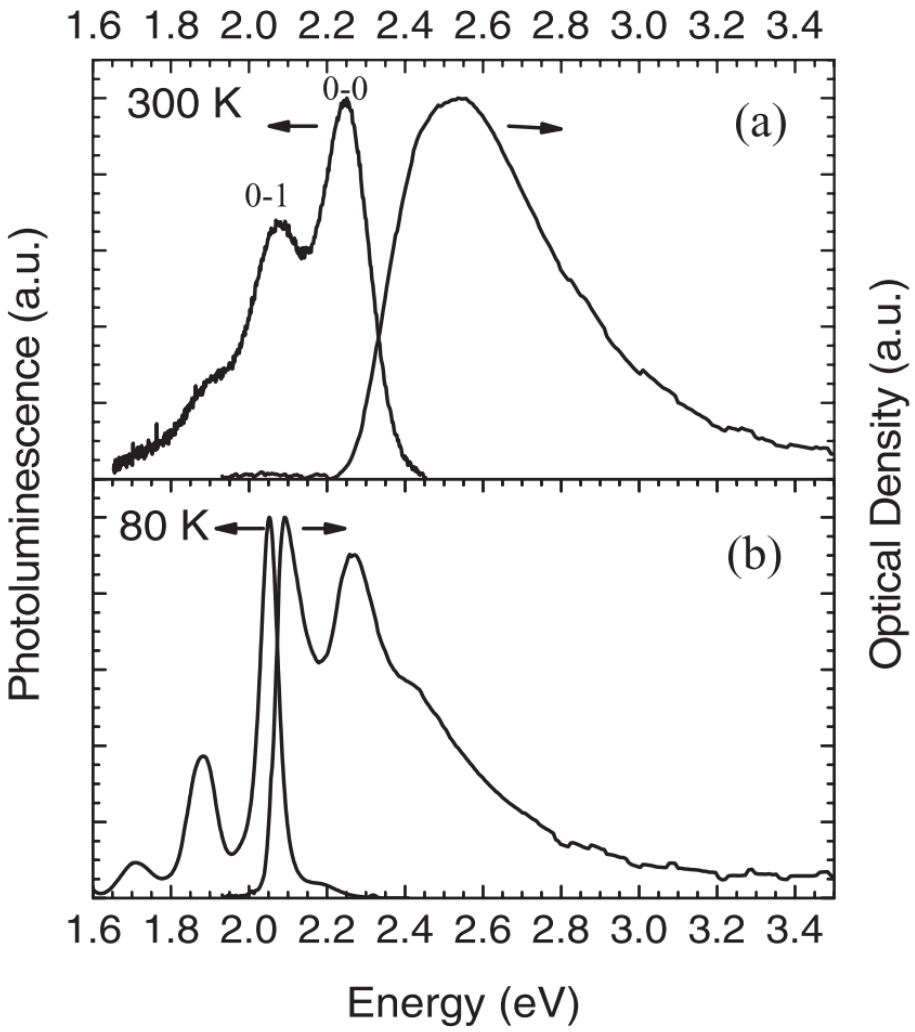


Figure 1.7: Absorption and emission spectra of MEH-PPV, (a) blue phase at 300 K, and (b) red phase at 80 K. Figure reproduced from [112].

OPVs, control over the charge transport properties of MEH-PPV can be useful to guarantee efficient power conversion [117, 118].

1.2.3 Solvent effects on the structure

Similarly to the thermal effects discussed in Section 1.2.2 solvent interactions significantly influence the conformation of MEH-PPV and other conjugated polymers; however, the effects of solvents are often less generalisable, as they vary depending on the specific polymer. Aromatic solvents such as toluene have a preferential

affinity for the hydrophobic backbone of MEH-PPV, promoting a more planarised or extended structure of the polymer chains [119, 120]. Planar chains are more prone to stronger interchain interactions that manifest in a red-shift in the fluorescence spectrum, which is analogous to observations of temperature-induced aggregation in the red phase [99, 118, 121].

In contrast, solvents that preferentially interact with the polymer's side chains, such as polar aprotic solvents like tetrahydrofuran (THF), induce more disordered and coiled conformations.[119, 122].

Weakly interacting solvents, such as non-polar, non-aromatic aliphatic alkanes and alkyl alcohols, which are considered poor solvents for MEH-PPV, favour the formation of tightly coiled polymer chains [123]. The resulting coiled chains minimise unfavourable interactions with the solvent but also reduce interchain interactions, leading to a blue shift in the fluorescence spectra.

At higher concentrations, poor solvents induce precipitation of conjugated polymers [114, 119, 120]. Although this study focusses mainly on solution and film samples, it is worth noting that one of the most significant applications of solvent effects in conjugated polymers is the formation of nanoparticles, which are widely used in fields such as bioimaging and sensing [109, 124, 125].

Although a significant portion of research on conjugated polymers is conducted in solution, solid-state films are generally preferred for most practical applications. The structure of these films directly affects the performance of the devices; however, attaining uniform films presents considerable challenges, largely due to the impact of the processing conditions, including parameters like solvent choice and temperature, on the final film structure [99, 122, 126, 127].

Significant differences in structure have been observed between films cast from THF and toluene, mirroring the observations in solution, with toluene-cast films

exhibiting stronger intermolecular interactions, including π-stacking, compared to THF films [123]. In support of these suggestions, atomic force microscopy (AFM) has also revealed that surface roughness in these films is related to aggregation in solution [128]. Figure 1.8 exemplifies these variations in the morphology of P3HT films, arising from differences in processing methods, with films processed from xylene and those annealed after spin-casting exhibiting better molecular alignment and connectivity [129].

Importantly, even when polymers exhibit comparable solubility in different solvents, the physical properties of the solvents can still significantly influence the resulting film morphology, as observed in the comparison between xylene and chloroform in Figure 1.8. For instance, studies have found that solvents with higher boiling points, like butanol and propanol, enhance crystallinity in P3HT films, in comparison to methanol and ethanol, due to their slower evaporation rates, despite having similar solvation capabilities for P3HT [130]. Furthermore, deposition techniques such as spin coating and drop casting lead to distinct film morphologies. Spin coating typically produces films with small, randomly ordered polymer crystallites interwoven with amorphous areas, while drop casting forms larger domains or almost perfect ordered structures [131].

As heterogeneous films, consisting of domains with varying degrees of alignment and structural order, are commonly observed, it becomes necessary to establish a methodology to measure how domain size, arrangement, and connectivity influence intermolecular interactions [74, 132, 133].

These variations resulting from the heterogeneity of conjugated polymer films extend beyond optoelectronic properties, influencing mechanical attributes such as elasticity and hardness [134]. Significant differences in film stability have been observed; films processed in THF exhibit gradual changes in optical and electrical

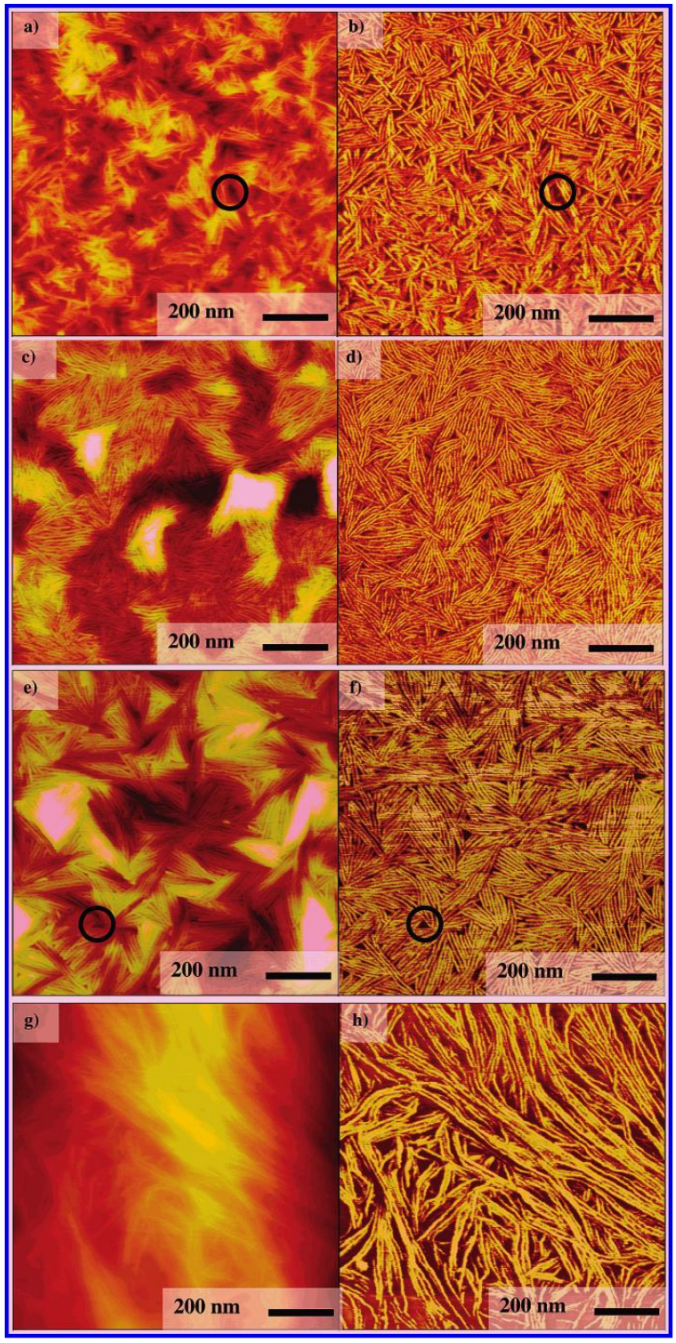


Figure 1.8: Atomic force microscopy images of P3HT films processed with different solvents and casting methods. Figures of the topography (a, c, e, g) and phase images (b, d, f, h) for: (a, b) spin-cast from chloroform, (c, d) spin-cast from xylene, (e, f) annealed after spinning from chloroform, and (g, h) drop-cast from chloroform. The xylene-cast and annealed films exhibit better alignment of the polymer chains and connectivity compared to the more disordered chloroform spin-cast film. Dark areas in the phase images correspond to depressions in topography (indicating local surface variations, not material absence). Figure reproduced from [129].

properties over time, whereas those cast from toluene display greater long-term stability [135]. Such distinctions could have profound implications for the practical applications and durability of these materials.

1.2.4 Spectroscopic probes for the study of exciton dynamics in conjugated polymers

Excitons, which are excited quasiparticles formed by the coupling of an electron and a hole resulting from electronic excitations within conjugated polymers, influence the optoelectronic characteristics of these materials [136]. A comprehensive analysis of the theoretical framework used to describe their evolution will be presented in Chapter 2. However, before engaging with the theoretical analysis, it is beneficial to first present a concise overview of the experimental methodologies frequently employed in the study of excitons, alongside a summary of the prevailing understanding of exciton dynamics.

Three-Pulse Photon Echo Peak Shift

The Three-Pulse Photon Echo Peak Shift (3PEPS) method involves three temporally separated ultrafast laser pulses that initiate and track the system's dephasing and rephasing processes. The first pulse induces coherence within the system, initiating the dephasing of the exciton states. The second pulse pauses the dephasing and creates a population state where exciton dynamics occurs. A third pulse then restores coherence, leading to the emission of a photon echo. By varying the time delay between the pulses, particularly the population time, it is possible to monitor how the photon echo evolves, thus providing time-resolved information about exciton dynamics and coherence loss [137].

The 3PEPS technique is widely used to distinguish between homogeneous and inhomogeneous broadening of spectral lines, which provides information about the

dephasing and localisation of excitons. MEH-PPV 3PEPS studies have revealed that interactions with nuclear vibrations cause the excitons to dephase within 50 fs. [138–140]. Additionally, oscillations at a frequency of 600 cm^{-1} with a duration of approximately 200 fs have been observed in MEH-PPV 3PEPS signals, demonstrating the presence of vibrational coherence during the initial stages of exciton dynamics [141]. These results provide concrete evidence of exciton-phonon coupling affecting exciton-dynamics within π-conjugated polymer systems.

Two colour three-pulse photon echo peak shift

A variation of 3PEPS, the Two-Colour Three-Pulse Photon Echo Peak Shift (2C3PEPS), uses two light sources at different wavelengths and allows for the probing of more complex dynamical processes than those addressed by 3PEPS.

This method enables the direct measurement of intermolecular coupling constants, allowing for a precise characterisation of exciton migration dynamics [137]. In P3HT, 2C3PEPS has revealed strong exciton-phonon which results in long-lasting coherent-transport (for about 200 fs) [142].

Two-dimensional electronic spectroscopy

Another nonlinear optical technique closely related to 3PEPS is two-dimensional electronic spectroscopy (2DES). In 2DES, four laser pulses are applied in sequence to the sample, generating a third-order signal that reveals electronic excitation energies, population relaxation, and coherence pathways [143]. The measured signal contains both amplitude and phase information, which through a Fourier transform produces a two-dimensional correlation spectrum that maps excitation and emission frequencies. The off-diagonal peaks within this spectrum correspond to couplings between states. Thus, 2DES can be used to investigate energy transfer processes,

the relative strength of exciton interactions, and the effects of inhomogeneous broadening in complex systems [144].

Using 2DES, strong evidence for polaron pair formation and exciton-polaron coupling within the first 20 fs following excitation in P3HT films has been observed [145]. Similarly, 2DES has been used to survey the impact of interchain exciton migration on exciton dynamics, showing significant relaxation driven primarily by intermolecular processes with decay times of approximately 10 ps in solution and 4 ps in films [146].

Fluorescence depolarisation

Fluorescence depolarisation measures the change in the polarisation of emitted light after excitation with polarised light, which provides information about the molecular reorientation during exciton migration. Fluorescence depolarisation studies of MEH-PPV in solution show that the decay rate of excitons on partially conjugated polymers is considerably slower than for fully conjugated MEH-PPV chains. This difference implies a significant influence of exciton coupling to nuclear degrees of freedom in determining depolarisation dynamics within the ultrafast regime [147]. Vibrationally induced fluorescence depolarisation has also been observed in the femtosecond regime in m-LPPP, PPV, and PDA, where initial coherence between nuclear motions and electronic states decays within the first 10 fs after photoexcitation [148]. Furthermore, fluorescence depolarisation studies have been instrumental in observing intermolecular stochastic migration in a myriad of conjugated polymers, including a $2-3$ ps timescale in m-LPPP, $5-6$ ps in MDMO-PPV, and distinct anisotropy fluctuations in MEH-PPV and PDOPT as a result of conformational disorder [149–151].

1.3 Thesis structure

The primary aim of this thesis is to explore exciton dynamics within π-conjugated polymer systems, with a focus on PPV derivatives. Chapter 2 outlines the theoretical foundation of this work, which includes a comprehensive introduction into Frenkel excitons and the Frenkel-Holstein Hamiltonian used to describe the evolution of such quasiparticles, as well as, their interactions with the surrounding lattice. The chapter concludes with a theoretical description of fluorescence polar anisotropy.

The numerical and computational approaches required to conduct the large simulations presented throughout this thesis are discussed in Chapter 3. The Time-Evolving Block Decimation (TEBD) method, which is applied to reduce the dimensionality of the system's Hamiltonian, and the quantum jump trajectory method, which is used to account for the energy dissipation that results from the interactions of the system with the surrounding environment, are described therein.

Chapter 4 presents the results of large scale simulations of single MEH-PPV chains which describe the ultrafast exciton dynamics that occur immediately following photoexcitation, fluorescence anisotropy predictions are used in order to determine the relevant timescales within the system. The results presented in this chapter reveal that a high energy exciton which is delocalised upon creation, undergoes rapid decoherence within tens of femtoseconds due to strong coupling with high-frequency vibrational phonons. This is followed by a non-adiabatic relaxation into a localised lower-energy state, which further localises within 10 monomer units as a result of the interactions with slower torsional degrees of freedom. All the steps here described are predicted to occur within the first 200 fs of the life of the exciton.

Chapter 5 is dedicated to the later stages of exciton dynamics, addressing processes that occur after the first ultrafast relaxation processes and before radiative

decay. To this end, this chapter explores the non-coherent migration of excitons between different polymer chains as described by Förster Resonance Energy Transfer (FRET). The influence of structural disorder and film heterogeneity on these migration pathways is examined, and fluorescence polar anisotropy is tested as an effective probe to determine the structural properties of π-conjugated polymer surfaces.

Chapter 6 provides a concise discussion of the key results found in this work and provides a comparison with experimental observations, highlighting the potential implications of these findings in the target design of conjugated polymers for real-world applications.

2
Theoretical background

This chapter presents the theoretical framework used to simulate exciton dynamics in π-conjugated polymers, providing the foundation for the study of both isolated fibres and interacting chains within polymer aggregates. The Frenkel–Holstein Hamiltonian is used to describe intrachain exciton dynamics via nearest-neighbour electronic interactions and the coupling to both vibrational and torsional nuclear degrees of freedom. This model allows for the analysis of the effects of nuclear dynamics on exciton localisation and self-trapping. Disorder is included explicitly through fluctuations in site energies and structural defects that modify the transfer integrals between neighbouring sites, leading to a separation of the eigenstates of the system into highly localised low-energy exciton ground states (LEGS), which define the chromophores of the material, and higher-energy quasi-extended exciton states (QEES). Finally, the chapter concludes with a discussion of experimental spectroscopic techniques capable of probing exciton dynamics, thus offering empirical validation to the theoretical predictions presented in this work.

2.1 Excitons in π-conjugated polymers

Upon photoexcitation in a semiconducting material, an electron is promoted from the valence band to the conduction band, leaving behind a positively charged hole in the valence band. The electron and the resulting hole remain closely bound due to the electrostatic interaction between them, forming a quasiparticle known as the exciton. Excitons are classified based on the strength of their bond and the spatial extent separating the electron and the hole. The two primary types of excitons are Wannier-Mott excitons, common in inorganic materials [152] and Frenkel excitons used to describe the processes in organic semiconductors [153] and rare-gas crystals [154, 155].

2.1.1 Wannier-Mott excitons

Wannier-Mott excitons are characteristic of materials with a large dielectric constant and small effective electron and hole masses [156]. The initial references to this type of exciton and their behaviour were first made by Gregory Wannier and Nevill Mott in the context of excitations within insulating crystals and narrow-gap semiconductors [157, 158]. In these materials, the large dielectric constant effectively screens the Coulomb attraction between the electron and the hole, resulting in a weakly bound electron-hole pair. This weak binding constitutes a Wannier-Mott exciton which has a large electron-hole separation, often extending over several unit cells of the crystal lattice.

Wannier-Mott excitons are modelled using a hydrogenic approach, with exciton binding energies being much smaller than the bandgap energies of the material.

The exciton binding energy and the effective Bohr radius are given by [159]:

$$E_b = \frac{\mu e^4}{2\hbar^2\epsilon^2} = \frac{R_H}{\epsilon^2}\frac{\mu}{m_0} \tag{2.1.1}$$

$$a_B = \frac{\epsilon\hbar^2}{\mu e^2} = \epsilon a_0 \frac{m_0}{\mu} \tag{2.1.2}$$

where μ is the reduced mass of the electron-hole pair. The standard constants are: R_H the Rydberg constant, a_0 the Bohr radius, and m_0 the free electron mass.

Wannier-Mott excitons result in discrete energy levels similar to those found in the hydrogen atom but scaled by the material's dielectric constant and the corresponding effective masses. These energy levels manifest as sharp lines in the absorption spectrum below the bandgap energy. Although the binding energy of these excitons is smaller than the energy band gaps of the material, Wannier-Mott excitons significantly influence the optical properties near the absorption edge

Wannier-Mott excitons are often found in semiconductors with relatively low energy band gap corresponding to the so called low-coupling limit.

2.1.2 Frenkel excitons

Frenkel excitons are characterised by a strong Coulomb interaction between the electron and the hole, leading to a tightly bound exciton with a small radius [160, 161]. Frenkel excitons are typically confined to a single molecule, often within a localised segment of the molecular structure. Due to this spatial restriction, they are more prevalent in materials with larger band gaps, such as molecular and ionic crystals [162].

The theoretical framework of Frenkel excitons is relevant for understanding the optical properties of π-conjugated polymers, which frequently exhibit low dielectric constants around $\varepsilon_r = 3 - 4$ [163, 164]. The high degree of localisation inherent to Frenkel excitons reduces the spatial overlap between different excitons,

leading to reduced mobility compared to Wannier-Mott excitons, which are more delocalised [162].

Frenkel excitons in crystalline materials are often described using the Bloch state formalism. However, in systems where excitons are not only localised but are also influenced by a strong exciton-lattice coupling, the Bloch state formalism may be insufficient for a full understanding of the underlying physics. The strong electron-phonon coupling in these materials significantly influences exciton behaviour, leading to phenomena such as polaron formation [159].

Relevance for π-conjugated polymers

The quasi-one-dimensional nature of most conjugated polymers reduces the screening of Coulombic attractions, resulting in a strong Coulomb interaction between the electron and the hole. Consequently, excitons in conjugated polymers are tightly bound, with binding energies around 1 eV [165, 166] forming Frenkel excitons. These highly localised excitons dominate optical transitions in π-conjugated polymers. However, their localisation and high binding energy limit charge transport, as they are less likely to dissociate into free charge carriers, affecting the efficiency of devices such as organic solar cells. Beyond Frenkel excitons, charge-transfer excitons are also prevalent in low-dimensional materials and conjugated polymers. These are bound states of an electron and hole localised on adjacent molecules or neighbouring sites in the polymer chain, exhibiting characteristics between Frenkel and Wannier-Mott excitons. Due to their lower binding energy, around 0.2 eV in PPP, charge-transfer excitons dissociate into free carriers more readily and play a significant role in the electronic properties of π-conjugated polymers, though they are less influential in optical spectra [167, 168].

2.2 Exciton dynamics

Excitons are described by a two-particle wavefunction:

$$\Phi_{p,j}(m,n) = \psi_p(m)\Psi_j(n) \tag{2.2.1}$$

where $\psi_p(m)$ represents the relative motion of the electron-hole pair, and $\Psi_j(n)$ describes the overall position of the exciton's centre-of-mass.

The lowest-energy photoexcited states in conjugated polymers with principal quantum number $p = 1$ correspond to highly localised Frenkel excitons, each characterised by a centre-of-mass momentum indexed by j. In PPV derivatives, the lowest optically active exciton is the 1Bu state [169, 170]. While the relative wavefunction ψ_p determines the exciton binding energy, it remains largely unchanged during optical transitions. In contrast, the centre-of-mass wavefunction Ψ_j dictates the spatial extent and localisation of the exciton along the polymer chain and its dynamics influences the optical processes [171]. Thus, the following discussion focusses on the evolution of Ψ_j.

2.2.1 The Frenkel Hamiltonian

To describe the dynamics of the excitons in π-conjugated polymers, the Frenkel Hamiltonian is used, which considers the energy and interactions of the excitons as they move between sites on a polymer chain. The Frenkel model is described by:

$$\hat{H}_{\text{ex}} = \sum_{n=1}^{N} \epsilon_n \hat{N}_n - \sum_{n=1}^{N-1} J_n(\hat{a}_{n+1}^{\dagger}\hat{a}_n + \hat{a}_n^{\dagger}\hat{a}_{n+1}) \tag{2.2.2}$$

where the operators $\hat{a}_n^{\dagger}$ and $\hat{a}_n$ create or destroy a Frenkel exciton at the n-th moiety, and $\hat{N}_n \equiv \hat{a}_n^{\dagger}\hat{a}_n$ is the number operator that measures the number of excitons at a given site n. J_n represents the coupling strength or transfer integral between neighbouring sites.

Derivation of the terms in the Frenkel Hamiltonian

The transfer integral J_n determines the strength of the nearest-neighbour interactions, enabling excitons to transfer between sites within the polymer chain through two distinct mechanisms [166, 171]. For even parity singlet excitons, there is a through space mechanism analogous to the intramolecular Förster energy transfer. The transfer integral is expressed using the point-dipole approximation as:

$$J_{DA}^{mn} = \frac{\kappa_{mn}\mu_0^2}{4\pi\epsilon_r\epsilon_0 R_{mn}^3} \tag{2.2.3}$$

where μ_0 is the transition dipole moment of a single moiety and $\hat{R}_{mn}$ is the distance between the moieties m and n. The orientation factor κ_{mn} is defined as:

$$\kappa_{mn} = \hat{r}_m \cdot \hat{r}_n - 3(\hat{R}_{mn} \cdot \hat{r}_m)(\hat{R}_{mn} \cdot \hat{r}_n) \tag{2.2.4}$$

in here, $\hat{r}_m$ is a unit vector parallel to the dipole on moiety m and $\hat{R}_{mn}$ is a unit vector along the vector joining moieties m and n. For collinear dipoles within the same chain, the nearest-neighbour transfer integral is simplified to:

$$J_{DA} = -\frac{2\mu_0^2}{4\pi\epsilon_r\epsilon_0 d^3} \tag{2.2.5}$$

In addition to the through-space mechanism, there exists the super-exchange mechanism, which originates from a virtual fluctuation involving a transition from a Frenkel exciton on single moiety to a charge-transfer exciton spanning two moieties, before returning to a Frenkel exciton on an adjacent moiety. The exciton transfer integral for this process, derived via second order perturbation theory [16], is expressed as:

$$J_{SE}(\theta) \propto -\frac{t(\theta)^2}{\Delta E} \tag{2.2.6}$$

where $t(\theta)$ is proportional to the overlap of p-orbitals on neighbouring moieties, modulated by the dihedral angle θ_n between adjacent moieties: $t(\theta)_n \propto \cos\theta_n$.

Here, ΔE is the difference in energy between a charge-transfer exciton and Frenkel exciton. The total exciton transfer integral is thus:

$$J_n = J_{DA} + J_{SE}^0 \cos^2 \theta_n \tag{2.2.7}$$

2.2.2 The role of disorder

In an ideal uniform chain, excitons delocalise over the entire chain. The solutions to the Frenkel Hamiltonian, in the absence of disorder, are analogous to the 1-dimensional particle in a box model, with wavefunctions given by:

$$\Psi_j^n = \sqrt{\frac{2}{N+1}} \sin\left(\frac{j\pi n}{N+1}\right) \tag{2.2.8}$$

However, structural irregularities, such as variations in bond lengths or dihedral angles, introduce disorder that disrupts this ideal delocalisation. According to Anderson's theory of localisation in disordered one-dimensional systems, all wavefunctions become exponentially localised, regardless of the magnitude of the disorder [172]. This phenomenon is mathematically described by:

$$|\Psi(R)|^2 \sim e^{-|R-R_0|/L}, \tag{2.2.9}$$

where R_0 represents the centre of the localised state, and L is the Anderson localisation length which can be directly linked to the disorder in the system. This localisation is the direct result of constructive and destructive interference of the wavefunction due to multiple scattering events from irregularly spaced and energy barriers [166, 173]. The difference between the predicted exciton density across a polymer chain in the presence and absence of disorder can be seen in Figure 2.1.

In conjugated polymers like MEH-PPV, disorder can be categorised into diagonal disorder, which affects the on-site energies, and off-diagonal disorder, which modifies the electronic coupling between moieties. This classification follows from the Frenkel

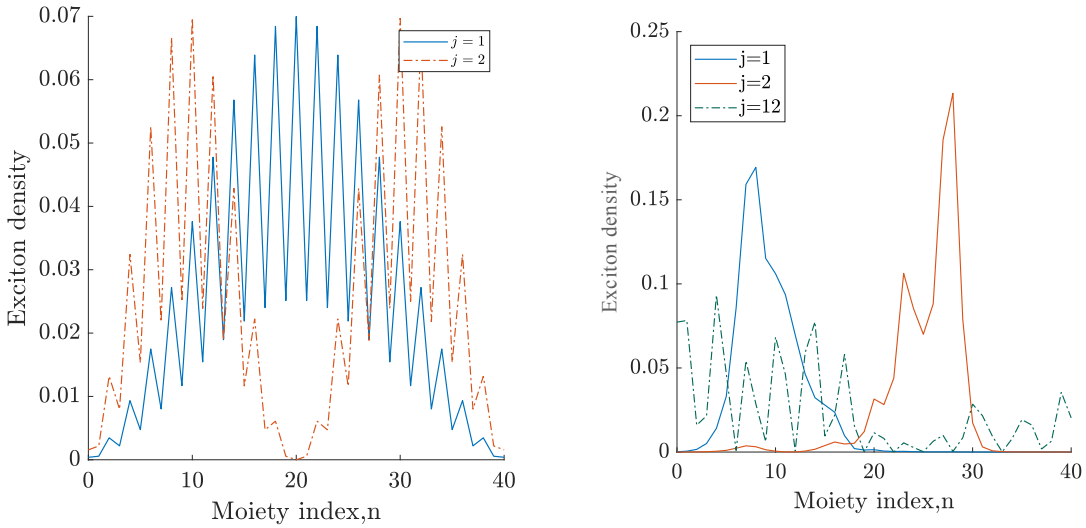


Figure 2.1: Exciton density distribution across the polymer chain for different eigenstates of: (a) uniform system (b) disordered-system.

Hamiltonian presented in Equation 2.2.2. Diagonal disorder primarily arises from fluctuations in the surrounding dielectric environment, which can be induced by temperature variations or solvent interactions. These fluctuations alter the local dielectric constant (ϵ_r) and can also impact intermolecular separation, leading to variations in the electrostatic potential and site energies experienced by the exciton [171, 174, 175]. The resulting energy disorder follows a normal distribution, with the standard deviation proportional to the magnitude of dielectric fluctuations [171, 174, 175]. This disorder is included in the Frenkel Hamiltonian model through variations in the on-site energies of the form $\epsilon_n = \epsilon_n^0 + \delta\epsilon_n$, with a normal distribution in $\delta\epsilon_n$.

Off-diagonal disorder, conversely, originates from the inherent flexibility of the polymer chains and thermal fluctuations, which cause variations in the dihedral angles between moieties [171, 176, 177]. These variations in dihedral angles modify the transfer integral between sites, resulting in a disorder described by:

$$\sigma_{t_{ij}} = \sigma_{\theta_{ij}}(t_0 \sin\theta_0) \tag{2.2.10}$$

where σ_θ represents the standard deviation for a normal distribution around the dihedral angle θ_0 and t_0 is the transfer integral in the absence of disorder.

LEGS and QEES

Both diagonal and off-diagonal disorder break the translational symmetry of the polymer chains, thereby allowing for localised exciton states. The eigenstates

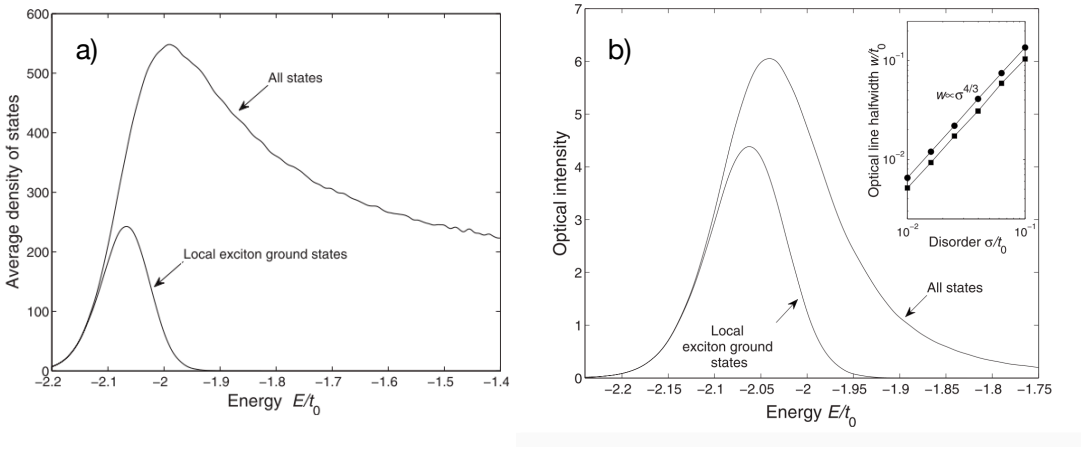


Figure 2.2: (a) Theoretical calculations of the density of states considering disorder in the Frenkel model and (b) the optical absorption of the excited states and the LEGS. Figures reproduced from [178].

for the disordered Frenkel Hamiltonian can be divided into local exciton ground states (LEGS) and quasi-extended exciton states (QEES) [178–181]. As shown in Figure 2.3, LEGS are spatially localised, nodeless, and non-overlapping states that predominantly occupy the lower-energy region of the density of states (DOS), as seen in Figure 2.2. As a result, the spatial extent of the LEGS define the chromophores in disordered conjugated polymers which determine the optical properties of the material. In order to quantitatively classify a state as a LEGS the "signed value" α is used, which measures how closely a state approximates a nodeless ground

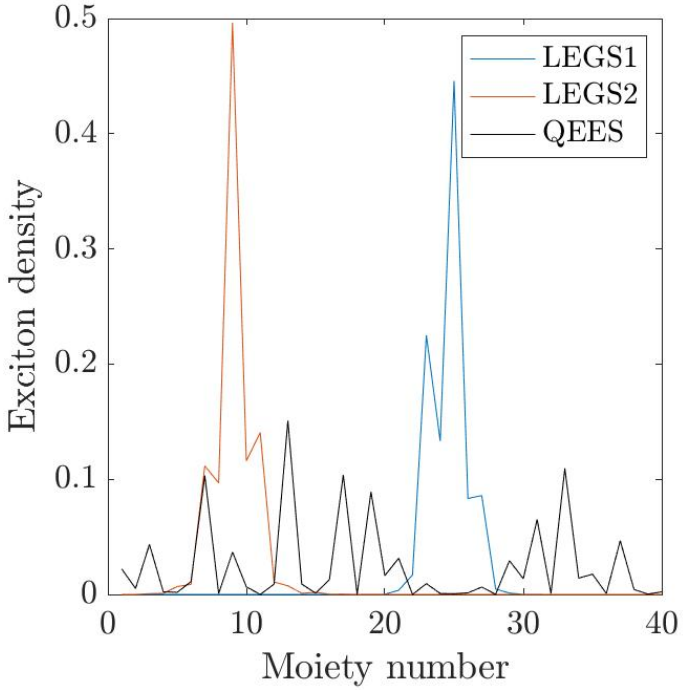


Figure 2.3: Exciton density for localised states as a result of the inclusion of disorder in the Frenkel model, includes the exciton density for the 2 lowest energy LEGS and an arbitrary QEES.

state. A state is defined as a LEGS for $\alpha \geq 0.95$ [178]:

$$\alpha = \left| \int \Psi(R)|\Psi(R)|dR \right|, \tag{2.2.11}$$

The extent of localisation in LEGS is characterised by the localisation length L, given by:

$$L = 2R_{\text{rms}} \equiv 2\sqrt{\langle R^2 \rangle - \langle R \rangle^2}, \tag{2.2.12}$$

where,

$$\langle R^n \rangle = \sum_R |\Psi(R)|^2 R^n, \tag{2.2.13}$$

The Anderson localisation length for these states, as defined in Equation 2.2.9, scales with the disorder of the system depending on their energy within the band.

$$L \sim (t_0/\sigma)^{(v(E)} \tag{2.2.14}$$

At the band edges $v(E) = 2/3$, while near the band centre, $v(E) = 3/2$ [171]. Additionally, the total number of LEGS is directly related to the extent of the polymer chain and the degree of disorder scaling as $\sigma^{2/3}$, indicating an increase in small localised states as a function of disorder [171, 178]. Figure 2.2 showcases how LEGS dominate the low-energy absorption spectrum and contribute approximately 50% of the total optical intensity. Interestingly, while disorder might be expected to decrease absorption efficiency, the formation of these localised states broadens the polymer's absorption spectrum, enhancing its ability to capture light over a wider range of wavelengths [138, 182].

At higher energies in the spectrum, most states are nearly delocalised. These states, known as quasi-extended exciton states (QEES), extend over a larger portion of the polymer chain and are characterised by multiple nodes, where the probability amplitude of the exciton density is zero [179, 183]. One such state is shown in Figure 2.3, providing a comparison to the exciton density of LEGS.

2.2.3 Exciton-phonon interactions

Phonons in π-conjugated systems strongly influence exciton dynamics through their interaction with electronic excitations, leading to exciton self-localisation, polaron formation, and other dynamic processes [184]. In the case of PPV and its derivatives, Frenkel excitons interact strongly with local normal modes, including the C=C stretching vibrations in the vinyl units, the characteristic C-C stretching and C-H bending modes of the phenylene unit, and low-frequency torsional and rotational modes [18].

These modes have been represented within our coarse-grain model in Figures 2.4-2.5.

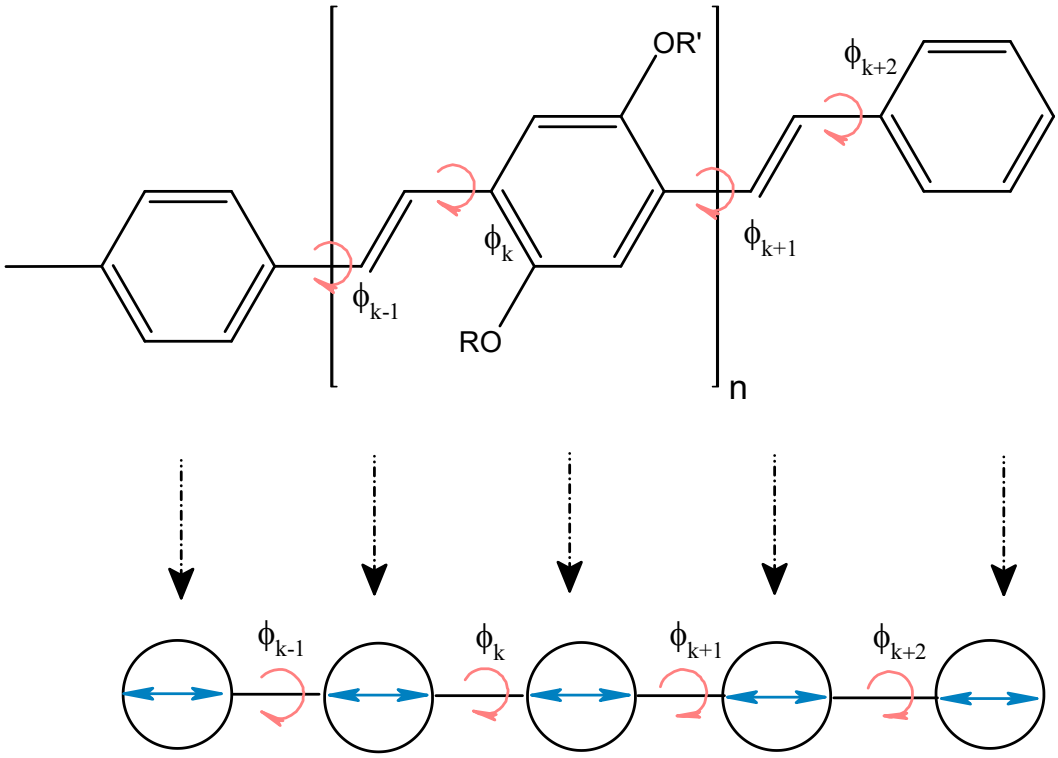


Figure 2.4: A coarse-grained model of a PPV derivative, illustrating both vibrational and torsional phonon modes.

The interactions between the Frenkel excitons and phonons, are widely described through the Frenkel-Holstein Hamiltonian [185, 186].

$$\begin{aligned}\hat{H}_{\mathrm{FH}} &\equiv \hat{H}_{\mathrm{F}} + \hat{H}_{\text{ex-ph}} + \hat{H}_{\mathrm{ph}} \\ &= \hat{H}_{\mathrm{F}} + \sum_{n=1}^{N} g_n(\hat{b}_n^{\dagger} + \hat{b}_n)\hat{N}_n + \sum_{n=1}^{N} \hbar\omega_n \left(\hat{b}_n^{\dagger}\hat{b}_n + \frac{1}{2}\right) \quad (2.2.15)\end{aligned}$$

In this Hamiltonian, the exciton Hamiltonian is still represented within the Frenkel formalism as defined in Equation 2.2.2, and the new terms account for the phonon energy and the phonon-exciton coupling. The operators $\hat{b}_n^{\dagger}$ and $\hat{b}_n$ are the corresponding creation and annihilation operators for the phonon with energy $\hbar\omega_n$ at site n. The second term describes the linear phonon-exciton coupling,

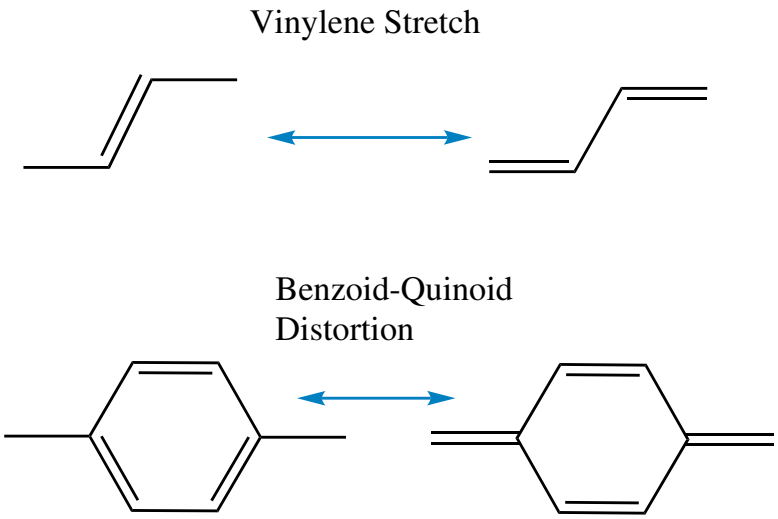


Figure 2.5: The vibrational modes within PPV derivatives.

modulated by g_n, the coupling constant between the exciton and phonon at site n. The exciton–phonon coupling constant g can be theoretically obtained from:

$$g = \Gamma^{(1)} \sqrt{\frac{2\hbar}{\mu\omega}} \tag{2.2.16}$$

where $\Gamma^{(1)}$ is the linear vibronic coupling constant, defined as the change in the Frenkel exciton site energy in relation to the displacement of the vibrational normal mode. $\Gamma^{(1)}$ is estimated theoretically as $\Gamma^{(1)} \approx 0.85\frac{\alpha}{\sqrt{N}}$ for the fundamental electron–phonon coupling constant α and N is the number of monomers over which the normal mode is delocalised [187]. Here, μ is the reduced mass associated with the normal mode, and ω is its angular frequency. This model may be better understood by considering the classical limit, which corresponds to the adiabatic approximation where $\hbar\omega \ll J$, within this limit, the electronic motion is much faster than the vibrational motion of the lattice. In this regime, the vibrational degrees of freedom are treated as classical oscillators with fixed positions, while the electronic excitations adjust instantaneously to these positions. For this approximation, the

coupling term is considered uniform throughout the system and is not site-dependent. Additionally, the phonon frequencies, which are associated with each site n in the quantum model, are also considered uniform, with a site-independent frequency ω_{vib}. Starting from the Hamiltonian in equation 2.2.15, in the classical limit, the phonon operators $\hat{b}_n^\dagger$ and $\hat{b}_n$ are replaced by their classical counterparts given by the nuclear momentum and displacement operators:

$$\hat{b} = \frac{(\hat{\tilde{Q}} + i\hat{\tilde{P}})}{\sqrt{2}} \quad \hat{b}^\dagger = \frac{(\hat{\tilde{Q}} - i\hat{\tilde{P}})}{\sqrt{2}} \tag{2.2.17}$$

where $\hat{\tilde{Q}}$ and $\hat{\tilde{P}}$ correspond to the nuclear displacement and nuclear momentum from site n. The Hamiltonian can be further simplified by using a dimensionless description defined as:

$$\hat{\tilde{Q}}_n = \left(\frac{M\omega_{vib}}{\hbar}\right)^{1/2} \hat{Q}_n, \quad \hat{\tilde{P}}_n = \left(\frac{\hbar}{M\omega_{vib}}\right)^{1/2} \hat{P}_n \tag{2.2.18}$$

Thus, the adiabatic limit of the Holstein Hamiltonian can be conveniently expressed as [185, 188]:

$$\hat{H}_{FH} = \hat{H}_F - A\hbar\omega_{vib} \sum_{n=1}^{N} \hat{\tilde{Q}}_n \hat{N}_n + \frac{\hbar\omega_{vib}}{2} \sum_{n=1}^{N} (\hat{\tilde{Q}}_n^2 + \hat{\tilde{P}}_n^2) \tag{2.2.19}$$

In this formulation, the linear coupling of the exciton to the local vibrational mode in Equation 2.2.19 is dependent on the nuclear displacement and the localisation of the exciton through the coupling A which is related to the Huang-Rhys factor for a single site through $S(1) = A^2/2$. In terms of the original parameters A is given by $A = \frac{g\sqrt{2}}{\hbar\omega_{vib}}$ [187, 188]. The Huang-Rhys factor measures the strength of the exciton-phonon coupling by characterizing the nuclear displacement in the nuclear coordinate between the electronic ground and excited states. For a single monomer and a single normal mode this can be mathematically described as [189]:

$$S = \frac{M\omega_0(Q_{eq})^2}{2\hbar} = \frac{\tilde{Q}_{eq}}{2} \tag{2.2.20}$$

where Q_{eq} is the equilibrium displacement of the normal mode, which characterises the lattice deformations as a result of the electronic excitation, which is represented in Figure 2.6, and $\tilde{Q}_{eq}$ is the equivalent dimensionless quantity.

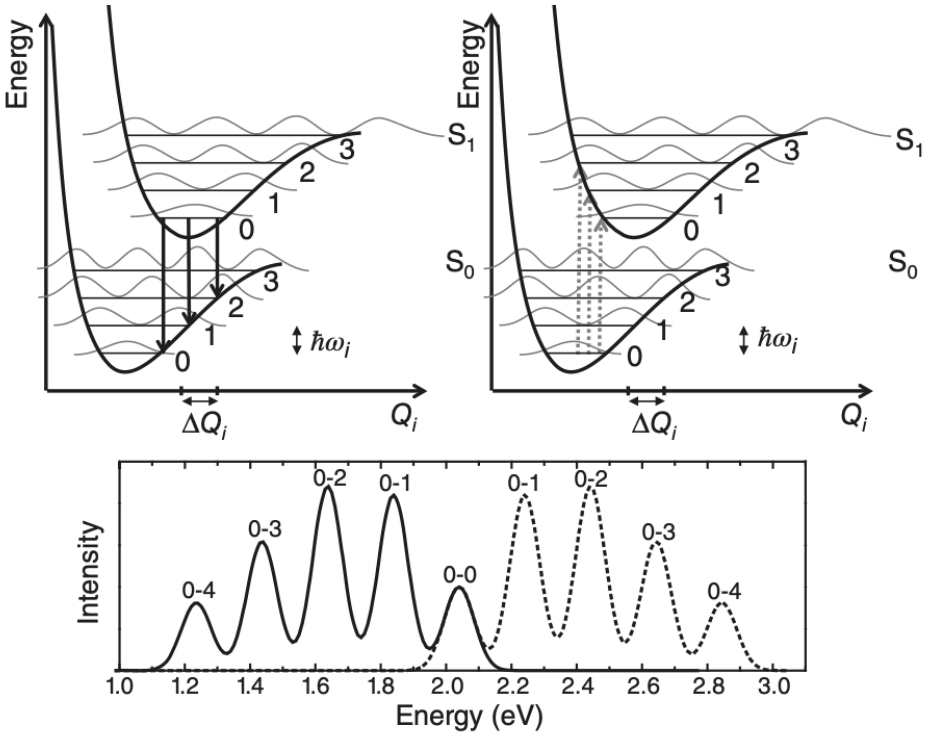


Figure 2.6: Representation of the Franck-Condon principle, including the potential energy curves of the electronic ground state (S_0) and excited state (S_1) for a single vibrational mode and the corresponding vibrational wavefunctions. The nuclear displacement in the excited state is marked with ΔQ and determines the Huang-Rhys factor S, and the relaxation energy. Electronic transitions occur vertically with the relative intensities of vibronic transitions in the absorption (dotted lines) and emission spectra (solid lines) governed by the Franck–Condon factors, which depend on the Huang–Rhys parameter. Figure reproduced from [190].

The equilibrium dimensionless displacement can be found by minimising the expectation value of the energy with respect to this coordinate : $E(\tilde{Q}) \equiv \langle \Psi | \hat{H}(\tilde{Q}) | \Psi \rangle$ which can be easily obtained from the Hellman-Feynmann theorem that states:

$$\frac{dE}{d\tilde{Q}_n} = \left\langle \Psi \left| \frac{d\hat{H}}{d\tilde{Q}_n} \right| \Psi \right\rangle \tag{2.2.21}$$

Therefore, $\tilde{Q}_{eq}$ is found from Equation 2.2.19 at:

$$\tilde{Q}_{eq}(n) = |A||\Psi_j(n)|^2 \tag{2.2.22}$$

which represents the equilibrium dimensionless nuclear displacement at the n-th site for the j-th electronic level. By considering the local exciton density and normal mode at each site, the local Huang-Rhys parameter $S_j(n)$ characterising the strength of the exciton-phonon per site can be defined. Given that the exciton in a polymer extends over multiple monomers rather than being confined to a single site, the total exciton-phonon interaction must account for all monomers the exciton delocalises over, as a result, the significant parameter is the effective Huang-Rhys parameter defined by:

$$S_{\text{eff},j} = \sum_m S_j(m). \tag{2.2.23}$$

Using Equations 2.2.20, 2.2.22, the effective Huang-Rhys parameter can be represented as:

$$S_{\text{eff},j} = \sum_m S_j(m) = \frac{|A|^2}{2} \sum_m |\Psi_j(m)|^4. \tag{2.2.24}$$

As shown in this expression, the level of delocalisation of the exciton has a strong influence on the resulting exciton-phonon coupling strength. The extent of the exciton localisation, can be described through the participation number (PN), defined as:

$$PN = \left(\sum_n |\psi_n|^4 \right)^{-1} \tag{2.2.25}$$

Using this quantity, the effective Huang-Rhys parameter can be rewritten as:

$$S_{\text{eff},j} = \frac{1}{PN} \frac{|A|^2}{2} \tag{2.2.26}$$

It follows that as exciton delocalisation increases, the effective Huang-Rhys parameter decreases. For uniform polymer chains, where excitons delocalise over the full chain, this results in a decrease of the Huang-Rhys parameter and the strength of the exciton-phonon coupling with length, which can be observed in multiple experimental observations [18, 191–194]. More generally, the strength of the exciton-phonon coupling which directly impacts exciton dynamics is directly related to the localisation length of the exciton.

Having addressed exciton interactions with vibrational phonons, it is important to consider the classical limit where the vibrational frequency ω_{vib} approaches zero. In this regime, the phonon momenta $\hat{\tilde{P}}_n$ become negligible, and the nuclear displacements $\widetilde{Q}_n$ can be treated as quasi-static variables. This allows for a simplification of the Frenkel-Holstein Hamiltonian, where the nuclear degrees of freedom are treated as parameters that modify the electronic states. In this limit, exciton self-trapping and subsequent self-localisation is expected, leading to the formation of Landau polarons. In PPV derivatives and other π-conjugated polymers, high-frequency vibrational modes under standard conditions do not lead to self-localisation (for such regimes self-localisation as a result of disorder as already discussed dominates). However, low-frequency torsional modes have been found to induce exciton localisation and self-trapping effects under certain conditions [195]

2.2.4 Exciton-polarons

In materials with strong exciton-phonon coupling, such as low-dimensional π-conjugated polymers, the presence of an exciton induces local fluctuations of the charge density despite its overall neutrality, due to the finite spatial separation between the constituent electron and hole. These fluctuations produce lattice

distortions that result in localisation and energetic stabilisation of the exciton, thereby forming a coupled quasi-particle known as an exciton-polaron.

The formation of an exciton-polaron lowers the energy of the system relative to that for a "free" exciton by an energy difference defined as the polaron binding energy [174]. The relaxation energy associated to the formation of the exciton-polaron is given by:

$$E_{\text{relax}} = \frac{\hbar\omega|A|^2}{2PN} = \hbar\omega S_{\text{eff}} \tag{2.2.27}$$

Thus, as exciton delocalisation increases the polaron binding energy decreases which reduces the influence of self-trapping effects. The spatial extent of the exciton-polaron can be characterised using either the exciton-phonon correlation function or the exciton-polaron localisation length. Firstly, the exciton-phonon correlation function describes the coupling between the local phonon displacements and the exciton density [196, 197]:

$$C_n^{\text{ex-ph}}(t) = \frac{1}{N}\sum_m \langle N_m Q_{m+n}\rangle \tag{2.2.28}$$

Trends in the exciton-polaron correlation function have been used in previous research to identify the formation of the exciton-polaron in PPV at an ultrafast timescale within 10 fs after exciton formation [198]. A characteristic feature of the exciton-polaron is the exponential decay of its correlation function. Figure 2.7 exemplifies this behaviour: the initial broad delocalised profile of $C_n^{\text{ex-ph}}(t)$ rapidly adopts an exponential form $C_n^{\text{ex-ph}}(t) = C_0\exp(-n/\xi)$ with localisation length of $\xi = 10$ monomer units, indicating self-trapping. The correlation function exhibits oscillations in time with a period of 20 fs corresponding to the frequency of the vibrational phonon [199].

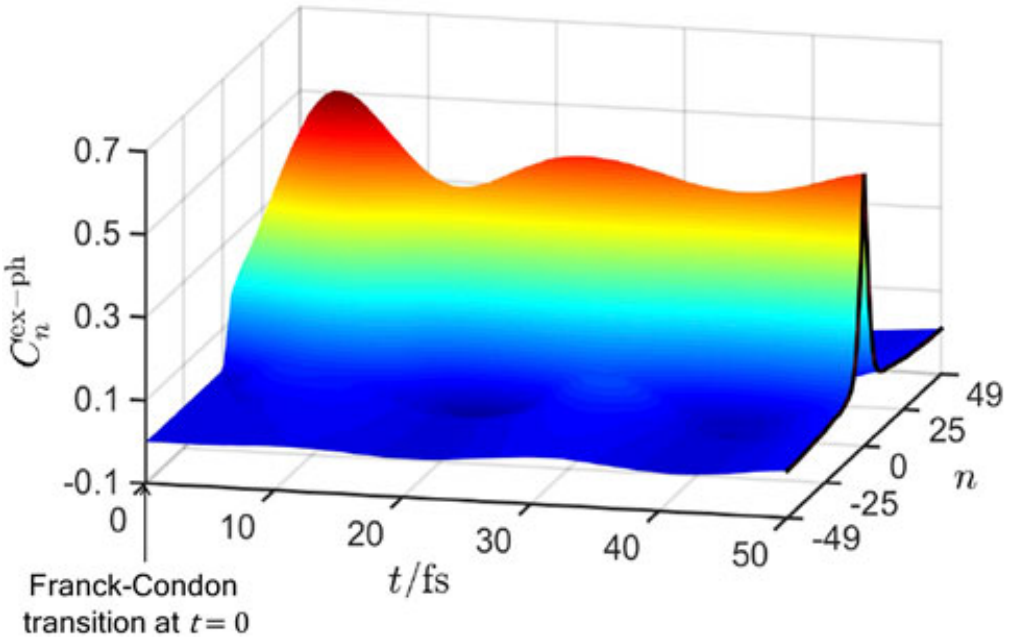


Figure 2.7: The characteristic time evolution and site dependence of the exciton-phonon correlation function $C_n^{\text{ex-ph}}(t)$ for an exciton-polaron. Figure reproduced from [199].

Alternatively, the exciton-polaron's overall spatial extent is determined by its localisation length, which describes how far the polaron itself is spread across the polymer chain. This is given by the root-mean-square spread of the exciton wavefunction:

$$\ell = 2\sqrt{\langle n^2 \rangle - \langle n \rangle^2}, \tag{2.2.29}$$

where

$$\langle n^p \rangle = \frac{\sum_n n^p \left\langle \hat{N}_m \right\rangle}{\sum_n \left\langle \hat{N}_m \right\rangle} \tag{2.2.30}$$

Since the expectation value of the nuclear displacement follows the particle density, ℓ directly quantifies the magnitude of nuclear displacements [174]. The localisation length ℓ is influenced by multiple factors, including the strength of exciton-phonon interactions and disorder effects. In the strong-coupling limit, self-trapping by the exciton-phonon coupling predominantly determines ℓ, whereas in disordered

systems, Anderson or disorder driven is the main mechanism for exciton-polaron localisation [174, 195].

In the adiabatic limit, exciton-phonon interactions lead to self-localisation, with a localisation length given by l_c.

$$l_c = \frac{4t_0}{g^2\hbar\omega} \tag{2.2.31}$$

where t_0 is the transfer integral defined in the Frenkel Hamiltonian. Menwhile, in strongly disordered systems, localisation occurs primarily due to Anderson localisation, with localisation lengths dictated by Equation 2.2.14. Moreover, considering the exciton-polaron quasi-particle, its increased effective mass as a result of the exciton phonon coupling ($m^* > m_0$), modifies the disorder induced localisation length slightly:

$$l_d \sim \left(\frac{m_0 t_0}{m^* \sigma}\right)^{\nu(E)} \tag{2.2.32}$$

If the exciton-phonon coupling is weak, $m^* \approx m_0$, and the disorder-induced localisation follows the standard free-particle behaviour. In contrast, as coupling increases, the exciton-polaron becomes heavier, reinforcing the effects of the disorder and reducing the localisation length.

In conjugated polymers, the adiabatic regime $\left(\frac{\hbar\omega}{4t_0} = \omega' < 1\right)$ and the large polaron regime ($\lambda < 1$) are typically applicable. Within these regimes, classical treatments predict self-localisation, though quantum effects must be considered and become relevant under certain conditions. High-frequency vibrational phonons generally do not result in self-localisation, but exciton-polaron formation still significantly influences exciton dynamics contributing to ultrafast decoherence effects, which will be further examined in Chapter 4. On the other hand, torsional phonons have been connected to significant localisation and self-trapping effects, particularly in polymers with a staggered ground-state conformations [174, 195, 200].

2.2.5 Coupling of the exciton to torsional degrees of freedom

Exciton dynamics in conjugated polymers is strongly influenced by the torsional degrees of freedom of individual moieties, which modify the corresponding electronic coupling and, in turn, induce exciton localisation. The interaction between localised excitons and vibrational phonons, as captured in the Frenkel-Holstein model given by Equation 2.2.15, can be extended to include torsional phonons as follows [200]:

$$\hat{H}_{ROT} + \hat{H}_{EX-ROT} = \sum_{n=1}^{N-1} J(\theta_n)\hat{T}_{n,n+1} + \sum_{n=1}^{N}\left(\frac{K}{2}(\Delta\phi_n)^2 + \frac{L_n^2}{2I}\right) \tag{2.2.33}$$

where the dihedral angle between adjacent moieties in the polymer chain is represented as $\theta_n = (\phi_{n+1} - \phi_n)$, and $\Delta\phi_n$ corresponds to the angular displacements from the equilibrium position, such that $\phi_n = \phi_n^0 + \Delta\phi_n$. The parameter K_n is the elastic force constant which provides information about the rigidity of the bond, and I_n is the moment of inertia for the corresponding moiety. The bond order operator $\hat{T}$ is used for simplicity in order to describe exciton migration between neighbouring sites:

$$\hat{T}_{n,n+1} = \sum_{n=1}^{N-1}\left(\hat{a}_{n+1}^{\dagger}\hat{a}_n + \hat{a}_n^{\dagger}\hat{a}_{n+1}\right) \tag{2.2.34}$$

For sufficiently small angular displacements from the respective equilibrium positions ($\Delta\phi_n \rightarrow 0$ for all n), the transfer integral associated with the through-bond superexchange transfer (dependent on the bond angles in Equation 2.2.6) can be linearised as:

$$J(\theta_n) \simeq J_n^0 - J_{SE}\sin 2\theta_n^0 \times (\Delta\phi_{n+1} - \Delta\phi_n) \tag{2.2.35}$$

A dimensionless representation of the Hamiltonian is obtained by applying the following transformations:

$$\tilde{\phi} = \left(\frac{K}{\hbar\omega_{rot}}\right)^{1/2}\phi, \quad \tilde{L} = \left(\frac{\omega_{rot}}{\hbar K}\right)^{1/2}L \tag{2.2.36}$$

where $\omega_{rot} = (K/I)^{1/2}$ is the rotational angular frequency. Thus, the expression of the Hamiltonian given by Equation 2.2.33 can be rearranged as:

$$\hat{H} = \sum_{n=1}^{N-1} \left[J_n^0 - \hbar\omega_{rot} D(\theta_n^0)(\Delta\tilde{\phi}_{n+1} - \Delta\tilde{\phi}_n) \right] \hat{T}_{n,n+1} + \frac{\hbar\omega_{rot}}{2} \sum_{n=1}^{N} \left((\Delta\tilde{\phi}_n)^2 + \tilde{L}_n^2 \right) \tag{2.2.37}$$

where $D(\theta_n^0)$ is the dimensionless exciton-roton coupling constant, defined as:

$$D(\theta_n^0) = \frac{J_{SE} \sin(2\theta_n^0)}{(\hbar\omega_{rot} K)^{1/2}} \tag{2.2.38}$$

To fully describe the torsional dynamics in a quantum mechanical framework, the Hamiltonia in Equation 2.2.37 is quantised by introducing the operators for the canonically conjugate variables $\Delta\tilde{\phi}_n$ and $\tilde{L}_n$. This is achieved by introducing the harmonic oscillator raising and lowering operators corresponding to the roton excitations, $\hat{c}_n^\dagger$ and $\hat{c}_n$.

$$\Delta\tilde{\phi}_n \rightarrow \Delta\hat{\phi}_n = \frac{1}{\sqrt{2}}(\hat{c}_n^\dagger + \hat{c}_n) \equiv \hat{C}_n \tag{2.2.39}$$

and

$$\tilde{L}_n \rightarrow \hat{L}_n = \frac{i}{\sqrt{2}}(\hat{c}_n^\dagger - \hat{c}_n) \tag{2.2.40}$$

Thus, the Hamiltonian becomes:

$$\hat{H} = \sum_{n=1}^{N-1} \left[J_n^0 - \hbar\omega_{rot} D(\theta_n^0)(\hat{C}_{n+1} - \hat{C}_n) \right] \hat{T}_{n,n+1} + \hbar\omega_{rot} \sum_{n=1}^{N} \left(\hat{c}_n^\dagger \hat{c}_n + \frac{1}{2} \right) \tag{2.2.41}$$

The final expression shows how variations of the torsional angle θ_n^0 have a direct impact in the exciton dynamics. The term $D(\theta_n^0)(\hat{C}_{n+1} - \hat{C}_n)$ illustrates how torsional modulation can lead to dynamic localisation of excitons [199].

Within a polymer chain, the exciton is not restricted to interactions with a single torsional phonon but instead couples to multiple torsional modes along the polymer backbone. The interaction between the exciton and torsional phonons induces significant planarisation of the polymer chain which modifies the local electronic

structure and directly influences exciton dynamics. The exciton-roton coupling results in the formation of an exciton-polaron, arising from the self-localisation of the exciton as it distorts the lattice or polymer chain.

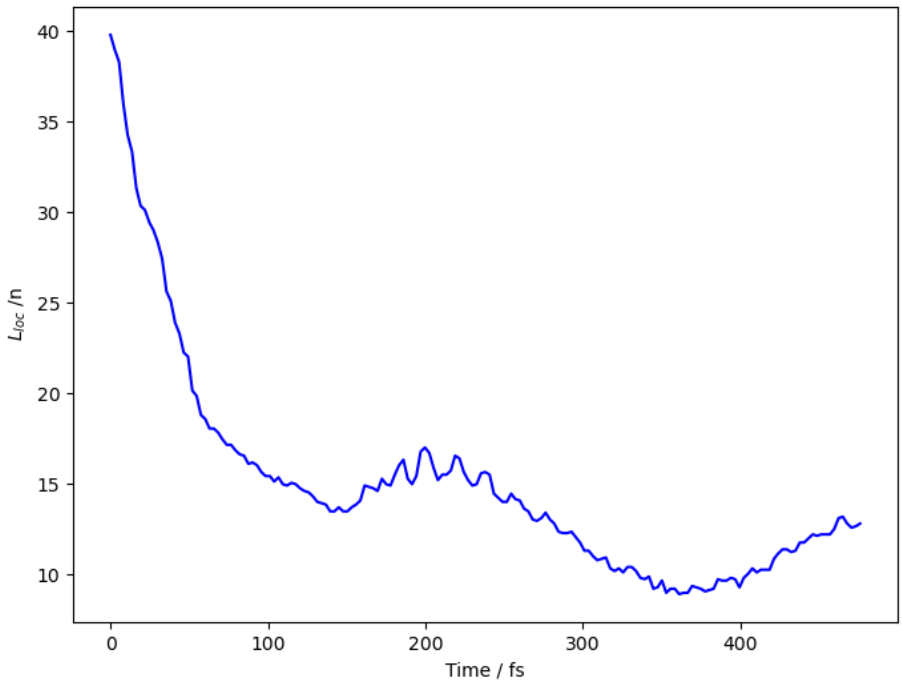


Figure 2.8: Localisation length along the chain, for the first 2 torsional periods. Results obtained for a chain of 40 sites with physical parameters corresponding to PPV. The exciton localisation is a result of the coupling of excitons with torsional rotons with no external dissipation included.

The formation of the exciton-polaron through coupling with torsional modes differs from vibrationally induced self-trapping extending over a characteristically longer period of time (in PPV derivatives this ratio is calculated to be 10 times slower for torsional motion [174]). Due to the extended timescales associated with torsional motion, a hybrid treatment of the exciton-torsion coupling seems appropriate, in which the torsional motion is treated classically but including quantum fluctuations and the exciton-phonon coupling is still treated quantum mechanically.

Figure 2.8 illustrates the effect of exciton coupling to torsional degrees of freedom on localisation dynamics. Initially, the exciton is fully delocalised across the entire polymer chain (40 sites). Within one torsional period (200 fs), it rapidly localises over approximately 15 sites and further localises to 10 sites at 400 fs. This behaviour aligns with other theoretical predictions, where the localisation length for self-trapped excitons is estimated to be $10-14$ nm, extending over $12-15$ sites [199, 201]. The figure also showcases persistent dynamical modulation of localisation length with a period of 200 fs, consistent with the torsional period.

A classical approach to torsional dynamics

Given the role of torsional degrees of freedom in exciton localisation, this section outlines how torsional motion is treated in our simulations. In the classical limit, where $\hbar\omega \ll J$, the rotational motion of each moiety follows a deterministic trajectory driven by the torque acting on the system. The equation of motion for the torsional displacement is obtained by differentiating the rotational Hamiltonian with respect to the angular displacement ϕ_n:

$$\Gamma_n = -\frac{\partial\langle\hat{H}\rangle}{\partial\Delta\tilde{\phi}_n} = -\Delta\tilde{\phi}_n + \lambda_n \tag{2.2.42}$$

where λ_n represents an additional torque arising from exciton-induced modifications to the torsional potential. This coupling term is given by

$$\lambda_n = D(\theta^0_{n-1})\langle\hat{T}_{n-1,n}\rangle - D(\theta^0_n)\langle\hat{T}_{n,n+1}\rangle \tag{2.2.43}$$

This expression accounts for the coupling between neighbouring rings at sites $n-1$ and $n+1$, with $D(\theta^0_n)$ representing the dependence on the equilibrium torsional angles.

The equilibrium angular displacement is obtained by setting $\Gamma_n = 0$, which results in the expression:

$$\Delta\tilde{\phi}_n^{\mathrm{eq}} = \lambda_n \tag{2.2.44}$$

This equilibrium angular displacement establishes the initial torsional deformations caused by exciton-induced forces in the absence of external dissipation. In particular, for a polymer with a staggered torsional ground state, it has been shown that the equilibrium displacement follows $\lambda_n \propto \sum\langle\hat{T}_{n,n+1}\rangle$, leading to significant planarisation and self-trapping of the exciton density, consistent with the formation of a Landau exciton-polaron [200].

Hybrid treatment of rotons

Building on the calculated equilibrium angular displacements, torsional fluctuations around these values are introduced as:

$$\Delta\tilde{\phi}_n = \Delta\phi_n^{\mathrm{eh}} + \delta\tilde{\phi}_n \tag{2.2.45}$$

here $\Delta\phi_n^{\mathrm{eh}}$ originally represents the equilibrium displacement $\Delta\phi_n^{\mathrm{eh}} = \Delta\tilde{\phi}_n^{\mathrm{eq}}$ but it is allowed to evolve following classical dynamics, while being influenced by fluctuations in the exciton density. On the other hand, $\delta\tilde{\phi}_n$ are treated quantum mechanically having a direct impact on exciton dynamics. which is treated quantum mechanically in Hamiltonian that includes a quantum mechanical treatment of the fluctuations. Thus, the classical component evolves according to Ehrenfest equations of motion:

$$\frac{d\Delta\tilde{\phi}_n^{\mathrm{eh}}}{dt} = \tilde{L}_n^{eh} \tag{2.2.46}$$

$$\frac{d\tilde{L}_n^{eh}}{dt} = \Gamma_n = -\Delta\tilde{\phi}_n^{eh} + \lambda_n - \gamma\tilde{L}^{eh} \tag{2.2.47}$$

where γ represents the damping coefficient, which accounts for external forces that resist the torsional motion. These forces arise from the interaction of the system with

the environment, for example from solvent effects, limits in the motion imposed by the temperature, and steric hindrance from the side chains. In polymers with bulky side chains, such as MEH-PPV, the damping term can be significantly larger than in simpler systems like PPV, which results in damped torsional oscillations. As a result:

$$\omega' = (\omega^2 - \gamma^2/4)^{1/2} \tag{2.2.48}$$

The torsional fluctuations introduced in Equation (2.2.45) on the other hand are evolved quantum mechanically, which is incorporated via an effective Hamiltonian. This requires the introduction of the new displaced ladder operators for the harmonic oscillators controlling the fluctuations:

$$\Delta\tilde{\phi} = \frac{\hat{c}^\dagger + \hat{c}}{\sqrt{2}}, \quad \delta\tilde{\phi} = \frac{\hat{c}'^\dagger + \hat{c}'}{\sqrt{2}}. \tag{2.2.49}$$

$$\hat{C}' = \hat{C} - \lambda, \tag{2.2.50}$$

It can be shown (included in Appendix C) that the resulting effective Hamiltonian takes the form:

$$\begin{aligned}\hat{H}_{\text{eff}} = &\sum_{n=1}^{N-1}\left[J_N^0 - \hbar\omega D(\theta_n^0)\left(\Delta\tilde{\phi}_{n+1}^{eh} - \Delta\tilde{\phi}_n^{eh}\right)\right]\hat{T}_{n,n+1} \\ &- \hbar\omega\sum_{n=1}^{N-1} D(\theta_n^0)\left(\hat{C}'_{n+1} - \hat{C}'_n\right)\left(\hat{T}_{n,n+1} - \langle\hat{T}_{n,n+1}\rangle\right) \\ &+ \hbar\omega\sum_{n=1}^{N}\left(\hat{c}_n'^\dagger\hat{c}'_n + \frac{1}{2}\right) \\ &+ \frac{\hbar\omega}{2}\sum_{n=1}^{N-1} D(\theta_n^0)\left(\Delta\tilde{\phi}_{n+1}^{eh} - \Delta\tilde{\phi}_n^{eh}\right)\langle\tilde{T}_{n,n+1}\rangle\end{aligned} \tag{2.2.51}$$

This Hamiltonian provides a description of the coupled dynamics between excitons and torsional fluctuations including quantum correction to the exciton-hopping dynamics due to fluctuations in the torsional modes. The initial angular displacements are used to calculate the evolution of the exciton dynamics for a given number of steps, after which the exciton density is used to update the angular displacements

via the Ehrenfest equations of motion as described earlier. This hybrid approach allows for a more precise representation of exciton localisation and decoherence which define ultrafast dynamics in conjugated polymers.

2.3 Intermolecular dynamics: FRET

Förster Resonance Energy Transfer (FRET) is a non-radiative energy transfer process that arises from the Coulombic interaction between the oscillating transition dipole moments of two chromophores. The efficiency of FRET is highly dependent on the distance between the interacting chromophores; under the point-dipole approximation, this relation follows an inverse proportionality to the sixth power of the separation distance $\propto R^{-6}$. Consequently, FRET interactions can occur over relatively long ranges compared to the Dexter exchange interaction, which necessitates direct overlap of the donor and acceptor wavefunctions.

In π-conjugated polymers characterised by a singlet first excited state, both FRET and Dexter mechanisms, as represented in Figure 2.9, contribute to energy migration. However, FRET emerges as the dominant mechanism for long-range energy transfer, typically extending up to approximately 10 nm [202]. This mechanism gains relevance in disordered regions where larger interchain separations make the wavefunction overlap required for Dexter transfer less probable [203]. In contrast, Dexter transfer, which decays exponentially with distance, dominates over short-range energy transfer processes with separations up to a few ångströms, particularly for highly ordered structures like H-aggregates [204]. Notably, unlike FRET, Dexter transfer does not rely on dipole-dipole interactions and therefore is the only available energy transfer mechanism between triplet states.

FRET occurs through a quantum mechanical process wherein an excited donor molecule non-radiatively transfers energy to an acceptor molecule through the

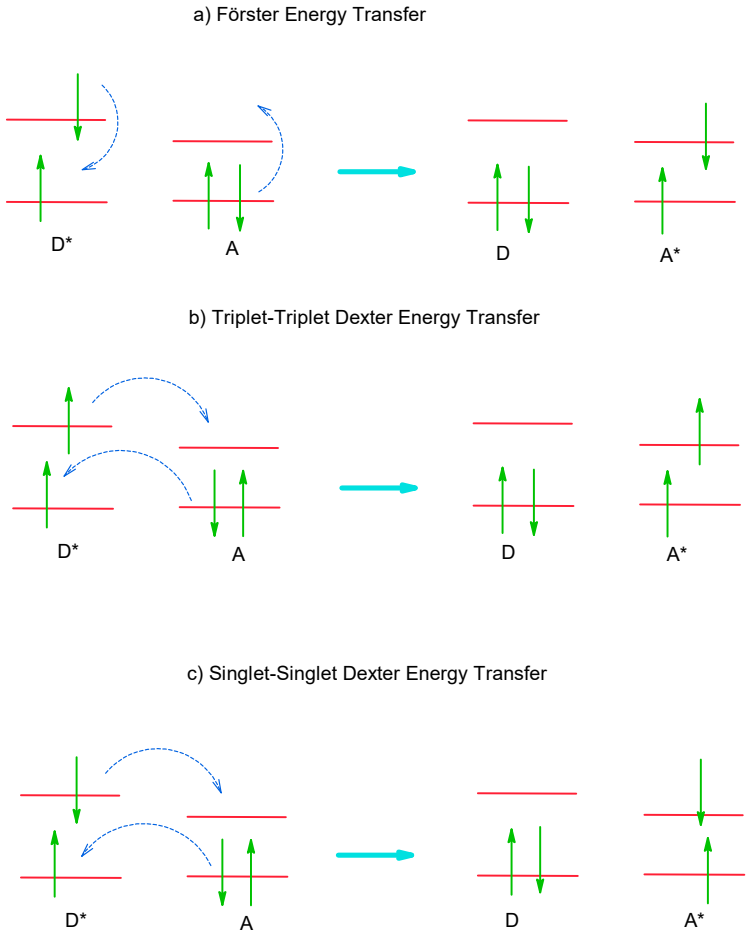


Figure 2.9: FRET and Dexter energy transfer processes. Both FRET and Dexter are non-radiative mechanisms. (a) FRET is a quantum mechanical process where an excited donor molecule transfers its excitation energy to an acceptor molecule through the resonance between their energy levels. The Dexter energy transfer, shown in (b) and (c), involves the direct exchange of electrons between donor and acceptor molecules. Dexter transfer can mediate energy transfer between both triplet-triplet and singlet-singlet systems.

coupling of their transition dipole moments [205]. The transition rate for this process can be derived through the Fermi's golden rule [206, 207]:

$$k_{\mathrm{FRET}} = \frac{2\pi}{\hbar} \left|\langle D, A^* | H_{\mathrm{int}} | D^*, A\rangle\right|^2 I_{\mathrm{overlap}} \tag{2.3.1}$$

Here, $\langle D, A^* | H_{int} | D^*, A\rangle \equiv J_{DA}$ defines the transfer integral from the initial state $|D^*, A\rangle$ to the final state $|D, A^*\rangle$, in which $|D\rangle, |A\rangle$ represent the basis at the donor and acceptor sites. The spectral overlap integral I_{overlap} measures the overlap

between the donor's fluorescence emission and the acceptor's absorption spectra, both shaped by vibronic coupling.

$$I_{\text{overlap}} = \frac{\int_0^\infty F_D(\lambda)\varepsilon_A(\lambda)\lambda^4\, d\lambda}{\int_0^\infty F_D(\lambda)\, d\lambda} \tag{2.3.2}$$

where $F_D(\lambda)$ is the fluorescence emission spectrum of the donor, and $\varepsilon_A(\lambda)$ is the molar extinction coefficient of the acceptor, both dependent on the wavelength of the electromagnetic radiation, λ. While this integral form is most commonly used in experimental and computational studies, it can also be understood as the continuous counterpart of a discrete sum over vibronic transitions:

$$I_{\text{overlap}} = \sum_{\nu_D,\nu_A} F_{\nu_D}^{(D)} F_{\nu_A}^{(A)} \delta(E_{D,\nu_D} - E_{A,\nu_A}). \tag{2.3.3}$$

Here, $F_{\nu_D}^{(D)}$ and $F_{\nu_A}^{(A)}$ are the Franck-Condon factors, which will be introduced in Section 2.4.1, and the Dirac delta function enforces energy conservation between donor emission and acceptor absorption.

A derivation for the interaction Hamiltonian for this process can start from considerations of the Coulomb's law which describes the potential energy between two point charges q_1 and q_2.

$$V_{\text{Coulomb}} = \frac{1}{4\pi\epsilon_0}\frac{q_1 q_2}{|\mathbf{r}_1 - \mathbf{r}_2|} \tag{2.3.4}$$

For neutral chromophores, the charge distribution is described using a multipole expansion, where the first non-zero term in the interaction is the dipole-dipole coupling. Higher-order terms, such as quadrupole or octupole contributions, become relevant at shorter distances. Thus, from considerations of the corresponding electrostatic potential of two interacting dipoles at a distance (R), the resulting Hamiltonian is given by:

$$\hat{H}_{\text{int}} = -\frac{1}{4\pi\epsilon_0}\left[\frac{\mu_D \cdot \mu_A}{R^3} - 3\frac{(\mu_D \cdot \mathbf{R})(\mu_A \cdot \mathbf{R})}{R^5}\right] \tag{2.3.5}$$

where μ_D, μ_A are the dipole moments for the interacting chromophores, and $\mathbf{R}$ is the vector along the line connecting the two dipoles, with scalar magnitude R corresponding to the distance between the interacting sites. While the first term captures the corresponding interaction for parallel dipoles, the second term includes a correction to this. Under the point-dipole approximation, where the interaction strength scales as R^{-3}, this leads to the frequently quoted transfer rate scaling as R^{-6}. However, for spatially extended chromophores, such as those in conjugated polymers, extending over multiple monomers, this scaling is modified. Under these circumstances the effective interaction strength depends on the spatial distribution of the transition dipole moment, and the FRET rate may deviate from the R^{-6} dependence, following less steep decay with distance depending on chain length and their relative orientation [208].

$$k_{\mathrm{FRET}} \propto \frac{\kappa^2}{R^6} \tag{2.3.6}$$

where κ^2 is the orientation factor, as derived from Equation 2.3.5, which accounts for the relative alignment of the donor and acceptor dipoles.

$$\kappa^2 = [\mu_D \cdot \mu_A - 3(\mu_D \cdot \mathbf{R})(\mu_A \cdot \mathbf{R})]^2 \tag{2.3.7}$$

The orientation factor κ^2 can take values between 0, for two dipoles perpendicular to each other, and 4, for collinear dipoles. This sensitivity to dipole alignment allows FRET to be used as a probe for detecting changes in molecular orientation and conformation within π-conjugated polymers.

Traditionally, the point-dipole approximation, as reflected in Equation 2.3.7, has been used to model the transfer rates within π-conjugated polymers. This approximation, which assumes the dipole moment of a chain or a chromophore is concentrated at an infinitesimally small point, is valid within systems where

the spatial extent of the chromophore is much smaller than the distance between the donor and acceptor molecules. In conjugated polymers, however, the length of a single chromophore can become comparable to the interchromophoric separation, leading to significant deviations from the point-dipole approximation. For instance, with this approximation, a linear increase in the transfer integral with the dimensions of the chromophore is expected. Nevertheless, high-accuracy computational studies and experimental observations indicate that transfer integrals tend to zero as the chromophore length increases, corresponding to a reduction in Davydov splitting [208–210].

Therefore, as the chromophores increase in size, the spatial extent of the dipole cannot be accurately represented as a single point. Consequently, the line-dipole approximation, which calculates the dipole moment distribution over the entire chromophore length, offers a more realistic model. A comprehensive framework for calculating transfer integrals within the line-dipole approximation is detailed elsewhere [208]. Within this model, the transfer integral incorporates the corresponding contribution from different points along the donor and acceptor chains.

$$J_{DA} = \int_{L_D}\int_{L_A}\left[\frac{\mu_D(s)\cdot\mu_A(s')}{R(s,s')^3} - 3\frac{(\mu_D(s)\cdot\mathbf{R}(s,s'))(\mu_A(s')\cdot\mathbf{R}(s,s'))}{R(s,s')^5}\right]ds\,ds' \tag{2.3.8}$$

where L_D and L_A represent the lengths of the donor and the acceptor polymer chains, and $\mu(s)$ is the local transition dipole moment density as a function along the polymer chain. Since the basis used in this work is explicitly quantised, and the Franck-Condon factors can be directly obtained from theoretical calculations presented in Section 2.4.1, it is most practical to express the energy transfer rate in a discrete form. Thus, the final rate expression is given by [206]:

$$k_{\mathrm{FRET}} = |J_{DA}|^2 F^D_{\nu_i\nu_f} F^A_{\nu'_i\nu'_f} I_{\mathrm{overlap}} \tag{2.3.9}$$

where $F^{D}_{\nu_i\nu_f}$ and $F^{A}_{\nu'_i\nu'_f}$ are the Franck-Condon factors for the donor relaxation and the acceptor excitation transitions respectively, and J_{DA} is the electronic exciton transfer integral, which under the line-dipole approximation, is given by:

$$J_{DA} = \left(\frac{1}{4\pi\varepsilon_r\varepsilon_0}\right) \sum_{n\in D} \sum_{n'\in A} \frac{\kappa_{nn'}}{R^3_{nn'}} \mu_{n'} \Psi^0_{n'} \mu_n \Psi^0_n \tag{2.3.10}$$

2.3.1 Efficiency of FRET

The efficiency of FRET measures the probability of energy transfer from an initially excited donor to an acceptor via FRET. This efficiency is directly related to the distance between interacting chromophores and their relative alignment. Additionally, the spectral overlap integral, defined in Equation 2.3.2 quantifies the degree of overlap between the donor's emission spectrum and the acceptor's absorption spectrum. The efficiency of FRET can be found in terms of the corresponding rates as:

$$E = \frac{k_{ET}}{k_f + k_{ET} + \sum k_i} \tag{2.3.11}$$

where k_{ET} is the FRET rate, k_f is the rate of the fluorescence relaxation, and $\sum_i k_i$ encompasses the total of the non-radiative decays. This equation can be rearranged as:

$$E = \frac{1}{1 + (\frac{r}{R_0})^6} \tag{2.3.12}$$

where r is the distance between the donor and acceptor chromophores and R_0 is the characteristic distance at which the efficiency reaches 50% known ad the Förster radius. The Förster radius is dependent on the overlap integral, I_{overlap}, the quantum yield of the donor, Φ_D, and the orientation factor, κ [211]:

$$R_0^6 = \frac{9000\,(\ln 10)\,\kappa^2\,\Phi_D\,I_{\text{overlap}}}{128\pi^5 N_A n^4} \tag{2.3.13}$$

Here N_A is Avogadro's number, while (n) the refractive index of the medium considering the solution or the polymer itself for calculations in films.

This expression can be used to extend on the previous Equation 2.3.6 for energy transfer rates:

$$k_t = \frac{1}{\tau_D}\left(\frac{R_0}{r}\right)^6 \tag{2.3.14}$$

where τ_D is the donor's fluorescence lifetime.

In summary, FRET efficiency is predominantly determined by the distance between chromophores, their relative alignment, and the spectral overlap between emission and absorption spectra. As a result, FRET efficiency varies depending not only on the specific properties of the individual polymer but also with the morphology of individual chains and the structure of the packing, such as the formation of ordered and disordered regions.

2.4 Spectroscopical methods as a probe of conformational order in conjugated polymers

In Section 2.2.2, it has been shown that the degree of delocalisation is directly related to structural defects and the inherent disorder within the polymer chains. Similarly, it can be established that the optical spectrum of these materials is determined by the exciton localisation. As a result, a variety of spectroscopic methods can be used to survey exciton dynamics and determine the structural properties of these materials. This section aims to introduce the relationship between the theoretical model for exciton dynamics described so far and available experimental probes.

2.4.1 Vibronic structure

The vibronic structure of absorption and photoluminescence spectra provides information about exciton delocalisation. We first consider transitions in a uni-

form polymer chain, in the absence of disorder, within the adiabatic limit where $J \gg \hbar\omega$. Using the Born-Oppenheimer approximation, the total wavefunction can be factorised into an electronic and a vibrational component:

$$|\Phi\rangle = |\Psi_i\rangle \prod_m |\Upsilon^{(i)}_{\nu_m}\rangle\rangle_m \tag{2.4.1}$$

where $|\Psi_i\rangle = \sum_n \Psi_n |n\rangle$ is the exciton wavefunction and $|\Upsilon^{(i)}_{\nu_m}\rangle\rangle_m$ represents the vibrational state of the system with an exciton described in the state $|\Psi_i\rangle$. This factorisation simplifies the evaluation of the transition dipole moment, which determines the probability of optical transitions. The transition dipole moment between an initial state $|\Phi_i\rangle$ and a final state $|\Phi_f\rangle$ is given by:

$$\mu_{if}^{\nu'\nu} = \langle\Phi_f|\hat{\mu}|\Phi_i\rangle = \langle\Psi_f|\hat{\mu}|\Psi_i\rangle \prod_m \langle\langle \nu'^{(f)}_m | \nu^{(i)}_m\rangle\rangle_m \tag{2.4.2}$$

where $\hat{\mu}$ is the dipole moment operator, therefore, the first term in this equation represents the electronic transition dipole moment, while the second term describes the overlap between vibrational wavefunctions in the initial and final electronic states. Since the intensity of an optical transition is proportional to the squared magnitude of the transition dipole moment, $I_{if} \propto |\mu_{if}|^2$ we must evaluate the squared expression for the dipole moment.

$$\left|\mu_{if}^{\nu\nu'}\right|^2 = |\mu_{if}|^2 \prod_m F_{i,m}^{\nu\nu'} = |\mu_{if}|^2 F_i^{\nu\nu'} \tag{2.4.3}$$

where $|\mu_{if}|$ is the magnitude of the electronic dipole moment and $F^{\nu\nu'}$ is the Franck-Condon factor which has been identified as the squared magnitude of the vibrational overlap. Within the harmonic approximation, where the nuclear potential surfaces are considered to be nearly parabolic, the Franck-Condon factors follow a distribution

associated to the Laguerre polynomials ($L_{\nu}^{(\nu'-\nu)}(S)$) [189, 212, 213]:

$$F_j^{\nu'\nu} = \prod_m e^{-S_j(m)} \frac{S_j(m)^{|\nu'-\nu|}}{|\nu'-\nu|!} L_{\nu}^{(|\nu'-\nu|)}(S_j(m)) \tag{2.4.4}$$

For practical purposes, it is often convenient to describe these transitions in terms of the effective Huang-Rhys factor, $S_{\text{eff},j}$ introduced in Section 2.2.3, which accounts for the total exciton-phonon coupling strength across the entire polymer chain, it can be shown that this results in [214]:

$$F_j^{\nu'\nu} = e^{-S_{\text{eff},j}} \frac{(S_{\text{eff},j})^{\nu'-\nu}}{(\nu'-\nu)!} L_{\nu}^{(\nu'-\nu)}(S_{\text{eff},j}) \tag{2.4.5}$$

For transitions with an initial ground vibrational state, the Laguerre polynomial simplifies to unity ($L_0^{(\nu')}(S) = 1$) and so the Franck-Condon factor is reduced to a Poisson distribution, given by:

$$F_j^{0v} = \frac{(S_{\text{eff},j})^v e^{-S_{\text{eff},j}}}{v!} \tag{2.4.6}$$

At room temperature, the initial vibrational state can generally be expected to be the ground state, as a consequence of the Boltzmann distribution. Specifically, for a vibrational frequency of $\hbar\omega = 0.19$ eV, at room temperature, $T = 300$ K, the probability of occupying the ground vibrational state is $P_0 > 0.99$, while higher vibrational states have exponentially suppressed occupation probabilities. Consequently, absorption transitions can be considered to originate primarily from the ground vibrational state. Similarly, for the emission spectra, photoluminiscence primarily occurs from the lowest energy vibrational state in the excited state as a result of fast vibrational relaxation, as stated in Kasha's rule.

The dipole moment for specific transitions can be obtained following from these derivations. The dipole moment for a transition between the electronic and ground states where the vibrational state remains in the ground state, the $0-0$ transition, is:

$$\left|\mu_{ge}^{00}\right| = \left|\left\langle \Psi_{(EX)} \right| \hat{\mu} \left| \Psi_{(GS)} \right\rangle\right|^2 \prod_m \left|\langle\langle \Upsilon_0^{(EX)}(m) | \Upsilon_0^{(GS)}(m) \rangle\rangle\right|^2 \tag{2.4.7}$$

$$\left|\mu_{ge}^{00}\right|^2 = |\mu_{ge}|^2 e^{-S_{\text{eff}}} \tag{2.4.8}$$

Similarly, the transition from the ground electronic in its ground vibrational state to the excited electronic state in its excited electronic state, corresponding to the $0-1$ absorption transition has a dipole moment of [170]:

$$\left|\mu_{ge}^{01}\right|^2 = |\mu_{ge}|^2 \left|\langle\langle \Upsilon_1^{(EX)}(m)|\Upsilon_0^{(GS)}(m)\rangle\rangle\right|^2 \prod_{p\neq m} \left|\langle\langle \Upsilon_0^{(EX)}(p)|\Upsilon_0^{(GS)}(p)\rangle\rangle\right|^2 \tag{2.4.9}$$

which highlights the exciton transition occurs on a single monomer.

$$\langle\langle \Upsilon_1^{(EX)}(m)|\Upsilon_0^{(GS)}(m)\rangle\rangle = S_m^{1/2} e^{-S_m/2} \tag{2.4.10}$$

$$\langle\langle \Upsilon_0^{(EX)}(p)|\Upsilon_0^{(GS)}(p)\rangle\rangle = e^{-S_p/2} \tag{2.4.11}$$

Accounting for all possibilities of p, Equation 2.4.9

$$|\mu_{ge}^{01}|^2 = |\mu_{ge}|^2 S_{\text{eff}} e^{-S_{\text{eff}}}. \tag{2.4.12}$$

Finally, the transition from the excited state in its ground vibrational state to the ground electronic state in its excited vibrational state, the $0-1$ emission transition:

$$\mu_{eg}^{01} = \left\langle \Psi_{(GS)} \right| \hat{\mu} \left| \Psi_{(EX)} \right\rangle \langle\langle \Upsilon_1^{(GS)}(m)|\Upsilon_0^{(EX)}(m)\rangle\rangle \prod_{p\neq m} \langle\langle \Upsilon_0^{(GS)}(p)|\Upsilon_0^{(EX)}(p)\rangle\rangle \tag{2.4.13}$$

$$|\mu_{eg}^{01}|^2 = |\mu_{eg}|^2 S_{\text{eff}} e^{-S_{\text{eff}}} \tag{2.4.14}$$

In this example it becomes evident the symmetry of these Franck-Condon factors which under the harmonic approximation, and under no considerations of non-adiabatic effects satisfy the following relation:

$$|\langle\langle \Upsilon_v^{(EX)}|\Upsilon_0^{(GS)}\rangle\rangle|^2 = |\langle\langle \Upsilon_0^{(GS)}|\Upsilon_v^{(EX)}\rangle\rangle|^2 \tag{2.4.15}$$

The absorption intensity, $A_j^{0\nu}$, and the emission intensity, $I_j^{0\nu}$, are defined as follows:

$$A_j^{0\nu} = E_j \left|\mu_j^{0\nu}\right|^2 \tag{2.4.16}$$

$$I_j^{0\nu} = (E_j)^3 \left|\mu_j^{0\nu}\right|^2 \tag{2.4.17}$$

Applying Equations 2.4.8, 2.4.12, and 2.4.14, the intensity ratio of the 0–1 - 0-0 vibronic transition for both emission and absorption is given by:

$$\frac{I_j^{01}}{I_j^{00}} = S_{\text{eff}} \tag{2.4.18}$$

$$\frac{A_j^{01}}{A_j^{00}} = S_{\text{eff}} \tag{2.4.19}$$

Since the intensity ratio is directly proportional to S_{eff}, exciton localisation is seen to have a significant effect on the relative intensity of the vibronic transitions. Overall, in low disorder systems where excitons are delocalised over large sections or the entire chain, the effective Huang-Rhys parameter S_{eff} remains small. Consequently, the 0–0 transition is dominant over the 0-1 transition. As disorder increases and exciton localisation becomes more pronounced, S_{eff} also increases, resulting in a relative enhancement of the 0–1 transition intensity.

However, these derivations rely on the Condon approximation, which assumes that the electronic transition dipole moment is independent of nuclear displacement. This approximation is valid for highly ordered, planar chains, where transitions follow Franck-Condon selection rules. In contrast, strongly disordered or bent polymer chains experience Herzberg-Teller coupling, which introduces non-Condon contributions and alters transition probabilities [170].

While disorder generally increases S_{eff}, its effect is seen to vary slightly depending on whether the system is in the adiabatic or antiadiabatic regime. In the adiabatic limit, where $\hbar\omega/|J| \to 0$, nuclear motion is slow relative to exciton dynamics, and phonon interactions remain weak. As a result, both emission and absorption intensity ratios scale equally with S_{eff} following Equations 2.4.18-2.4.19. This symmetry arises as Franck-Condon factors determine the vibronic structure and

from the symmetry relation discussed in Equation 2.4.15. In this region, the intensity of the $0-1$ transition increases with the increase of disorder, but nonetheless the $0-0$ transition remains dominant.

As $\hbar\omega$ increases, the system moves towards the antiadiabatic limit ($\hbar\omega/|J| \to \infty$). In this regime, exciton-phonon coupling introduces additional corrections that modify the intensity ratio differently for absorption and emission. The absorption ratio follows [170]:

$$\frac{A_{00}}{A_{01}} = \left(\frac{1 + 0.96|J|/\hbar\omega}{1 - 0.29|J|/\hbar\omega}\right)^2. \tag{2.4.20}$$

The dependence on $|J|/\hbar\omega$ introduces deviations from the expected Franck-Condon behaviour, as the vibration energy increases, this rate approaches a constant value ($\hbar\omega/|J| \to \infty$, $A_{00}/A_{01} \to 1$) and the absorption for the $0-0$ and $0-1$ transition become nearly equal. In contrast, the emission ratio takes the form [170]:

$$\frac{I_{00}}{I_{01}} \times S_{\text{eff}} = \frac{1}{1 + \frac{2}{3}\left(\frac{|\mu_{00,y,j=2}|^2}{|\mu_{00,x,j=1}|^2}\right)\left(\frac{\hbar\omega}{\Delta E_{21}^E}\right)^2}. \tag{2.4.21}$$

Here, as $\hbar\omega$ increases, the denominator grows, causing I_{00}/I_{01} to decrease. This equation also reflects the influence of the Herzberg-Teller effect: while in a linear polymer, transitions are restricted to be parallel to the chain axis, bending defects introduce perpendicular components of the dipole moment. Greater curvature of the polymer chains increases $|\mu_{00,y,j=2}|^2$ while lowering $|\mu_{00,x,j=1}|^2$, further reducing the intensity ratio I_{00}/I_{01}.

For uniform polymers the transition between the adiabatic and the antiadiabatic regimes depends on the strength on polymer size, as finite-length effects influence exciton delocalisation and vibronic coupling. Thus, variations in the vibronic spectra can provide insight into the degree of structural disorder in conjugated polymers. In particular, recent optical modelling studies have demonstrated that the ratio

of the 0–1 to 0–0 vibronic peaks can be used to infer exciton coherence lengths, chromophore sizes, and torsional disorder [110, 215].

2.4.2 Polar fluorescence anisotropy

Fluorescence anisotropy measurements can use the radiative decay of excitons to record fluctuations in the orientation of polymer chains in conjugated polymers. When a material is irradiated by polarised light, it preferentially excites fluorophores within the sample whose transition dipole moments are aligned with the excitation polarisation axis. Additionally, due to the molecular environment and electronic relaxation processes, the orientation of the emission dipole may differ from that of the absorption dipole. Consequently, the emitted fluorescence exhibits an anisotropic intensity distribution, which reflects both the initial preferential absorption and the angular displacement between the absorption and emission dipoles. This anisotropy can be analysed to infer structural order within the material [216]. The relationship between fluorescence anisotropy and molecular orientation is particularly useful for examining long-range order, such as nematic phases in polymer films.

Fluorescence anisotropy, denoted as r, is defined by the relative intensity of the emitted light in the directions parallel and perpendicular to the excitation polarisation, as given by [217]:

$$r = \frac{I_{\parallel} - I_{\perp}}{I_{\parallel} + 2I_{\perp}} \tag{2.4.22}$$

The theoretical limits of anisotropy range from $r = -\frac{1}{2}$ to $r = 1$. However, the physical limits for macroscopic isotropic samples, such as polymer films, depend on the angular displacement δ between the absorption and the emission dipoles as a result of the delay between excitation and fluorescence and also the orientational distribution of the molecules [218]. This angle and the orientational distribution

can vary in time as a result of structural changes in the molecules due to the environment like solvation effects, Brownian motion and internal processes including energy exchange [219, 220].

In the most general case, the fluorescence intensity observed along an arbitrary laboratory axis depends on the projection of the molecular absorption and emission dipoles onto the laboratory axes. The intensity of light emitted along axis j, after absorption along axis i, is given by [218]:

$$I_{ij} = \frac{1}{(2\pi)^2} \int_0^{2\pi} \int_0^{\pi} \mu_{a_i}^2 \mu_{e_j}^2 f(\theta) \sin\theta \, d\theta \, d\phi \tag{2.4.23}$$

where $f(\theta)$ corresponds to the molecular distribution function and $\mu_{a_i}^2 \mu_{e_j}^2$ are the squares of the absorption and emission dipole moments projected onto the laboratory axes. The projections are given by:

$$\mu_{a_i}^2 = [a \cdot \mathbf{O} \cdot u_i]^2 \tag{2.4.24}$$

$$\mu_{e_j}^2 = [e \cdot \mathbf{O} \cdot u_j]^2 \tag{2.4.25}$$

where a_i and e_j are unit vectors along the absorption and emission dipoles, respectively, and u_i and u_j are the unit vectors along the laboratory axes. For subsequent calculations, the absorption angle is assumed to align with the molecular directional axes, which simplifies the transformation between molecular and laboratory frames. To account for the molecular orientation relative to the laboratory frame, the dipole moment components are transformed using the rotation matrix:

$$\mathbf{O} = \begin{pmatrix} \cos\theta\cos\phi & \cos\theta\sin\phi & -\sin\theta \\ -\sin\phi & \cos\phi & 0 \\ \sin\theta\cos\phi & \sin\theta\sin\phi & \cos\theta \end{pmatrix} \tag{2.4.26}$$

As noted above, the expression for the fluorescence anisotropy is often simplified by assuming that the absorption dipole moment is aligned along the molecular axis. In the case of fully absorbing molecules, often represented as rod-like structures,

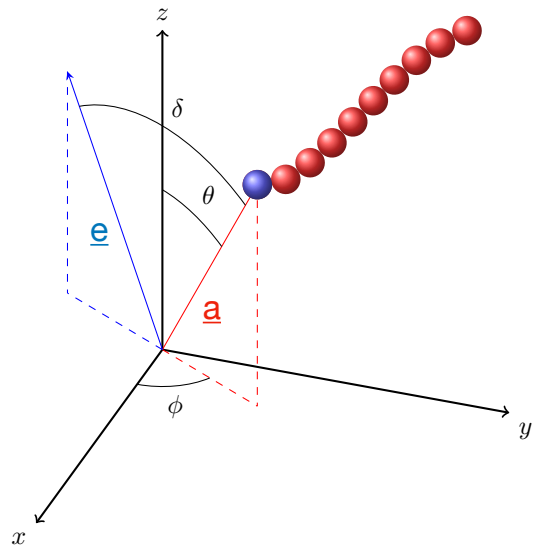


Figure 2.10: The angle between the absorption and emission dipoles in fluorescence anisotropy emission. The line in red marks the directional axis for the absorption chromophore (unitary vector $\underline{a}$) and the blue line represents the directional axis of the emission chromophore (unitary vector $\underline{e}$). The angle between the absorption and emission axes is marked as $\delta \equiv \arccos(\underline{a} \cdot \underline{e})$. The polymer chain orientation is given by the spherical polar axes coordinates at θ, ϕ, and in this case is figure is considered that the absorption chromophore is aligned with the chain.

this assumption is valid as absorption naturally follows the molecular orientation. However, for conjugated polymers, where chromophores are distributed along different segments of the chain, their transition dipole moments are not necessarily aligned with the polymer backbone. Some chromophores may be aligned along the molecular axis, while others may be tilted at varying angles due to the polymer's flexibility and local electronic environment. This variability can be accounted for by introducing intramolecular angle θ_{intra} defined as the chromophore relative angle to the polymer backbone with an angle θ_{inter} with respect to the frame of reference. In this discussion, we define θ and ϕ as the angular coordinates of the chromophore

dipole relative to the molecular frame, as illustrated in Figure 2.10. However, in general, the chromophore's orientation would be a composite of θ_{inter} and θ_{intra}.

The fluorescence intensity observed along an arbitrary laboratory axis depends on the projection of the molecular absorption and emission dipoles onto the laboratory frame, as well as, the angular displacement between the absorption and emission dipoles, defined as δ, as represented in Figure 2.10. The fluorescence intensity is computed by averaging over the ensemble of molecular orientations [218]:

$$I_{\parallel} = I_{zz} = \cos^2\delta \cdot \langle \cos^4\theta \rangle + \frac{1}{2}\sin^2\delta \cdot \Big(\langle \cos^2\theta \rangle - \langle \cos^4\theta \rangle \Big) \tag{2.4.27}$$

Similarly, the perpendicular intensity, $I_{\perp}$, is expressed as:

$$I_{\perp} = I_{xy} = \frac{1}{2}\cos^2\delta \cdot \Big(\langle \cos^2\theta \rangle - \langle \cos^4\theta \rangle \Big) + \frac{1}{4}\sin^2\delta \cdot \Big(\langle \cos^2\theta \rangle + \langle \cos^4\theta \rangle \Big) \tag{2.4.28}$$

Using these intensities, and Equation 2.4.22 the expression for the maximum polar fluorescence anisotropy in a system where the emission and absorption dipoles are parallel, such that $\delta = 0$. For an isotropic sample this can be further simplified by using the known integrals over all space:

$$< \cos^2\theta > = \int_0^{\pi} \cos^2\theta \sin\theta d\theta = \frac{2}{3} \tag{2.4.29}$$

$$< \cos^4\theta > = \frac{2}{5} \tag{2.4.30}$$

the previous equations reduce to $I_{\parallel} = 2/5$ and $I_{\perp} = 2/15$. Substituting these values yields $I_{\parallel} = 2/5$ and $I_{\perp} = 2/15$, resulting in an anisotropy of $r_0 = 2/5$, the maximum value for the case of no angular displacement between the absorption and emission dipoles ($\delta = 0$). Thus, for a fixed intramolecular angle of δ, the fluorescence anisotropy for an ensemble of chromophores is [218, 221, 222]:

$$r_0 = \frac{\langle 3\cos^2\delta \rangle - 1}{5} \tag{2.4.31}$$

2.4.3 Time-resolved polar fluorescence anisotropy

While steady-state anisotropy measurements provide information about the average orientation of the chromophores at a specific time, time-resolved measurements are necessary to survey the evolution of the molecular orientation in time, this is obtained through time-resolved fluorescence anisotropy (TRFA). Furthermore, in systems with minimal rotational diffusion, such as polymer films, TRFA can be used to follow the exciton dynamics. This enables TRFA to probe exciton coupling interactions and intermolecular transfer events, including FRET [87, 223]. These measurements provide information about exciton coupling interactions and intermolecular transfer events such as FRET [87, 223]. The time-dependent anisotropy is described in the same manner as the steady-state measurements in Equation 2.4.22 by obtaining time-resolved measurements of the emission intensity parallelly and perpendicularly to the initial excitation polarisation direction, this is given by:

$$r(t) = \frac{I_{\parallel}(t) - I_{\perp}(t)}{I_{\parallel}(t) + 2I_{\perp}(t)} \tag{2.4.32}$$

Over time, the decay of the fluorescence intensity as a result of the reorientation of the chromophores can be described as a multi-exponential function, reflecting the distinct dynamical processes in the system [223]:

$$r(t) = \sum_i r_0^{(i)} \exp\left(-\frac{t}{\tau_i}\right) \tag{2.4.33}$$

where $r_0^{(i)}$ represents the initial contribution to the total anisotropy from the i-th dynamic process, with a $\tau_{\text{rot}}^{(i)}$ rotational correlation time. For polymer systems, the multi-exponential decay model better captures both the slow molecular reorientation caused by restricted rotational diffusion and the faster exciton migration between chains or chromophores [224].

In summary, the combined use of these spectroscopic probes provides a direct means of studying the relationship between molecular structure and internal optoelectronic processes in conjugated polymers. The intensity ratio of vibronic peaks in absorption and emission reveals further details about exciton localisation and the effects of disorder on electronic transitions. Fluorescence anisotropy, in turn, allows for the study of the mesoscopic order in these materials and provides a better understanding of the spatial distribution of chromophores within conjugated polymer chains. Furthermore, time-resolved anisotropy enables the tracking of exciton migration over time.

3
Computational methods

Despite the considerable reduction in dimensionality offered by the coarse-grained Frenkel–Holstein model, obtaining an exact analytical solution remains unattainable due to the exponential scaling of the Hilbert space with the number of sites and phonon modes included. This chapter presents the computational methods chosen to address this challenge and model exciton dynamics.

The Matrix Product State (MPS) formalism is adopted to truncate the Hilbert space while preserving the most significant entanglement and quantum mechanical details. The system is evolved using the Time-Evolving Block Decimation (TEBD) algorithm. These methods have demonstrated significant success in accurately describing highly correlated one-dimensional systems. Finally, an accurate description of the relaxation dynamics after photoexcitation requires including interactions between the system and its environment. The system-environment relationship is described using the Lindblad master equation, a standard framework for modelling Markovian open quantum systems. However, direct integration of the Lindblad equation is computationally infeasible. As a result, a stochastic quantum jump trajectory method is explored. This approach simulates the system's evolution

through an ensemble of trajectories, each evolving under a non-Hermitian effective Hamiltonian and punctuated by randomised quantum jumps that capture the dissipative effects of environmental interactions.

3.1 From conventional methods to TEBD: addressing computational limitations

Capturing the full dynamics of excitons in π-conjugated polymers requires a computational approach that can accurately describe their interactions with nuclear degrees of freedom while remaining manageable for large-scale simulations. The challenge arises as a result of the exponential growth of the Hilbert space with system size, scaling as $(2\times(n_{\max}+1)))^N$ where N is the number of sites and $n_{\max}$ is the truncation of the phonon basis per site. As a result, direct diagonalisation becomes impractical, requiring the use of alternative methods to improve computational efficiency.

One of the most widely recognised approaches to this problem is the use of mean-field methods like the Ehrenfest approximation, which treats nuclear motion classically while maintaining a quantum mechanical description of the exciton. This approach is particularly successful in describing adiabatic processes but also has several limitations. A major drawback of the Ehrenfest formalism is its inability to account for purely quantum mechanical effects such as zero-point energy and nuclear tunnelling. Additionally, it fails to correctly describe decoherence, as the exciton and nuclear wavefunctions remain unentangled within this formalism [199]. Furthermore, Ehrenfest dynamics does not accurately capture exciton relaxation and breaks down at conical intersections, where multiple potential energy surfaces interact, leading to incorrect electronic population transfer [225].

To improve upon Ehrenfest dynamics, various alternative approaches have been proposed, for example, Fewest-Switches Surface Hopping (FSSH) which introduces

stochastic transitions between electronic states to accommodate the non-adiabatic effects. As FSSH trajectories propagate on a single potential energy surface at a given time while at determined points hopping between different surfaces, the nuclei are still treated semi-classically, resulting in an inaccurate description of decoherence effects [226–228]. Furthermore, previous research has shown that FSSH frequently miss-calculate population transfers, which makes it an unreliable method for modelling exciton relaxation in conjugated polymers [225]. On the other hand, the Multiconfigurational Time-Dependent Hartree-Fock (MC-TDHF) method provides a more rigorous quantum mechanical treatment by explicitly solving the time-dependent Schrödinger equation using a multiconfigurational expansion of the wavefunction [229]. However, this direct approach remains constrained by the the exponential growth of the Hilbert space with the system size, restricting its use for practical applications since it significantly limits the dimensionality of the systems that can be studied.

As an alternative to traditional quantum dynamics approaches, renormalisation group techniques provide an efficient framework for studying many-body systems by systematically truncating the Hilbert space, retaining only the most physically relevant states. This enables the study of larger systems while preserving the quantum mechanical nature of the coupling between interacting degrees of freedom and remaining computationally feasible. One successful application of these principles is the Density Matrix Renormalisation Group (DMRG), first developed by S. White in 1992 in response to the failures of the real-space renormalisation group to produce accurate results in some well-known models like the Heisenberg model and the simpler, particle in a box problem [230]. DMRG has demonstrated high accuracy in capturing the low-energy properties of one-dimensional quantum systems with short-range interactions [231]. In this work, we have made use of

the Time-Evolving Block Decimation (TEBD) algorithm, an extension of DMRG within the Matrix Product State (MPS) formalism, proposed by G.Vidal [232–234].

The DMRG algorithm follows an iterative scheme that systematically reduces the Hilbert space to a manageable subspace while preserving the most relevant quantum correlations. DMRG performs this truncation by retaining the eigenstates of the reduced density matrix of the system, in contrast to a truncation based on energy alone, as in traditional renormalisation group approaches [235, 236]. This entanglement-based truncation ensures an efficient and controlled approximation of the system's wavefunction, which renders DMRG a particularly well-suited formalism for strongly correlated one-dimensional quantum systems [235, 236].

3.1.1 Density Matrix Renormalisation Group

DMRG is implemented by dividing the system into two blocks, referred to as the "system" and "environment". At each iteration, the system block is enlarged by adding a new site, creating a superblock. The reduced density matrix of this is then constructed, and the eigenstates corresponding to the largest eigenvalues are retained, defining an optimal subspace for the subsequent iteration. This procedure is repeated until the desired system size is reached, in what is known as the infinite algorithm because the accuracy of the description of the central sites can only be guaranteed for the thermodynamic limit in which $L \to \infty$ [235]. This process and the finite system algorithm are represented in Figure 3.1. As seen on this figure, for the refinement of the ground state of finite size systems, the finite algorithm consists on repeated "sweeps" in which the system is divided in two blocks one of which is allowed to expand while the other shrinks from one end of the system to the other. The wavefunction is optimised by performing consecutive sweeps in opposite directions until convergence is reached.

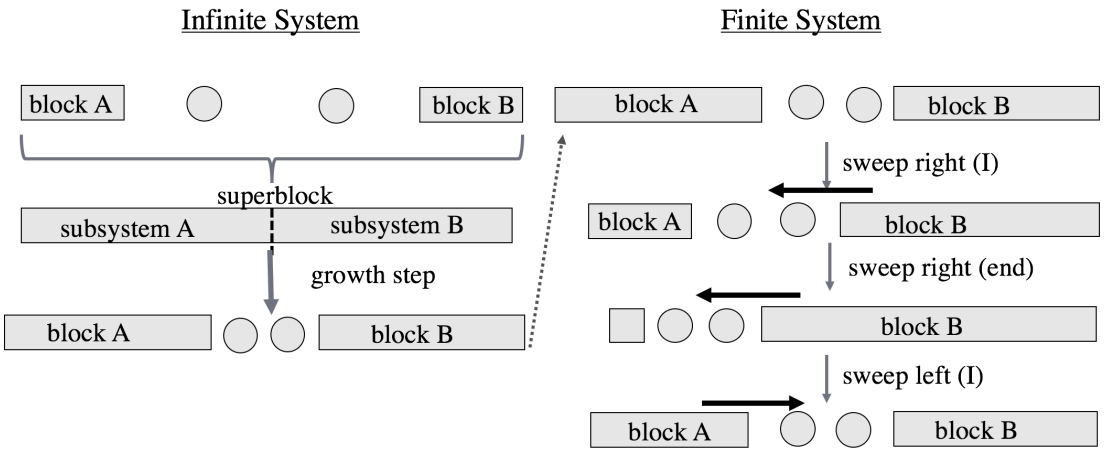


Figure 3.1: Graphical representation of the infinite and finite DMRG algorithms. Usually the finite algorithm is used after obtaining a final state of length L from the infinite algorithm. The methods for the expansion of a block are equal in both cases, however, while the finite system expands simultaneously both blocks, the infinite system allows for the expansion of one block by reducing the size of the other, in order to hold the length of the overall superblock constant.

3.1.2 The Matrix Product State formalism

The connection between the DMRG method and MPS was first found by Rommer and Östlund, who showed the equivalence between the thermodynamic limit of the DMRG methodology and position-independent MPS. It can be shown that any quantum mechanical state can be represented as an MPS, defined as follows [233]:

$$|\Psi\rangle = \sum_{\sigma_1 \ldots \sigma_L} \sum_{\alpha_1 \ldots \alpha_L} M^{\sigma_1}_{1,\alpha_1} M^{\sigma_2}_{\alpha_1,\alpha_2} \ldots M^{\sigma_L}_{\alpha_L,1} |\sigma_1 \sigma_2 \ldots \sigma_L\rangle \tag{3.1.1}$$

In the description above, $|\sigma_i\rangle$ represent the site basis, (the Local Hilbert space at any site i) while α_i are known as the internal indices.

A left-canonical matrix satisfies the normalisation restriction given by:

$$\sum_{\sigma_L} A^{\sigma_l \dagger} A^{\sigma_l} = \mathbb{1} \tag{3.1.2}$$

To illustrate this we can consider the example of an L-sites linear lattice of $\frac{1}{2}$ spins,

with d-dimensional local state spaces σ_i, the more general state can be written as:

$$|\Psi\rangle = \sum_{\sigma_1 ... \sigma_L} c_{\sigma_1 ... \sigma_L} |\sigma_1 ... \sigma_L\rangle \tag{3.1.3}$$

The prefactor can be rewritten by means of a diagonalisation (using SVD which is described in Section 3.1.2) as [235]:

$$c_{\sigma_1 ... \sigma_L} = \Psi_{\sigma_1,(\sigma_2 ... \sigma_L)} = \sum_{a_1}^{r_1} U_{\sigma_1,a_1} S_{a_1,a_1} (V^\dagger)_{a_1,(\sigma_2 .. \sigma_L)} \tag{3.1.4}$$

which can be directly transformed into the canonical MPS form:

$$c_{\sigma_1 .... \sigma_L} = \sum_{a_1}^{r_1} A^{\sigma_1}_{a_1} \Psi_{(a_1 \sigma_2),(\sigma_3 ... \sigma_L)} \tag{3.1.5}$$

This process is repeated until the a_{L-1}-th site is reached.

$$\begin{aligned} c_{\sigma_1 .... \sigma_L} &= \sum_{a_1}^{r_1} \sum_{a_2}^{r_2} A^{\sigma_1}_{a_1} U_{(a_1 \sigma_2),a_2} S_{a_2,a_2} (V^\dagger)_{a_2,(\sigma_3 .. \sigma_L)} \\ c_{\sigma_1 .... \sigma_L} &= \sum_{a_1}^{r_1} \sum_{a_2}^{r_2} A^{\sigma_1}_{a_1} A^{\sigma_2}_{a_1,a_2} \Psi_{(a_2 \sigma_3),(\sigma_4 ... \sigma_L)} \\ &... \\ c_{\sigma_1 .... \sigma_L} &= \sum_{a_1 ... a_{L-1}} A^{\sigma_1}_{a_1} A^{\sigma_2}_{a_1,a_2} ... A^{\sigma_{L-1}}_{a_{L-2},a_{L-1}} A^{\sigma_L}_{a_{L-1}} \Psi_L \end{aligned} \tag{3.1.6}$$

In this, Ψ_L is only required for non normalised states and contains the norm of the original state $|\Psi\rangle$. The final state is then presented in a left-canonical form as [235]:

$$|\Psi\rangle = \sum_{\boldsymbol{\sigma}} \sum_{a_1 ... a_{L-1}} A^{\sigma_1}_{a_1} A^{\sigma_2}_{a_1,a_2} ... A^{\sigma_{L-1}}_{a_{L-2},a_{L-1}} A^{\sigma_L}_{a_{L-1}} \Psi_L |\boldsymbol{\sigma}\rangle \tag{3.1.7}$$

where $|\boldsymbol{\sigma}\rangle \equiv |\sigma_1 ... \sigma_L\rangle$. Similarly, by using the $V^\dagger$ instead, the MPS can be written in a right-canonical state, which is defined by: $\sum_{\sigma_L} B^{\sigma_l} B^{\sigma_l \dagger} = \mathbb{1}$, the method will not be expanded here in order to avoid repetition. These are combined to form a mixed canonical with [235]:

$$c_{\sigma_1 .... \sigma_L} = A^{\sigma_1}_{a_1,a_2} ... A^{\sigma_l}_{a_{l-1},a_l} S_{a_l,a_l} B^{\sigma_{l+1}}_{a_{l+1},a_{l+2}} B^{\sigma_{L-1}}_{a_L,1} \tag{3.1.8}$$

Truncation of the MPS

The construction of the reduced density matrix for an MPS is as follows:

$$\rho_{ij}^{s's} = \sum_{k} A_{ik}^{s'*} A_{jk}^{s} \tag{3.1.9}$$

Following the DMRG algorithm, ρ is diagonalised in order to obtain the highest χ values. The diagonalisation is performed through the singular value decomposition (SVD), which allows for diagonalisation of matrices beyond the limitations of the eigenvalue-based methods. For any matrix M of dimensions $(h\ x\ k)$:

$$M = USV^{\dagger} \tag{3.1.10}$$

where, U is composed by the left singular vectors, $U^{\dagger}U = \mathbb{1}$, such that $SS^{\dagger}U = US^2$ containing orthogonal columns and has $(h\ x\ min(h,k))$ size. Similarly, $V^{\dagger}$ is comprised by right singular vectors in orthonormal rows, $VV^{\dagger} = \mathbb{1}$, with dimensions $(min(h,k)\ x\ k)$. S is a diagonal matrix formed by the singular values of dimensions $(min(h,k)\ \ x\ \ min(h,k))$.

Applied to quantum systems this corresponds to the Schmidt decomposition, which expresses the wavefunction of a system as a sum of orthonormal product states weighted by singular values. From the Schmidt decomposition, the reduced density matrices are found as [235]:

$$\hat{\rho}_L = \sum_{a=1}^{\chi} s_a^2 \left|a\right\rangle_L \left\langle a\right|_L \qquad \hat{\rho}_R = \sum_{a=1}^{\chi} s_a^2 \left|a\right\rangle_R \left\langle a\right|_R \tag{3.1.11}$$

The reduced density matrix can also be used to measure the level of entanglement of a system from the von Neumann entropy, defined as

$$S = -Tr(\rho_L \log \rho_L) \tag{3.1.12}$$

which in terms of the Schmidt coefficients can be rewritten as:

$$S = -\sum_{a=1}^{\chi} s_a^2 log(s_a^2) \tag{3.1.13}$$

The truncation process discards the less significant Schmidt coefficients, which in turn reduces the entanglement that the MPS can represent. Therefore, the truncation process needs to be carefully controlled in order to avoid a significant loss on the accuracy of the simulation by means of loss of the quantum correlations. The truncated singular values and the corresponding von Neumann entropy are measured and monitored after each step, allowing for modifications on the truncation threshold for any significant increase of the von Neumann entropy.

Matrix Product Operators

It can be shown that all Hamiltonian operators with a finite range of interactions have an exact matrix product representation, allowing the expansion of the MPS formalism to operators. Operators have a dependency on the outgoing as well as on the incoming state such as [235]:

$$\langle\sigma|\,\hat{O}\,|\sigma'\rangle = W^{\sigma_1,\sigma'_1} W^{\sigma_2,\sigma'_2} ... W^{\sigma_L,\sigma'_L} \tag{3.1.14}$$

Thus, the general form of a Matrix Product Operator (MPO) as:

$$\hat{O} = \sum_{\sigma,\sigma'} W^{\sigma_1,\sigma'_1} W^{\sigma_2,\sigma'_2} ... W^{\sigma_L,\sigma'_l}\,|\sigma\rangle\,\langle\sigma'| \tag{3.1.15}$$

Ground state calculations

The ground state is found by obtaining the $|\Psi\rangle$ that minimises the energy, given by:

$$E = \frac{\langle\Psi|\,\hat{H}_{RL}\,|\Psi\rangle}{\langle\Psi|\Psi|\Psi|\Psi\rangle} \tag{3.1.16}$$

To achieve this, a Lagrange multiplier is included to maintain the norm of the

$|\Psi\rangle$ state while minimising the energy. Thus, the final problem has the form of $\langle\Psi|\,\hat{H}_{RL}\,|\Psi\rangle - \lambda\langle\Psi|\Psi|\Psi|\Psi\rangle$. However, this equation is highly non-linear due to the product states expansion, as a result, a variational approach is taken in which only one M^{σ_i} matrix is considered at a time, leaving the rest of the terms in the expansion fixed.

The standard algorithm used to find the states variationally can be briefly described as follows [235]:

1. The initial state is taken from a prediction in the form of a canonical normalised $|\Psi\rangle$

2. The resulting MPS expressions for $\langle\Psi|\,\hat{H}_{RL}\,|\Psi\rangle$ are found for all sites (1 to L from a left-canonical initial state)

3. In the opposite direction (from L to 1), the standard eigenvalue problem is solved for a single site $M^{\sigma_i}_{\alpha_i,\alpha_{i+1}}$. This is followed by an SVD to transform $M^{\sigma_i}_{\alpha_i,\alpha_{i+1}}$ into its right-canonical form $B^{\sigma_i}_{\alpha_i,\alpha_{i+1}}$. This process is repeated on each site before continuing to the next lattice site.

4. Once the final site is reached, the equivalent process is conducted in the opposite direction. This requires solving the diagonalisation problem again and transforming the result into its left-canonical $A^{\sigma_i}_{\alpha_i,\alpha_{i+1}}$ expression per site.

5. Steps $2 \rightarrow 4$ are rerun until convergence is achieved, given by : $\langle\Psi|\,\hat{H}^2_{RL}\,|\Psi\rangle - \langle\Psi|\,\hat{H}_{RL}\,|\Psi\rangle^2$.

3.1.3 Time evolution: the TEBD algorithm

The time-dependent Schrödinger equation (TDSE) provides the fundamental framework for describing the unitary evolution of a quantum system over time. For a

given quantum state $|\Psi(t)\rangle$ and a Hamiltonian $\hat{H}$, the TDSE is written as [237]:

$$i\hbar\frac{d}{dt}|\Psi(t)\rangle = \hat{H}|\Psi(t)\rangle \tag{3.1.17}$$

The solution to the TDSE can be expressed in terms of the time-evolution operator $e^{-i\hat{H}t}$ as:

$$|\Psi(t)\rangle = e^{-i\hat{H}t/\hbar}|\Psi(0)\rangle \tag{3.1.18}$$

where $|\Psi(0)\rangle$ represents the initial state of the system, which can be written as an MPS. The critical step in the accurate description of the time evolution for an MPS lies in finding the accurate MPO representation for $e^{-i\hat{H}t}$ [235]. The dimensions of the resulting MPO often exceeds numerically manageable limits, necessitating the use of the Trotter-Suzuki approximation.

In order to calculate the final state $|\Psi(T)\rangle$, the interval T is split into N steps, of length τ. Following this, the time evolution operator can be expressed as:

$$e^{-i\hat{H}t} = \prod_{k=1}^{N} e^{-i\hat{H}\tau} \tag{3.1.19}$$

where the summation in k is over the *Trotter* steps, this description increases accuracy for N approaching ∞, as the size of the time steps diminishes, $\tau \to 0$ while $N\tau = T$.

For this calculation, usually only the nearest-neighbour interactions are considered, which is a limitation already taken into account in the Hamiltonian. The Hamiltonian can then be divided into the “bond" terms which contain the in-site energy and the nearest-neighbours interaction contribution: $\hat{H} = \sum_{n=1}^{L-1}\hat{H}_{n,n+1}$. However, since most Hamiltonians consist of non-commuting terms, a further decomposition becomes necessary. Typically, this is mediated by grouping the nearest-neighbour interactions into the even and odd terms such that:

$$\hat{H} = \hat{H}_{\text{even}} + \hat{H}_{\text{odd}} \tag{3.1.20}$$

where:

$$\hat{H}_{\text{even}} = \sum_{n \text{ even}} \hat{H}_{n,n+1}, \quad \hat{H}_{\text{odd}} = \sum_{n \text{ odd}} \hat{H}_{n,n+1} \tag{3.1.21}$$

This factorisation ensures that each term within $\hat{H}_{\text{even}}$ and $\hat{H}_{\text{odd}}$ commute with other terms of the same group. Firstly, the first-order Trotter decomposition results in an error of $O(\tau^2)$, arising from the non-commutativity of $\hat{H}_{\text{even}}$ and $\hat{H}_{\text{odd}}$:

$$e^{-i\hat{H}\tau} \approx e^{-i\hat{H}_{\text{even}}\tau} e^{-i\hat{H}_{\text{odd}}\tau} + O(\tau^2) \tag{3.1.22}$$

However, this approximation can be further improved. In the second-order symmetrised expansion, a correction is introduced to preserve time-reversal symmetry, reducing the error to $O(\tau^3)$:

$$e^{-i\hat{H}\tau} \approx e^{-i\frac{\tau}{2}\hat{H}_{\text{even}}} e^{-i\tau\hat{H}_{\text{odd}}} e^{-i\frac{\tau}{2}\hat{H}_{\text{even}}} + O(\tau^3) \tag{3.1.23}$$

With this definition, the evolution operator for a single Trotter step is given by [238]:

$$e^{-i\hat{H}\tau} \approx e^{\frac{-i}{2}\hat{H}_{1,2}\tau} e^{\frac{-i}{2}\hat{H}_{2,3}\tau} \ldots e^{\frac{-i}{2}\hat{H}_{2,3}\tau} e^{\frac{-i}{2}\hat{H}_{1,2}\tau} + O(\tau^3) \tag{3.1.24}$$

Generally, the given terms in this Hamiltonian do not commute, resulting in an error of the approximation of $O(\tau^3)$. This error is negligible for arbitrarily small time steps.

This reduces the required calculations by allowing for MPO calculations over 2 sites simultaneously. Briefly, the time-evolution of a state $|\Psi\rangle$ via the TEBD algorithm is represented in Figure 3.2, the steps are briefly summarised below [198]:

1. Starting from an MPS $|\Psi\rangle$ at $t = 0$, a new state is formed by with the evolution operator acting on the n-th link:

$$|\Psi'\rangle = \sum_{\sigma} A^{\sigma_1}_{1,\alpha_1} A^{\sigma_2}_{\alpha_1,\alpha_2} .. \theta^{\sigma'_n,\sigma'_{n+1}}_{\sigma_n,\sigma_{n+1}} A^{\sigma_{n+2}}_{\alpha_{n+2}} ... A^{\sigma_L}_{\alpha_L,1} |\sigma\rangle \tag{3.1.25}$$

where:

$$\theta^{\sigma'_n,\sigma'_{n+1}}_{\alpha_n,\alpha_{n+1}} = \sum_{\sigma_n,\sigma_{n+1},\alpha_n} U^{\sigma'_n,\sigma'_{n+1}}_{\sigma_n,\sigma_{n+1}} A^{\sigma_n}_{\alpha_{n-1},\alpha_n} A^{\sigma_{n+1}}_{\alpha_n,\alpha_{n+1}} \tag{3.1.26}$$

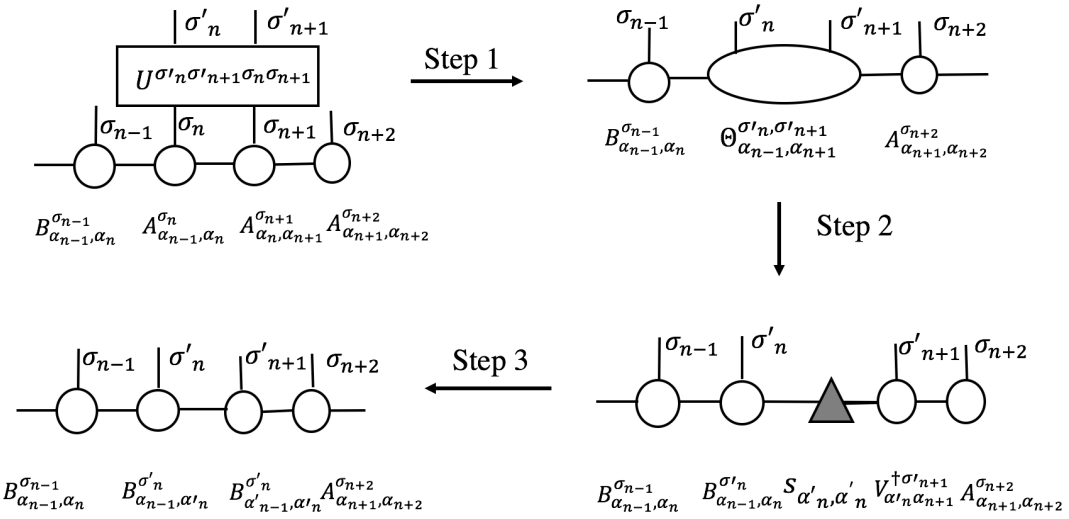


Figure 3.2: The TEBD algorithm. The first step shows the use of the time-evolution MPO for the $n, n+1$ bond. The MPO is represented as a rectangle, when applied to an MPS (represented as circles), a new MPS state is formed. As the operator $U^{\sigma'_n \cdots}$ acts on the 2 bonding sites, the resulting tensor structure θ retains information of both sites $(\sigma'_n, \sigma'_{n+1})$, this is marked in the figure by an oval shape. Step 2 and 3 lead to the SVD decomposition and truncation (triangle) and return to a standard MPS representation (circle), while the triangle represents the diagonal matrix containing the singular values. Connected lines represent indices that have been integrated over, while open lines serve as new degrees of freedom.

and

$$U^{\sigma'_n \sigma'_{n+1} \sigma_n \sigma_{n+1}} = \left\langle \sigma'_n \sigma'_{n+1} \right| e^{\frac{-i\tau}{2} \hat{H}_{n,n+1}} \left| \sigma_n \sigma_{n+1} \right\rangle \tag{3.1.27}$$

2. The state is modified by using a SVD decomposition on the $\theta^{\sigma'_n, \sigma'_{n+1}}_{\alpha_n, \alpha_{n+1}}$ term, in order to return $|\Psi\rangle$ into a canonical form.

$$\theta^{\sigma'_n, \sigma'_{n+1}}_{\alpha_n, \alpha_{n+1}} = B^{\sigma'_n}_{\alpha_{n-1}, \alpha'_n} S_{\alpha'_n, \alpha'_n} V^{\dagger \sigma'_{n+1}}_{\alpha'_n, \alpha_{n+1}} \tag{3.1.28}$$

As a result of this step the size of the original basis sees an increase of dimension from χ to $d\ x\ \chi$, given a site basis of size d. Therefore, the new basis is truncated following the same decompositions. The resulting error as a consequence of this truncation can be tracked by the value of the sum of the singular values for the discarded states.

3. Using the projections on the reduced basis, the remaining terms from the SVD decomposition and included in the n+1-th term:

$$B^{\sigma'_{n+1}}_{\alpha'_n,\alpha_{n+1}} = S_{\alpha'_n,\alpha'_n} V^{\dagger\sigma'_{n+1}}_{\alpha'_n,\alpha_{n+1}} \tag{3.1.29}$$

4. Finally the time evolution operator is used in the following $(n+1)$-th term, following steps $1 \rightarrow 3$.

The substeps defined above are carried through from the first site to the L-th site, corresponding to a single Trotter step, and in order to advance $|\Psi\rangle$ to a final state, this is repeated for the N number of time steps considered above.

3.2 Open quantum systems

In order to accurately describe the relaxation of QEES to lower energy states, it is essential to account for energy dissipation to the surrounding environment. Open quantum systems represent a more realistic framework, where interactions with the external environment result in decoherence and energy dissipation, offering a more faithful representation of real quantum systems. These interactions are essential in determining the dynamical behaviour of the time evolution of a quantum system.

The main mathematical framework used to describe the evolution of such systems is the Lindblad master equation, also referred as the Gorini-Kossakowski-Sudarshan-Lindblad (GKSL) equation [239–241]:

$$\frac{\partial\hat{\rho}}{\partial t} = -\frac{i}{\hbar}[\hat{H},\hat{\rho}] + \sum_{n,m=1}^{N^2-1} \gamma_{nm}(\hat{L}_n\rho\hat{L}^\dagger_m - 1/2\{\hat{L}^\dagger_m\hat{L}_n,\rho\}) \tag{3.2.1}$$

Here, the density matrix operator ρ is obtained as described in Section 3.1.2, the Hamiltonian corresponds to the standard unitary Hamiltonian. The Lindblad operators given as $\hat{L}_n$ and $\hat{L}^\dagger_m$ describe the effects of the system's interaction with

its environment. In the context of this work, these are $\hat{L}_n, \hat{L}_m^\dagger = \hat{b}_n, \hat{b}_m^\dagger$, which correspond to the vibrational modes of the nuclei, representing phonon emission which is the standard energy dissipation mechanism in conjugated polymers.

In practice, a direct solution of the Lindblad master equation for large systems is computationally inaccessible due to the exponential growth of the size of the density matrix, as a result, stochastic methods have been developed to address the challenges that arise in such systems [242]. This includes the quantum trajectory method as first devised by Carmichael and the Monte Carlo Wave Function method proposed by Dalibard, Castin, and Mølmer which simulate the evolution of the quantum state as a series of stochastic events known as quantum jumps [243–245].

3.2.1 The quantum jump trajectories method

The quantum jump trajectories method evolves an initial state $|\Psi(0)\rangle$ through an effective Hamiltonian while at each time step a quantum "jump" may take place with a given probability, accounting for the dissipative interactions with the environment. Each quantum trajectory represents a possible realisation of the system's evolution, where quantum jumps correspond to discrete events that are associated with the system's interaction with the environment [243]. In this way, the quantum jump trajectory consists of the averaging over many trajectories which correspond to the evolution of a given state rather than the evolution of the density matrix, thus the dimensionality of the problem scales linearly with dimensions of the Hilbert space rather than quadratically [244].

The deterministic part of the evolution follows an effective Hamiltonian given as:

$$\hat{H}_{\text{eff}} = \hat{H} - \frac{i\gamma\hbar}{2} \sum_m \hat{b}_m^\dagger \hat{b}_m \tag{3.2.2}$$

This non-Hermitian Hamiltonian describes the evolution of the system between quantum jumps, with the dissipation factor γ initially assumed to be uniform across all sites throughout the chain. However, γ, is in general not a constant but frequency-dependent, as it is determined by the spectral density of the environment, which modulates the coupling strength of different normal modes. A common choice is an Ohmic spectral density, where dissipation increases linearly with frequency, leading to irreversible system evolution (Markovian dynamics) in the weak-coupling limit [246]. The dissipation term, introduced by γ, introduces an imaginary part into the Hamiltonian, reflecting the gradual loss of probability amplitude between jumps due to the possibility of a quantum jump at any time step. This probabilistic loss causes the norm of the wavefunction to decrease between jumps, effectively representing the stochastic nature of decay processes [244]. Accordingly, given an initial pure state $|\psi(t)\rangle$ the evolution after dt is given by [247]:

$$|\psi(t+\delta t)_{trial}\rangle = e^{-\frac{i\hat{H}_{\text{eff}}\delta t}{\hbar}}|\psi(t)\rangle \tag{3.2.3}$$

For sufficiently small time steps in which the evolution operator can be approximated linearly:

$$e^{-\frac{i\hat{H}_{\text{eff}}\delta t}{\hbar}} \approx 1 - \frac{i\hat{H}_{\text{eff}}\delta t}{\hbar} + \dots \tag{3.2.4}$$

$$\left(e^{-\frac{i\hat{H}_{\text{eff}}\delta t}{\hbar}}\right)^{\dagger}\left(e^{-\frac{i\hat{H}_{\text{eff}}\delta t}{\hbar}}\right) \approx \left(1 + \frac{i\hat{H}^{\dagger}_{\text{eff}}\delta t}{\hbar}\right)\left(1 - \frac{i\hat{H}_{\text{eff}}\delta t}{\hbar}\right) \tag{3.2.5}$$

Hence, the square of the norm can be approximated as follows:

$$\begin{aligned}\langle\psi(t+\delta t)_{trial}|\psi(t+\delta t)_{trial}\rangle &= \langle\psi(t)|\left(1 + \frac{i\hat{H}^{\dagger}_{\text{eff}}\delta t}{\hbar}\right)\left(1 - \frac{i\hat{H}_{\text{eff}}\delta t}{\hbar}\right)|\psi(t)\rangle \\ &= 1 - \delta p\end{aligned} \tag{3.2.6}$$

In which we have defined δp, the probability of a quantum jump for each time step δt given as:

$$\delta p = \sum_m \delta p_m, \quad \delta p_m = \gamma \delta t \, \langle \psi(t) | \, \hat{b}_m^\dagger \hat{b}_m \, | \psi(t) \rangle \tag{3.2.7}$$

If a jump occurs, its location is determined by the probability of a jump occurring at site n is given by:

$$P_n = \frac{\langle \psi(t) | \hat{b}_n^\dagger \hat{b}_n | \psi(t) \rangle}{\sum_m \langle \psi(t) | \hat{b}_m^\dagger \hat{b}_m | \psi(t) \rangle}. \tag{3.2.8}$$

Once the site is selected, the wavefunction collapses into a new state through the jump operator $\hat{b}_m$:

$$|\psi(t + \delta t)\rangle = \frac{\hat{b}_m \, |\psi(t)\rangle}{\sqrt{\delta p_m / \gamma \delta t}} \tag{3.2.9}$$

If a jump does not occur, with probability $1 - \delta p$, the system is evolved as (considering the renormalisation required as the Hamiltonian described in Equation 3.2.2 is non-unitary):

$$|\psi(t + \delta t)\rangle = \frac{e^{-\frac{i \hat{H}_{\text{eff}} \delta t}{\hbar}} \, |\psi(t)\rangle}{\sqrt{1 - \delta p}} \tag{3.2.10}$$

This process is repeated over many time steps, allowing for multiple quantum jumps. Since the timing and location of each jump vary across trajectories, their outcomes can differ significantly. This variability is illustrated in Figure 3.3, which depicts exciton relaxation and localisation resulting from interactions with rotons. At any given time, the density matrix is reconstructed by averaging over a sufficiently large ensemble:

$$\rho(t) = \frac{1}{N_{\text{traj}}} \sum_{j=1}^{N_{\text{traj}}} |\psi_j(t)\rangle \, \langle \psi_j(t)| \tag{3.2.11}$$

Since this method relies on averaging over a finite number of trajectories, the final

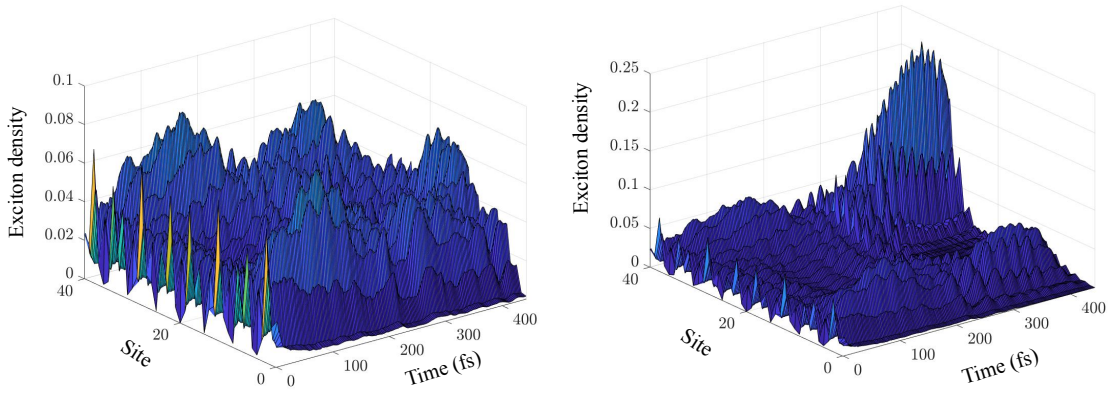


Figure 3.3: Two instances of different quantum trajectories from the same initial state. Both simulations include exciton-phonon coupling to two rotons with timescales of $T = 200$ fs.

result will contain statistical fluctuations. These fluctuations can be minimised by increasing the number of trajectories used in the averaging; as the fluctuations decrease the solution approaches the exact solution of the Lindblad equation. This convergence is markedly different for the calculation of global quantities, such as the total energy, and local quantities, including specific site occupation or the local density, as the latter requires a higher number of trajectories to produce reliable observations [247].

As such, when working within the quantum trajectory formalism the reliability of the results depends on the correct evaluation of the statistical error associated with the calculation. Given an observable A whose expectation value is $\langle A \rangle$, the estimated value for a set of N_{traj} independent trajectories is obtained through the mean as:

$$\langle A \rangle = \frac{1}{N_{traj}} \sum_{j}^{N_{traj}} A_j \tag{3.2.12}$$

where A_j is the computed observable for the j-th trajectory The corresponding error of this averaging is given as the standard variance of the mean which is proportional to $1/\sqrt{N_{\text{traj}}}$, for a given N_{traj} number of trajectories.

4
Intramolecular dynamics

This chapter presents the results of large-scale simulations of intramolecular exciton dynamics in poly(para-phenylene vinylene) (PPV) and its methoxy-substituted derivative (MEH-PPV) with the objective of providing a comprehensive analysis of the initial stages of exciton dynamics following photoexcitation in π-conjugated polymers. By examining these early processes, this study characterises the key mechanisms driving sub-ps fluorescence depolarisation, including exciton-site decoherence, energy dissipation, and exciton localisation.

Exciton dynamics is modelled following the theoretical framework described in Chapter 2 with explicit consideration of the exciton coupling to fast vibrational phonons and slower torsional modes. System-bath interactions are accounted for using the quantum trajectory formalism, enabling a detailed representation of exciton relaxation processes.

Disclaimer: Some of the content included in this chapter has also been included in previously published work: "Ultrafast fluorescence depolarisation in conjugated polymers" by I. Gonzalvez and W. Barford [224].

Structure

This chapter begins with a brief overview of the current understanding of pi-conjugated polymer systems as a result of experimental observations of the early stages of exciton dynamics in Section 4.1. This is followed in Section 4.2 with a discussion of the theoretical considerations necessary to accurately reproduce intramolecular dynamics in conjugated polymers, in particular the need for a quantum treatment of the exciton-phonon coupling which in this work is modelled through a Frenkel-Holstein Hamiltonian. Section 4.3 expands on the effects of the exciton-phonon including exciton-site decoherence and exciton localisation. Furthermore, in order to accurately describe the evolution of hot-excitons, energy exchange between the system and the environment needs to be considered, Section 4.4 explores the model used to represent energy dissipation mechanisms. The effects of coupling of the exciton to the slower torsional fluctuations of the individual moieties within the polymer chain are discussed in Section 4.5. Finally, a discussion of the results presented in this chapter and a comparison of theoretical predictions with experimental results is carried out in Section 4.6.

4.1 Experimental observations and contextualisation

Exciton dynamics, including exciton formation, localisation, energy transfer, and recombination, is strongly influenced by the molecular structure and the chain morphology, as well as, by environmental factors [139]. Consequently, understanding how these processes evolve over time provides a foundation for optimising device performance for the practical applications of π-conjugated polymers.

In order to understand the multiscale nature of exciton dynamics, multiple studies have employed ultrafast fluorescence depolarisation [139, 147, 248, 249], along with other time-resolved spectroscopic techniques such as three-pulse photon echo [140–142, 250] and coherent two-dimensional electronic spectroscopy [146] revealing relaxation times ranging from a few femtoseconds to the nanosecond scale, as summarised in Table 4.1.

From these results, it can be observed the initial delocalised nature of excitons, with the exciton density extending over the full length of the polymer chain [251]. However, the exciton is seen to localise to a single chromophore within a short timeframe, this localisation has been seen within 100 fs after photo-excitation for a series of different polymers such as P3HT, P3MT and P3DT [142, 249, 252]. In MEH-PPV, studies indicate that this localisation process occurs at a slightly faster rate, typically within $20 - 50$ fs, and it is suggested to be driven by the conformational disorder present within the polymer chain [139, 140, 250, 253].

Moreover, some research on partially conjugated samples of MEH-PPV suggests that this fast localisation and the associated depolarisation results primarily from dynamic self-trapping due to exciton coupling to lattice phonons [147].

Table 4.1: Some of the dynamical timescales observed in conjugated polymers.

Polymer	Sample	Timescales found	Research
MEH-PPV	Solution	$\tau_1 = 50$ fs $\tau_2 = 1 - 2$ ps	Ruseckas *et al.* 2005 [147]
MEH-PPV	Solution	$\tau_1 = 5 - 10$ fs $\tau_2 = 100 - 200$ fs	Collini *et al.* 2009 [254]
PDAs,	Film	$\tau = 120 - 150$ fs	Kobayashi T. 1992 [252]
PDTs	Film	$\tau = 70 - 100$ fs	Kobayashi T. 1992 [252]
PTOPT	Solution	$\tau = 40$ fs	Grage *et al.* 2003 [248]
PDOPT	Film	$\tau_1 = 0.5 - 4$ ps	Westenhof *et al.* 2006 [255]
PDOPT	Solution	$\tau_1 < 1$ ps $\tau_2 = 15 - 23$ ps	Westenhof *et al.* 2006 [255]
P3HT	Film	$\tau_1 = 300$ fs $\tau_2 = 2.5$ ps $\tau_3 = 40$ ps	Banereji *et al.* 2011 [251]
P3HT	Solution	$\tau_1 = 700$ fs $\tau_2 = 6.0$ ps $\tau_3 = 41$ ps $\tau_4 = 530$ ps	Banereji *et al.* 2011 [251]
P3HT	Solution	$\tau_1 = 60 - 200$ fs $\tau_2 = 1 - 2$ ps $\tau_3 = 14 - 20$ ps	Busby *et al.* 2011 [256]
P3HT	Solution	$\tau_1 < 100$ fs $\tau_2 = 1 - 10$ ps	Wells *et al.* 2007 [249]

After localisation, excitons undergo energy relaxation and spectral diffusion, migrating to lower energy states on a timescale of approximately 200 fs, through a

process which is expected to be also driven by exciton-phonon interactions [249, 252]. This coherent exciton diffusion is seen to be temperature-dependent and it is predicted to be due to fluctuations of the torsional angles of the individual moieties within a polymer chain [257].

As a result of these processes, spectroscopical probes of fluorescence depolarisation have shown to follow a biexponential decay, with a fast component, on the order of tens of femtoseconds, attributed to phonon-vibrational interactions, and a slower component on the picosecond timescale, suggested to arise as a result of the coupling to torsional degrees of freedom [142, 253, 257].

Finally, inter-chromophore exciton migration between different chains is expected to follow through resonance energy transfer, this process occurs within a few picoseconds and is sensitive to the interchain distance and the spectral overlap between interacting chromophores in different polymer chains [248–250, 258, 259]. This process will be the focus of the work in Chapter 5.

4.2 Modelling intrachain exciton dynamics in conjugated polymers

In order to accurately model exciton dynamics in π-conjugated polymers, a combination of effective theoretical models and computationally efficient numerical techniques is required due to the size and the interacting nature of these systems. Firstly, as each polymer fibre comprises hundreds of monomers, resulting in a system with thousands of interacting particles, and as the Hilbert Space grows exponentially with the number of degrees of freedom in the system our first approximation consists of a coarse grained model. This representation reduces the dimensionality of the problem by mapping each phenylene and vinylene moiety onto a single site of a one-dimensional chain. As discussed in Chapter 2, the evolution of the excitons

in this one-dimensional chain are represented with a Frenkel Hamiltonian. To this end, this coarse-grained Frenkel model has shown promising results with high accuracy predictions at describing the low energy states in PPP and PPV [225]. This Hamiltonian is given by:

$$\hat{H}_{\text{ex}} = \sum_{n=1}^{N} \epsilon_n \hat{N}_n - \sum_{n=1}^{N-1} J_n(\hat{a}_{n+1}^{\dagger}\hat{a}_n + \hat{a}_n^{\dagger}\hat{a}_{n+1}) \tag{4.2.1}$$

where ϵ_n represents the site energies, J_n denotes the electronic coupling between adjacent sites, and $\hat{N}_n$ is the exciton number operator, with $\hat{a}_n^{\dagger}$ and $\hat{a}_n$ being the exciton creation and annihilation operators, respectively. When disorder is included in the system, the resulting eigenstates of this model are classified into Local Exciton Ground States (LEGS) and Quasi-Extended Exciton States (QEES). LEGS are spatially localised, nodeless states that dominate the low-energy region of the density of states (DOS), while QEES extend over multiple monomers, exhibit nodal structures, and contribute to higher-energy excitations.

Furthermore, it has been established that within conjugated polymers, the evolution of the exciton is significantly influenced by its interactions with the nuclear degrees of freedom. Consequently, a precise representation of the relaxation processes requires that the electronic and nuclear degrees of freedom are treated with an equivalent level of quantum mechanical detail [140, 177, 199]. However, the inclusion of the nuclear degrees of freedom represents a further challenge for any theoretical analysis, because exponential growth of the Hamiltonian space with the size of the systems renders the diagonalisation of these Hamiltonians and their direct solution unfeasible. Consequently, numerous approaches have been explored, each with its own advantages and limitations, among these, one of the most widely used is the Ehrenfest formalism. However, its application to the relaxation of high-energy excitons, as discussed in this chapter, introduces

significant inaccuracies. The limitations of the Ehrenfest approximation in capturing the fastest steps of exciton relaxation are twofold: it treats the nuclei fully classically, thereby disregarding zero-point energy and tunnelling effects, and assumes that the total wavefunction is separable into independent electronic and nuclear parts, neglecting their entanglement. As a result of these limitations, this approach fails to correctly reproduce exciton dynamics and the wavepacket splitting at conical intersections [179, 225, 260, 261].

The fast relaxation from a QEES to a LEGS, as discussed in this chapter, involves interactions with multiple potential energy surfaces and traverses several conical intersections and avoided crossings. Due to the inherently nonadiabatic nature of this process, Ehrenfest dynamics fails to provide an accurate description, as it cannot correctly capture wavepacket splitting or quantum coherence effects. For this purpose, the fast C-C bond vibrations are treated fully quantum mechanically through a Frenkel-Holstein model, which describes the exciton coupling to a ladder of harmonic oscillators at each site. The Hamiltonian governing this interaction is given by:

$$\hat{H}_{\mathrm{FH}} = \hat{H}_{\mathrm{F}} + \sum_{n=1}^{N} g_n(\hat{b}_n^\dagger + \hat{b}_n)\hat{N}_n + \sum_{n=1}^{N} \hbar\omega_n \left(\hat{b}_n^\dagger \hat{b}_n + \frac{1}{2}\right) \tag{4.2.2}$$

where $\hat{H}_{\mathrm{F}}$ represents the Frenkel Hamiltonian, $\hat{b}_n^\dagger$ and $\hat{b}_n$ are the phonon creation and annihilation operators, g_n denotes the exciton-phonon coupling strength, $\hat{N}_n$ is the exciton number operator, with the associated vibrational frequency of the phonon at site n ω_n.

While vibrational phonons drive initial exciton relaxation torsional degrees of freedom have been found to be essential for exciton localisation and self-trapping [195]. Given that torsional phonons have a significantly lower frequency, they can

be treated using a combined classical-quantum mechanical approach, the TEBD-Ehrenfest algorithm. A complete description of this method can be found in Section 2.2.5. In this approach, the angular displacement variables incorporate small fluctuations around the main value, expressed as:

$$\Delta\tilde{\phi}n = \Delta\phi_n^{\mathrm{eh}} + \delta\tilde{\phi}n \tag{4.2.3}$$

The primary angular displacement evolves classically according to the Ehrenfest equations of motion:

$$\frac{d\Delta\tilde{\phi}_n^{\mathrm{eh}}}{dt} = \tilde{L}_n^{\mathrm{eh}} \tag{4.2.4}$$

$$\frac{d\tilde{L}_n^{\mathrm{eh}}}{dt} = \Gamma_n = -\Delta\tilde{\phi}_n^{\mathrm{eh}} + \lambda_n - \gamma\tilde{L}^{\mathrm{eh}} \tag{4.2.5}$$

where γ represents the damping coefficient and for $\theta_n = (\phi_{n+1} - \phi_n)$. Fluctuations around this mean value behave quantum mechanically via an effective Hamiltonian:

$$\begin{aligned}\hat{H}_{\mathrm{eff}} = &\sum_{n=1}^{N-1}\left[J_N^0 - \hbar\omega D(\theta_n^0)\left(\Delta\tilde{\phi}_{n+1}^{eh} - \Delta\tilde{\phi}_n^{eh}\right)\right]\hat{T}_{n,n+1} \\ &- \hbar\omega\sum_{n=1}^{N-1} D(\theta_n^0)\left(\hat{C}'_{n+1} - \hat{C}'_n\right)\left(\hat{T}_{n,n+1} - \langle\hat{T}_{n,n+1}\rangle\right) \\ &+ \hbar\omega\sum_{n=1}^{N}\left(\hat{c}_n'^{\dagger}\hat{c}'_n + \frac{1}{2}\right) \\ &+ \frac{\hbar\omega}{2}\sum_{n=1}^{N-1} D(\theta_n^0)\left(\Delta\tilde{\phi}_{n+1}^{eh} - \Delta\tilde{\phi}_n^{eh}\right)\langle\tilde{T}_{n,n+1}\rangle\end{aligned} \tag{4.2.6}$$

However, the explicit treatment of nuclear degrees of freedom presents a significant challenge due to the increased dimensionality of the Hilbert space. To efficiently address this issue, the Time-Evolving Block Decimation (TEBD) algorithm is employed. As introduced in Section 3.1, TEBD reduces the effective dimensionality of the problem by truncating the exciton density matrix while preserving essential quantum correlations. In this work, TEBD methods are implemented using the Tensor Network Theory Library [262].

4.2.1 Truncation errors arising from the TEBD algorithm

Although TEBD has been successful in obtaining numerically accurate results in low dimensional entangled systems [231], the approximations taken during the TEBD algorithm could result in deviations from the exact time-evolution of the exciton, arising from two types of truncation errors. Firstly, during the truncation process of the reduced density matrix representation of a state, only a reduced number of Schmidt values are retained. This truncation is controlled directly by the size of the internal index dimension, and the ratio between the largest and the smallest singular value retained. The accumulated error from the truncation can be obtained

Parameter	**Symbol**	**Value**
Internal index dimension	χ	150
Singular value ratio	S_{ratio}	2×10^{-5}
Maximum occupation number	n_{vmax}	2
Dimensionless time step	$\delta\tilde{t} = \omega\delta t$	2×10^{-4}

Table 4.2: Effective parameter set for TEBD algorithm simulations.

from the retained Schmidt values through calculations of the Von Neumann Entropy $S = -\sum_{a=1}^{\chi} s_a^2 log(s_a^2)$ (s_a describes the individual Schmidt values, as detailed in Section 3.1.2). Additionally, the number of allowed phonon basis states at each site, given by n_{vmax}, also results in an increase of the dimensionality of the Hilbert space proportionally to $2(n_{vmax}+1)^L$ and is limited in order to reduce the computational cost of the calculations. Lastly, the time evolution carries an error of δt^3 as a result of the Trotter-Suzuki decomposition, as shown in Section 3.1.

In order to minimise the accumulated error to maintain a high level of accuracy in this representation, the choice for the values used for the TEBD parameters follows the results of an analysis on the accuracy of TEBD steady state predictions

against results from direct diagonalisation in smaller systems [225]. The parameters used are presented in Table 4.2.

4.3 Exciton decoherence

Immediately after photoexcitation, the initial state of the system can be well described as a direct product of the exciton and nuclear wavefunctions. The electronic wavefunction is a non-stationary superposition of multiple eigenstates due to the finite duration of the excitation laser pulse. Since photoexcitation primarily occurs at higher energies it is expected that the initial state has a high degree of delocalisation corresponding to multiple QEES. In contrast, the nuclear wavefunction remains in its vibrational ground state at the moment of excitation, as the electronic transition occurs considerably faster than that required for nuclear reorganisation.

Subsequent relaxation processes take place as the nuclear coordinates adjust to accommodate the new electronic distribution, leading to the formation of an exciton-polaron on ultrafast timescales [263, 264]. The formation of the exciton-polaron induces exciton-site decoherence which is characterised by the loss of the phase coherence between electronic states, as the system transitions from an initially delocalised, non-stationary quantum state to a more localised state where the exciton behaves in a slightly more classical, particle-like manner. This transition is observed as a loss of off-diagonal long-range order in the exciton's reduced density matrix and can be quantified by measuring the degree of coherence between exciton states, expressed through the coherence correlation function, $C_n^{\mathrm{coh}}(t)$ [196, 197]:

$$C_n^{coh}(t) = \sum_m |\rho_{m,m+n}| \tag{4.3.1}$$

where $\rho_{m,m'}$ is the exciton reduced density matrix obtained by tracing over the vibrational degrees of freedom, which is obtained following Equation 3.1.9. This

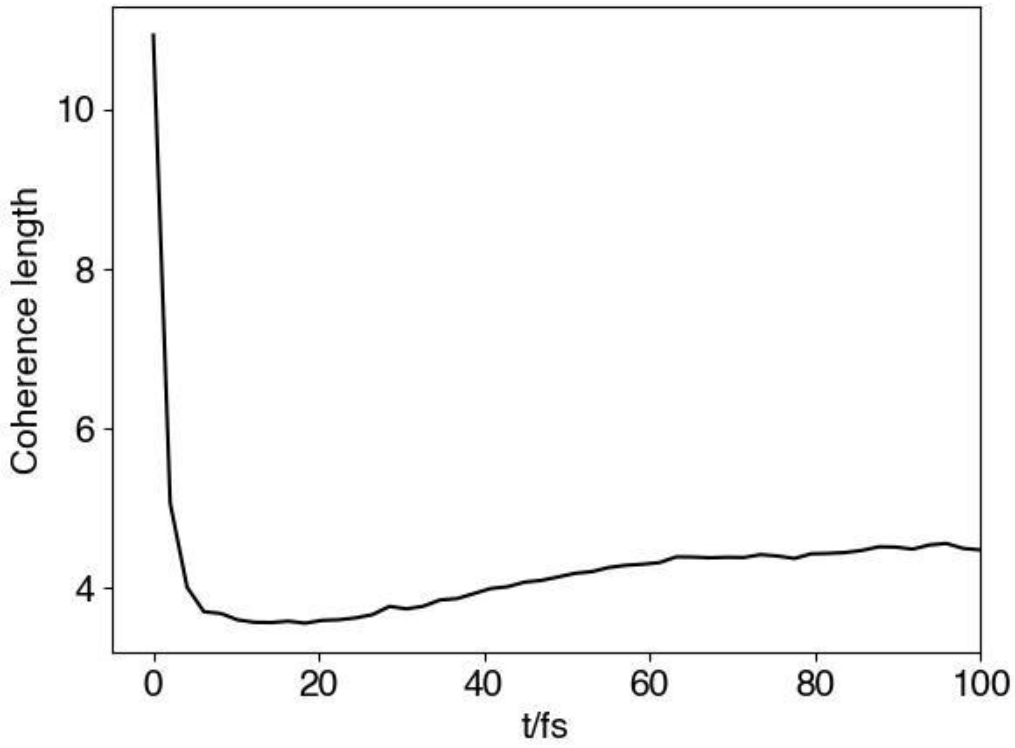


Figure 4.1: The exciton coherence length L_{coh} (in number of moieties) as a function of time in PPV chains of 40 moieties. These results are calculated from an ensemble of delocalised high-energy sates (i.e QEES) at $t = 0$.

function measures the spatial coherence between different exciton basis states separated by n sites. As the system evolves, the spatial coherence of the exciton decay driven by exciton-phonon interactions, this is followed by exciton localisation. In order to measure these changes, the coherence length is used, which describes the spatial extent of the exciton coherence and is defined as:

$$L_{\text{coh}} = \sum_{n} C_n^{coh} \tag{4.3.2}$$

Figure 4.1 shows a fast decay of the exciton localisation function, L_{coh} which approaches 4 moieties within $\sim$ 10 fs. This fast decay demonstrates the effects short range exciton-phonon correlations in the exciton localisation length. A slight increase in the coherence length after the initial rapid decay is also observed in

Figure 4.1. This recovery in L_{coh} may indicate small reintroduction of coherence through coupling with the torsional degrees of freedom or result from fluctuations due to static disorder in the system (which favours small fluctuations and the extension of coherence in certain regions).

4.4 Energy dissipation and further localisation

Energy dissipation following initial decoherence occurs through exciton-phonon interactions. This process allows excitons in high-energy states, such as the QEES, to relax into lower energy states, LEGS, confining the exciton density within a single chromophore. As a result, the redistribution of exciton density shapes the exciton interactions and impacts the optical properties of conjugated polymers.

While the relaxation mechanism for lower energy excitons is well established, proceeding via adiabatic relaxation along a single potential energy surface and resulting in vibrationally relaxed states [18, 265–267], the dynamics are significantly more intricate for higher energy states. For an initial QEES, the relaxation pathway deviates from the adiabatic regime due to the intricate coupling between exciton states and the vibrational and torsional modes of the C-C bonds [136]. Thus, this non-adiabatic process requires a quantum mechanical treatment to accurately describe the coherent exciton–phonon interactions responsible for mediating energy dissipation and exciton relaxation into a LEGS.

The quantum trajectory method, as detailed in Section 3.2 is used throughout this work to model the quantum mechanical treatment of system-bath interactions. Figures 4.2 and 4.3 illustrate two representative trajectories for MEH-PPV chains consisting of 100 moieties. In both cases, the trajectories result in exciton density localisation, corresponding to the relaxation of the QEES into a LEGS. The “jump” observed at approximately 38 fs on Figure 4.2 reflects a transition to a lower-energy,

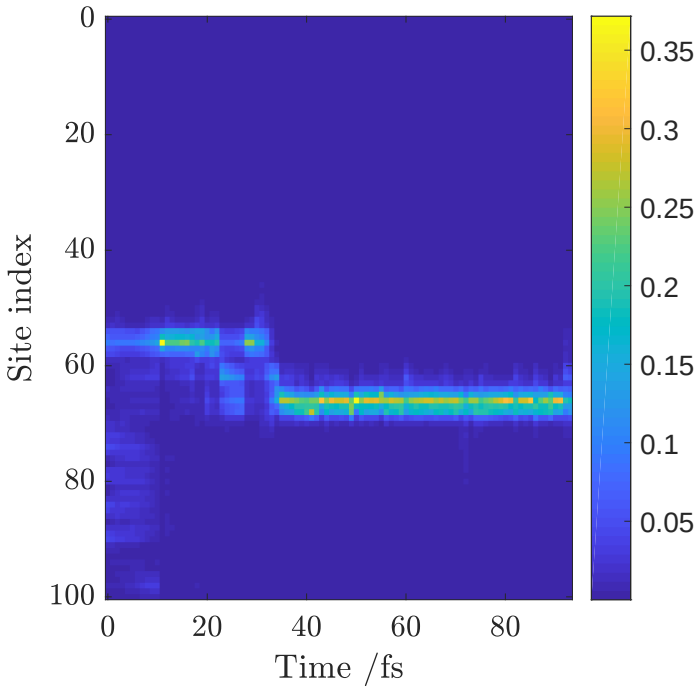


Figure 4.2: Time evolution of the exciton density distribution during the relaxation of a QEES to a LEGS in a 100-moiety MEH-PPV chain. The plot illustrates the spatial localisation of the exciton density across the moieties as a function of time, highlighting the transition to a more localised state.

more localised state. Figure 4.3 on the other hand, presents multiple instances of such jumps and highlights segments where the exciton density becomes more delocalised after localisation events, as observed between 40 and 60 fs. While quantum jumps are predominantly induced by vibrational phonons which facilitate the transition between different exciton states, torsional motion influences the overall localisation dynamics by reshaping the polymer backbone. The torsional angular momentum L_n induced by the presence of the exciton modifies the torsional angles ϕ_n which in turn affect the transfer integrals $J_n(\theta)$ between adjacent moieties. As the polymer relaxes, this coupling changes, momentarily allowing excitons to spread over larger segments before stabilising into a fully localised exciton-polaron state. This delocalisation can be observed in the lower panel of Figure 4.3(b) through the exciton density differences at 40 fs (corresponding to T) and 80 fs (corresponding

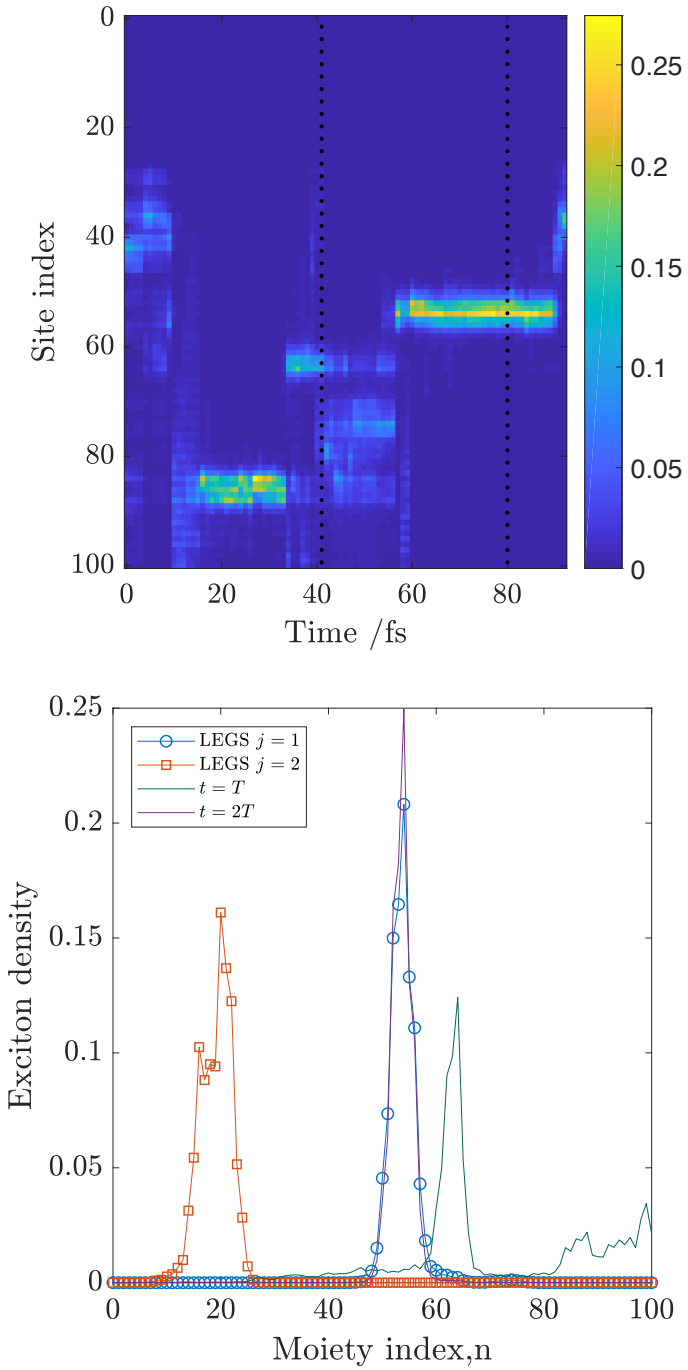


Figure 4.3: Relaxation of a QEES to a LEGS state in a 100-moiety MEH-PPV chain. (a) Time-resolved exciton density distribution along the polymer chain, illustrating transitions and delocalisation events. The dashed lines mark the time points at $t = T = 40$ fs and $t = 2T = 80$ fs. (b) Exciton density distribution at two distinct time points, $t = T$ and $t = 2T$, overlaid with the density distribution corresponding to two lower-energy LEGS states.

to 2T). The variation between different trajectories underscores the probabilistic nature of quantum jump processes. Notably, while vibrational relaxation dominates the ultrafast localisation dynamics, the longer evolution observed at T and $2T$ suggests an additional contribution from torsional relaxation. As the polymer backbone adjusts to the exciton presence over a prolonged period further increasing the stability of localised exciton states.

The trajectories in Figures 4.2 and 4.3 include a quantum mechanical treatment of the vibrational phonons and a hybrid treatment of the rotons, including a quantum correction of the torsional displacements as derived in Equations 4.2.3−4.2.6. It is observed that full localisation into the LEGS state requires consideration of the coupling to the slower torsional phonons, which are necessary for facilitating the exciton relaxation process.

The treatment of the torsional motion of the nuclei can be approached quantum mechanically following similar derivations as those used in the Frenkel-Holstein hamiltonian for the inclusion of the vibrational phonons, following Equation 2.2.37. However, as torsional phonon modes exhibit significantly slower dynamics, with periods exceeding 200 fs, depending on the steric constraints imposed by the chemical environment of the conjugated polymer backbone, these modes can be accurately represented using a classical approach without compromising the accuracy of the system's description [200]. To this end, simulations were performed incorporating a classical treatment of the torsional degrees of freedom. This process follows the derivation outlined in Chapter 2, Section 2.2.5.

The resulting coupling of the exciton to multiple torsional modes can be understood by extending the analysis to the equivalent of a chain of torsional oscillators. The interaction between excitons and torsional modes induces the reorganisation of the polymer backbone, resulting in a spatially varying planarisation

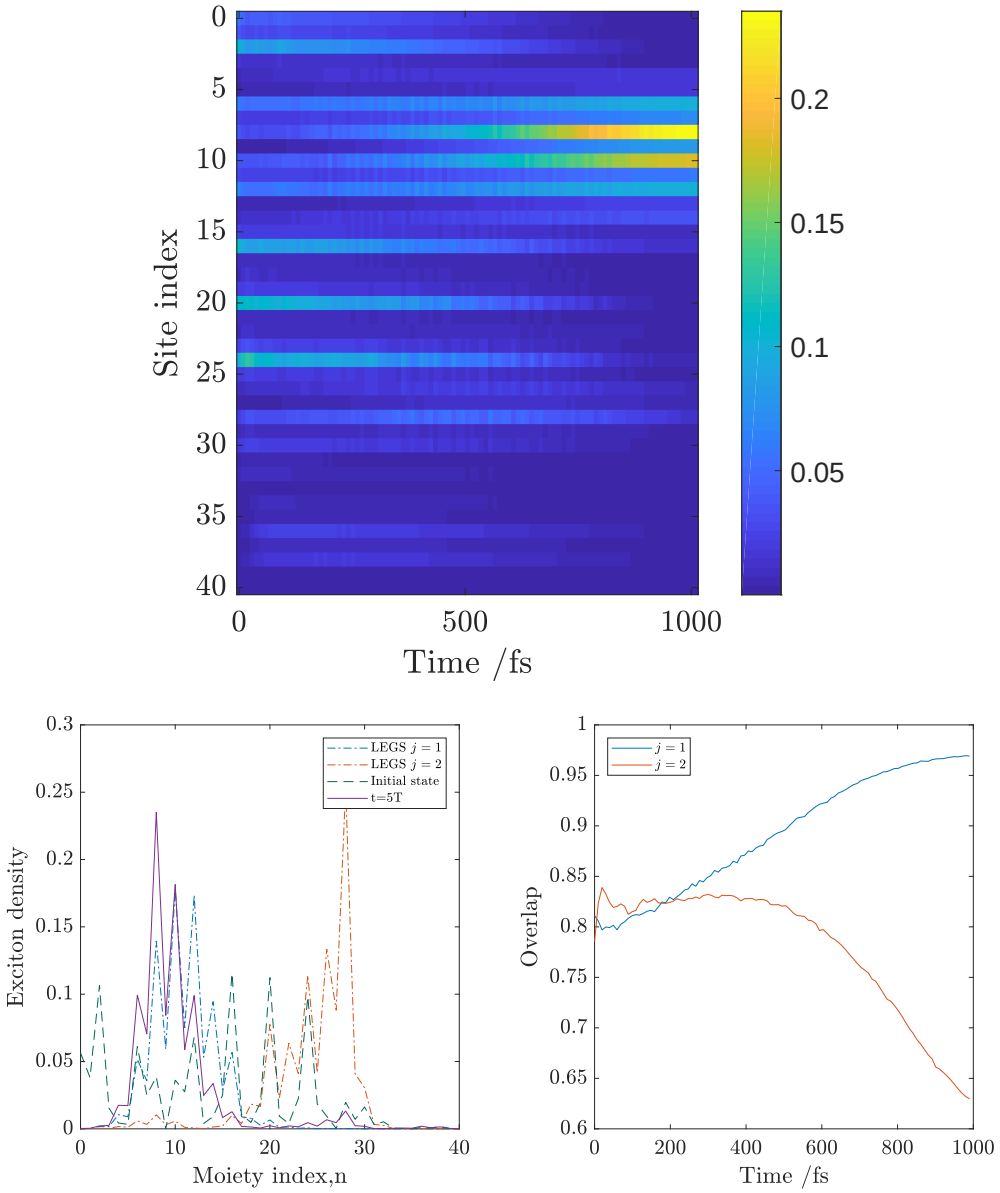


Figure 4.4: Exciton density localisation driven by coupling to torsional phonon modes (a) displays the exciton density distribution over the chain over time, (b) represents a slice of this distribution providing a comparison of the exciton density between the initial and final states and with the lowest LEGS of the system, marked by $j = 1$ and $j = 2$ (c) the overlap between the final exciton density at 1000 fs and the known LEGS of the system.

of the conjugated segments [200]. As a consequence, torsional relaxation further localises the exciton, forming what is often referred to as an exciton-polaron, described in Section 2.2.4. In contrast to the rapid localisation induced by the coupling to vibrational nuclear motion, which occurs over a few moieties within tens

of femtoseconds, torsional relaxation enforces a more gradual exciton localisation over extended periods (up to a few picoseconds) and across larger segments of the polymer. Such planarisation and the corresponding exciton localisation have been experimentally observed in MEH-PPV films [268].

This slow but sustained effect of the coupling to the torsional degrees of freedom can be observed in Figure 4.4. This localisation persists until the picosecond timescale, at which point the contribution of intermolecular chain interactions becomes significantly more pronounced. It is worth noting that the localisation effects of the coupling to the torsional degrees of freedom is not always accompanied by a full relaxation into a LEGS state which needs to be taken into account by the system-bath interactions mediated through coupling to the vibrational motion of the nuclei.

The spatial extent of the exciton density, as described in Equation 2.2.12, is an essential aspect of characterising the localisation of excitons within conjugated polymer systems. This quantity, averaged across numerous quantum trajectories and several disorder realisations, reflects the degree of exciton confinement as influenced by the coupling of the exciton to the vibrational and torsional phonons. The localisation length can be expressed in terms of the average length of a moiety from considerations of the physical parameters of the systems and a multiplication over the average length of a moiety [16, 178, 214]:

$$L = \ell \left(\frac{12\pi^2}{\pi^2 - 6} \right)^{1/2} \approx 5.6\ell \tag{4.4.1}$$

thus,

$$L_{loc} = 5.6(\left\langle L^2 \right\rangle - \langle L \rangle^2)^{1/2} \tag{4.4.2}$$

where L_{loc} is obtained in terms of moieties and $\left\langle L^k \right\rangle = \sum_m m^k \rho_{mm}$, where ρ_{mm} is the exciton density on the m-th moiety. This formalism provides a means of tracking the spatial confinement of the exciton in response to exciton-phonon interactions.

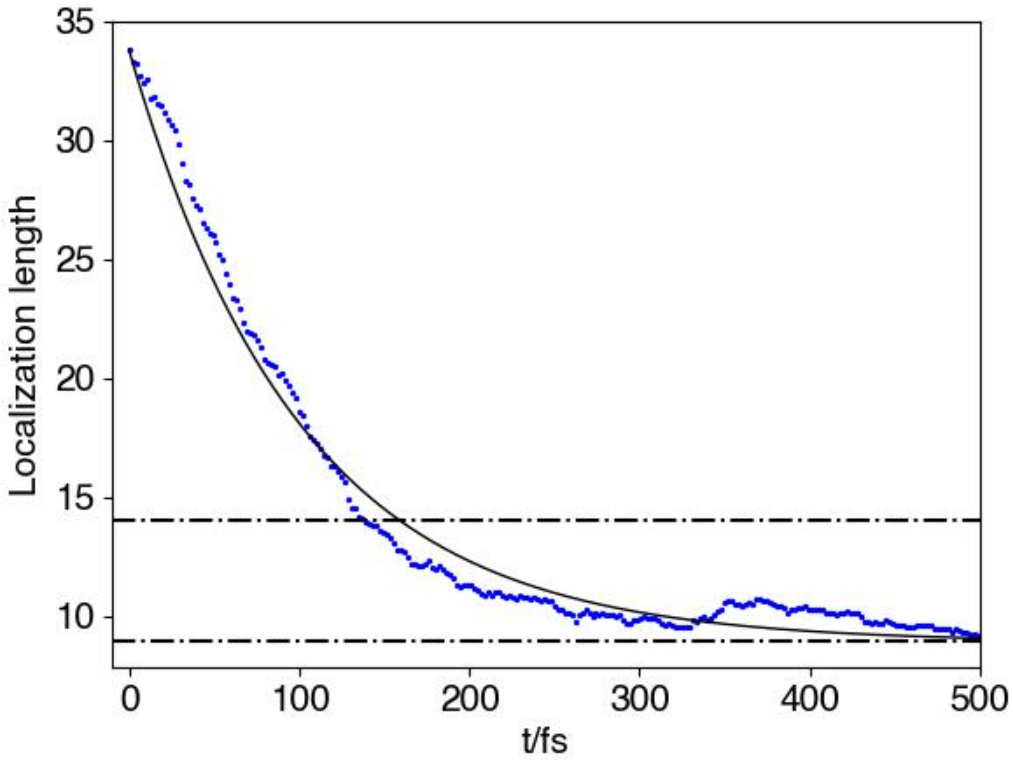


Figure 4.5: The exciton localisation length L_{loc} (in number of moieties) as a function of time in PPV chains of 40 moieties. These results are calculated from an ensemble of delocalised high energy states (i.e QEES) at $t = 0$. The horizontal dashed line at 14 moieties corresponds to the average chromophore size in the absence of exciton-torsional coupling. The asymptotic value of 9 moieties is a consequence of additional localisation caused by torsional relaxation. The curve is a one-exponential fit with a time constant of 100fs.

Figure 4.5 shows the evolution of the localisation length in time, in which the influence of the external dissipation time $\gamma^{-1} = 100$ fs can be easily observed [266]. This dissipation time represents the timescale over which energy is transferred from the exciton to its surrounding environment, leading to rapid localisation.

In Figure 4.5, initially, the exciton is highly delocalised, however, as time progresses, it becomes increasingly confined due to exciton-phonon interactions.

The localisation length exhibits an exponential decay with a timescale of 100 fs, reflecting the period over which torsional relaxation drives the exciton-polaron formation process. The average localisation lengths for simulations without torsional coupling (showing a broader distribution around 14 moieties) are compared to the decreasing trend observed in simulations that account for dissipation via torsional phonon modes. In the latter case, localisation lengths fall below 10 moieties, demonstrating the effect of torsional interactions on exciton confinement.

4.5 Ultrafast fluorescence depolarisation

The exciton-phonon coupling, discussed in Section 4.3, induces a significant reduction in the off-diagonal long-range order which can be monitored by the exciton coherence function. This loss of coherence is closely associated with the localisation of the exciton, resulting in a reduction in magnitude and a rotation in orientation of the transition dipole moment [269]. This reorientation of the transition dipole can be directly observed through fluorescence anisotropy measurements, as described in Sections 2.4.2 and 2.4.3. Theoretical predictions for the polarised intensities in Equation 2.4.22 can be derived from the components of the transition dipole moment, thus linking the fluorescence depolarisation directly to molecular-level changes in dipole orientation. For a general quantum state $|\Psi\rangle$ the intensity of fluorescence polarised along a specific axis, such as the e_j-th axis can be expressed as [216, 223]:

$$I_{e_j} \propto \sum_{\nu} \left| \langle \Psi | \, \hat{\mu}_{e_j} \, | GS, \nu \rangle \right|^2 \tag{4.5.1}$$

where $|GS, \nu\rangle$ corresponds to the ground electronic state, with the nuclear degrees of freedom in state ν. This equation highlights the connection between the observed fluorescence intensity and the molecular transition dipole moments of the chromophores active in the transition. The use of experimental observations of

anisotropy provides information about these transitions. Equation 4.5.1 can be directly expressed in terms of the exciton reduced density matrix ρ as follows:

$$I_{e_j} \propto \sum_{m,n} s_m^{e_j} s_n^{e_j} \rho_{mn} \tag{4.5.2}$$

where $s_m^{e_j}$ is the e_j component of the unit vector for the m-th moiety. This expression has a close link to Equation 4.3.1, and as a result, a decay in the fluorescence anisotropy is expected to follow the rapid decoherence of the exciton.

Figure 4.6 presents the simulated fluorescence anisotropy $\langle r(t) \rangle$ calculated for an ensemble of QEES within disordered polymer chains. The anisotropy decay reflects the depolarisation dynamics due to rapid exciton migration and the loss of coherence within the first few femtoseconds. Such ultrafast depolarisation is indicative of strong exciton-phonon coupling, where both vibrational and torsional phonon modes contribute to the localisation of the exciton and the corresponding rotation of the transition dipole moment.

The time evolution of $\langle r(t) \rangle$ closely follows the behaviour of $L_{coh}(t)$ presented in Figure 4.1 as shown in Equation 4.5.2. Within the first 10 fs, a substantial decay in fluorescence anisotropy is observed in Figure 4.6, this decay parallels the rapid decline of L_{coh} over the same period. These decay rates align with the ultrafast loss of fluorescence anisotropy reported in experimental work by Wells *et al.* [249].

The slower exciton localisation observed in Figure 4.5 occurs in two stages: first, through stochastic migration, and second, via coupling to low-frequency torsional modes, which contribute to further depolarisation in the sub-ps scale. However, as shown by the inset in Figure 4.6 the majority of fluorescence depolarisation within the sub-picosecond regime occurs within the first few femtoseconds. This observation is corroborated by the best-fit function applied to the data, described

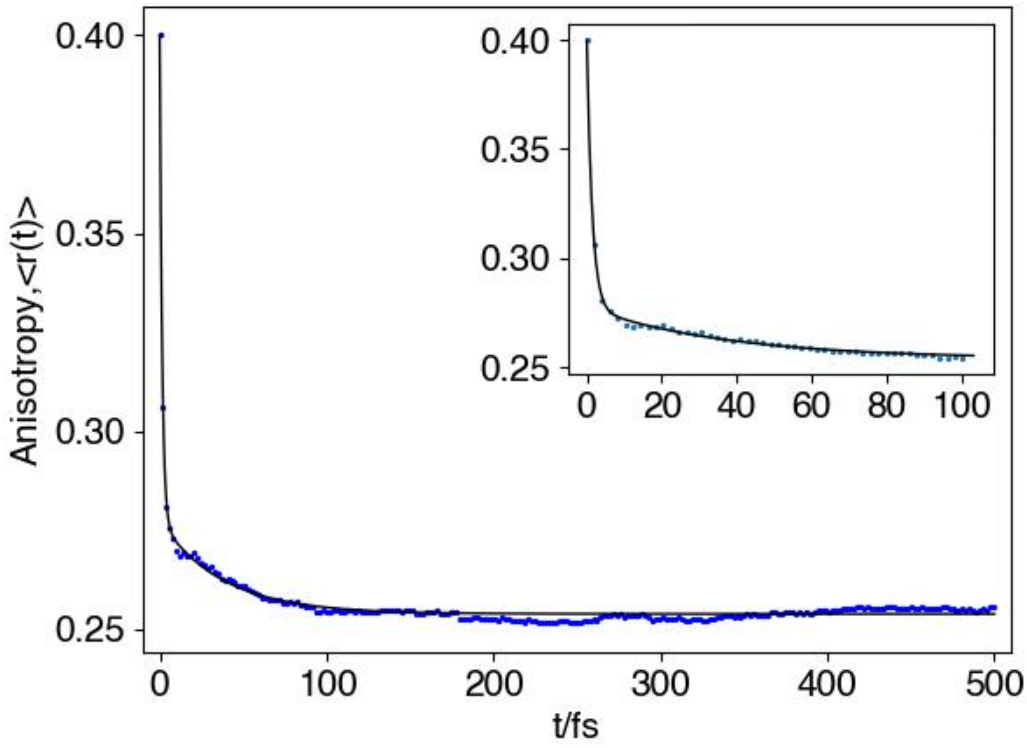


Figure 4.6: The fluorescence anisotropy $\langle r(t) \rangle$ calculated from an ensemble of delocalised high-energy states (QEES) at $t = 0$. The black curve is a two exponential fit given by Equation 4.5.3 with $\tau_1 = 2$ fs $\tau_2 = 37$ fs, $r_1 = 0.122$, $r_2 = 0.024$ and $r_\infty = 0.254$.

by the following biexponential form:

$$\langle r(t) \rangle = r_1 \exp\{-(t/\tau_1\} + r_2 \exp\{-(t/\tau_2\} + r_\infty \tag{4.5.3}$$

where $\tau_1 = 2$ fs and $\tau_2 = 37$ fs, and amplitudes of $r_1 = 0.122$, $r_2 = 0.024$ and $r_\infty = 0.254$ correspond to the various components of the depolarisation. A slower and less pronounced depolarisation phase, with a characteristic time constant of approximately 40 fs, follows the initial rapid decay.

4.6 Discussion and concluding remarks on ultrafast exciton dynamics

In this chapter, ultrafast exciton dynamics in conjugated polymer systems is investigated using large-scale theoretical simulations of intrachain dynamics and predictions of the fluorescence anisotropy decay. The results presented illustrate a cascade of events occurring on the sub-picosecond timescale, starting from the initial photoexcitation of the polymer and leading to the localisation of the exciton within a single chromophore.

These findings demonstrate that exciton dynamics within conjugated polymers are heavily influenced by the coupling between the exciton states and the vibrational modes of the polymer backbone. Firstly, high-frequency $C-C$ bond stretches significantly influence the initial stages of exciton relaxation, leading to a loss of coherence and the ultrafast depolarisation, which is observed within the first 10 fs after photoexcitation. These theoretical predictions are in agreement with experimental observations of the ultrafast fluorescence polar anisotropy decay in π-conjugated polymers [249, 254]. Beyond the initial rapid depolarisation, the subsequent evolution of the exciton is driven by energy dissipation to the environment mediated by vibrational phonons. This interaction initiates a nonadiabatic relaxation process that dictates the QEES to LEGS transition. The timescale of this energy transfer is determined by the strength of the coupling to the nuclear degrees of freedom.

As the exciton localises onto a LEGS, the transition dipole moment also becomes more localised which directly influences the resulting polarisation of the molecule. This localisation process affects the other optical properties as well, such

as spectral broadening, and is dependent on the exciton density localisation within chromophores[174], which is also modulated by coupling to slower torsional phonons.

In PPV, the relatively free rotation of the independent moieties facilitates the formation of exciton-polarons through coupling with low-frequency torsional modes. The formation of an exciton-polaron, is accompanied by a planarisation of the polymer backbone, which further confines the exciton density. The results from the simulations presented in this chapter show a slower depolarisation within 40 fs which is associated with the exciton-polaron formation. This timescale is in agreement with the experimental observations of Ruseckas *et al.* [147].

The analysis of the depolarisation mechanics discussed in here demonstrates the existence of multiple timescales associated with different stages of exciton relaxation, even within the intramolecular interactions regime. The fastest component, with a time constant of 2 fs in simulations and shown experimentally to occur before the first 10 fs after photoexcitation, corresponds to exciton-phonon entanglement and the resulting exciton-site decoherence. This is followed by a slower depolarisation with a time constant of 37 fs, attributed to exciton localisation via coupling to torsional degrees of freedom. The depolarisation process extends beyond the sub-picosecond timescale, driven by interchromophore exciton diffusion which depends on the aggregation degree and material structure. These interchain dynamics are further discussed in Chapter 5.

The results presented in this chapter bridge the current theoretical understanding of π-conjugated molecules with experimental observations of their optical properties. As discussed in Chapter 1, a theoretical framework that connects the material structure with their optical properties decisively has potential applications in optimizing the performance of optoelectronic devices. This has significant importance

in organic photovoltaics and light-emitting diodes, which rely on efficient exciton migration and charge dissociation.

5
Intermolecular dynamics

The initial stages following photoexcitation in conjugated polymer materials have been examined in Chapter 4. Following these intramolecular processes, which occur over a few hundred femtoseconds, the resulting highly localised exciton migrates between chromophores both along the polymer backbone and between chromophores on distinct polymer chains.

This chapter focusses on intermolecular exciton diffusion in conjugated polymer films and describes how this process is influenced by the structural properties and the degree of order of the material.

Structure

Section 5.1 begins with a brief introduction of intermolecular interactions in π-conjugated polymers and the physical parameters and considerations necessary for the theoretical calculations presented in this chapter. This discussion continues in Section 5.1.2, which examines simulations involving multiple chains, focussing on how variations in structural order within π-conjugated polymer films influence intermolecular exciton dynamics.

In Section 5.2 fluorescence anisotropy measurements are introduced as a viable probe to assess structural disorder in polymer films. The analysis is extended in 5.3, which examines how the heterogeneity within these films influences the energy transfer pathways.

This chapter concludes with a comparison of the theoretical predictions with experimental observations and an examination of the possible implications for the practical applications of π-conjugated polymers in Section 5.3.1 and 5.4.

5.1 Exciton evolution through intermolecular interactions

Up to this point, this work has examined ultrafast intrachain exciton dynamics, which required a computationally intensive quantum mechanical treatment to fully account for the exciton-phonon interactions. The results presented in Chapter 4 addressed the evolution of excitons in single polymer chains over a duration of 500 femtoseconds. Notably, in most instances, equilibrium values were found within the first 100 to 200 femtoseconds, as excitons rapidly relaxed into a single LEGS, which as discussed in Section 2.2.2, defines the chromophore sites, relevant for further energy transfer. Building on these results, the focus now shifts to interchain interactions within conjugated polymers, which occur on longer timescales in the range of a few picoseconds. Furthermore, the nature of interchain transport requires the study of considerably larger systems to evaluate the multiple interactions between chromophores at different chains. Accordingly, the simulations included in this chapter comprise ensembles of $100 - 200$ polymer chains within a simulation box, the final structure and the process to produce these simulation boxes are detailed in Appendix B. However, this transition toward larger system size and

longer simulations presents new challenges for the modelling of exciton interchain migration in solid films.

In order to address these new challenges, the kinetic Monte Carlo (KMC) algorithm is used to model exciton diffusion in conjugated polymer films. This framework has been widely applied in studies of incoherent exciton transport to analyse the effects of energetic disorder, morphological heterogeneity, and the presence of trap states [270–272]. This approach stochastically models exciton hopping dynamics using transition probabilities obtained from Fermi's Golden Rule and Poisson statistics, tracking exciton motion through sequential hops between localised states while accounting for radiative recombination [201]. In the KMC framework, the probability that an exciton remains in its initial state over a time interval Δt follows an exponential decay law:

$$P(\Delta t) = \exp(-k\Delta t) \tag{5.1.1}$$

where k is the total transition rate, incorporating all possible donor-acceptor hopping pathways and radiative recombination events $k_{\text{total}} = \sum_A k_{DA} + k_{\text{rec}}$. This expression is used to determine the transition time using a random variable x from a uniform distribution on the interval $(0, 1)$ as follows:

$$\Delta t = -\frac{\ln(x)}{k} \tag{5.1.2}$$

Once the transition time is determined, the exciton either migrates to another chromophore or undergoes radiative recombination. If a transfer occurs, the acceptor chromophore is chosen according to the relative Förster transfer rates, and the acceptor becomes the donor state for the next cycle. This process is repeated until all of the initial excitons have decayed radiatively or the simulation reaches maximum time.

During this process, the energy transfer rates are calculated using the Förster Resonance Energy Transfer (FRET) formalism, which is developed in greater detail in Section 5.1.2. This process is induced by dipole-dipole interactions between a donor and an acceptor chromophore and enables energy transfer across distances of up to approximately 10 nm. Under the point-dipole approximation, the transfer rate scales as $\sim \frac{1}{R^6}$. However, this approximation holds only when the spatial extent of the chromophore, L, is significantly smaller than the inter-chromophore separation, R. Conversely, for $L \geq R$, the point-dipole approximation breaks down. In this regime, the line-dipole approximation is used, and the transition rate showcases a more complex, geometry-dependent scaling with L and R. Analytically, the transfer rate is seen to scale as $\Gamma \sim \frac{1}{R^2 L^4}$ for collinear chains and $\Gamma \sim \frac{1}{L^2 R^4}$ for parallel chains; in order to achieve both of these expressions, uniform exciton delocalisation is assumed. Numerical calculations of physically relevant systems show that the transfer integral ($J \equiv \sqrt{\Gamma}$) scales as $J \sim L^{-2}$ for collinear chains and $J \sim L^{-1.8}$ for parallel chains [199, 208].

Moreover, in all cases, the efficiency of FRET is highly sensitive to both the separation and the relative orientation of the interacting chromophores, leading to considerable variability across different types of π-conjugated materials and fluctuations corresponding to the supramolecular structures within samples of the same polymer [273].

While exciton migration within individual polymer chains is frequently considered a one-dimensional process constrained to the polymer backbone, interchain interactions in dense solutions or films introduce a quasi-three-dimensional framework. This is exemplified in lamellar films, where π-stacking of polymer backbones enhances exciton transport between adjacent chains, improving energy transfer efficiency [274, 275].

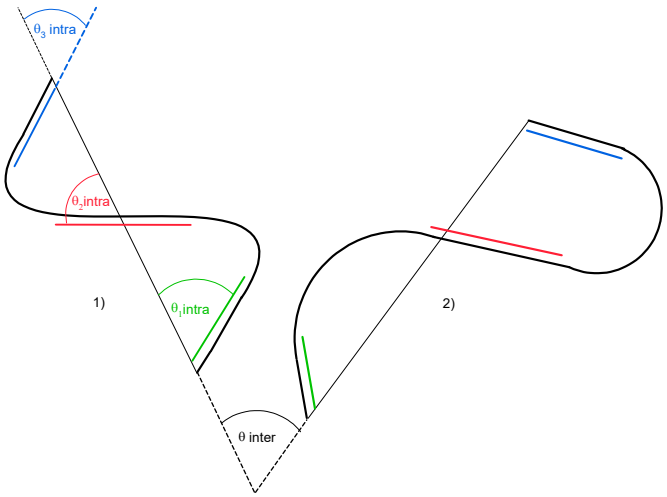


Figure 5.1: Schematic representation of interchain and intrachain angular nomenclature. In this representation, the lines marked in red, blue, and green along the chains depict the spatial extent of the chromophores within the polymer system. The intramolecular angles ($\theta_i$intra), are used to assess the mean alignment of each chromophore relative to the polymer backbone. The angle labeled (θ inter) corresponds to the angle between the molecular axes of the chains of the interacting chromophores 1) and 2).

Additionally, the solid-state morphology of conjugated polymers is inherently complex and heterogeneous. Within a single film, the coexistence of crystalline aggregates, amorphous regions, and phase-separated domains shapes the nature of intrachain and interchain exciton dynamics [276, 277]. For example, aggregates formed during film casting can lead to exciton trapping and reduced photoluminescence efficiency, while highly ordered crystalline domains promote more efficient energy transfer and charge transport [278–281].

Following the ultrafast relaxation dynamics, a pronounced decay in polar fluorescence anisotropy was observed, with the anisotropy decreasing from an initial value of 0.4, the theoretical maximum for one-phonon excitation [87, 221], to approximately 0.254 upon reaching equilibrium, as detailed in Chapter 4. This

reduction reflects the relaxation of the excited state into a single chromophore and serves as an indicator of the mean angular distribution of chromophores relative to the polymer backbone, quantified by the intramolecular angle θ_{intra}, shown in Figure 5.1.

In order to extend the analysis beyond considerations of the effect of chain morphology, the intramolecular angles are maintained at a constant range, while evaluating fluctuations in the distribution of the intermolecular angle θ_{inter} between different chains. The relationship between the variable intermolecular angles and the fixed intramolecular angles is represented in Figure 5.1. These angles are related to the measured angular displacement through δ and θ, represented in Figure 2.10, this process is further explained in Section 5.2.

By constraining the intrachain angles, a systematic evaluation of how molecular alignment and structural order affect FRET efficiency can be conducted.

5.1.1 FRET transfer rate calculations: vibronic transitions

The transition rates are obtained following the discussion in Section 2.3, using Fermi's Golden Rule, given by:

$$k_{I\to F} = \frac{2\pi}{\hbar}\sum_{\nu} |\langle I|\hat{V}_F|F\rangle|^2 \delta(E_I - E_F) \tag{5.1.3}$$

where the initial and final states include the exciton and vibrational states from both the donor and acceptor chromophores:

$$|I\rangle = |i, \mu_D\rangle_D |GS, \mu'_A\rangle_A \tag{5.1.4}$$

$$|F\rangle = |GS, \nu_D\rangle_D |f, \nu'_A\rangle_A \tag{5.1.5}$$

The wavefunction is described by the combined exciton and vibrational phonon components:

$$|i, \nu\rangle = \sum_n \Psi_n^i |n\rangle \prod_m |\nu_m\rangle\rangle_m \tag{5.1.6}$$

As seen in Equation 5.1.3 the probability of these transitions depends on the overlap between the vibrational wavefunctions for the donor and the acceptor chromophores, which is described by the Franck-Condon factors [84, 85]:

$$F_{\mu\nu} = |\prod_{m} \langle\langle \mu_i | \nu_f \rangle\rangle_m|^2 \tag{5.1.7}$$

where μ_i, ν_f correspond to the vibrational wavefunctions of the initial and final states for each vibrational mode involved in the transition. Under the displaced harmonic oscillator model, this overlap is described in terms of the Huang-Rhys parameter, which characterises the strength of exciton-phonon coupling within the material [187, 188], detailed in Section 2.2.3. The Franck-Condon factors, written in terms of the Huang-Rhys parameter S, take the form:

$$F_{0\nu} = \frac{e^{-S} S^{\nu}}{\nu!} \tag{5.1.8}$$

The transitions from the lowest energy vibrational states have been graphically represented in Figure 5.2. At low and room temperatures, the majority of the

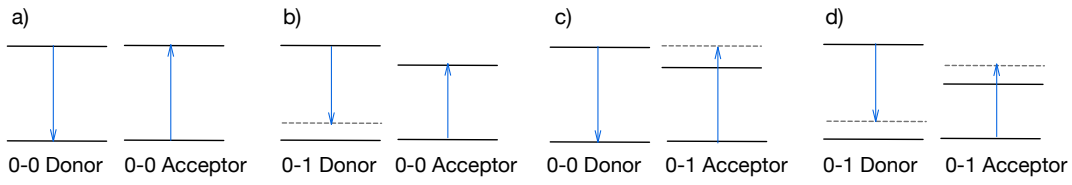


Figure 5.2: Schematic representation of the exciton transfer processes for the lowest vibrational states. The transitions correspond to: (a) $k_{00(D)}^{00(A)}$; (b) $k_{01(D)}^{00(A)}$; (c) $k_{00(D)}^{01(A)}$, ; and (d) $k_{01(D)}^{01(A)}$.

exciton occupy the vibrational ground state, therefore, it is justified to consider transitions from the $v = 0$ state. The lowest energy transition is the $0-0$ transition, which describes energy transfer from the vibrational ground state of the donor

to the vibrational ground state of the acceptor, graphically described in Figure 5.2. The transfer rate for the $0-0$ transition, derived from 5.1.3 and using the expression for $|J_{DA}|$ in Equation 2.3.10, is given by [206]:

$$k_{00(D)}^{00(A)} = \left(\frac{2\pi}{\hbar}\right)|J_{DA}|^2 F_{00}^{D} F_{00}^{A} \delta(E_D - E_A) \tag{5.1.9}$$

where the Franck-Condon factors F_{00}^{D} and F_{00}^{A} represent the overlap between the vibrational wavefunctions of the donor and acceptor in their respective ground states. This factor is given by $F_{00}^{N} = \exp(-S_{\text{eff,N}})$, with the effective Huang-Rhys parameter derived in Equation 2.2.26.

For transitions involving higher vibrational states, the corresponding transition rates are given by [206]:

$$k_{01(D)}^{00(A)} = \left(\frac{2\pi}{\hbar}\right)|J_{DA}|^2 F_{01}^{D} F_{00}^{A} \delta(E_D - E_A) \tag{5.1.10}$$

$$k_{00(D)}^{01(A)} = \left(\frac{2\pi}{\hbar}\right)|J_{DA}|^2 F_{00}^{D} F_{01}^{A} \delta(E_D - E_A) \tag{5.1.11}$$

$$k_{01(D)}^{01(A)} = \left(\frac{2\pi}{\hbar}\right)|J_{DA}|^2 F_{01}^{D} F_{01}^{A} \delta(E_D - E_A) \tag{5.1.12}$$

These transitions have been schematically represented in Figure 5.2 b), c) and d). Equation 5.1.10 represents a transition where the donor begins in the vibrational ground state and transfers to a vibrationally excited state, while the acceptor remains in its ground state ($0-1$ transition for the donor state and $0-0$ transition in the acceptor state). On the other hand, Equation 5.1.11 describes a transition where the donor remains in its ground state, and the acceptor is excited from the ground state to a vibrationally excited state, ($0-0$ transition for the donor state and $0-1$ transition in the acceptor state). Finally, in Equation 5.1.12 both the donor and the acceptor are vibrationally excited during the energy transfer transition, ($0-1$ transition for the donor state and $0-1$ transition in the acceptor

state). In these Equations 5.1.10-5.1.12 the Franck-Condon factor for the first excited vibrational state is given by $F_{01}^{N} = S_{\mathrm{eff,N}} \exp(-S_{\mathrm{eff,N}})$.

The energy levels in conjugated polymers are broadened by thermal fluctuations, structural disorder, and exciton-phonon interactions [282]. The energetic disorder in these systems is reflected in the size and distribution of the LEGS which in turn influences the spectral overlap function that contributes to the transfer rates. Energy transfer rates are also affected by the finite lifetime of phonons, which introduces an additional broadening mechanism. In the ideal theoretical description, exciton transfer is strictly allowed only when the energy released during donor relaxation exactly matches the energy required for acceptor excitation. This is mathematically represented by a Dirac delta function in the transition rate equations. However, in real systems, this strict resonance condition is relaxed due to the finite phonon lifetime, which introduces an energy uncertainty [206]. To account for this effect, the ideal delta function is replaced by a Lorentzian distribution that describes the probability of energy transfer as a function of energy differences:

$$\delta(E_D - E_A) = \frac{\Gamma/2\pi}{(E_D - E_A)^2 + (\Gamma/2)^2} \tag{5.1.13}$$

where Γ represents the broadening parameter, which corresponds to the inverse phonon lifetime, takes a value of 0.06 eV in this work.

5.1.2 Effects of disorder in FRET

Conjugated polymer films exhibit diverse structural variations depending on the synthesis and processing conditions, as reviewed in Section 1.2.3. These structural variations influence the efficiency of FRET through multiple mechanisms. Most notably, structural defects at the chain level such as fluctuations in the dihedral angles between moieties can lead to changes in the super-exchange transfer integrals

thus, resulting in variations in the eigenstates of the system. To this end, it has been previously observed that an increase in the disorder within the dihedral angles in a polymer chain results in more localised LEGS, which in turn results in a decrease in the efficiency of FRET [179, 206]. Furthermore, additional variations in the rate of

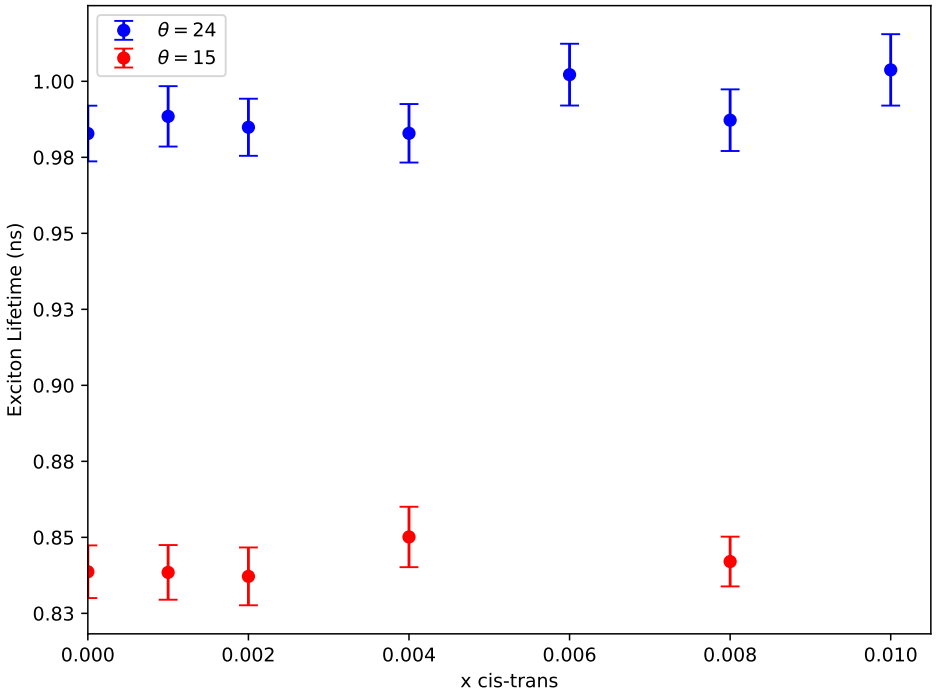


Figure 5.3: Effect of torsional disorder on the exciton lifetime. The blue dots represent simulations with dihedral angles given by a Gaussian distribution with $\theta_{\text{mean}} = 24°$ $\sigma = 8°$; while the red dots represent $\theta_{\text{mean}} = 15°$ $\sigma = 5°$, which are representative of the average angular distributions observed in the blue and red phases of MEH-PPV. An increase of disorder arising from larger distributions of the torsional angle results in higher lifetimes.

this energy transfer can also occur as a result of variations in distance and alignment between interacting chromophores which is included in the electronic term J_{DA}.

As a result of the complex interplay between different sources of disorder, it becomes necessary to differentiate between the effects of torsional or conformational disorder, which arises from variations within the chain morphology, and structural disorder, which refers to deviations from the ideal long-range order. To isolate

the effects of internal chain disorder, computational simulations were conducted on systems with varying degrees of torsional disorder and proportions of cis-trans defects while maintaining a constant intermolecular packing structure.

Figure 5.3 illustrates the relationship between the exciton lifetime and the proportion of cis-trans defects and differences in the dihedral-angle distributions. For these simulations, homogeneous polymer structures with parallel chain alignment were used, these are shown in Figure B.4 in the Appendix B. The two data-sets are created from configurations with internal dihedral angle distributions of $\theta_{\text{mean}} = 24°$, $\sigma = 8°$ in blue, and, $\theta_{\text{mean}} = 15°$, $\sigma = 5°$, in red. Higher torsional disorder leads to an increase in exciton lifetime due to an increase in the exciton localisation. From the data presented, the effect is more pronounced in variations in the torsional angle, whereas changes in the proportion of cis-trans defects exert a weaker influence. The comparatively smaller contribution of the cis-trans defects, which also result in distortions of the polymer backbone planarity, may be a result of the limited maximum value of cis-trans effects that have been explored. These limits are justified within physically realistic systems [110, 283].

On the other hand, the exciton diffusion length decreases with increasing torsional disorder, as observed in Figure 5.4. In more coiled chains, torsional disorder disrupts π-conjugation along the backbone, inducing exciton decoherence and enhancing dephasing. The smaller transition dipole moments associated with localised chromophores diminish the magnitude of the electronic coupling J_{DA}. While in some instances an increase in the disorder can result in a broadening of the absorption and emission spectra and thereby enhance spectral overlap, the dominant effect observed in these simulations is a reduction in the diffusion length, corresponding shortening of the exciton jump distances. In highly disordered systems, excitons are confined to small, localised chromophores, resulting in shorter

hops and lower overall diffusion lengths. In contrast, in more ordered systems, where chromophores are larger and excitonic states are more delocalised, excitons can migrate over longer distances through more efficient FRET.

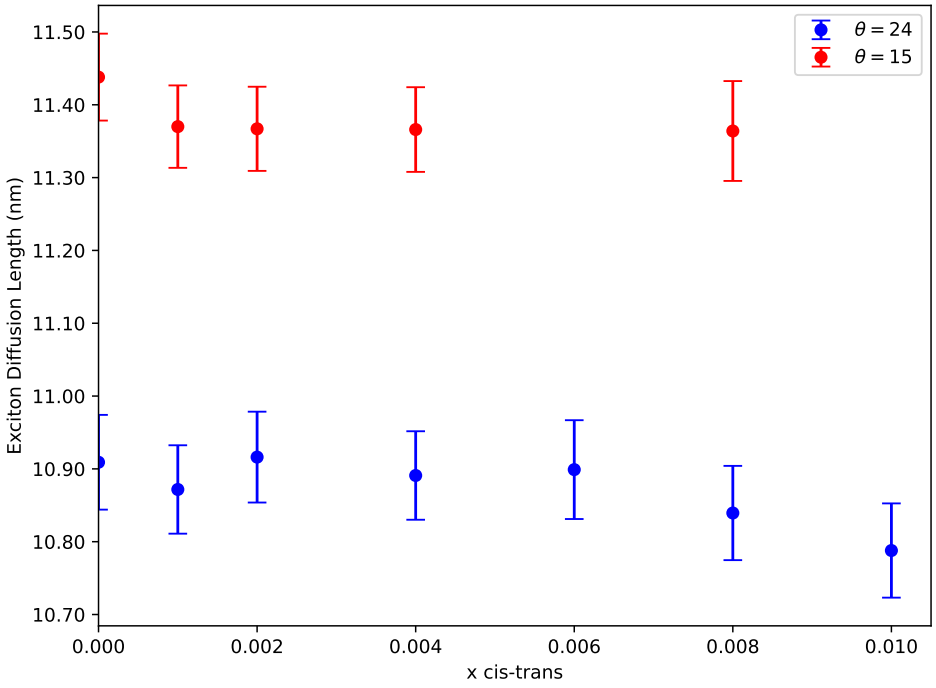


Figure 5.4: Effect of torsional disorder on exciton diffusion length. The blue dots represent simulations with dihedral angles given by a Gaussian distribution with $\theta_{\text{mean}} = 24°$ $\sigma = 8°$; while the red dots represent $\theta_{\text{mean}} = 15°$ $\sigma = 5°$. An increase in the torsional disorder of the system leads to lower values for the exciton diffusion.

Both of these observations, the increase in the exciton lifetime and the decrease in the exciton diffusion length, are a result of the reduced efficiency of FRET in the presence of torsional disorder. The decrease of the FRET efficiency in turn can be directly linked to a reduction in the spectral overlap between interacting chromophores, which reduce the magnitude of $|J_{DA}|$ as defined in Equation 2.3.10 and results in an overall decline in the FRET transition rates, described in Equation 2.3.9.

Aside from variations in the chain conformations, conjugated polymers can

exhibit different types of long-range order which in turn influence exciton transport. Research has shown that nematic ordering is favoured in most π-conjugated materials, however, smectic phases which include more positional order as well as alignment is observed in highly structured polymers. In many cases, films display a mixture of domains with different structural properties, leading to morphological heterogeneity [129, 203, 284].

Origin of the nematic order parameter

The orientation of molecules in a nematic liquid crystal is described by a unit vector along the long axis of each molecule $\mathbf{s}^{(i)}$. For molecules with a centre of symmetry, the first-rank tensor is zero, and as a result, it is insufficient to describe the molecular alignment within these systems. Consequently, the second-order tensor is employed as the order parameter to quantify the degree of alignment within the polymer chain and is defined as [285]:

$$Q_{\alpha\beta}(r) = \frac{1}{N}\sum_{i}\left(s_{\alpha}^{i}s_{\beta}^{i} - \frac{1}{3}\delta_{\alpha\beta}\right) \tag{5.1.14}$$

where $s_{\alpha}^{i}s_{\beta}^{i}$ are the α and β components of the directional unit vectors of the i-th molecule in the system, and the summation is performed over the N molecules within the region of interest. The term with the Kronecker delta function $\frac{1}{3}\delta_{\alpha\beta}$ ensures that this tensor is traceless, a necessary condition for maintaining symmetry within isotropic systems.

When transformed to spherical polar coordinates, the molecular orientation vectors are expressed as:

$$\begin{aligned} s_x &= \sin\theta\cos\phi \\ s_y &= \sin\theta\sin\phi \\ s_z &= \cos\theta \end{aligned} \tag{5.1.15}$$

leading to the form of the order tensor:

$$Q_{\alpha\beta} = \int_0^{2\pi} d\phi \int_0^{\pi} \sin\theta d\theta f(\theta,\phi)\left(s_\alpha s_\beta - \frac{1}{3}\delta_{\alpha\beta}\right) \tag{5.1.16}$$

where $f(\theta,\phi)$ denotes the probability distribution function of the molecular orientation at angles θ and ϕ. In the isotropic phase, where orientations are uniformly distributed, $f_{\text{iso}}(\theta,\phi) = \frac{1}{4\pi}$, all components vanish $Q_{\alpha\beta} = 0$. However, in a perfectly aligned nematic phase, where the molecular axes are oriented along a principal axis n, the order tensor simplifies to $Q_{zz} = 2/3$ and $Q_{xx} = Q_{yy} = -1/3$.

Upon diagonalising the tensor for systems in the nematic phase, the largest eigenvalue corresponds to the scalar order parameter S, and the associated eigenvector defines the preferred molecular alignment direction, n. Therefore, for an uniaxial system, the order parameter simplifies to:

$$Q_{ab} = S\left(n_\alpha n_\beta - \frac{1}{3}\delta_{\alpha\beta}\right) \tag{5.1.17}$$

The scalar order parameter S is described in terms of the molecular angular distribution $f(\theta)$ by considering a direct comparison of Equation 5.1.16 with the known form of $\boldsymbol{Q}$ for nematic ordered systems. It can be shown that if choosing the alignment along the z axis $Q_{zz} = 2S/3$ and $Q_{xx} = Q_{yy} = -S/3$. Thus, normalising the parameter to $S = 1$ for perfect alignment in the nematic phase, S is defined as:

$$S = \int_0^{2\pi} d\phi \int_0^{\pi} \frac{3}{2}\left(\cos^2\theta - \frac{1}{3}\right) f(\theta,\phi)\sin\theta d\theta \tag{5.1.18}$$

The distribution of molecular orientations $f(\theta)$, can be expanded in terms of Legendre polynomials [218, 286]:

$$f(\theta) = \sum_{l=0}^{\infty} \frac{2l+1}{2}\langle P_l(\cos\theta)\rangle P_l(\cos\theta) \tag{5.1.19}$$

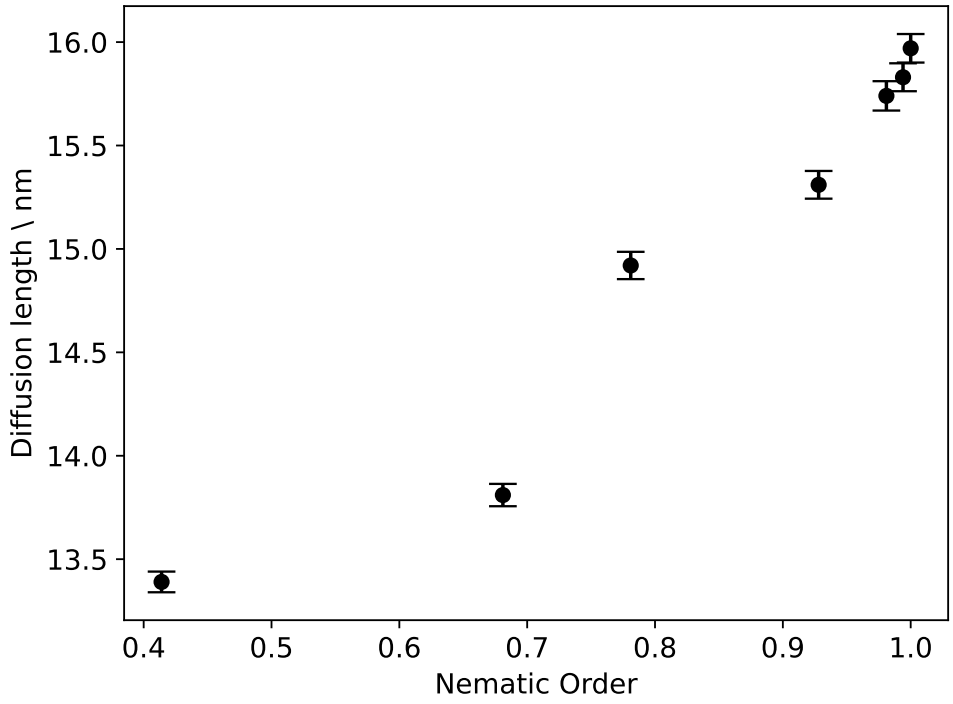


Figure 5.5: Exciton diffusion length in MEH-PPV as a function of nematic order, fixed $x_{\text{cis-trans}} = 0.08$, for $\theta = 14°$, $\sigma_\theta = 5°$ obtained from simulations of 500 polymer chains of 200 moieties length. A decrease of the nematic order parameter, correlated with an increase in the disorder, results in a decrease of the exciton diffusion length.

this expansion is typically truncated after the second term, corresponding to the second-order Legendre polynomial:

$$\langle P_2 \rangle = \frac{1}{2}(3\langle \cos^2 \theta \rangle - 1) \tag{5.1.20}$$

The following analysis assumes only deviations from the ideal nematic phase, which is usually favoured by the specific geometrical and structural characteristics of π-conjugated polymers films that show no indication of cholesteric phase formation under standard conditions [287]. Henceforth, the scalar order parameter S will be referred to as the nematic order parameter (NOP) as it effectively fully captures the degree of molecular alignment within the system [288, 289].

Figure 5.5 shows an increase in the diffusion length in more materials with higher

nematic order, which indicates that despite intermolecular interactions having a significantly smaller impact on the characteristics of the Frenkel-Holstein Hamiltonian eigenstates and thus the spatial extent of the chromophores, intermolecular alignment and an increase in the structural order can result in higher FRET rates. The effects of the intermolecular order are considered to be due to an increase in the alignment of interacting chromophores which is introduced into the FRET rate through the directional component (κ) in $|J_{DA}|$ as shown in Equation 2.3.10.

5.2 Fluorescence anisotropy as a probe of intermolecular dynamics

The use of fluorescence anisotropy (FA) to probe exciton dynamics has been discussed in Chapter 2. This method is widely used to investigate molecular orientation and rotational diffusion within π-conjugated polymers, as it provides information into the angular displacement between the absorbing and emitting fluorophores, δ as shown in Figure 2.10. Furthermore, in solid state polymer films it can also provide indirect information about exciton migration as energy transfer and the exciton-polaron interactions contribute to the depolarization of emitted fluorescence over time [216, 290]. The anisotropy decay can be related back to the angular distribution through Equation 2.4.31. While FA is experimentally accessible, NOP is considered a more fundamental description of the molecular alignment, hence, establishing a relationship between FA and NOP provides a direct connection between experimental observables and theoretical studies. The time evolution of FA reflects the gradual randomisation of chromophore orientations as the exciton hops across progressively larger distances from its initial position. Similarly, the nematic order parameter decays with distance as a consequence of the inherent loss of molecular alignment at increasing distance. The relationship between the

fluorescence anisotropy decay, controlled by the angle δ described in Figure 2.10, and the decrease in the nematic order parameter (NOP, referred also as S in the previous section) which depends on the intermolecular angle θ can be obtained as follows:

- At any given time, the nematic order parameter is found by averaging over the angular distribution. If the local director of an absorbing chain is given as $\hat{n} = \hat{z}$, the NOP can be calculated via:

$$\mathrm{NOP}(t) = P_2(t) = \frac{\int_0^\pi \frac{1}{2}\left(3\cos^2\theta - 1\right) P_{\mathrm{inter}}(\theta, \sigma_{\mathrm{inter}}(t)) \sin\theta \, d\theta}{\int_0^\pi P_{\mathrm{inter}}(\theta, \sigma_{\mathrm{inter}}(t)) \sin\theta \, d\theta} \tag{5.2.1}$$

  Assuming that the chromophore orientation follows a Gaussian probability distribution such that:

$$P_{\mathrm{inter}} = N e^{-\theta^2/2\sigma^2_{\mathrm{inter}}}, \tag{5.2.2}$$

  where $\sigma_{\mathrm{inter}}(t)$ describes the evolving angular spread of orientations as a function of distance and thus in time as the exciton diffuses. As the polymer chains experience increasing orientational disorder with distance, $\sigma_{\mathrm{inter}}(t)$ increases.

- On the other hand, fluorescence anisotropy ($r(t)$) is described in Equation 2.4.31. Given that chromophores within a single chain exhibit an orientation distribution that follows a Gaussian spread about their local director, the initial anisotropy at $t = 0$ is given by:

$$\langle r_0 \rangle = 0.4 \, \frac{\int_0^\pi \frac{1}{2}\left(3\cos^2\theta - 1\right) P_{\mathrm{intra}}(\theta, \sigma_{\mathrm{intra}}(0)) \sin\theta \, d\theta}{\int_0^\pi P_{\mathrm{intra}}(\theta, \sigma_{\mathrm{intra}}(0)) \sin\theta \, d\theta} \tag{5.2.3}$$

  where P_{intra} is the probability distribution of angles within a single polymer chain, and $\sigma_{\mathrm{intra}}(0)$ is the initial angular spread of this distribution.

- As a result of the analysis of exciton relaxation in Chapter 4, where we obtained a steady state value for the fluorescence anisotropy after QEES-LEGS decay, the initial intrachain angular distribution can be obtained:

$$\sigma_{\text{intra}}(0) = 0.39 \text{ radians}, \quad \langle r_0 \rangle \approx 0.26. \tag{5.2.4}$$

  As time progresses, the distribution of chromophore orientations broadens due to interchain interactions and exciton diffusion. The total angular spread at time t is expressed as:

$$\sigma^2_{\text{intra}}(t) = \sigma^2_{\text{intra}}(0) + \sigma^2_{\text{inter}}(t) \tag{5.2.5}$$

  with $\sigma_{\text{intra}}(0)$ for the initial intrachain angular disorder, and, $\sigma_{\text{inter}}(t)$ which describes the time-dependent broadening of the chain director orientation due to interchain exciton dynamics. This relationship holds under the assumption that the time dependent fluctuations are uncorrelated with the emitting chromophore.

- Thus, the fluorescence anisotropy at any time t follows:

$$\langle r(t) \rangle = 0.4 \, \frac{\int_0^\pi \frac{1}{2} \left(3\cos^2\theta - 1\right) P_{\text{intra}}(\theta, \sigma_{\text{intra}}(t)) \sin\theta \, d\theta}{\int_0^\pi P_{\text{intra}}(\theta, \sigma_{\text{intra}}(t)) \sin\theta \, d\theta}. \tag{5.2.6}$$

  This integral can be calculated numerically for a range of σ_{inter}, with a known σ_{intra}, which has been used to find the predicted values of the FA as a function of the calculated values of NOP, these relations are represented in Figure 5.6.

A closer inspection about the non-linear relationship between the numerically obtained NOP and FA is presented in Figure 5.7 where the ratio between FA nad NOP has been plotted as a function of σ_{inter}.

Conjugated polymer films display a wide range of structural arrangements, primarily induced by variations in the chemical and morphological structure of

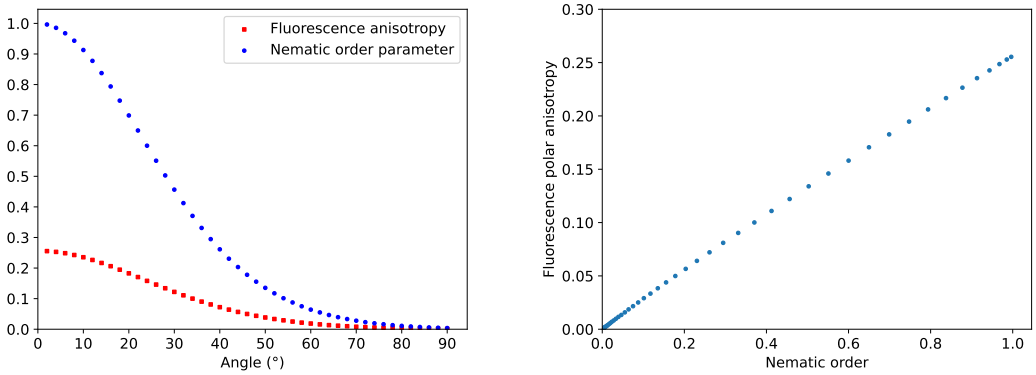


Figure 5.6: (a) Theoretical predictions of nematic order (blue) and polar fluorescence anisotropy (red) as functions of the mean alignment angle between polymer chains, controlled by σ_{inter}. (b) Calculated fluorescence anisotropy as a function of nematic order, showcasing a near linear relationship between anisotropy and molecular alignment in systems with varying degrees of nematic order.

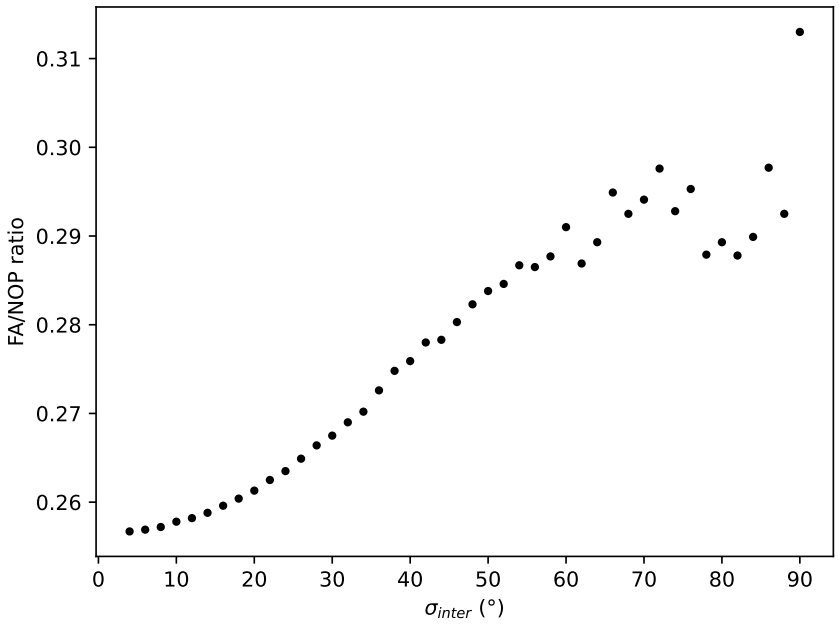


Figure 5.7: The calculated ratio between the fluorescence anisotropy (FA) and the nematic order parameter (NOP) as a function of the variation in the angular distribution σ_{inter}, fixed $\sigma_{intra} = 22.36°$.

individual polymer chains and the specific environmental factors encountered during film casting, such as deposition methods and post-processing treatments [131, 132, 291–293]. While these conditions are widely accepted to modify the overall order of

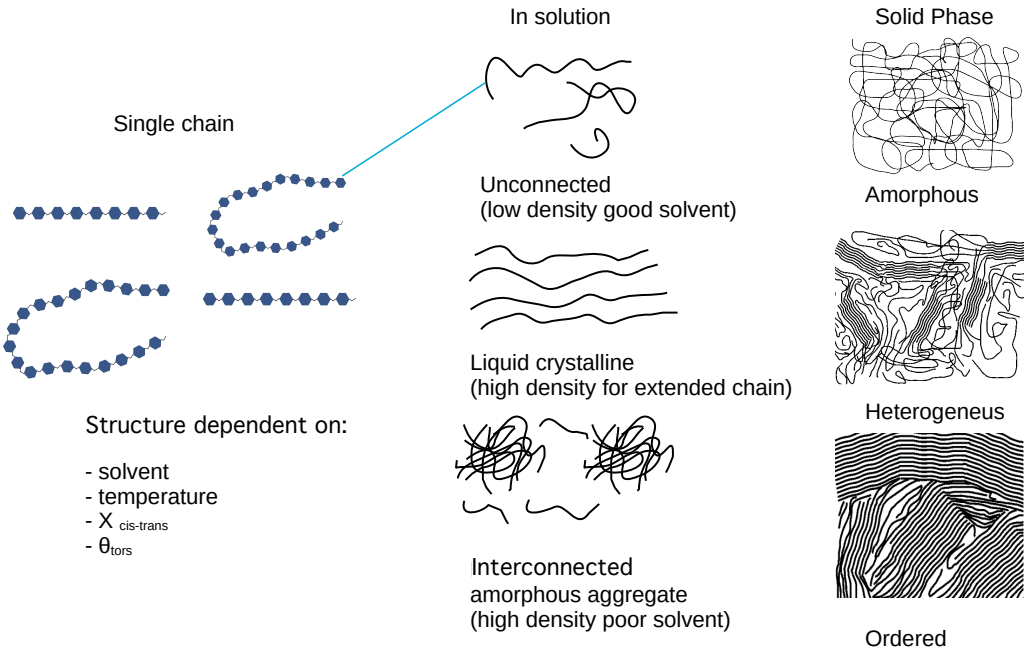


Figure 5.8: Structural and morphological variation in π-conjugated polymers. Differences in morphology and coiling seen within single chains, can arise from differences in the chemical structure and environmental conditions in solution. These factors can lead to aggregation within solutions which results in heterogeneity within films which can be fully amorphous or contain ordered domains.

the sample, they also lead to the creation of non-homogeneous films. These films are characterised by regions of high molecular order coexisting with amorphous areas, resulting in complex spatial arrangements [132, 294]. Therefore, the structure of such films can vary significantly, depending on the respective order within these domains, their size, their overall alignment, and their proximity to one another within the film; this, in turn, affects the optoelectronic properties of the conjugated polymer and the efficiency of any device fabricated from these materials [133, 295–298]. A brief schematic representation of the possible structures and level of order within π-conjugated films is found in Figure 5.8. Experimental observations of structurally different ordered films were also included in Figure 1.8.

Consequently, significant efforts are dedicated towards characterising the align-

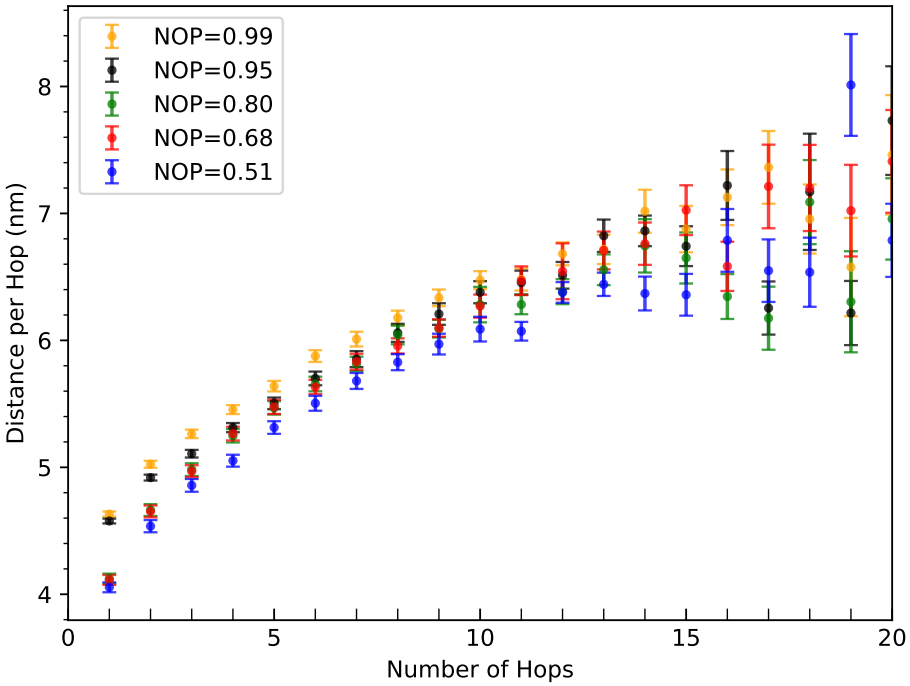


Figure 5.9: Average exciton displacement at each Monte-Carlo hop event, a comparison of ensembles with different structural order with fixed torsional disorder at $\theta = 20°$; $\sigma_\theta = 8°$. Systems with higher NOP have an initial longer average of their jumps, but this difference becomes indiscernible as the simulation continues.

ment and distribution of these domains. Among the available spectroscopical techniques, as described, FA emerges as suitable candidate. The difference within the nematic order between domains gives rise to complex energy migration patterns. In more ordered regions, where chromophores are densely packed and aligned, energy transfer is enhanced, while in disordered regions, it is reduced. Therefore, the overall variability diminishes the total FRET efficiency and introduces inconsistencies in migration patterns [299, 300]. These effects can be directly translated into the fluorescence anisotropy spectra, providing a valuable means of probing the extent of structural order and disorder within the film.

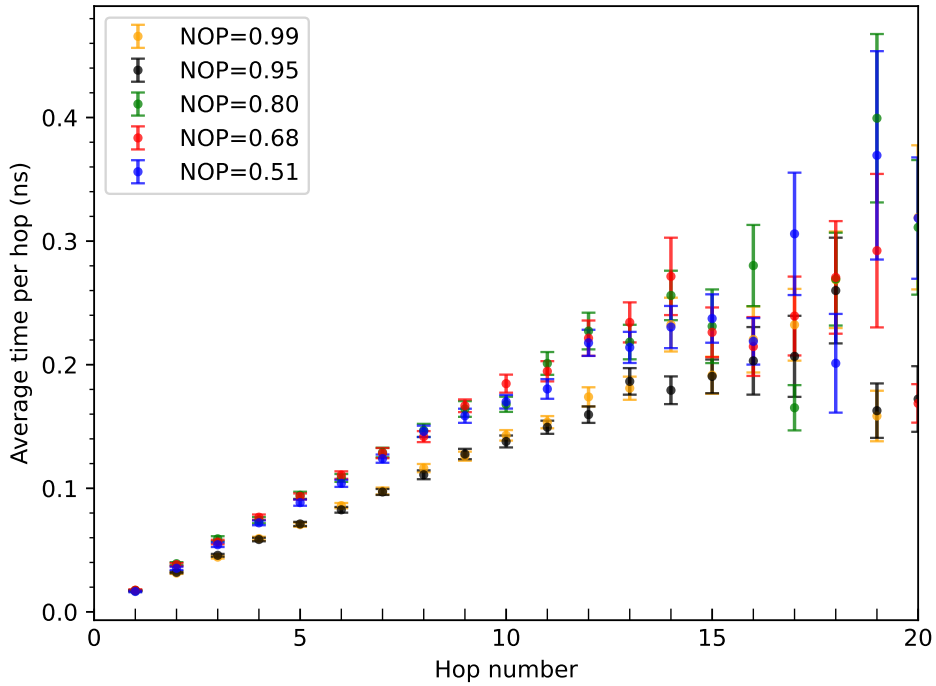


Figure 5.10: Average dwell time per hop, a comparison of ensembles with different structural order. Initially disordered states take longer per hop, with less difference towards the end of the calculation, as there is also more variance of the time per jump similar systems with identical initial distributions.

5.3 Exciton migration in films

The evolution of the mean exciton displacement per hop and the average dwell time per hop in Figures 5.9 - 5.10 can further showcase the effects of structural order in FRET rates. As shown in Figure 5.9, systems with higher NOP initially exhibit longer average hop distances, this could indicate enhanced chromophore alignment and stronger electronic coupling, increasing the efficiency of FRET. As disorder increases, both the relative orientation and the spatial separation between adjacent chains become more variable. This variation impacts the efficiency of FRET which is controlled by the distance between chromophores, and their relative alignment (through the orientation factor κ^2), within the electronic coupling J_{DA}.

This difference is less significant at later stages of the simulation.

Similarly, the evolution of the mean dwell time per hop, shown in Figure 5.10 indicates that on average the time taken per hop in more ordered structures is lower than for disordered structures. It should be noted that at later stages of exciton migration with $N_{\text{hop}} > 12$ significant differences arise between different simulations within the same ensemble, resulting in higher standard deviation values. This, combined with the lower number of jumps at these later stages results in larger uncertainties on the predicted data; therefore, only the 12 initial steps are used for any further analysis.

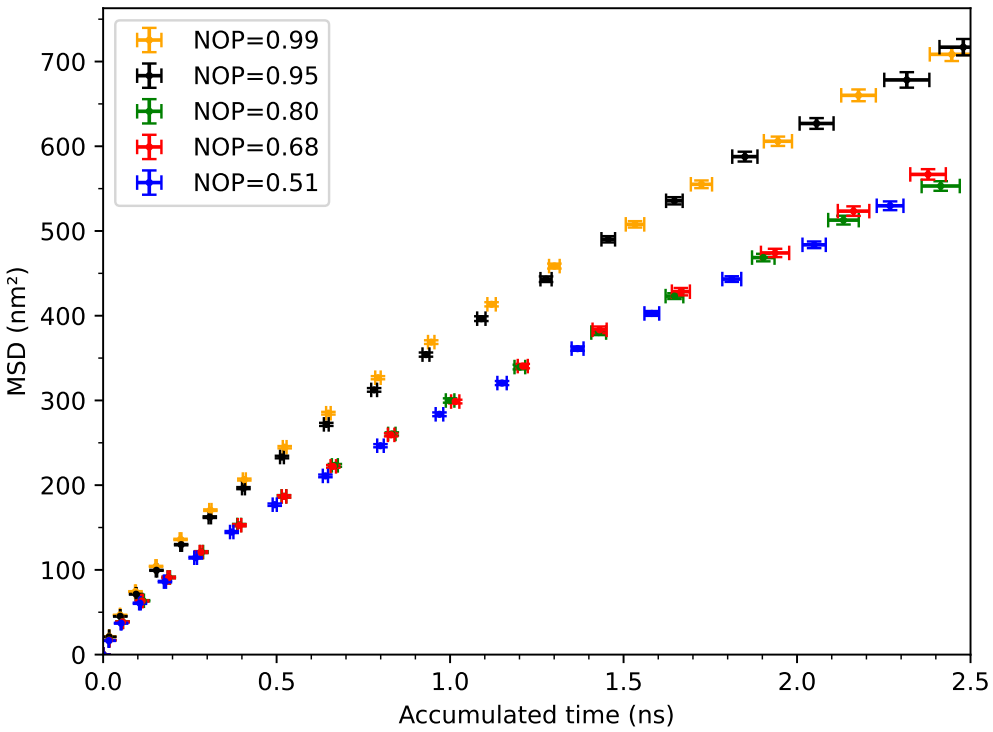


Figure 5.11: Mean square displacement (MSD) as a function of time for configurations with different structural order. More ordered structures (higher NOP, yellow and black points) show larger lengths for the exciton migration with time.

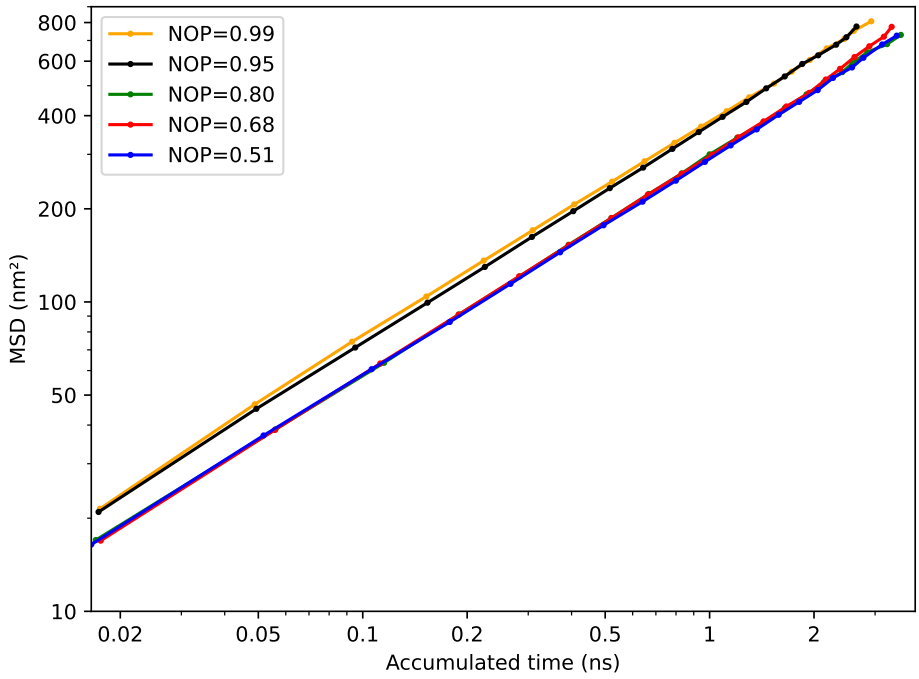


Figure 5.12: Log–log plot of the MSD as a function of accumulated time. The gradient corresponds to an effective scaling $\mathrm{MSD}(t) \sim t^{0.7}$.

The time evolution of the MSD, presented in Figure 5.11, indicates that ensembles with higher NOP initially exhibit more efficient diffusion. This trend persists throughout the observed time window with higher values of MSD in more ordered ensembles; however, the relative separation between different curves does not increase significantly with time, suggesting that the rate of sublinear growth is comparable between ensembles. The MSD scales approximately as $\mathrm{MSD}(t) \sim t^{0.7}$ over the time range surveyed, as shown in Figure 5.12. The analysis of this dependence of MSD on time is further discused in Appendix D. This subdiffusive behaviour is consistent with prior studies of exciton transport in disordered materials, including structurally ordered molecular crystals and conjugated polymers [301, 302]. Physically, slower diffusion rates at later stages can be attributed to the progressive energetic relaxation of excitons into lower-energy states over time, a process commonly referred to as spectral diffusion. As excitons migrate and relax within the disordered density of

states, their decreasing energy reduces the number of energetically accessible acceptor sites available for efficient transfer, thereby diminishing the overall exciton mobility. This gradual relaxation restricts the phase space for Förster-type transitions rather than being solely due to a reduction in spectral overlap. The underlying logarithmic dependence of the exciton energy on time, characteristic of spectral diffusion in disordered systems, is showcased in Figure 5.13.

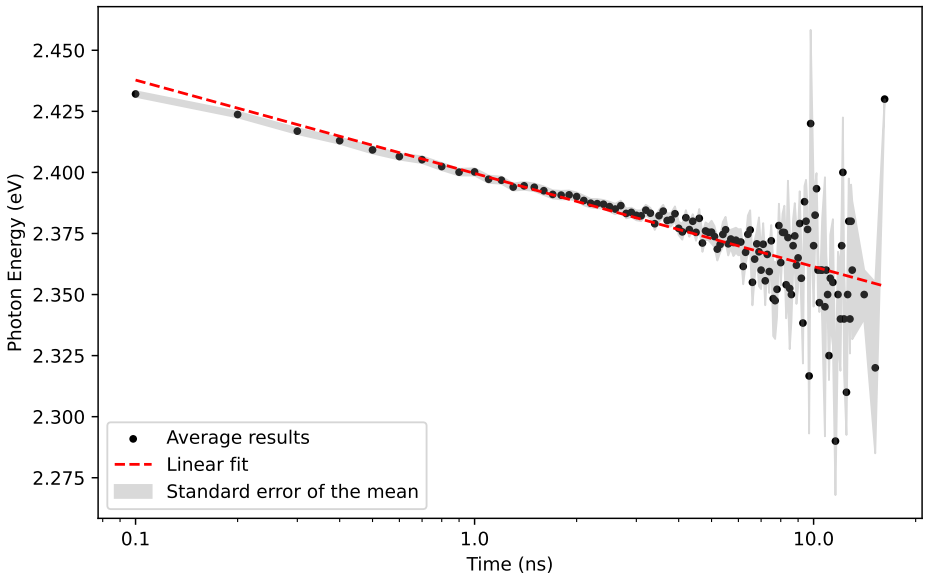


Figure 5.13: Energy relaxation as a function of time. The energetic logarithmic decay in time results in a significant decrease of the spectral overlap between donor and acceptor chromophores which results in a natural decrease in the rate of FRET. These results present the average calculation for 300 different initial configurations and time evolution simulations (all with the same exact statistical angular distribution parameters (θ ; ϕ) and a calculated NOP =0.95).

5.3.1 Structural observations through fluorescence anisotropy

By leveraging experimental TRFA measurements from Gaab and Bardeen on MEH-PPV, alongside the theoretical predictions developed in this chapter, a comprehensive model that connects the observed polar fluorescent anisotropy to the underlying nematic order of the film has been developed [303, 304]. This

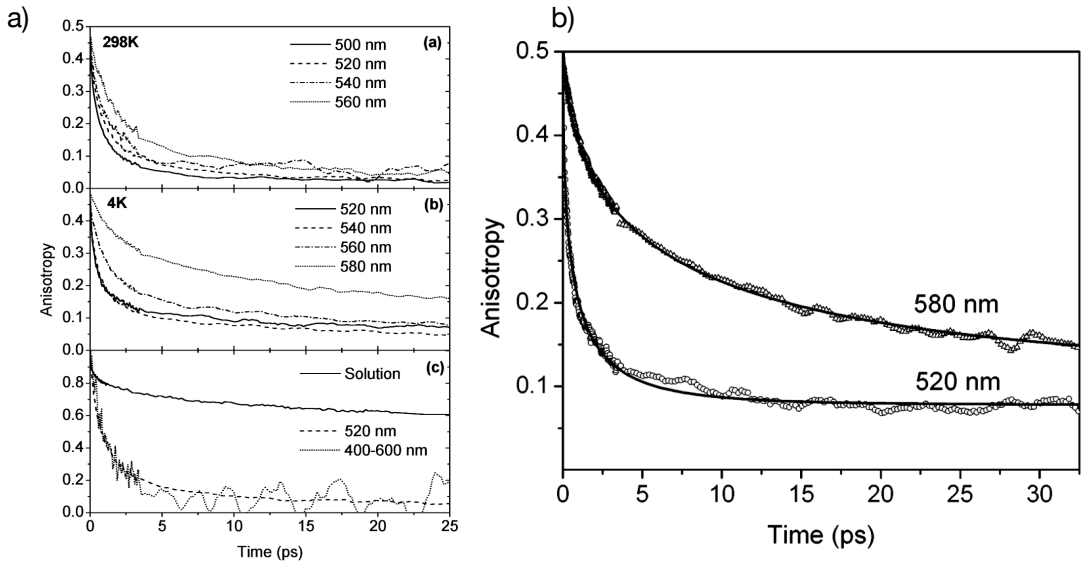


Figure 5.14: Experimental pump-probe anisotropy decays for MEH-PPV films, reproduced without any modifications from [303]. (a) Degenerate pump-probe anisotropy decays for thin films, showing significant wavelength dependence, particularly at lower temperatures. The bottom panel provides a comparison with the pump-probe anisotropy signal from MEH-PPV in a toluene solution. (b) Experimental anisotropy decays at 4 K (dots) for MEH-PPV films, with corresponding polynomial fits (solid lines), highlighting the slower decay at longer wavelengths.

work assists in probing how the disorder and the possible domain structure, shape the intermolecular interactions in this system and impact exciton dynamics on the femtosecond to picosecond scale.

The experimental observations from the TRFA measurements of MEH-PPV films are presented in Figure 5.14 [303]. This research provides a discussion on the dependence of experimental observations of TRFA in π-conjugated films on the excitation wavelength. The authors attribute this dependence to trap states arising from static energetic disorder. At high temperature, thermal activation enables excitons to overcome local energy barriers and continue migrating. At low temperature, exciton diffusion is suppressed as excitons become increasingly confined within trap states corresponding to local energy minima, leading to a slower wavelength-dependent anisotropy decay.

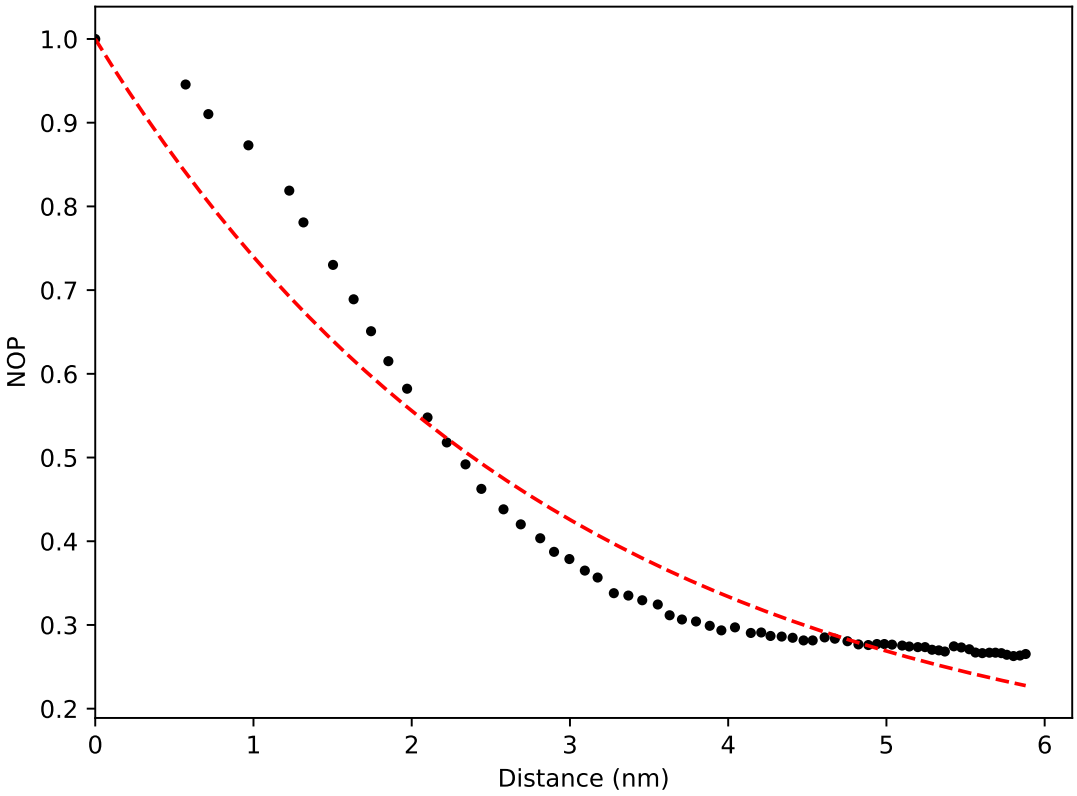


Figure 5.15: Nematic order profile as a function of the total displacement of the exciton migration, derived from theoretical calculations and experimental data from Figure 5.14.

Figure 5.14 a) shows a rapid non-exponential decay of the fluorescence anisotropy in time for these materials, with increasing temperature independence near the absorption maximum $500 - 520$ nm and stronger wavelength dependence at lower temperatures near 4 K. Figure 5.14 b) provides a higher detail of the time-resolved experimental values and fittings that show that the decay does not follow a simple monoexponential decay rate. Temperature and wavelength effects showcase a close relationship between exciton dynamics and lattice phonons as discussed in Chapter 4 and in the discussion of the disorder effects on FRET migration in Section 5.1.2. A significant decrease of the temperature hinders the movement of the nuclei and thus reduces the proportion of quenching due to polaron formation and the presence of trap states is minimised [305–307], therefore, the material maintains

a non-isotropic character for a prolonged period.

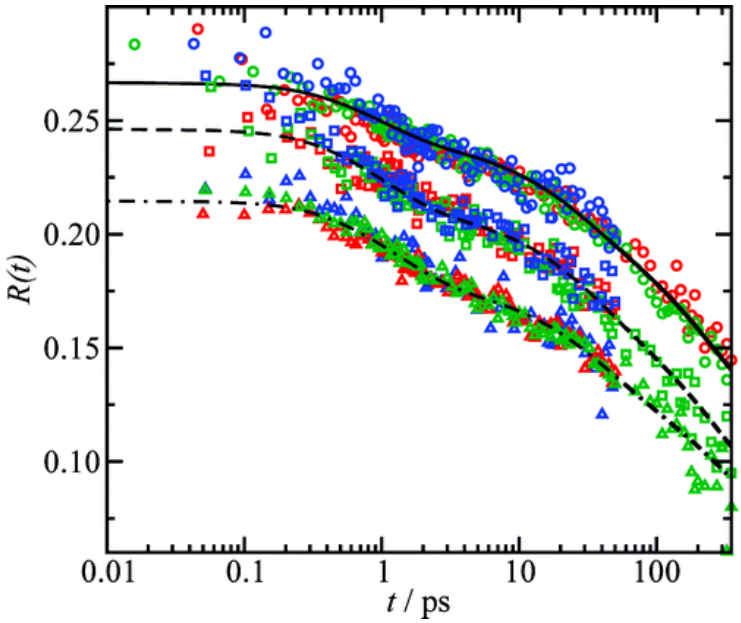


Figure 5.16: Fluorescence anisotropy decay of P3HT, adapted from Wells et al. [249]. Circles describe P3HT with molecular weight $M_w = 6490\,\text{Da}$, squares $M_w = 18130\,\text{Da}$, and triangles $M_w = 27860\,\text{Da}$. The blue symbols correspond to emission at 2.30 eV, the green symbols to emission at 2.18 eV, and the red symbols to emission at 2.05 eV, all samples were excited at 2.64 eV. The data illustrates a prolonged anisotropy decay in comparison to the previously discussed TRFA measurements in MEH-PPV.

Figure 5.15 is constructed by combining the previous results discussed in this chapter with the experimental data in Figure 5.14. First, the time evolution obtained from the experimental data was related to the predictions for the total displacement from simulations of the exciton migration, using the RMSD as a measure of the total displacement at any given time, closely related to Figure 5.11, the RMSD calculated is included in Appendix D. Then, the fluorescence anisotropy at any given time was connected with the corresponding nematic order parameter through their dependence on the intermolecular angle distribution, which was obtained in Figures 5.6, 5.7. Crucially, the exciton migration simulations showed a high sensitivity to the relative orientation and distance between chromophores, thus allowing for the

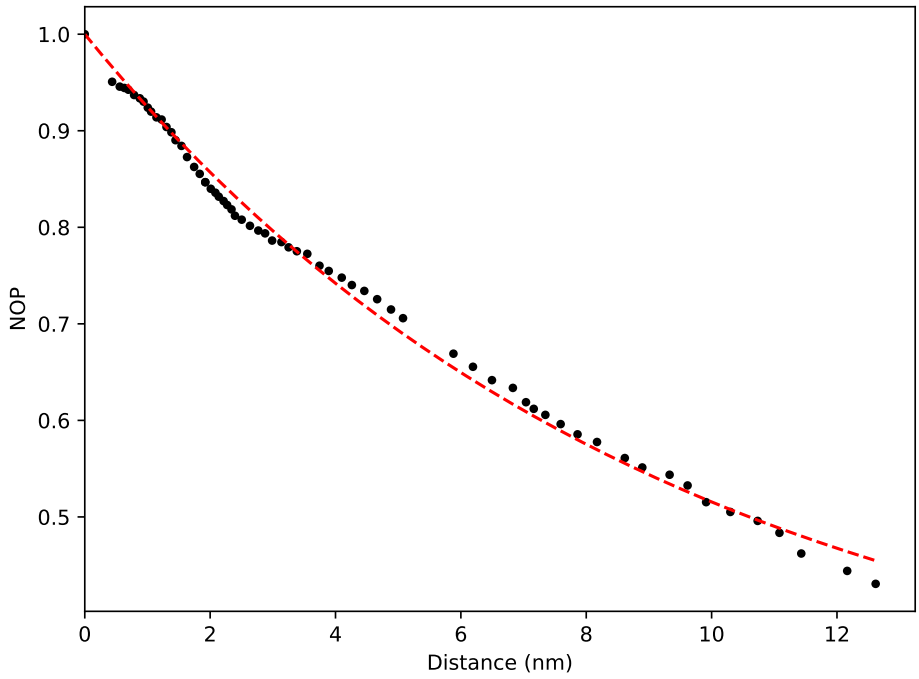


Figure 5.17: Nematic order profile obtained from experimental P3HT data shown in Figure 5.16 and MEH-PPV computational simulations. The decay follows an exponential trend, with a persistence length of approximately 9.15 nm. A steeper decline within the first 4 nm with a more marked exponential form is seen.

prediction of how the nematic order evolves spatially within the film. Figure 5.15 corresponds to the nematic order profile across distances.

By fitting the decay of nematic order to an exponential function, the persistence length defined ξ as:

$$\mathrm{NOP}(L) = (1 - C)\exp^{(-\frac{L}{\xi})} + C \tag{5.3.1}$$

is extracted. This characteristic length represents the distance over which significant structural alignment persists, thus facilitating efficient exciton migration. The persistence length, was determined to be $\xi = 2.89$ nm (with $C = 0.12$). The existence of multiple domains with distinct degrees of nematic order and varying exciton-migration efficiencies, could explain deviations from the theoretically predicted mono-exponential decay of anisotropy observed in TRFA measurements.

Following the same procedure with experimental data on exciton migration dynamics in P3HT obtained by Wells et al. [249], a nematic order profile was derived for this material as a proof of concept. P3HT is structurally different from the PPV-derivatives studied computationally through this work, notably possessing greater backbone rigidity. Despite these differences, the observed similarities in the exciton dynamics between PPV and P3HT suggest that this study remains relevant for validating the approach discussed in this section.

The FA measurements from P3HT shown in Figure 5.16 show fluorescence anisotropy decay extending over a significantly longer timescale than available studies on MEH-PPV, making this a valuable benchmark for our theoretical calculations. The nematic order profile obtained from this experimental data is presented in Figure 5.17, demonstrating an exponential decay down to approximately 0.5 over a spatial range of 13 nm. By fitting this decay to an exponential function, the persistence length ξ is found in 9.15 nm (for $C = 0.27$). Notably, a more pronounced decay is observed in the first 4 nm.

5.4 Discussion

This chapter has presented a theoretical study of intermolecular interactions in conjugated polymers, continuing the previous analysis on intramolecular exciton dynamics and thus providing an overall view of the full lifecycle of an exciton in these materials. By including simulations with varying degrees of morphological and structural disorder, a relation has been established between the material structure and exciton diffusion. The results indicate that disorder strongly influences FRET efficiency, leading to longer exciton lifetimes and reduced diffusion lengths in more disordered and less structurally organised films.

The results presented in this chapter highlight that the structural heterogeneity shown within π-conjugated polymers has a significant impact on exciton migration. Differences in the nematic order between domains induce significant fluctuations in exciton transport efficiency across the material. Theoretical predictions have been validated against experimental fluorescence anisotropy measurements, providing further insight into the structure-properties relationship.

The results further expand on previous conclusions on the effects of internal chain disorder in conjugated polymers and the resulting changes in the LEGS distribution. An increase in torsional disorder is seen to correlate with increase exciton diffusion lifetimes and reduced diffusion lengths. A significant distinction made throughout this study is the differentiation between the disorder stemming from variations in the polymer backbone conformation and the structural disorder resulting from changes in the chain alignment with each other and the overall packing structure of the material. While prior studies predominantly focused on intrachain disorder, the simulations presented systematically measure how structural differences at the mesoscale impact FRET efficiency. This is further supported by the results, which show that in cases where chain conformations remain relatively unchanged, variations in the spatial arrangement and orientation of chromophores lead to a significant decrease in energy transfer efficiency.

These results can be directly applied to interpreting experimental TRFA spectra, making this a useful probe for surveying structural disorder within π-conjugated polymer films. Improvements in the theoretical understanding of exciton transport can, in turn, refine the predictive power of TRFA as probe of the structure and morphology in these materials.

Similarly, a better understanding of the effects of structural changes in polymer films on exciton dynamics and the optoelectrical properties of such materials can

help direct the targeted design of new conjugated polymers and optimise the synthesis process of optoelectronic devices with existing π-conjugated polymers. For example, in OPVs large diffusion lengths are desirable in order to guarantee the excitons reach the junction and guarantee charge separation and high efficiency [308, 309]. To this end, the findings of this study suggest that films with large ordered domains and minimal energetic disorder would be beneficial for this application. On the other hand, OLEDs benefit from limiting exciton migration while also aiming to reduce the number of quenching sites. To this end, structurally disordered materials may be considered, however, while non-radiative decay pathways have not been explicitly modelled in this work, prior research has established that increased disorder correlates with a higher density of quenching sites [310]. This implies that fine-tuning the degree of disorder, while considering the interchange between variations in morphology, long range order or the presence of heterogeneous domains could be considered. Similarly, multiple experimental studies have shown variations in the emission colour and efficiency of OLEDs induced by aggregation in solid conjugated polymer structures, thus further highlighting the need for a robust understanding of the connection between structural changes and exciton dynamics in these materials [116].

6
Conclusions and further work

Over the past five decades, π-conjugated polymers have steadily advanced to the forefront of technological design, becoming indispensable in applications such as organic photovoltaics, light-emitting devices, sensors, and biomedical systems. To this end, the theoretical study of exciton dynamics within these materials is essential for optimising their performance across these technologies.

The goal of this thesis is to create a framework in order to connect the current theoretical understanding of exciton dynamics within conjugated polymers with the experimental observations from these materials. In this regard, this project presents a complete description of the multiple relaxation processes that occur during the lifecycle of an exciton, from ultrafast intramolecular relaxation to interchain energy transfer mechanisms.

Firstly, high-detail simulations on single chains were performed for the initial stages of exciton dynamics, which, critically, included the effects of the exciton coupling to nuclear motion. Initially, excitons experience rapid decoherence and localisation within the first 10 fs after photoexcitation due to exciton-phonon interactions, followed by relaxation to lower energy states and further localisation

mediated through the slower torsional motion of the nuclei. Importantly, the results presented demonstrate the significance of coupling in exciton dynamics for initially higher-energy delocalised states.

Subsequently, the slower interchain regime, spanning picoseconds, was studied using simulations that address the heterogeneity of physical systems. Following the initial ultrafast localisation processes, excitons undergo non-coherent interchain migration, which is seen to be significantly impacted by the structural disorder within the conjugated polymer films. The influence on the efficiency of intermolecular migration of variations in the chain morphology and macromolecular structure, which induce fluctuations in the alignment and distance between chromophores, is analysed. Thus, this theoretical approach more closely reflects physical systems, allowing for the formation of ordered domains that exhibit distinct structures and nematic order.

There has been significant discussion in the literature regarding the need for more refined models capable of handling interactions between individual chromophores, while factoring in disorder-induced variations in chromophoric distances beyond the limitations of the Förster Resonance Energy Transfer (FRET) formalism. The wavelength and temperature dependence observed in the fluorescence spectra of MEH-PPV suggest that vibrational structure and inhomogeneous broadening must be included into any model for an accurate description of the exciton relaxation processes [303, 304]. In response, this work presents a comprehensive model that incorporates both exciton localisation and disorder, allowing for the monitoring of fluctuations in the distance travelled and the efficiency of migration as excitons move through the non-uniform material over time. In the context of interchain interactions, increasing disorder leads to a reduction in chain alignment, resulting in less favourable orientations between neighbouring chromophores. Since the FRET rate depends not only on the distance between donor and acceptor sites

but also on their relative alignment through the orientation factor κ^2, decreased alignment directly suppresses the electronic coupling J_{DA} and thereby reduces the efficiency of exciton transfer.

The simulations included in this work employed a variety of computational methods tailored to the specific requirements of the different stages within the exciton dynamics process. For ultrafast intrachain dynamics, the Time-Evolving Block Decimation (TEBD) method was used, which allows for the quantum mechanical treatment of large systems. Although truncation errors inherent to the TEBD process need to be monitored, the techniques for calculating these errors are well established, allowing for reliable tracking of the errors throughout the simulations [238, 311]. The simulations demonstrated good convergence and maintained low levels of Von Neumann entropy, as long as a sufficiently large basis was preserved after truncation.

The Ehrenfest approximation was employed for the slower torsional modes; although classical methods are not accurate for the faster initial timescales, the system can be considered adiabatic at this stage, rendering the approximation reasonable. Additionally, a damping factor derived from experimental measurements was incorporated in the treatment of torsional modes. From the analysis presented in this thesis, the experimental damping parameter provided accurate and reliable results. Nevertheless, this parameter could be further tested and refined against other experimental observations or with considerations of other theoretical analysis.

This method does not provide an exact description of the system; however, the approximation becomes necessary to accurately account for energy exchange with the environment while ensuring that the simulations remain computationally feasible. It has been shown that, as long as a sufficiently high number of

trajectories are computed, this approach provides an accurate description for open quantum systems [312].

Measurements of the fluorescence polar anisotropy decay, a widely used method for tracking exciton dynamics in the studied polymers, were employed in the experimental observations. The results demonstrated that fluorescence anisotropy decay serves as an indirect but effective probe of structural disorder in conjugated polymer films. By correlating disorder-induced variations in FRET efficiencies with anisotropy decay rates, this work establishes anisotropy measurements as a viable method for characterising morphological heterogeneity in disordered polymer systems. This approach provides a non-destructive means of evaluating disorder effects in thin-film devices.

This analysis could be expanded by including a wider sample for the fluorescence anisotropy spectra from different films and by considering a wider range of distinct π-conjugated polymers. Furthermore, other characterisation techniques, such as AFM, could be employed to study the structure of π-conjugated films directly in order to provide a robust comparison with the theoretical predictions. Finally, these models for exciton dynamics in π-conjugated polymers could be used to draw theoretical predictions for two-dimensional electronic spectroscopy (2DES) which could be tested against existing experimental studies, providing further information about the characteristic exciton-phonon interactions.

Appendices

A

Simulation parameters

A.1 Physical parameters for the simulations

Table A.1: Parameters used in the modelling of exciton intrachain dynamics.

Parameter	**Value**
J_{DA}	-0.60 eV
J^0_{SE}	-1.68 eV
ϵ_{phenyl}	4.5 eV
$\epsilon_{\text{vinylene}}$	8.6 eV
Monomeric Huang-Rhys factor, $S = A^2/2$	8
Mean torsional angle, θ^0	25°
$T_{\text{vib}} = \frac{2\pi}{\omega_{\text{vib}}}$	21 fs
$T_{\text{rot}} = \frac{2\pi}{\omega_{\text{rot}}}$	210 fs
System-bath dissipation timescale, γ^{-1}	100 fs
Dihedral angle distribution, mean deviation, σ_θ	10°
Fraction of cis-trans defects, $x_{\text{cis-trans}}$	0.08

The parameters used in the simulations, and included in Table A.1 are obtained from optical modelling in MEH-PPV [110] and [200]. The torsional damping parameter is obtained from calculations of the autocorrelation function of the bond dynamics performed in [266].

A.2 Computational details: intramolecular simulations

Results of simulations in Chapter 4 are averaged over 1000 different initial polymer conformations, with characteristic Gaussian distribution of the torsional angle $\theta = 25°, \quad \sigma = 10°$ and a probability of 8% cis-trans defects. Considerations are made for over 10 different initial QEES. Calculations presented are averaged over 20-50 different trajectories per each initial configuration.

A.3 Computational details: intermolecular simulations

The analysis presented in Chapter 5 uses a dataset comprising 2000 distinct structural configurations, systematically categorised into five subsets, according to their nematic order.

Each subset is characterised by a specific maximum in the polar and the azimuthal angles, corresponding to the imposed alignment for the polymer chain axis. A detailed explanation of the subset setup and initial structures is provided in the Appendix B. While configurations within a subset share similar nematic order, subtle variations from these angles and slightly different distributions will provide slightly different results, thus the points presented in this work correspond to the averaging over $200 - 300$ simulations. Consequently, the error bars in the distance and time per hop figures in Chapter 5 represent the standard error of the mean. For quantities derived from these values, such as accumulated time and MSD, the corresponding error bars extend from these through error propagation given from $\delta f(e_i) = \sum_{e_i} \frac{\partial f}{\partial e_i} \delta e_i$.

The internal disorder included in previous chapters is still included, thus, these multiple conformers are created with a probability of a structural defect in the form of a cis bond of 8% (unless otherwise stated for the cases of testing the effects of variations of these on the system) and with a mean torsional angle of $\theta = 25°$ and $\sigma_\theta = 10°$ (unless otherwise stated). This approach ensures a comprehensive exploration of the conformational landscape while maintaining a controlled degree of disorder.

B

Technical details of the simulations

B.1 Simulation box: initial configurations

The results on exciton migration due to intermolecular interactions presented in this work are based on a range of simulations with different chain distributions controlled by the spatial arrangement and the alignment of the individual chains. In order to arrange the polymer chains in relation to each other, the following steps are followed:

1. Firstly, the boundaries of the simulation box are defined. For this purpose, the mean expected length for multiple chains is obtained from considerations of different chain expansions, this is defined as $\langle L_z \rangle = \langle Z(N) - Z(1) \rangle$ (for N moieties). The first box boundary which will correspond to the axis of alignment of the incident light for fluorescence anisotropy calculations is then obtained as $L_z = \langle L_z \rangle + \langle L_z/2 \rangle$.

   Following this, the corresponding L_x and L_y are obtained, considering the number of chains to include per simulation and a minimum interchain distance of $d = 4$ Åas $L_x L_y = N_{\text{ring}} N_{\text{polymer}} d^3$. This corresponds to the box dimensions described in Figure B.1 a).

2. From these measurements, each polymer chain is propagated from an origin point. To allow for a wider distribution across the box, half of the chains are propagated antiparallel to each other. Namely, half of the polymers chains will start from an origin polymer with $0 < x(0) < L_x; 0 < y(0) < L_y; L_z/4) < z(0) < 3L_z/4$ expanding along the positive z-axis.

   The rest of the chains expand in the opposite direction along the $-z$ axis with initial position $0 < x(0) < L_x; 0 < y(0) < Ly; 3L_z/4 < z(0) < 5L_z/4$. This process is shown in Figures B.1 b) and B.1 c).

3. For each of the constructed chains, the axis of alignment is tilted in order to randomise their alignment with respect to each other. This randomisation is implemented with by choosing a φ with equal probability for $0 \leq \varphi \leq 2/\pi$ and using θ from a half Gaussian distribution around 0 with $\sigma_\theta = \frac{\pi}{x}$, which enforces $0 \leq \theta \leq \pi$. The x value is used to control the measured nematic order of the simulations. Noticeably for the case of $\theta = 0$ the polymer chains will be quasi-parallel to each other, with a resulting nematic order $S = 1$, this case is shown in Figure B.3. The axis alignment is schematically shown in B.1 b).

The final output of this process is schematically shown in Figure B.2, and initial configurations from different disorders are shown in Figures B.4 and B.3 The broad range of initial chain configurations examined in this chapter is illustrated by the two examples shown in Figures B.3 and B.4. Surveying multiple initial arrangements enables us to investigate the optoelectronic characteristics of MEH-PPV in relation to the structural order of the polymer.

B.2 Nematic order parameter calculations

In this study, the reorientation of the molecule axis alignment corresponds to a half-Gaussian distribution, with only positive values of θ allowed within a Gaussian distribution around $\theta_0 = 0$ with $\sigma_\theta = \frac{\pi}{x}$. The different values of x correspond to restrictions in the distribution, and thus different values of the nematic order with x.

For this distribution, the nematic order parameter S, is given by:

$$S = \frac{\int_0^\pi \left(\frac{1}{2}(3\cos^2(\theta) - 1)\right) e^{-(\theta^2/2\sigma_\theta^2)} \sin(\theta) d\theta}{\int_0^\pi e^{-(\theta^2/2\sigma_\theta^2)} \sin(\theta)\, d\theta} \tag{B.2.1}$$

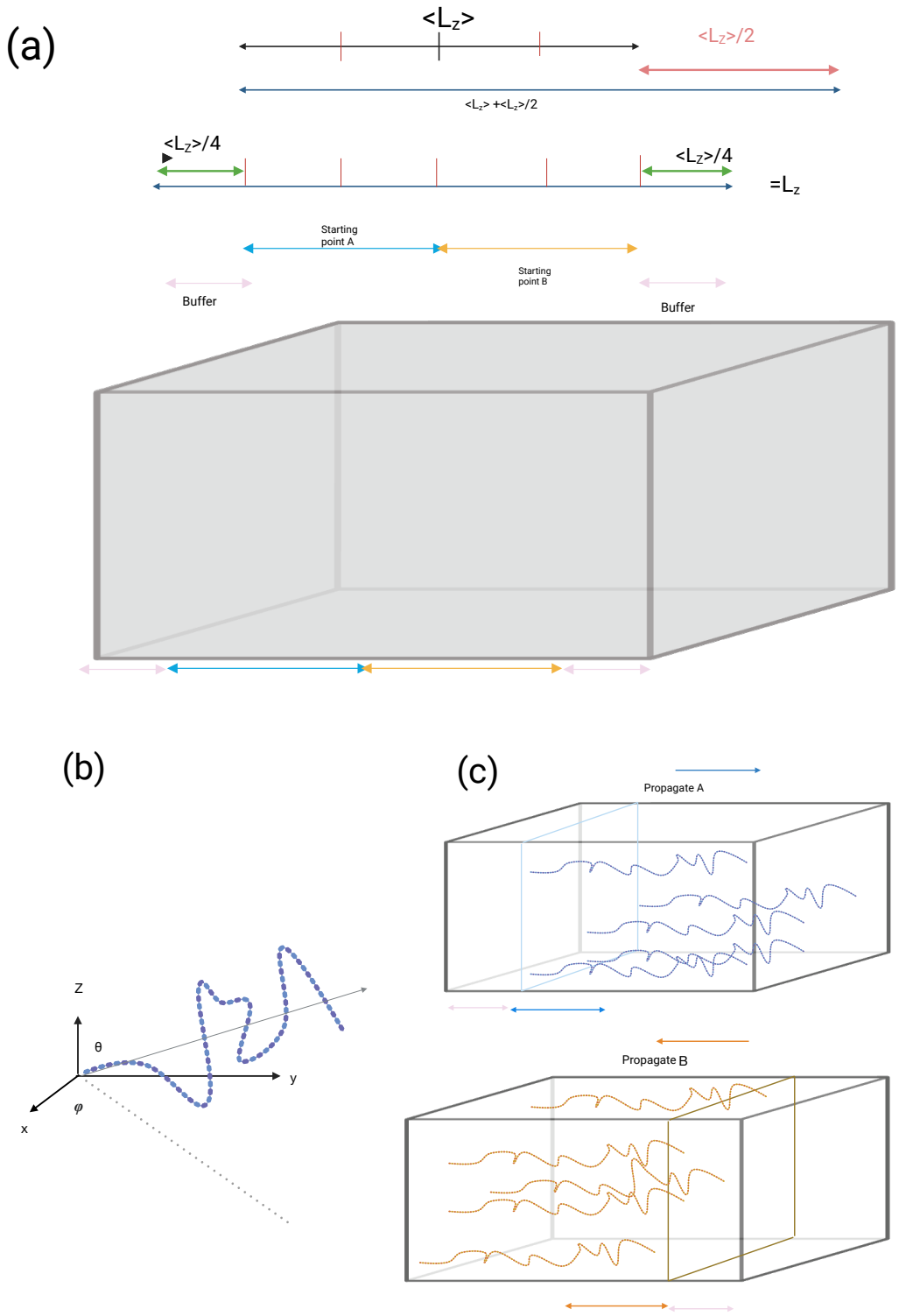


Figure B.1: Configuration of the simulation box: a) Definition of the limits of the simulation box; b) Propagation of the conjugated polymer chains and realignment of the directional axis for a given θ and φ. c) Propagation in positive and negative directions to create more amorphous films.

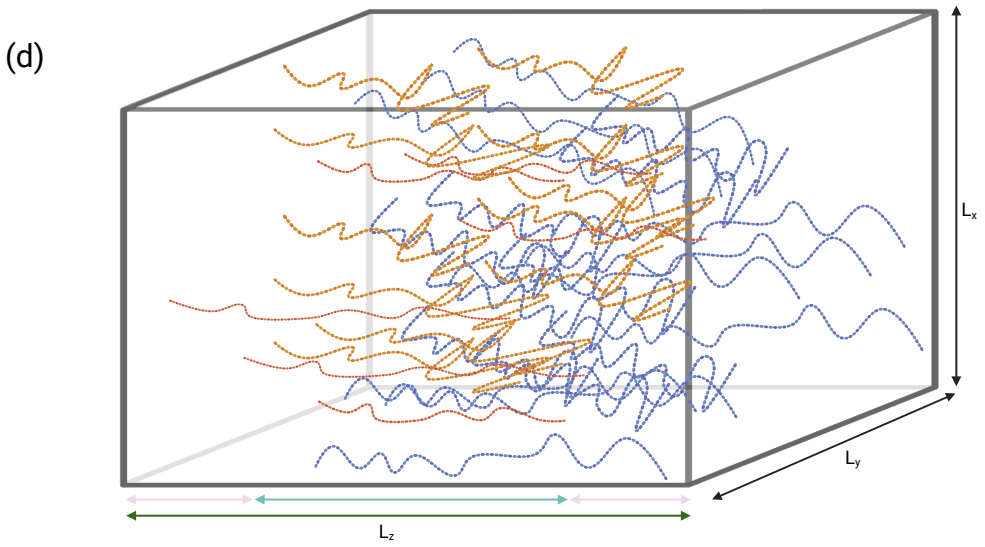


Figure B.2: Schematic representation of the initial configuration for the simulation box

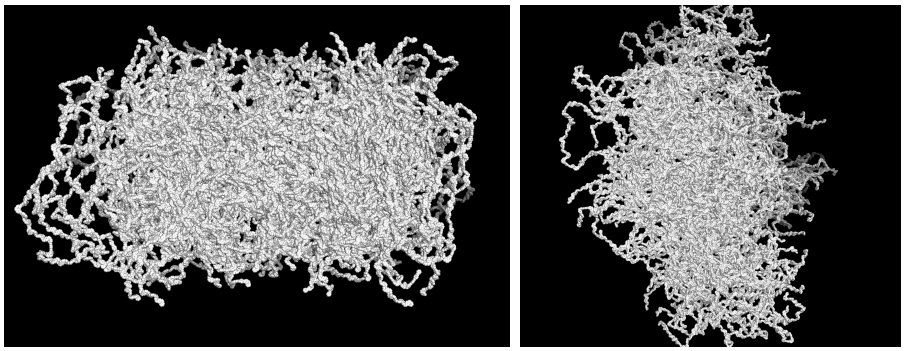


Figure B.3: Initial configuration for polymer samples with nematic order a) $S = 0.45$, b) $S = 0.5$.

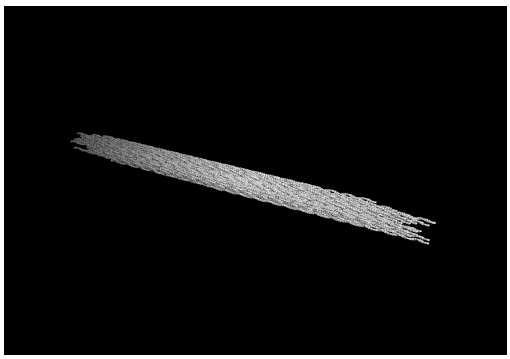


Figure B.4: Initial configuration for a simulation with quasi-parallel chains describe by nematic order parameter $S = 1.0$.

C

The effective Hamiltonian

C.1 Derivation of the effective Hamiltonian

The derivation presented here follows from the TEBD-Ehrenfest algorithm, derived in [225], which accounts for quantum mechanical effects on torsional fluctuations in conjugated polymers. This method extends the Ehrenfest approach by incorporating quantum coherence effects using a time-evolving block decimation (TEBD) formalism. To describe the coupled exciton-phonon dynamics, we consider a general state vector:

$$|\Psi\rangle = \sum_{j} \sum_{\{p\}} \zeta_{j,p(t)}(t) \, |j\rangle \, |\{p(t)\}\rangle \tag{C.1.1}$$

where the torsional basis states:

$$|\{p(t)\}\rangle = |p_1(t)\rangle \ldots |p_n(t)\rangle \ldots |p_N(t)\rangle \tag{C.1.2}$$

and

$$|p_n(t)\rangle = \frac{(c'^{\dagger}_n)^p}{\sqrt{p!}} \, |\alpha_n\rangle \tag{C.1.3}$$

represents displaced excitations of the coherent state (α_n) given by:

$$|\alpha_n\rangle = e^{\frac{-|\alpha_n|^2}{2}} \sum_{q} \frac{\alpha_n^q}{\sqrt{q!}} (c_n^{\dagger})^q \, |0\rangle \tag{C.1.4}$$

Where, c' is redefined from the equilibrium displacement:

$$c'^{\dagger}_{n} = c^{\dagger}_{n} - \alpha^{*}_{n}(t) \tag{C.1.5}$$

Here, α_n parametrizes the displacement and is subject to the Ehrenfest EOM, such that:

$$\alpha_n = \frac{\Delta\tilde{\phi}^{eh}_{n} + i\tilde{L}^{eH}_{n}}{\sqrt{2}} \tag{C.1.6}$$

The time differential of this quantity is given by:

$$\dot{\alpha}_n = -i\alpha_n + i\frac{\lambda_n}{\sqrt{2}}. \tag{C.1.7}$$

By substituting $|\Psi\rangle$ into the TDSE:

$$i\frac{d}{dt}|\Psi\rangle = \hat{H}|\Psi\rangle \tag{C.1.8}$$

which gives, (using $\hbar = 1$):

$$i\sum\frac{d}{dt}\zeta_{j,\{p\}}|j,\{p\}\rangle + \zeta_{j,\{p\}}\left|j,\frac{d\{p\}}{dt}\right\rangle = \sum\zeta_{j,\{p\}}\hat{H}|j,\{p\}\rangle \tag{C.1.9}$$

If the second term is defined as $\left|j,\frac{d\{p\}}{dt}\right\rangle = i\hat{H}'|j,\{p\}\rangle$, then defining the efficient Hamiltonian such that $\hat{H}_{eff} = \hat{H} + \hat{H}'$. This equation can be rearranged into:

$$i\frac{d}{dt}\zeta_{j,\{p\}} = \sum_{j',\{p'\}}\langle j,\{p\}|\hat{H}_{eff}|j',\{p'\}\rangle\,\zeta_{j',\{p'\}} \tag{C.1.10}$$

This is the equation of motion (EOM) for $\zeta_{j,p}$ in the TEBD algorithm, which uses displaced oscillators as the basis states.

Evolution of $|\{p\}\rangle$

To determine $\hat{H}'$the time derivative of the torsional basis states is considered, given by:

$$\frac{d}{dt}|p_n(t)\rangle = \frac{d}{dt}\left[\frac{(c'^{\dagger}_{n}(t))^p}{\sqrt{p!}}|\alpha_n(t)\rangle\right]. \tag{C.1.11}$$

Expanding:

$$\frac{d}{dt}\left|p_n(t)\right\rangle = p(c'^{\dagger}_n)^{p-1}\left(\frac{dc'^{\dagger}_n}{dt}\right)\left|\alpha_n\right\rangle + \frac{(c'^{\dagger}_n)^p}{\sqrt{p!}}\frac{d}{dt}\left|\alpha_n\right\rangle \tag{C.1.12}$$

Using C.1.5 and C.1.4:

$$\frac{d}{dt}c'^{\dagger}_n = -\dot{\alpha_n}^* \tag{C.1.13}$$

This can be expanded from:

$$\left|\dot{\alpha}_n\right\rangle = -\frac{1}{2}(\dot{\alpha}^*_n\alpha_n + \alpha^*_n\dot{\alpha}_n)\left|\alpha_n\right\rangle + e^{-|\alpha_n|^2/2z}\dot{\alpha_n}\sum_q \frac{q\alpha_n^{q-1}}{\sqrt{q!}}\left|q\right\rangle. \tag{C.1.14}$$

These can be combined to arrange into

$$\left|\dot{p}_n\right\rangle = \left[+\frac{1}{2}\left(\alpha^*_n\dot{\alpha}_n - \dot{\alpha}^*_n\alpha_n\right) - \dot{\alpha}^*_n c'_n + \dot{\alpha}_n c'^{\dagger}_n\right]\left|p_n\right\rangle \tag{C.1.15}$$

Using the previous definitions at C.1.6, C.1.7 and C.1.5 this can be further simplified into:

$$\left|\dot{p}_n\right\rangle = i\left[-|\alpha_n|^2 + \lambda_n\frac{\Delta\tilde{\phi}^{eh}_n}{2} - \left(\alpha_n c'^{\dagger}_n + \alpha^*_n c'_n\right) + \lambda_n\delta\hat{\phi}_n\right]\left|p_n\right\rangle \tag{C.1.16}$$

This expression over all n can be used to define $\hat{H}'$: $\hat{H}_{\text{eff}} = \hat{H} + \hat{H}'$ Finally, using the Frenkel Holstein Hamiltonian for the standard H and substituting in the expressions for $\hat{c} \to (\hat{c}' + \alpha)$ and $\hat{C} \to \left(\hat{C}' + \Delta\phi^{\text{eh}}\right)$ the effective Hamiltonian can be defines as:

$$\begin{aligned}
\hat{H}_{\text{eff}} = &\sum_{n=1}^{N-1}\left[J^0_N - \hbar\omega A(\theta^0_n)\left(\Delta\tilde{\phi}^{eh}_{n+1} - \Delta\tilde{\phi}^{eh}_n\right)\right]\hat{T}_{n,n+1} \\
&- \hbar\omega\sum_{n=1}^{N-1} A(\theta^0_n)\left(\hat{C}'_{n+1} - \hat{C}'_n\right)\left(\hat{T}_{n,n+1} - \langle\hat{T}_{n,n+1}\rangle\right) \\
&+ \hbar\omega\sum_{n=1}^{N}\left(\hat{c}'^{\dagger}_n\hat{c}'_n + \frac{1}{2}\right) \\
&+ \frac{\hbar\omega}{2}\sum_{n=1}^{N-1} A(\theta^0_n)\left(\Delta\tilde{\phi}^{eh}_{n+1} - \Delta\tilde{\phi}^{eh}_n\right)\langle\tilde{T}_{n,n+1}\rangle
\end{aligned} \tag{C.1.17}$$

where:

$$\hat{C}'_n = \frac{1}{\sqrt{2}}\left(\hat{c}^{\dagger}_n + \hat{c}'_n\right) \equiv \delta\hat{\phi}_n \tag{C.1.18}$$

D

Extraction of transport coefficients from kinetic data

This appendix documents the fitting parameters used to analyse simulation data presented in Chapter 5.

D.1 Dwell time and distance per hop

The dwell time per hop $\delta t(n)$ increases linearly with hop index n following:

$$\delta t(n) = k_t n \tag{D.1.1}$$

Figure D.1 shows the averaged simulation results alongside the corresponding fits, with the fitted values of the temporal constant k_t reported in Table D.1. Each data group represents an ensemble of approximately 300 independent disorder realisations, characterised by the mean nematic order parameter (NOP). While individual simulations within a group exhibit slight variations in NOP due to different initial chain alignments, the group is identified by the ensemble-averaged NOP for that set, obtained as described in the Appendix B.

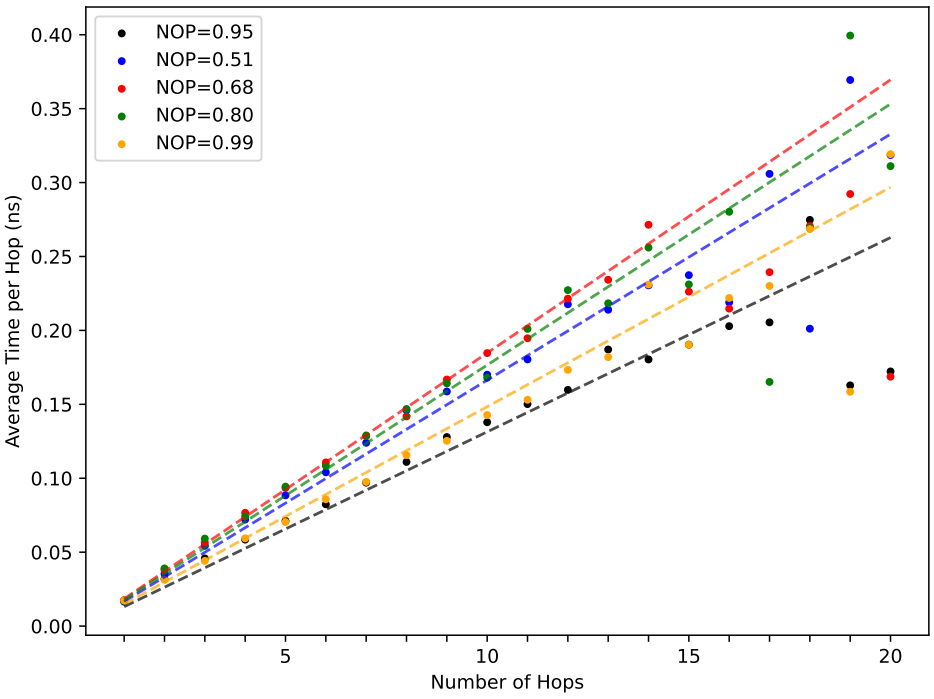


Figure D.1: Average dwell time per hop as a function of hop index. The lines represent a linear fit for the corresponding simulation data.

Similarly, the hop distance increases sublinearly with the number of hops and is modelled by:

$$l(n) = l_0 + k\sqrt{n} \tag{D.1.2}$$

The fit for the sublinear increase in distance per hop is shown in Figure D.2, with the fitted parameters reported in Table D.1.

NOP	l_0 (nm)	k (nm)	k_t (ns)
0.99	3.832 ± 0.036	0.823 ± 0.014	0.0146
0.95	3.721 ± 0.043	0.818 ± 0.017	0.0137
0.80	3.373 ± 0.088	0.908 ± 0.034	0.0180
0.68	3.277 ± 0.056	0.956 ± 0.022	0.0185
0.51	3.261 ± 0.068	0.896 ± 0.027	0.0171

Table D.1: Fitting parameters for the average distance at hop n and the average dwell time per hop, calculated for ensembles with different structural orders characterised by NOP. Both of the fittings only consider data points for $n < 12$ as a result of the increase in variance for the final hops in the simulations.

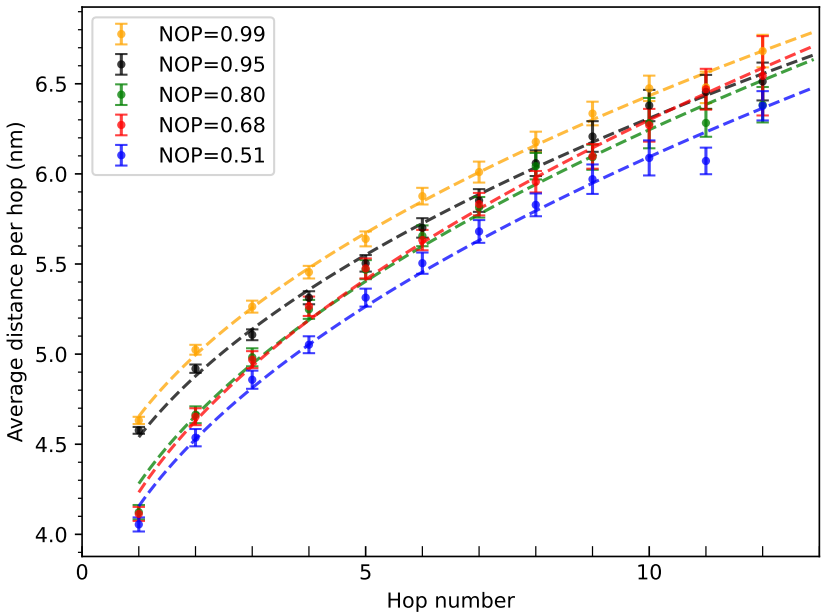


Figure D.2: Distance per hop as a function of hop number. The lines follow a fit for the function $l(n) = l_0 + kn^{1/2}$.

D.2 Evolution in time of the mean squared displacement

Following classical diffusion theory, the MSD is expected to increase linearly with time as described by the Einstein relation:

$$\mathrm{MSD}(t) = 6Dt \tag{D.2.1}$$

This expression applies in three dimensions and is derived under the assumption of Markovian dynamics, where successive displacements are uncorrelated in time. Figure D.3 shows the MSD as a function of time extracted directly from the simulation data, without consideration of the fitting functions discussed above. This figure also includes linearised fits for each data set, the parameters of which are included in Table D.2.

However, in systems with structural and energetic disorder, the evolution in

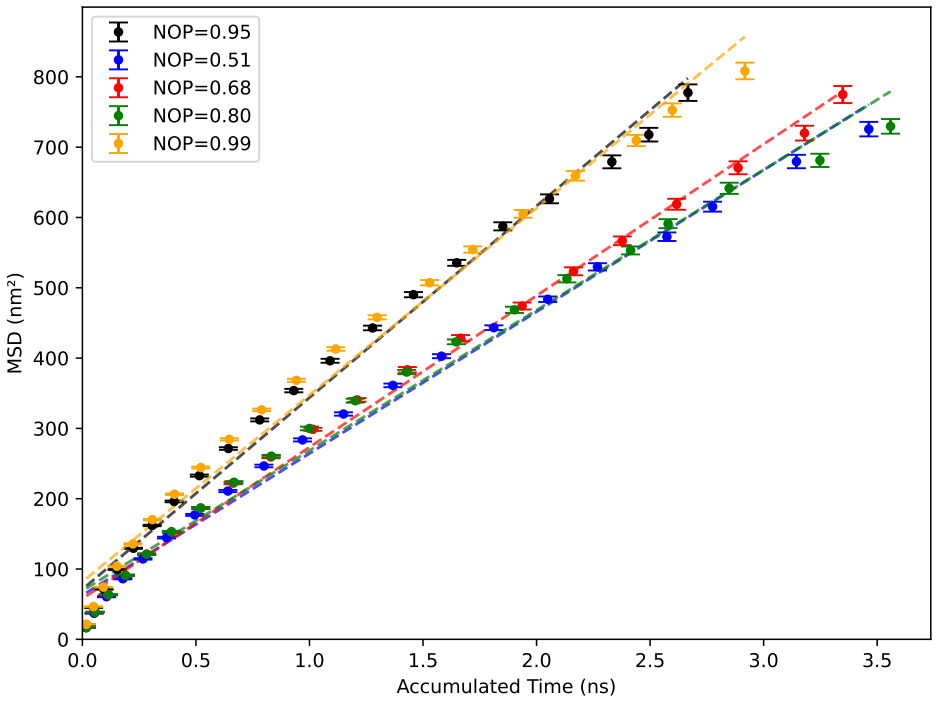


Figure D.3: MSD as a function of time for different configurations characterised by their NOP. The scatter points represent the averaged simulation data, while the fitted lines indicate the linear trend used to extract the diffusion coefficient.

NOP	**Slope** a (nm²/ns)	**Intercept** b (nm²)	**Diffusion Coeff** D (nm²/ns)
0.99	265.7831	81.7671	44.2972
0.95	272.5674	71.2052	45.4279
0.80	199.5697	69.0110	33.2616
0.68	215.4968	57.7630	35.9161
0.51	201.5815	62.7295	33.5969

Table D.2: Linear fitting parameters for the MSD as a function of total time and the computed diffusion coefficients.

time of the MSD may exhibit non-linear behaviour. In order to further investigate this, a theoretical analysis can be undertaken to find the theoretical evolution of the MSD in time

The total accumulated time after N hops can be obtained from Equation D.1.1 following:

$$t(N) = \sum_{n=1}^{N} \delta t(n) = \frac{k_t N^2}{2} \tag{D.2.2}$$

The inverse relation gives the number of hops as a function of time:

$$N(t) = \left(\frac{2t}{k_t}\right)^{1/2} \tag{D.2.3}$$

which is then used in combination with Equation D.1.2 to obtain the total MSD after N hops:

$$\begin{aligned} \mathrm{MSD}(N) &= \sum_{n=1}^{N} l^2(n) = \sum_{n=1}^{N} \left(l_0^2 + 2l_0 k n^{1/2} + k^2 n\right) \\ &\Rightarrow \int_0^N \mathrm{d}n \Rightarrow \mathrm{MSD}(N) = l_0^2 N + \frac{4l_0 k}{3} N^{3/2} + \frac{k^2}{2} N^2 \end{aligned} \tag{D.2.4}$$

$$\mathrm{MSD}(t) = \left[l_0^2 \left(\frac{2}{k_t}\right)^{1/2} t^{1/2}\right] + \left[\frac{4l_0 k}{3} \left(\frac{2}{k_t}\right)^{3/4} t^{3/4}\right] + \left(\frac{k^2}{k_t}\right) t \tag{D.2.5}$$

$$= A_1 t^{1/2} + A_2 t^{3/4} + A_3 t \tag{D.2.6}$$

The coefficients A_1, A_2, and A_3 determine the relative contributions of the $t^{1/2}$, $t^{3/4}$, and linear t terms, respectively, in the time evolution of the MSD. Their values, extracted from the previously discussed fits of the simulation data, are listed in Table D.3.

NOP	A_1 ($\mathrm{nm}^2/\mathrm{ns}^{1/2}$)	A_2 ($\mathrm{nm}^2/\mathrm{ns}^{3/4}$)	A_3 ($\mathrm{nm}^2/\mathrm{ns}$)
0.99	171.87	168.37	46.39
0.95	167.29	170.44	48.89
0.80	119.93	139.75	45.80
0.68	111.66	140.04	49.40
0.51	115.01	138.56	46.95

Table D.3: Coefficients A_1, A_2, and A_3 for the MSD expression $\mathrm{MSD}(t) = A_1 t^{1/2} + A_2 t^{3/4} + A_3 t$.

Time regimes for long range exciton transport

In principle, there are three time regimes of transport. Assuming $A_1 > A_2 > A_3$, the crossover times are defined as follows:

1. For $\frac{A_1 t^{1/2}}{A_2 t^{3/4}} > 1$, this implies

$$t < t_{R1} = \left(\frac{A_1}{A_2}\right)^4 \tag{D.2.7}$$

so the first term in MSD dominates, i.e. MSD $\sim t^{1/2}$

2. For $\frac{A_2 t^{3/4}}{A_3 t} > 1$, this implies

$$t_{R1} < t < t_{R2} = \left(\frac{A_2}{A_3}\right)^4 \tag{D.2.8}$$

so the second term dominates, i.e. MSD $\sim t^{3/4}$

3. For $t > t_{R2}$, the last term dominates, i.e. MSD $\sim t$

NOP	t_{R1} (ns)	t_{R2} (ns)
0.99	1.09	173.50
0.95	0.93	148.32
0.80	0.54	86.66
0.68	0.40	64.58
0.51	0.47	75.86

Table D.4: Estimated transition times t_{R1} and t_{R2} separating the $t^{1/2}$, $t^{3/4}$, and t regimes of MSD for systems with varying NOP.

Figure 5.12 showcases the log-log plot for the msd evolution which shows a consistent effective power-law exponent of $\alpha \approx 0.7$ across all ensembles. This is in agreement with the intermediate regime predicted in this section, and is consistent with subdiffusive transport previously reported in both polymers [313] and molecular crystals [301, 302].

Bibliography

[1] H. Spanggaard, F. C. Krebs, "A brief history of the development of organic and polymeric photovoltaics", *Solar Energy Materials and Solar Cells* **2004**, *83*, 125–146.

[2] H. Shirakawa, E. J. Louis, A. G. MacDiarmid, C. K. Chiang, A. J. Heeger, "Synthesis of electrically conducting organic polymers: Halogen derivatives of polyacetylene, (CH)x", *Journal of the Chemical Society Chemical Communications* **1977**, 578–580.

[3] C. Chiang, C. Fincher, Y. Park, A. Heeger, H. Shirakawa, E. Louis, S. Gau, A. MacDiarmid, "Electrical conductivity in Doped Polyacetylene", *Physical Review Letters* **1977**, *39*, 7380–7382.

[4] A. J. Heeger, "Nobel lecture: Semiconducting and metallic polymers: The fourth generation of polymeric materials", *Reviews of Modern Physics* **2001**, *73*, 681–700.

[5] H. Shirakawa, "The discovery of polyacetylene film - the dawning of an era of conducting polymers (Nobel Prize 2000 Lecture)", *Current Applied Physics* **2001**, *1*, 281–286.

[6] A. G. MacDiarmid, Synthetic metals: a novel role for organic polymers, Stockholm University, **2000**.

[7] N. Basescu, Z. X. Liu, D. Moses, A. J. Heeger, H. Naarmann, N. Theophilou, "High electrical conductivity in doped polyacetylene", *Nature 1987 327:6121* **1987**, *327*, 403–405.

[8] R. Friend, "Polymers show they're metal", *Nature News & Views* **2006**, *441*, 7.

[9] E. Hückel, "Quantentheoretische Beiträge zum Benzolproblem", *Zeitschrift für Physik* **1931**, *70*, 204–286.

[10] W. P. Su, J. R. Schrieffer, A. J. Heeger, "Solitons in polyacetylene", *Phys. Rev. Lett.* **1979**, *42*, 1698–1701.

[11] R. Pariser, R. G. Parr, "A semi-empirical theory of the electronic spectra and electronic structure of complex unsaturated molecules. I.", *The Journal of Chemical Physics* **1953**, *21*, 466–471.

[12] R. Pariser, R. G. Parr, "A semi-empirical theory of the electronic spectra and electronic structure of complex unsaturated molecules. II", *The Journal of Chemical Physics* **1953**, *21*, 767–776.

[13] J. A. Pople, "Electron interaction in unsaturated hydrocarbons", *Trans. Faraday Soc.* **1953**, *49*, 1375–1385.

[14] Z. G. Soos, G. W. Hayden, "Dimerization and Peierls instability in polyacetylene", *Molecular Crystals and Liquid Crystals Incorporating Nonlinear Optics* **1988**, *160*, 421–432.

[15] S. N. Dixit, S. Mazumdar, "Electron-electron interaction effects on Peierls dimerization in a half-filled band", *Phys. Rev. B* **1984**, *29*, 1824–1839.

[16] W. Barford, *Electronic and optical properties of conjugated polymers*, 1st, Oxford Univ. Press, **2005**.

[17] E. J. Meier, F. A. An, B. Gadway, "Observation of the topological soliton state in the Su-Schrieffer-Heeger model", *Nature Communications* **2016**, *7*, 1–6.

[18] S. Karabunarliev, E. R. Bittner, "Polaron-excitons and electron-vibrational band shapes in conjugated polymers", *Journal of Chemical Physics* **2003**, *118*, 4291–4296.

[19] Z. Sun, S. Li, S. Xie, Z. An, "A study on excited-state properties of conjugated polymers using the Pariser-Parr-Pople-Peierls model combined with configuration-interaction-singles", *Organic Electronics* **2018**, *57*, 277–284.

[20] R. E. Peierls, *Quantum theory of solids*, Clarendon Press, **1996**.

[21] M. Bourass, A. Touimi Benjelloun, M. Hamidi, M. Benzakour, M. Mcharfi, M. Sfaira, F. Serein-Spirau, J. P. Lère-Porte, J. M. Sotiropoulos, S. M. Bouzzine, M. Bouachrine, "DFT theoretical investigations of π-conjugated molecules based on thienopyrazine and different acceptor moieties for organic photovoltaic cells", *Journal of Saudi Chemical Society* **2016**, *20*, S415–S425.

[22] T. M. McCormick, C. R. Bridges, E. I. Carrera, P. M. Dicarmine, G. L. Gibson, J. Hollinger, L. M. Kozycz, D. S. Seferos, "Conjugated polymers: Evaluating DFT methods for more accurate orbital energy modeling", *Macromolecules* **2013**, *46*, 3879–3886.

[23] T. Schimitberger, G. R. Ferreira, L. C. Akcelrud, M. F. Saraiva, R. F. Bianchi, "X-rays sensing properties of MEH-PPV, Alq3 and additive components: A new organic dosimeter as a candidate for minimizing the risk of accidents of patients undergoing radiation oncology", *Medical Engineering and Physics* **2013**, *35*, 140–144.

[24] M. Freebody, "OLEDs: Step in where design matters", *Photonics Spectra (https://www.photonics.com/ Accessed 16/10/2024).*

[25] "Nanoscaled OFETs for circuit applications", *Institute of Nano and Microelectronic Systems (INES) University of Stuttgart (https://www.ines.uni-stuttgart.de/en/research/projects/ofets Accessed 16/10/2024).*

[26] "Field effect transistors", *Molecular Opto-Bio-Electronics Lab (MOBEL) (https://faculty.iisertvm.ac.in Accessed 16/1-/2024).*

[27] "LG shows its first OLED TV with curved screen", *Phys.org (https://phys.org/news/2013-01-lg-oled-tv-screen.html Accessed 16/10/2024).*

[28] "Organic photovoltaics: the path to lightweight, flexible and transparent solar cells", *Nature research custom media (https://www.nature.com/articles/d42473-022-00224-9 Accessed 16/10/2024).*

[29] A. J. Heeger, "Semiconducting and metallic polymers: the fourth generation of polymeric materials", *Current Applied Physics* **2001**, *1*, 247–267.

[30] D. Su, Y. Yao, Y. Chen, J. Peng, Z. Liang in *The World Scientific Encyclopedia of Nanomedicine and Bioengineering I*, **2016**, pp. 175–203.

[31] A. H. Malik, F. Habib, M. J. Qazi, M. A. Ganayee, Z. Ahmad, M. A. Yatoo, "A short review article on conjugated polymers", *Journal of Polymer Research* **2023**, *30*, 1–15.

[32] R. W. Miles, G. Zoppi, I. Forbes, "Inorganic photovoltaic cells", *Materials Today* **2007**, *10*, 20–27.

[33] "Best Research-Cell Efficiency, Photovoltaic Research", *National Renewable Energy Laboratory US Department of Energy (https://www.nrel.gov/pv/cell-efficiency.html Accessed 16/10/2024).*

[34] L. Zhu, M. Zhang, J. Xu, C. Li, J. Yan, G. Zhou, W. Zhong, T. Hao, J. Song, X. Xue, Z. Zhou, R. Zeng, H. Zhu, C. C. Chen, R. C. MacKenzie, Y. Zou, J. Nelson, Y. Zhang, Y. Sun, F. Liu, "Single-junction organic solar cells with over 19% efficiency enabled by a refined double-fibril network morphology", *Nature materials* **2022**, *21*, 656–663.

[35] H. Aqoma, S. H. Lee, I. F. Imran, J. H. Hwang, S. H. Lee, S. Y. Jang, "Alkyl ammonium iodide-based ligand exchange strategy for high-efficiency organic-cation perovskite quantum dot solar cells", *Nature Energy 2024 9:3* **2024**, *9*, 324–332.

[36] R. H. Friend, G. J. Denton, J. J. Halls, N. T. Harrison, A. B. Holmes, A. Köhler, A. Lux, S. C. Moratti, K. Pichler, N. Tessler, K. Towns, H. F. Wittmann, "Electronic excitations in luminescent conjugated polymers", *Solid State Communications* **1997**, *102*, 249–258.

[37] C. W. Tang, S. A. Vanslyke, "Organic electroluminescent diodes", *Applied Physics Letters* **1987**, *51*, 913–915.

[38] P. Coghi, C. Coluccini, "Literature review on conjugated polymers as light-sensitive materials for photovoltaic and light-emitting devices in photonic biomaterial applications", *Polymers* **2024**, *16*.

[39] H. Lu, X. Li, Q. Lei, "Conjugated conductive polymer materials and its applications: A mini-review", *Frontiers in Chemistry* **2021**, *9*.

[40] R. H. Friend, R. W. Gymer, A. B. Holmes, J. H. Burroughes, R. N. Marks, C. Taliani, D. D. Bradley, D. A. Dos Santos, J. L. Brédas, M. Lögdlund, W. R. Salaneck, "Electroluminescence in conjugated polymers", *Nature* **1999**, *397*, 121–128.

[41] S. W. Thomas, G. D. Joly, T. M. Swager, "Chemical sensors based on amplifying fluorescent conjugated polymers", *Chemical Reviews* **2007**, *107*, 1339–1386.

[42] W. Wu, G. C. Bazan, B. Liu, "Conjugated-polymer-amplified sensing, imaging, and therapy", *Chem* **2017**, *2*, 760–790.

[43] F. Lv, X. Feng, H. Tang, L. Liu, Q. Yang, S. Wang, "Development of film sensors based on conjugated polymers for copper (II) ion detection", *Advanced Functional Materials* **2011**, *21*, 845–850.

[44] I. W. Thomas, T. M. Swager, "Detection of explosives using amplified fluorescent polymers", *Aspects of Explosives Detection* **2009**, 203–221.

[45] T. N. Nguyen, V. D. Phung, V. V. Tran, "Recent advances in conjugated polymer-based biosensors for virus detection", *Biosensors* **2023**, *13*.

[46] N. A. L. Chenais, M. J. I. Airaghi Leccardi, D. Ghezzi, "Photovoltaic retinal prosthesis restores high-resolution responses to single-pixel stimulation in blind retinas", *Communications Materials* **2021**, *2*, 1–16.

[47] D. Ghezzi, M. R. Antognazza, R. MacCarone, S. Bellani, E. Lanzarini, N. Martino, M. Mete, G. Pertile, S. Bisti, G. Lanzani, F. Benfenati, "A polymer optoelectronic interface restores light sensitivity in blind rat retinas", *Nature Photonics* **2013**, *7*, 400–406.

[48] J. F. Maya-Vetencourt, D. Ghezzi, M. R. Antognazza, E. Colombo, M. Mete, P. Feyen, A. Desii, A. Buschiazzo, M. Di Paolo, S. Di Marco, F. Ticconi, L. Emionite, D. Shmal, C. Marini, I. Donelli, G. Freddi, R. MacCarone, S. Bisti, G. Sambuceti, G. Pertile, G. Lanzani, F. Benfenati, "A fully organic retinal prosthesis restores vision in a rat model of degenerative blindness", *Nature Materials* **2017**, *16*, 681–689.

[49] Z. Li, W. Lu, S. Jia, H. Yuan, L. H. Gao, "Design and application of conjugated polymer nanomaterials for detection and inactivation of pathogenic microbes", *ACS Applied Bio Materials* **2021**, *4*, 370–386.

[50] H. Bai, H. Yuan, C. Nie, B. Wang, F. Lv, L. Liu, S. Wang, "A supramolecular antibiotic switch for antibacterial regulation", *Angewandte Chemie International Edition* **2015**, *54*, 13208–13213.

[51] J. Ndayishimiye, T. Kumeria, A. Popat, J. R. Falconer, M. A. Blaskovich, "Nanomaterials: The new antimicrobial magic bullet", *ACS Infectious Diseases* **2022**, *8*, 693–712.

[52] H. Lin, H. Bai, Z. Yang, Q. Shen, M. Li, Y. Huang, F. Lv, S. Wang, "Conjugated polymers for biomedical applications", *Chem. Commun.* **2022**, *58*, 7232–7244.

[53] C. S. Almeida, I. K. Herrmann, P. D. Howes, M. M. Stevens, "Tailoring cellular uptake of conjugated polymer nanoparticles using modular amphiphilic peptide capping ligands", *Chemistry of Materials* **2015**, *27*, 6879–6889.

[54] L. Han, J. Liu, Z. Wei, Y. Gu, Y. Zhu, L. Chen, X. Zhang, W. Wu, F. He, L. Tian, "Structural morphology changes the fate of semiconducting polymers in afterglow luminescence imaging", *Chemistry of Materials* **2023**, *35*, 6920–6931.

[55] J. Sung, S. Chung, Y. Jang, H. Jang, J. Kim, C. Lee, D. Lee, D. Jeong, K. Cho, Y. S. Kim, J. Kang, W. Lee, E. Lee, "Unveiling the role of side chain for improving nonvolatile characteristics of conjugated polymers-based artificial synapse.", *Advanced science* **2024**, *11*.

[56] V. S. Verma, A. Pandey, A. K. Jha, H. K. R. Badwaik, A. Alexander, Ajazuddin, "Polyethylene glycol–based polymer-drug conjugates: novel design and synthesis strategies for enhanced therapeutic efficacy and targeted drug delivery", *Applied Biochemistry and Biotechnology* **2024**.

[57] A. Moquin, R. Hanna, T. Liang, H. Erguven, E. R. Gran, B. A. Arndtsen, D. Maysinger, A. Kakkar, "PEG-conjugated pyrrole-based polymers: one-pot multicomponent synthesis and self-assembly into soft nanoparticles for drug delivery", *Chem. Commun.* **2019**, *55*, 9829–9832.

[58] H. Omidian, R. L. Wilson, N. Babanejad, "Bioinspired polymers: transformative applications in biomedicine and regenerative medicine", *Life* **2023**, *13*.

[59] C. Liu, X. Li, P. A. Charpentier, W. Z. Xu, H. Guo, "Visible light-responsive all-organic polyurethane antibacterial coatings using a polythiophene derivative", *Colloid and Polymer Science* **2024**.

[60] Z. Huang, T. Yang, J. Yu, Y. Gao, Y. Weng, Y. Huang, S. Li, "Ultra-efficient delivery of CRISPR/Cas9 using ionic liquid conjugated polymers for genome editing-based tumor therapy", *Biomater. Sci.* **2024**, *12*, 1716–1725.

[61] A. K. Pearce, R. K. O'Reilly, "Polymers for biomedical applications: the importance of hydrophobicity in directing biological interactions and application efficacy", *Biomacromolecules* **2021**, *22*, 4459–4469.

[62] N. Biglari, E. N. Zare, "Conjugated polymer-based composite scaffolds for tissue engineering and regenerative medicine", *Alexandria Engineering Journal* **2024**, *87*, 277–299.

[63] F. Xu, X. Chen, Z. Tang, D. Wu, R. Fu, D. Jiang, "Redox-active conjugated microporous polymers: A new organic platform for highly efficient energy storage", *Chemical Communications* **2014**, *50*, 4788–4790.

[64] Y. Yang, X. Zhang, Y. Chen, X. Yang, J. Ma, J. Wang, L. Wang, W. Feng, "Bioinspired color-changing photonic polymer coatings based on three-dimensional blue phase liquid crystal networks", *ACS Applied Materials and Interfaces* **2021**, *13*.

[65] L. Beverina, G. A. Pagani, M. Sassi, "Multichromophoric electrochromic polymers: Colour tuning of conjugated polymers through the side chain functionalization approach", *Chemical Communications* **2014**, *50*, 5413–5430.

[66] X. Liu, M. E. Kleybolte, M. Hantro, C. Butler, S. I. Vagin, C. Dyck, van, M. Fleischauer, J. G. Veinot, B. Rieger, A. Meldrum, "A fluorescent polymer for facile one-step writing of polychromic hidden information in flexible films", *Advanced Functional Materials* **2024**, *2402033*, 1–11.

[67] T. Prechtl, K. Müllen in *Solution-Processable Components for Organic Electronic Devices*, John Wiley & Sons, Ltd, **2019**, Chapter 1, pp. 1–55.

[68] K. Müllen, U. Scherf, "Conjugated polymers: where we come from, where we stand, and where we might go", *Macromolecular Chemistry and Physics* **2023**, *224*, 1–15.

[69] R. Mabindisa, K. Tambwe, L. McIteka, N. Ross, "Organic nanostructured materials for sustainable application in next generation solar cells", *Applied Sciences* **2021**, *11*.

[70] C. A. Thomas, K. Zong, K. A. Abboud, P. J. Steel, J. R. Reynolds, "Donor-mediated band gap reduction in a homologous series of conjugated polymers", *Journal of the American Chemical Society* **2004**, *126*, 16440–16450.

[71] Z. G. Zhang, J. Wang, "Structures and properties of conjugated Donor-Acceptor copolymers for solar cell applications", *Journal of Materials Chemistry* **2012**, *22*, 4178–4187.

[72] M. C. Scharber, N. S. Sariciftci, "Low band gap conjugated semiconducting polymers", *Advanced Materials Technologies* **2021**, *6*.

[73] B. C. Thompson, Y.-G. Kim, J. Reynolds, "Spectral Broadening in MEH-PPV:PCBM-Based Photovoltaic Devices via Blending with a Narrow Band Gap Cyanovinylene-Dioxythiophene Polymer Barry", *Macromolecules* **2005**, *38*, 5359.

[74] Y. J. Kim, N. K. Kim, W. T. Park, C. Liu, Y. Y. Noh, D. Y. Kim, "Kinetically controlled crystallization in conjugated polymer films for high-performance organic field-effect transistors", *Advanced Functional Materials* **2019**, *29*, 1–9.

[75] H. Sirringhaus, "Device physics of solution-processed organic field-effect transistors", *Advanced Materials* **2005**, *17*, 2411–2425.

[76] Y. Huang, J. Xing, Q. Gong, L. C. Chen, G. Liu, C. Yao, Z. Wang, H. L. Zhang, Z. Chen, Q. Zhang, "Reducing aggregation caused quenching effect through co-assembly of PAH chromophores and molecular barriers", *Nature Communications* **2019**, *10*, 1–9.

[77] S. J. Lou, J. M. Szarko, T. Xu, L. Yu, T. J. Marks, L. X. Chen, "Effects of additives on the morphology of solution phase aggregates formed by active layer components of high-efficiency organic solar cells", *Journal of the American Chemical Society* **2011**, *133*, 20661–20663.

[78] A. B. Walker, "Multiscale modeling of charge and energy transport in organic light-emitting diodes and photovoltaics", *Proceedings of the IEEE* **2009**, *97*, 1587–1596.

[79] Y. Park, J. Jung, M. Chang, "Research progress on conducting polymer-based biomedical applications", *Applied Sciences* **2019**, *9*.

[80] F. Lin, Q. Y. Duan, F. G. Wu, "Conjugated polymer-based photothermal therapy for killing microorganisms", *ACS Applied Polymer Materials* **2020**, *2*, 4331–4344.

[81] Q. Long, W. Xi, Y. Chen, L. Xu, Z. Xu, Y. Zhu, J. Guo, "Biometabolizable conjugated polymers for photothermal therapy under the guidance of dual-modal imaging of prostate cancer", *ACS Applied Polymer Materials* **2022**, *4*, 4355–4363.

[82] T. W. Hagler, K. Pakbaz, K. F. Voss, A. J. Heeger, "Enhanced order and electronic delocalization in conjugated polymers oriented by gel processing in polythylene", *Physical Review B* **1991**, *44*.

[83] T. Prechtl, K. Müllen, "Precision and purity of conjugated polymers - to be ensured before processing", *Solution-Processable Components for Organic Electronic Devices* **2019**, 1–55.

[84] E. Condon, "A theory of intensity distribution in band systems", *Physical Review* **1926**, *28*, 1182–1201.

[85] J. Franck, E. Dymond, "Elementary process of photochemical reactions", *Transactions of the Faraday Society* **1926**, *21*.

[86] M. Kasha, "Characterization of electronic transitions in complex molecules", *Discuss. Faraday Soc.* **1950**, *9*, 14–19.

[87] J. R. Lakowicz, *Principles of fluorescence spectroscopy,* **2006**, p. 954.

[88] Y. V. Romanovskii, A. Gerhard, B. Schweitzer, U. Scherf, R. I. Personov, H. Bässler, "Phosphorescence of π-conjugated oligomers and polymers", *Physical Review Letters* **2000**, *84*, 1027–1030.

[89] T.-H. Le, H. Yoon in *Conjugated polymer nanostructures for energy conversion and storage applications*, Wiley, **2021**, Chapter 1, pp. 1–42.

[90] W. J. Feast, J. Tsibouklis, K. L. Pouwer, L. Groenendaal, E. W. Meijer, "Synthesis, processing and material properties of conjugated polymers", *Polymer* **1996**, *37*, 5017–5047.

[91] M. Stępień, E. Gońka, M. Żyła, N. Sprutta, "Heterocyclic nanographenes and other polycyclic heteroaromatic compounds: synthetic routes, properties, and applications", *Chemical Reviews* **2017**, *117*, 3479–3716.

[92] F. Liu, Z. Chen, X. Du, Q. Zeng, T. Ji, Z. Cheng, G. Jin, B. Yang, "High efficiency aqueous-processed MEH-PPV/CdTe hybrid solar cells with a PCE of 4.20%", *Journal of Materials Chemistry A* **2016**, *4*, 1105–1111.

[93] H. Bässler, B. Schweitzer, "Site-selective fluorescence spectroscopy of conjugated polymers and oligomers", *Accounts of Chemical Research* **1999**, *32*, 173–182.

[94] G. Mao, J. E. Fischer, F. E. Karasz, M. J. Winokur, "Nonplanarity and ring torsion in poly(p-phenylene vinylene). A neutron-diffraction study", *The Journal of Chemical Physics* **1993**, *98*, 71–77.

[95] S. Heunt, R. F. Mahrtt, A. Greinert, U. Lemmeri, H. Bssleri, D. A. Halliday, D. D. C. Bradley, P. L. Bums, A. B. Holmes, "Conformational effects in poly(p-phenylene vinylene)s revealed by low-temperature site- selective fluorescence", *Journal of Physics Condensed Matter* **1993**, *5*, 247–260.

[96] M. M. Faleiros, P. B. Miranda, "Photoluminescence of MEH-PPV with ultraviolet excitation", *Synthetic Metals* **2010**, *160*, 2409–2412.

[97] S. J. Martin, J. M. Lupton, I. D. Samuel, A. B. Walker, "Modelling temperature-dependent current-voltage characteristics of an MEH-PPV organic light emitting device", *Journal of Physics Condensed Matter* **2002**, *14*, 9925–9933.

[98] S. Liu, J. Wang, L. Wang, X. Wang, X. Zhou, J. Wang, "Polarized and blue-shifted fluorescent MEH-PPV@MOF synthesized via direct chain-introduction", *Polymer Testing* **2022**, *111*, 107609.

[99] T. Q. Nguyen, V. Doan, B. J. Schwartz, "Conjugated polymer aggregates in solution: Control of interchain interactions", *Journal of Chemical Physics* **1999**, *110*, 4068–4078.

[100] K. H. Ibnaouf, "Laser from external energy transfer of MEH–PPV conjugated polymer", *Optics & Laser Technology* **2012**, *44*, 710–713.

[101] A. N. Aleshin, E. L. Alexandrova, I. P. Shcherbakov, "Hybrid active layers from a conjugated polymer and inorganic nanoparticles for organic light emitting devices with emission colour tuned by electric field", *Journal of Physics D: Applied Physics* **2009**, *42*.

[102] A. H. Reshak, M. M. Shahimin, N. Juhari, R. Vairavan, "Photovoltaic characteristics of hybrid MEH-PPV-nanoparticles compound", *Current Applied Physics* **2013**, *13*, 1894–1898.

[103] G. Yu, J. Gao, J. C. Hummelen, F. Wudl, A. J. Heeger, "Polymer photovoltaic cells: enhanced efficiencies via a network of internal donor-acceptor heterojunctions", *Science* **1995**, *270*, 1789–1791.

[104] Z. E. Lampert, S. E. Lappi, J. M. Papanikolas, C. Lewis Reynolds, M. Osama Aboelfotoh, "Morphology and chain aggregation dependence of optical gain in thermally annealed films of the conjugated polymer poly[2-methoxy-5-(2'-ethylhexyloxy)-p-phenylene vinylene]", *Journal of Applied Physics* **2013**, *113*.

[105] T. Huser, M. Yan, L. J. Rothberg, "Single chain spectroscopy of conformational dependence of conjugated polymer photophysics", *Proceedings of the National Academy of Sciences of the United States of America* **2000**, *97*, 11187–11191.

[106] E. K. Miller, D. Yoshida, C. Y. Yang, A. J. Heeger, "Polarized ultraviolet absorption of highly oriented poly(2-methoxy, 5-(2'-ethyl-hexyloxy) paraphenylene vinylene)", *Physical Review B* **1999**, *59*, 4661–4664.

[107] K. Kanemoto, I. Akai, M. Sugisaki, H. Hashimoto, T. Karasawa, N. Negishi, Y. Aso, "Temperature effects on quasi-isolated conjugated polymers as revealed by temperature-dependent optical spectra of 16-mer oligothiophene diluted in a sold matrix", *Journal of Chemical Physics* **2009**, *130*, 1–8.

[108] Z. F. Yao, Z. Y. Wang, H. T. Wu, Y. Lu, Q. Y. Li, L. Zou, J. Y. Wang, J. Pei, "Ordered solid-state microstructures of conjugated polymers arising from solution-state aggregation", *Angewandte Chemie - International Edition* **2020**, *59*, 17467–17471.

[109] R. Liu, Y. Li, K. P. Seah, B. Liu, N. Tomczak, "Morphologically induced polychromism of MEH-PPV nanoparticles prepared using amphiphilic comb-polymer as encapsulation matrix", *European Polymer Journal* **2014**, *50*, 46–53.

[110] J. D. Milward, M. Marcus, A. Köhler, W. Barford, "Extracting structural information from MEH-PPV optical spectra", *Journal of Chemical Physics* **2018**, *149*.

[111] A. Köhler, S. T. Hoffmann, H. Bässler, "An order-disorder transition in the conjugated polymer MEH-PPV", *Journal of the American Chemical Society* **2012**, *134*, 11594–11601.

[112] H. Yamagata, N. J. Hestand, F. C. Spano, A. Köhler, C. Scharsich, S. T. Hoffmann, H. Bässler, "The red-phase of poly[2-methoxy-5-(2-ethylhexyloxy)- 1,4-phenylenevinylene] (MEH-PPV): A disordered HJ-aggregate", *Journal of Chemical Physics* **2013**, *139*.

[113] D. Tuncel, "π-Conjugated nanostructured materials: Preparation, properties and photonic applications", *Nanoscale Advances* **2019**, *1*, 19–33.

[114] A. Ghosh, B. B. Jana, S. Chakraborty, S. Maiti, B. B. Jana, H. N. Ghosh, A. Patra, "Exciton dynamics and formation mechanism of MEH-PPV polymer-based nanostructures", *Journal of Physical Chemistry C* **2017**, *121*, 21062–21072.

[115] S. Kumar, P. K. Yadav, P. Maiti, "Renewable cathode materials dependent on conjugated polymer composite systems", *Conjugated Polymers for Next-Generation Applications Volume 2: Energy Storage Devices* **2022**, 55–90.

[116] G. Sharma, S. Kattayat, S. Faheem Naqvi, S. Z. Hashmi, P. A. Alvi, "Role of MEH:PPV polymer in single layer OLEDs with its optoelectronic characteristics", *Materials Today: Proceedings* **2019**, *42*, 1678–1681.

[117] F. Abbassi, M. Mbarek, M. Almoneef, K. Alimi, "Photophysical properties of the PVK-MEH-PPV/PCBM composite for organic solar cells application: synthesis, characterization and computational study", *Polymers* **2021**, *13*.

[118] Y. Kwon, L. J. Kaufman, "Nearly isotropic conjugated polymer aggregates with efficient local exciton diffusion", *Journal of Physical Chemistry C* **2019**, *123*, 29418–29426.

[119] S. Quan, F. Teng, Z. Xu, L. Qian, Y. Hou, Y. Wang, X. Xu, "Solvent and concentration effects on fluorescence emission in MEH-PPV solution", *European Polymer Journal* **2006**, *42*, 228–233.

[120] A. C. Ribeiro, H. S. Camargo, D. H. Pereira, R. Custódio, T. D. Martins, "Photoluminescence of solvent-selected fluorescent moieties in MEH-PPV solutions and films", *Journal of the Brazilian Chemical Society* **2018**, *29*, 543–559.

[121] R. Traiphol, P. Sanguansat, T. Srikhirin, T. Kerdcharoen, T. Osotchan, "Spectroscopic study of photophysical change in collapsed coils of conjugated polymers: Effects of solvent and temperature", *Macromolecules* **2006**, *39*, 1165–1172.

[122] B. J. Schwartz, "Conjugated polymers as molecular materials: how chain conformation and film morphology influence energy transfer and interchain interactions", *Annual Review of Physical Chemistry* **2003**, *54*, 141–172.

[123] S. R. Amrutha, M. Jayakannan, "Probing the π-stacking induced molecular aggregation in π-conjugated polymers", *Journal of Physical Chemistry B* **2008**, *112*, 1119–1129.

[124] X. L. Fan, H. Y. Li, W. Y. Ye, M. Q. Zhao, D. Huang, Y. Fang, B. Q. Zhou, K. F. Ren, J. Ji, G. S. Fu, "Magainin-modified polydopamine nanoparticles for photothermal killing of bacteria at low temperature", *Colloids Surf. B* **2019**, *183*, 110423.

[125] E. J. Harbron, C. M. Davis, J. K. Campbell, R. M. Allred, M. T. Kovary, N. J. Economou, "Photochromic dye-doped conjugated polymer nanoparticles: photomodulated emission and nanoenvironmental characterization", *Journal of Physical Chemistry C* **2009**, *113*, 13707–13714.

[126] R. F. Cossiello, L. Akcelrud, T. D. Atvars, "Solvent and molecular weight effects on fluorescence emission of MEH-PPV", *Journal of the Brazilian Chemical Society* **2005**, *16*, 74–86.

[127] R. F. Cossiello, M. D. Susman, P. F. Aramendía, T. D. Atvars, "Study of solvent-conjugated polymer interactions by polarized spectroscopy: MEH-PPV and Poly(9,9'-dioctylfluorene-2,7-diyl)", *Journal of Luminescence* **2010**, *130*, 415–423.

[128] B. Kruczek, "Effect of solvent on properties of solution-cast dense SPPO films", *Journal of Applied Polymer Science* **2003**, *88*, 1100–1110.

[129] R. Kline, M. D. McGehee, E. N. Kadnikova, J. Liu, J. M. J. Fréchet, M. F. Toney, "Dependence of regioregular poly(3-hexylthiophene) film morphology and field-effect mobility on molecular weight", *Macromolecules* **2005**, *38*, 3312–3319.

[130] E. H. Kwon, G. W. Kim, M. Kim, Y. D. Park, "Effect of alcohol polarity on the aggregation and film-forming behaviors of poly(3-hexylthiophene)", *ACS Applied Polymer Materials* **2020**, *2*, 2980–2986.

[131] B. A. Weir, E. A. Marseglia, S. M. Chang, A. B. Holmes, "Changes in structure and morphology in the conjugated polymer meh-ppv", *Synthetic Metals* **1999**, *101*, 154–155.

[132] M. C. Chen, W. C. Hung, A. C. Su, S. H. Chen, S. A. Chen, "Nanoscale ordered structure distribution in thin solid film of conjugated polymers: Its significance in charge transport across the film and in performance of electroluminescent device", *Journal of Physical Chemistry B* **2009**, *113*, 11124–11133.

[133] M. Brinkmann, "Structure and Morphology Control in Thin Films of Regioregular Poly (3-hexylthiophene)", **2011**, 1218–1233.

[134] P. Wang, L. Lwu, D. Zhang, H. Q. Zhang, "Effect of chain conformation on micro-mechanical behaviour of MEH-PPV thin film", *Bulletin of Materials Science* **2013**, *36*, 833–837.

[135] J. P. Ferrance, K. E. Meissner, J. W. Pettit, "Solvent effects on the electrical and optical properties of composite carbon nanotube/MEH-PPV films", *Journal of Nanoparticle Research* **2010**, *12*, 405–415.

[136] O. P. Dimitriev, "Dynamics of Excitons in Conjugated Molecules and Organic Semiconductor Systems", *Chemical Reviews* **2022**, DOI `10.1021/acs.chemrev.1c00648`.

[137] E. L. Read, H. Lee, G. R. Fleming, "Photon echo studies of photosynthetic light harvesting", *Photosynthesis Research* **2009**, *101*, 233–243.

[138] G. D. Scholes, D. S. Larsen, G. R. Fleming, G. Rumbles, "Origin of line broadening in the electronic absorption spectra of conjugated polymers: Three-pulse-echo studies of MEH-PPV in toluene", *Physical Review B* **2000**, *61*, 13670–13678.

[139] T. E. Dykstra, V. Kovalevskij, X. Yang, G. D. Scholes, "Excited state dynamics of a conformationally disordered conjugated polymer: A comparison of solutions and film", *Chemical Physics* **2005**, *318*, 21–32.

[140] T. E. Dykstra, E. Hennebicq, D. Beljonne, J. Gierschner, G. Claudio, E. R. Bittner, J. Knoester, G. D. Scholes, "Conformational disorder and ultrafast exciton relaxation in PPV-family conjugated polymers", *Journal of Physical Chemistry B* **2009**, *113*, 656–667.

[141] J. Sperling, A. Nemeth, P. Baum, F. Šanda, E. Riedle, H. F. Kauffmann, S. Mukamel, F. Milota, "Exciton dynamics in a disordered conjugated polymer: Three-pulse photon-echo and transient grating experiments", *Chemical Physics* **2008**, *349*, 244–249.

[142] N. P. Wells, D. A. Blank, "Correlated exciton relaxation in poly(3-hexylthiophene)", *Physical Review Letters* **2008**, *100*, 1–4.

[143] P. Nuernberger, S. Ruetzel, T. Brixner, "Multidimensional electronic spectroscopy of photochemical reactions", *Angewandte Chemie - International Edition* **2015**, *54*, 11368–11386.

[144] S. Roeding, T. Brixner, "Coherent two-dimensional electronic mass spectrometry", *Nature Communications* **2018**, *9*, 1–9.

[145] A. De Sio, F. Troiani, M. Maiuri, J. Réhault, E. Sommer, J. Lim, S. F. Huelga, M. B. Plenio, C. A. Rozzi, G. Cerullo, E. Molinari, C. Lienau, "Tracking the coherent generation of polaron pairs in conjugated polymers", *Nature Communications* **2016**, *7*, 1–8.

[146] C. Consani, F. Koch, F. Panzer, T. Unger, A. Köhler, T. Brixner, "Relaxation dynamics and exciton energy transfer in the low-temperature phase of MEH-PPV", *Journal of Chemical Physics* **2015**, *142*, 1–11.

[147] A. Ruseckas, P. Wood, I. D. Samuel, G. R. Webster, W. J. Mitchell, P. L. Burn, V. Sundström, "Ultrafast depolarization of the fluorescence in a conjugated polymer", *Physical Review B - Condensed Matter and Materials Physics* **2005**, *72*, 1–5.

[148] G. Lanzani, G. Cerullo, D. Polli, A. Gambetta, M. Zavelani-Rossi, C. Gadermaier, "Photophysics of conjugated polymers: The contribution of ultrafast spectroscopy", *Physica Status Solidi (A) Applied Research* **2004**, *201*, 1116–1131.

[149] C. Gadermaier, G. Lanzani, "Photophysics of conjugated polymers: The contribution of ultrafast spectroscopy", *J. Phys.: Condens.Matter* **2002**, 9785–9802.

[150] F. Montilla, L. M. Frutos, C. R. Mateo, R. Mallavia, "Fluorescence emission anisotropy coupled to an electrochemical system: Study of exciton dynamics in conjugated polymers", *Journal of Physical Chemistry C* **2007**, *111*, 18405–18410.

[151] D. Thomsson, H. Lin, I. G. Scheblykin, "Correlation analysis of fluorescence intensity and fluorescence anisotropy fluctuations in single-molecule spectroscopy of conjugated polymers", *ChemPhysChem* **2010**, *11*, 897–904.

[152] G. La Rocca, "Wannier–Mott excitons in semiconductors", **2003**, *31*, 97–128.

[153] S. Giannini, W. T. Peng, L. Cupellini, D. Padula, A. Carof, J. Blumberger, "Exciton transport in molecular organic semiconductors boosted by transient quantum delocalization", *Nature Communications* **2022**, *13*, 1–13.

[154] R. S. Knox, "Exciton states in rare-gas crystals", *Journal of Physics and Chemistry of Solids* **1959**, *9*, 238–264.

[155] T. Nematiaram, D. Padula, A. Troisi, "Bright Frenkel excitons in molecular crystals: a survey", *Chemistry of Materials* **2021**, *33*, 3368–3378.

[156] M. Kuwata-Gonokami, "High-density excitons in semiconductors", *Comprehensive Semiconductor Science and Technology* **2011**, *1-6*, 213–255.

[157] G. H. Wannier, "The structure of electronic excitation levels in insulating crystals", *Physical Review* **1937**, *52*, 191–197.

[158] N. F. Mott, "Conduction in polar crystals. II. The conduction band and ultra-violet absorption of alkali-halide crystals", *Trans. Faraday Soc.* **1938**, *34*, 500–506.

[159] M. Ueta, H. Kanzaki, K. Kobayashi, E. Toyozawa Y Hanamura, *Excitonic processes in solids*, *Vol. 60*, 1st ed., (Ed.: P. Fulde), Springer, Tokyo, **1986**.

[160] J. Frenkel, "On the transformation of light into heat in solids. I", *Physical Review* **1931**, *37*, 17–44.

[161] J. Frenkel, "On the transformation of light into heat in solids II", *Physical Review* **1931**, *37*.

[162] K. W. Böer, U. W. Pohl, *Semiconductor physics*, **2018**, pp. 486–521.

[163] J. W. Zha, M. S. Zheng, B. H. Fan, Z. M. Dang, "Polymer-based dielectrics with high permittivity for electric energy storage: A review", *Nano Energy* **2021**, *89*, 106438.

[164] Y. Tamai, H. Ohkita, H. Benten, S. Ito, "Exciton Diffusion in Conjugated Polymers: From Fundamental Understanding to Improvement in Photovoltaic Conversion Efficiency", *Journal of Physical Chemistry Letters* **2015**, *6*, 3417–3428.

[165] M. Combescot, W. Pogosov, "Microscopic derivation of Frenkel excitons in second quantization", *Physical Review B - Condensed Matter and Materials Physics* **2008**, *77*, 1–16.

[166] W. Barford, "Excitons in conjugated polymers: A tale of two particles", *Journal of Physical Chemistry A* **2013**, *117*, 2665–2671.

[167] H. Schweitzer Bernd Bassler, "Excitons in conjugated polymers", *Synthetic Metals* **2000**, *109*, 1–6.

[168] G. Tirimbò, B. Baumeier, "Ab initio modeling of excitons: from perfect crystals to biomaterials", *Advances in Physics: X* **2021**, *6*.

[169] M. Y. Lavrentiev, W. Barford, S. J. Martin, H. Daly, R. J. Bursill, "A theoretical investigation of the low lying electronic structure of poly(p-phenylene vinylene)", **1999**, 1–19.

[170] W. Barford, M. Marcus, "Perspective: Optical spectroscopy in π-conjugated polymers and how it can be used to determine multiscale polymer structures", *Journal of Chemical Physics* **2017**, *146*, DOI `10.1063/1.4979495`.

[171] W. Barford, D. Trembath, "Exciton localization in polymers with static disorder", *Physical Review B - Condensed Matter and Materials Physics* **2009**, *80*, 1–12.

[172] P. W. Anderson, "Absence of diffusion in certain random lattices", *Physical Review* **1958**, *109*, 80–93.

[173] P. A. Lee, T. V. Ramakrishnan, "Disordered electronic systems", *Reviews of Modern Physics* **1985**, *57*, 287–337.

[174] O. R. Tozer, W. Barford, "Localization of large polarons in the disordered Holstein model", *Physical Review B - Condensed Matter and Materials Physics* **2014**, *89*, 1–7.

[175] W. Barford, I. Boczarow, T. Wharram, "Ultrafast dynamical localization of photoexcited states in conformationally disordered poly(p -phenylenevinylene)", *Journal of Physical Chemistry A* **2011**, *115*, 9111–9119.

[176] I. Avgin, D. L. Huber, "Excitons in disordered polymers", **2007**, *123*, 389–392.

[177] H. Yamagata, F. C. Spano, "Vibronic coupling in quantum wires: Applications to polydiacetylene", *Journal of Chemical Physics* **2011**, *135*.

[178] D. V. Makhov, W. Barford, "Local exciton ground states in disordered polymers", *Physical Review B - Condensed Matter and Materials Physics* **2010**, *81*, 1–6.

[179] O. R. Tozer, W. Barford, "Exciton Dynamics in Disordered Poly (p - phenylenevinylene). 1 . Ultrafast Interconversion and Dynamical Localization", **2012**, DOI 10.1021/jp307040d.

[180] A. V. Malyshev, V. A. Malyshev, "Statistics of low-energy levels of a one-dimensional weakly localized Frenkel exciton: A numerical study", *Physical Review B - Condensed Matter and Materials Physics* **2001**, *63*, 1–8.

[181] A. V. Malyshev, V. A. Malyshev, "Level and wave function statistics of a localized 1D Frenkel exciton at the bottom of the band", *Journal of Luminescence* **2001**, *94-95*, 369–372.

[182] L. Simine, P. J. Rossky, "Relating chromophoric and structural disorder in conjugated polymers", *Journal of Physical Chemistry Letters* **2017**, *8*, 1752–1756.

[183] O. R. Tozer, W. Barford, "Intrachain exciton dynamics in conjugated polymer chains in solution", *Journal of Chemical Physics* **2015**, *143*.

[184] M. Hoffmann, Z. G. Soos, "Optical absorption spectra of the Holstein molecular crystal for weak and intermediate electronic coupling", *Physical Review B - Condensed Matter and Materials Physics* **2002**, *66*, 243051–2430518.

[185] T. Holstein, "Studies of polaron motion. Part I. The molecular-crystal model", *Annals of Physics* **1959**, *8*, 325–342.

[186] G. D. Mahan, *Many-particle physics*, Springer, **2000**.

[187] W. Barford, M. Marcus, "Theory of optical transitions in conjugated polymers. I. Ideal systems", *Journal of Chemical Physics* **2014**, *141*, DOI 10.1063/1.4897984.

[188] M. Marcus, O. R. Tozer, W. Barford, "Theory of optical transitions in conjugated polymers . II . Real systems", *Journal of Chemical Physics* **2014**, *141*.

[189] K. Huang, A. Rhys, *Theory of light absorption and non-radiative transitions in F-centres*, **1950**, pp. 74–92.

[190] A. Köhler, H. Bässler, *Electronic processes in organic semiconductors*, Wiley-VCH Verlag, Weinheim, Germany, **2015**.

[191] J. Cornil, D. Beljonne, C. M. Heller, I. H. Campbell, B. K. Laurich, D. L. Smith, D. D. Bradley, K. Müllen, J. L. Brédas, "Photoluminescence spectra of oligo-paraphenylenevinylenes: A joint theoretical and experimental characterization", *Chemical Physics Letters* **1997**, *278*, 139–145.

[192] Z. Shuai, J. L. Brédas, W. P. Su, "Nature of photoexcitations in poly (paraphenylene vinylene) and its oligomers", *Chemical Physics Letters* **1994**, *228*, 301–306.

[193] Z. Shuai, J. L. Brédas, "Relaxation of the first Bu excited state in linear polyenes: From trans-butadiene to polyacetylene", *The Journal of Chemical Physics* **1992**, *97*, 5970–5976.

[194] J. Yu, M. Hayashi, S. H. Lin, K. K. Liang, J. H. Hsu, W. S. Fann, C. I. Chao, K. R. Chuang, S. A. Chen, "Temperature effect on the electronic spectra of poly(p-phenylenevinylene)", *Synthetic Metals* **1996**, *82*, 159–166.

[195] W. Barford, M. Marcus, O. R. Tozer, "Polarons in π-conjugated polymers: Anderson or Landau?", *Journal of Physical Chemistry A* **2016**, *120*, 615–620.

[196] O. Kühn, V. Sundström, "Pump–probe spectroscopy of dissipative energy transfer dynamics in photosynthetic antenna complexes: A density matrix approach", *The Journal of Chemical Physics* **1997**, *107*, 4154–4164.

[197] C. Smyth, F. Fassioli, G. D. Scholes, "Measures and implications of electronic coherence in photosynthetic light-harvesting", *Philosophical Transactions of the Royal Society A: Mathematical Physical and Engineering Sciences* **2012**, *370*, 3728–3749.

[198] J. R. Mannouch, W. Barford, S. Al-Assam, "Ultra-fast relaxation, decoherence, and localization of photoexcited states in π -conjugated polymers", *Journal of Chemical Physics* **2018**, *148*, 1–16.

[199] W. Barford, "Exciton dynamics in conjugated polymer systems", *Frontiers in Physics* **2022**, *10*, 1–22.

[200] W. Barford, J. R. Mannouch, "Torsionally induced exciton localization and decoherence in π -conjugated polymers", *Journal of Chemical Physics* **2018**, *149*, 214107.

[201] W. Barford, E. R. Bittner, A. Ward, "Exciton dynamics in disordered poly(p-phenylenevinylene). 2. Exciton diffusion", *Journal of Physical Chemistry A* **2012**, *116*, 10319–10327.

[202] M. Baibakov, S. Patra, J. B. Claude, A. Moreau, J. Lumeau, J. Wenger, "Extending single-molecule Förster resonance energy transfer (FRET) range beyond 10 nanometers in zero-mode waveguides", *ACS Nano* **2019**, *13*, 8469–8480.

[203] A. Rose, J. D. Tovar, S. Yamaguchi, E. E. Nesterov, Z. Zhu, T. M. Swager, "Energy migration in conjugated polymers: The role of molecular structure", *Philosophical Transactions of the Royal Society A: Mathematical Physical and Engineering Sciences* **2007**, *365*, 1589–1606.

[204] I. Hwang, G. D. Scholes, "Electronic energy transfer and quantum-coherence in π-conjugated polymers", *Chemistry of Materials* **2011**, *23*, 610–620.

[205] T. Förster, "Zwischenmolekulare Energiewanderung und Fluoreszenz", *Annalen der Physik* **1948**, *437*, 55–75.

[206] W. Barford, O. R. Tozer, "Theory of exciton transfer and diffusion in conjugated polymers", *Journal of Chemical Physics* **2014**, *141*, DOI 10.1063/1.4897986.

[207] A. Messiah, *Quantum mechanics*, 2nd, Dover Publications, New York, **2014**.

[208] W. Barford, "Exciton transfer integrals between polymer chains", *Journal of Chemical Physics* **2007**, *126*, DOI 10.1063/1.2714516.

[209] D. Beljonne, J. Cornil, R. Silbey, P. Millié, J. L. Brédas, "Interchain interactions in conjugated materials: The exciton model versus the supermolecular approach", *Journal of Chemical Physics* **2000**, *112*, 4749–4758.

[210] H. Haken, P. Reineker, "The coupled coherent and incoherent motion of excitons and its influence on the line shape of optical absorption", *Zeitschrift für Physik* **1972**, *249*, 253–268.

[211] R. M. Clegg, *Chapter 1 Förster resonance energy transfer-FRET what is it, why do it, and how it's done*, *Vol. 33*, 1st ed., Elesvier B.V., **2009**, pp. 1–57.

[212] F. Iachello, M. Ibrahim, "Analytic and algebraic evaluation of Franck-Condon overlap integrals", *Journal of Physical Chemistry A* **1998**, *102*, 9427–9432.

[213] G. Gangopadhyay, "A generating function for the product of the Laguerre polynomials: Franck-Condon factor for multiphoton processes", *Journal of Physics A: Mathematical and General* **1998**, *31*.

[214] O. Tozer, "Exciton Dynamics in Disordered Conjugated Polymers", PhD thesis, University of Oxford, Oxford, UK, **2016**.

[215] M. Marcus, J. D. Milward, A. Köhler, W. Barford, "Structural information for conjugated polymers from optical modeling", *Journal of Physical Chemistry A* **2018**, *122*, 3621–3625.

[216] J. R. Lakowicz, *Principles of fluorescence spectroscopy*, Boston, MA, **2006**.

[217] A. Jablonski, "On the notation of emission anisotropy", *Bull Acad Polon Sci Ser Sci Math Astr et Phys* **1960**, *6*, 259–264.

[218] L. L. Chapoy, D. B. DuPré, "Polarized fluorescent emission in uniaxial liquid crystals. The effect of intramolecular energy transfer and rotational Brownian motion on measurements of the orientational distribution function", *The Journal of Chemical Physics* **1978**, *69*, 519–524.

[219] D. W. Piston, T. Bilash, E. Gratton, "Compartmental analysis approach to fluorescence anisotropy: Perylene in viscous solvents", *Journal of Physical Chemistry* **1989**, *93*, 3963–3967.

[220] K. Sahu, S. K. Mondal, S. Ghosh, D. Roy, K. Bhattacharyya, "Temperature dependence of solvation dynamics and anisotropy decay in a protein: ANS in bovine serum albumin", *Journal of Chemical Physics* **2006**, *124*.

[221] G. Mocz, "Information content of fluorescence polarization and anisotropy", *Journal of Fluorescence* **2006**, *16*, 511–524.

[222] M. Ameloot, M. vandeVen, A. Ulises Acuña, B. Valeur, "Fluorescence anisotropy measurements in solution: Methods and reference materials (IUPAC Technical Report)", *Pure and Applied Chemistry* **2013**, *85*, 589–608.

[223] W. Becker, *Advanced time-correlated single photon counting applications*, **2015**.

[224] I. Gonzalvez Perez, W. Barford, "Ultrafast fluorescence depolarization in conjugated polymers", *Journal of Physical Chemistry Letters* **2021**, *12*, 5344–5348.

[225] J. Mannouch, "Exciton Dynamics in π -Conjugated Polymer Systems", PhD thesis, **2019**.

[226] J. C. Tully, "Molecular dynamics with electronic transitions", *The Journal of Chemical Physics* **1990**, *93*, 1061–1071.

[227] J. C. Tully, "Perspective: Nonadiabatic dynamics theory", *Journal of Chemical Physics* **2012**, *137*, DOI 10.1063/1.4757762.

[228] J. R. Mannouch, A. Kelly, "Towards a correct description of initial electronic coherence in nonadiabatic dynamics simulations", *Journal of Physical Chemistry Letters* **2024**, *15*, 11687–11695.

[229] M. H. Beck, A. Jäckle, G. A. Worth, H. D. Meyer, "The multiconfiguration time-dependent Hartree (MCTDH) method: A highly efficient algorithm for propagating wavepackets", *Physics Report* **2000**, *324*, 1–105.

[230] S. R. White, "Density matrix formulation for quantum renormalization groups", *Physical Review Letters* **1992**, *69*, 2863–2866.

[231] I. P. McCulloch, "From density-matrix renormalization group to matrix product states", *Journal of Statistical Mechanics: Theory and Experiment* **2007**, *10014*.

[232] G. Vidal, "Efficient classical simulation of slightly entangled quantum computations", *Physical Review Letters* **2003**, *91*, 1–4.

[233] S. Rommer, S. Östlund, "Thermodynamic limit of density matrix renormalization", *Physical Review Letters* **1995**, *75*, 3537–3540.

[234] G. Vidal, "Efficient simulation of one-dimensional quantum many-body systems", *Physical Review Letters* **2004**, *93*, 1–4.

[235] U. Schollwöck in *Strongly correlated systems*, (Eds.: A. Adolfo, F. Mancini), Springer, **2013**, pp. 67–98.

[236] U. Schollwöck, "The density-matrix renormalization group in the age of matrix product states", *Annals of Physics* **2011**, *326*, 96–192.

[237] E. Schrödinger, "Der stetige Übergang von der Mikro- zur Makromechanik", *Naturwissenschaften* **1926**, *14*, 664–666.

[238] S. R. White, A. E. Feiguin, "Real-time evolution using the density matrix renormalization group", *Physical Review Letters* **2004**, *93*, 2–5.

[239] T. Becker, C. Netzer, A. Eckardt, "Quantum trajectories for time-local non-Lindblad master equations", *Phys. Rev. Lett.* **2023**, *131*, 160401.

[240] V. Gorini, A. Kossakowski, E. C. Sudarshan, "Completely positive dynamical semigroups of N-level systems", *Journal of Mathematical Physics* **1975**, *17*, 821–825.

[241] G. Lindblad, "On the generators of quantum dynamical semigroups", *Communications in Mathematical Physics* **1976**, *48*, 119–130.

[242] N. Gisin, "Quantum measurements and stochastic processes", *Physical Review Letters* **1984**, *52*, 1657–1660.

[243] H. J. Carmichael, *An Open Systems Approach to Quantum Optics (Lectures Presented at Universite Libre de Bruxelles), Vol. 828*, 1st ed., Springer-Verlag Berlin, Heidelberg, **1993**.

[244] K. Mølmer, Y. Castin, J. Dalibard, "Monte Carlo wave-function method in quantum optics", *Journal of the Optical Society of America B* **1993**, *10*, 524.

[245] D. Jean, C. Yvan, M. Klaus, "Wave-function approach to dissipative processes in quantum optics", *Physical Review Letters* **1992**, *68*, 580–583.

[246] F. S. Sehdaran, M. Bina, C. Benedetti, M. G. Paris, "Quantum probes for ohmic environments at thermal equilibrium", *Entropy* **2019**, *21*, 1–11.

[247] A. J. Daley, "Quantum trajectories and open many-body quantum systems", *Advances in Physics* **2014**, *63*, 77–149.

[248] M. L. Grage, Y. Zaushitsyn, A. Yartsev, M. Chachisvilis, V. Sundström, T. Pullerits, "Ultrafast excitation transfer and trapping in a thin polymer film", *Physical Review B - Condensed Matter and Materials Physics* **2003**, *67*, 1–5.

[249] N. P. Wells, B. W. Boudouris, M. A. Hillmyer, D. A. Blank, "Intramolecular exciton relaxation and migration dynamics in poly(3-hexylthiophene)", *Journal of Physical Chemistry C* **2007**, *111*, 15404–15414.

[250] X. Yang, T. E. Dykstra, G. D. Scholes, "Photon-echo studies of collective absorption and dynamic localization of excitation in conjugated polymers and oligomers", *Physical Review B - Condensed Matter and Materials Physics* **2005**, *71*, 1–15.

[251] N. Banerji, S. Cowan, E. Vauthey, A. J. Heeger, "Ultrafast relaxation of the poly(3-hexylthiophene) emission spectrum", *Journal of Physical Chemistry C* **2011**, *115*, 9726–9739.

[252] T. Kobayashi, "Ultrafast relaxation in conjugated polymers with large optical nonlinearity", *Synthetic Metals* **1992**, *50*, 565–581.

[253] N. M. Albu, D. J. Yaron, "Brownian dynamics model of excited-state relaxation in solutions of conjugated oligomers", *Journal of Physical Chemistry C* **2013**, *117*, 12299–12306.

[254] E. Collini, G. D. Scholes, "Coherent intrachain energy migration in a conjugated polymer at room temperature", *Science* **2009**, *323*, 369–373.

[255] S. Westenhoff, W. J. Beenken, R. H. Friend, N. C. Greenham, A. Yartsev, V. Sundström, "Anomalous energy transfer dynamics due to torsional relaxation in a conjugated polymer", *Physical Review Letters* **2006**, *97*, 1–4.

[256] E. Busby, E. C. Carroll, E. M. Chinn, L. Chang, A. J. Moulé, D. S. Larsen, "Excited-state self-trapping and ground-state relaxation dynamics in poly(3-hexylthiophene) resolved with broadband pump-dump-probe spectroscopy", *Journal of Physical Chemistry Letters* **2011**, *2*, 2764–2769.

[257] R. Binder, I. Burghardt, "First-principles quantum simulations of exciton diffusion on a minimal oligothiophene chain at finite temperature†", *Faraday Discussions* **2020**, *221*, 406–427.

[258] R. Hildner, A. Köhler, P. Müller-Buschbaum, F. Panzer, M. Thelakkat, "Π-Conjugated Donor Polymers: Structure Formation and Morphology in Solution, Bulk and Photovoltaic Blends", *Advanced Energy Materials* **2017**, *7*.

[259] U. Lemmer, R. F. Mahrt, Y. Wada, A. Greiner, H. Bässler, E. O. Göbel, "Picosecond hopping relaxation in conjugated polymers", *Chemical Physics Letters* **1993**, *209*, 243–246.

[260] A. P. Horsfield, D. R. Bowler, H. Ness, C. G. Śnchez, T. N. Todorov, A. J. Fisher, "The transfer of energy between electrons and ions in solids", *Reports on Progress in Physics* **2006**, *69*, 1195–1234.

[261] T. Nelson, S. Fernandez-alberti, A. E. Roitberg, S. Tretiak, "Electronic Delocalization, Vibrational Dynamics, and Energy Transfer in Organic Chromophores", **2017**, DOI 10.1021/acs.jpclett.7b00790.

[262] S. Al-Assam, S. R. Clark, D. Jaksch, "The tensor network theory library", *Journal of Statistical Mechanics: Theory and Experiment* **2017**, *2017*.

[263] N. Banerji, "Sub-picosecond delocalization in the excited state of conjugated homopolymers and donor-acceptor copolymers", *Journal of Materials Chemistry C* **2013**, *1*, 3052–3066.

[264] M. Schlosshauer, *Decoherence and the quantum-to-classical transition*, Berlin, **2007**.

[265] S. Tretiak, A. Saxena, R. L. Martin, A. Bishop, "Conformational dynamics of photoexcited conjugated molecules", *Physical Review Letters* **2002**, *89*.

[266] F. Sterpone, P. J. Rossky, "Molecular modeling and simulation of conjugated polymer oligomers: Ground and excited state chain dynamics of PPV in the gas phase", *Journal of Physical Chemistry B* **2008**, *112*, 4983–4993.

[267] C. De Leener, E. Hennebicq, J. C. Sancho-Garcia, D. Beljonne, "Modeling the dynamics of chromophores in conjugated polymers: The case of poly(2-methoxy-5-(2'-ethylhexyl)oxy 1,4-phenylene vinylene) (MEH-PPV)", *Journal of Physical Chemistry B* **2009**, *113*, 1311–1322.

[268] K. H. Park, W. Kim, J. Yang, D. Kim, "Excited-state structural relaxation and exciton delocalization dynamics in linear and cyclic π-conjugated oligothiophenes", *Chemical Society Reviews* **2018**, *47*, 4279–4294.

[269] W. Barford, J. L. Gardner, J. R. Mannouch, "Using spectroscopy to probe relaxation, decoherence, and localization of photoexcited states in p-conjugated polymers", *Faraday Discussions* **2019**, *221*, 281–298.

[270] S. Athanasopoulos, E. Hennebicq, D. Beljonne, A. B. Walker, "Trap limited exciton transport in conjugated polymers", *Journal of Physical Chemistry C* **2008**, *112*, 11532–11538.

[271] S. Athanasopoulos, E. V. Emelianova, A. B. Walker, D. Beljonne, "Modelling exciton diffusion in disordered conjugated polymers", *Organic Photonics IV* **2010**, *7722*, 772214.

[272] L. Meng, Y. Shang, Q. Li, Y. Li, X. Zhan, Z. Shuai, R. G. Kimber, A. B. Walker, "Dynamic monte carlo simulation for highly efficient polymer blend photovoltaics", *Journal of Physical Chemistry B* **2010**, *114*, 36–41.

[273] Z. Hu, T. Adachi, R. Haws, B. Shuang, R. J. Ono, C. W. Bielawski, C. F. Landes, P. J. Rossky, D. A. V. Bout, "Excitonic energy migration in conjugated polymers: the critical role of interchain morphology", *Journal of the American Chemical Society* **2014**, *136*, 16023–16031.

[274] N. Banerji, S. Cowan, M. Leclerc, E. Vauthey, A. J. Heeger, "Exciton formation, relaxation, and decay in PCDTBT", *Journal of the American Chemical Society* **2010**, *132*, 17459–17470.

[275] H. Kobayashi, S. Onda, S. Furumaki, S. Habuchi, M. Vacha, "A single-molecule approach to conformation and photophysics of conjugated polymers", *Chemical Physics Letters* **2012**, *528*, 1–6.

[276] L. G. Yang, Q. H. Zhang, W. Peng, T. C. Huang, L. C. Zeng, P. F. Gu, X. Liu, "Concentration dependence of photoluminescence properties in poly[(2-methoxy,5-octoxy)1,4-phenylenevinylene] thin films", *Journal of Luminescence* **2005**, *114*, 31–38.

[277] J. Cornil, "Influence of interchain interactions in the absorption and luminescence of conjugated oligomers and polymers: A quantum-chemical characterization", *Journal of the American Chemical Society* **1998**, *120*, 1289–1299.

[278] B. Kuei, E. D. Gomez, "Chain conformations and phase behavior of conjugated polymers", *Soft Matter* **2017**, *13*, 49–67.

[279] C. J. Collison, L. J. Rothberg, V. Treemaneekarn, Y. Li, "Conformational effects on the photophysics of conjugated polymers: A two species model for MEH-PPV spectroscopy and dynamics", *Macromolecules* **2001**, *34*, 2346–2352.

[280] N. A. Kukhta, C. K. Luscombe, "Gaining control over conjugated polymer morphology to improve the performance of organic electronics", *Chemical Communications* **2022**, *58*, 6982–6997.

[281] R. Noriega, J. Rivnay, K. Vandewal, F. P. Koch, N. Stingelin, P. Smith, M. F. Toney, A. Salleo, "A general relationship between disorder, aggregation and charge transport in conjugated polymers", *Nature Materials* **2013**, *12*, 1038–1044.

[282] S. T. Hoffmann, H. Bässler, A. Köhler, "What determines inhomogeneous broadening of electronic transitions in conjugated polymers?", *Journal of Physical Chemistry B* **2010**, *114*, 17037–17048.

[283] I. H. Nayyar, E. R. Batista, S. Tretiak, A. Saxena, D. L. Smith, R. L. Martin, "Effect of trans- and cis-isomeric defects on the localization of the charged excitations in π-conjugated organic polymers", *Journal of Polymer Science Part B: Polymer Physics* **2013**, *51*, 935–942.

[284] G. H. Brown, "Structure, properties, and some applications of liquid crystals", *Optical Society of America* **1973**, *63*, 1505–1514.

[285] D. Andrienko, "Introduction to liquid crystals", *Journal of Molecular Liquids* **2018**, *267*, 520–541.

[286] A. Brasset, N. Colaneri, D. Bradley, R. Lawrence, F. R.H, "Optical excitations in poly(2,5-thienylene vinylene)", *Physical Review B* **1990**, *41*.

[287] R. K. Lammi, K. P. Fritz, G. D. Scholes, P. F. Barbara, "Ordering of single conjugated polymers in a nematic liquid crystal host", *Journal of Physical Chemistry B* **2004**, *108*, 4593–4596.

[288] P. Gemünden, C. Poelking, K. Kremer, D. Andrienko, K. C. Daoulas, "Nematic ordering, conjugation, and density of states of soluble polymeric semiconductors", *Macromolecules* **2013**, *46*, 5762–5774.

[289] W. S. Park, "Determination of the order parameters of nematic liquid crystals by infrared spectroscopy", *Journal of the Korean Physical Society* **2000**, *37*, 331–334.

[290] D. M. Jameson, J. A. Ross, "Fluorescence polarization / anisotropy in diagnostics and imaging", *Chem Rev* **2010**, *110*, 2685'2708.

[291] T. Huser, M. Yan, "Solvent-related conformational changes and aggregation of conjugated polymers studied by single molecule fluorescence spectroscopy", *Journal of Photochemistry and Photobiology A: Chemistry* **2001**, *144*, 43–51.

[292] Y. Y. Zhou, Y. C. Xu, Z. F. Yao, J. Y. Li, C. K. Pan, Y. Lu, C. Y. Yang, L. Ding, B. F. Xiao, X. Y. Wang, Y. Shao, W. B. Zhang, J. Y. Wang, H. Wang, J. Pei, "Visualizing the multi-level assembly structures of conjugated molecular systems with chain-length dependent behavior", *Nature Communications* **2023**, *14*.

[293] S. S. Shariffudin, N. Z. Abidin, N. Z. Yahya, A. A. Aziz, S. H. Herman, M. Rusop, "Effect of solution concentration on the morphology, electrical, and optical properties of MEH-PPV thin films", *2012 10th IEEE International Conference on Semiconductor Electronics ICSE 2012 - Proceedings* **2012**, 293–297.

[294] T. Schuettfort, B. Watts, L. Thomsen, M. Lee, H. Sirringhaus, C. R. McNeill, "Microstructure of polycrystalline PBTTT films: Domain mapping and structure formation", *ACS Nano* **2012**, *6*, 1849–1864.

[295] L. Balhorn, Q. MacPherson, K. C. Bustillo, C. J. Takacs, A. J. Spakowitz, A. Salleo, "Closing the loop between microstructure and charge transport in conjugated polymers by combining microscopy and simulation", *Proceedings of the National Academy of Sciences of the United States of America* **2022**, *119*, 1–9.

[296] R. Singh, E. Giussani, M. M. Mróz, F. Di Fonzo, D. Fazzi, J. Cabanillas-González, L. Oldridge, N. Vaenas, A. G. Kontos, P. Falaras, A. C. Grimsdale, J. Jacob, K. Müllen, P. E. Keivanidis, "On the role of aggregation effects in the performance of perylene-diimide based solar cells", *Organic Electronics* **2014**, *15*, 1347–1361.

[297] M. I. Alonso, M. Campoy-Quiles in *Ellipsometry of functional organic surfaces and films*, Springer, Barcelona, **2018**, pp. 335–353.

[298] A. J. Cadby, R. Dean, C. Elliott, R. A. Jones, A. M. Fox, D. G. Lidzey, "Imaging the fluorescence decay lifetime of a conjugated-polymer blend by using a scanning near-field optical microscope", *Advanced Materials* **2007**, *19*, 107–111.

[299] T. A. Smith, K. P. Ghiggino, "A review of the analysis of complex time-resolved fluorescence anisotropy data", *Methods and Applications in Fluorescence* **2015**, *3*.

[300] H. Wang, Y. Xu, X. Yu, R. Xing, J. Liu, Y. Han, *Structure and morphology control in thin films of conjugated polymers for an improved charge transport*, *Vol. 5*, **2013**, pp. 1272–1324.

[301] A. Carta, B. Wittmann, K. Kreger, H. W. Schmidt, T. L. Jansen, R. Hildner, "Spatial Correlations Drive Long-Range Transport and Trapping of Excitons in Single H-Aggregates: Experiment and Theory", *Journal of Physical Chemistry Letters* **2024**, *15*, 2697–2707.

[302] B. Wittmann, S. Wiesneth, S. Motamen, L. Simon, F. Serein-Spirau, G. Reiter, R. Hildner, "Energy transport and light propagation mechanisms in organic single crystals", *Journal of Chemical Physics* **2020**, *153*.

[303] K. M. Gaab, C. J. Bardeen, "Wavelength and Temperature Dependence of the Femtosecond Pump - Probe Anisotropies in the Conjugated Polymer MEH-PPV: Implications for Energy-Transfer Dynamics", *Journal of Physical Chemistry B* **2004**, *108*, 4619–4626.

[304] K. M. Gaab, C. J. Bardeen, "Anomalous exciton diffusion in the conjugated polymer MEH-PPV measured using a three-pulse pump-dump-probe anisotropy experiment", *Journal of Physical Chemistry A* **2004**, *108*, 10801–10806.

[305] O. Mirzov, F. Cichos, C. Von Borczyskowski, I. G. Scheblykin, "Direct exciton quenching in single molecules of MEH-PPV at 77 K", *Chemical Physics Letters* **2004**, *386*, 286–290.

[306] H. Lin, S. R. Tabaei, D. Thomsson, O. Mirzov, P. O. Larsson, I. G. Scheblykin, "Fluorescence blinking, exciton dynamics, and energy transfer domains in single conjugated polymer chains", *Journal of the American Chemical Society* **2008**, *130*, 7042–7051.

[307] I. Scheblykin, G. Zoriniants, J. Hofkens, S. De Feyter, M. Auweraer, Van der, F. C. De Schryver, "Photoluminescence intensity fluctuations and electric-field-induced photoluminescence quenching in individual nanoclusters of poly(phenylenevinylene)", *ChemPhysChem* **2003**, *4*, 260–267.

[308] Q. Bian, F. Ma, S. Chen, Q. Wei, X. Su, I. A. Buyanova, W. M. Chen, C. S. Ponseca, M. Linares, K. J. Karki, A. Yartsev, O. Inganäs, "Vibronic coherence contributes to photocurrent generation in organic semiconductor heterojunction diodes", *Nature Communications* **2020**, *11*, 1–9.

[309] S. Tomasi, S. Baghbanzadeh, S. Rahimi-Keshari, I. Kassal, "Coherent and controllable enhancement of light-harvesting efficiency", *Physical Review A* **2019**, *100*, 1–7.

[310] E. E. Nesterov, Z. Zhu, T. M. Swager, "Conjugation enhancement of intramolecular exciton migration in poly(p-phenylene ethynylene)s", *Journal of the American Chemical Society* **2005**, *127*, 10083–10088.

[311] M. Suzuki, "Generalized Trotter's formula and systematic approximants of exponential operators and inner derivations with applications to many-body problems", *Communications in Mathematical Physics* **1976**, *51*, 183–190.

[312] B. Donvil, P. Muratore-Ginanneschi, "Quantum trajectory framework for general time-local master equations", *Nature Communications* **2022**, *13*.

[313] R. Hildner, U. Lemmer, U. Scherf, J. Köhler, "Picosecond excitation energy relaxation processes in a ladder-type π-conjugated polymer", *Chemical Physics Letters* **2006**, *429*, 103–108.